# Feasibility of a User-Independent Systematic Method for Medical Image Quality Assessment

by

Fatimah Eashour

A Thesis submitted to the Faculty of Graduate Studies of

The University of Manitoba

in partial fulfilment of the requirements of the degree of

MASTER OF SCIENCE

Department of Physics and Astronomy

University of Manitoba

Winnipeg

# *Abstract*

Commonly used image quality assessment methods are influenced by the user manual selection, or the algorithm automatic selection, of a Region of Interest (ROI). An ROI is used in measurements of the signal mean, the signal standard deviation, and a signal representing the system response such as an Edge Spread Function (ESF). Noise, artefacts and the user manual selection of a ROI size affect the interpretation of a system's response. Challenges in image quality assessment are more prominent when dealing with poor SNR imaging systems. The aim of this thesis is to develop and evaluate the feasibility of a medical image quality assessment. The method simultaneously estimates image degradation factors, applies them to the known object in the image, and compares the output with the test image. The comparison is executed in the histogram space, removing the spatial dependence present in ROI-based methods. The proposed method was tested using Monte Carlo simulated planar images of a simple disk phantom. The limitations of the proposed method are discussed. The best test results were achieved at SNR values of at least 11.0 (+0.3, -0.2) with an average error in signal and noise measurements of no more than 0.1 (+0.1, -0.1) % and an average error in the measurement of the frequency at 10% Modulation Transfer Function (MTF) of 0.1 (+0.2, -0.1) cycle/mm. At SNR values less than $\sim$ 10, conventional methods of image quality assessments are expected to be superior to the proposed method.

# *Acknowledgements*

I would like to thank my supervisor, Dr. Stephen Pistorius, for his continuous support of my M.Sc. study and research, and for his patience and motivation. In addition, I would like to thank CancerCare Manitoba and King Abdullah Scholarship Program for the funding provided during this work.

# Contents

# List of Tables

# List of Figures

# List of Abbreviations

| | |
|---|---|
| **ALARA** | **A**s **L**ow **A**s **R**easonably **A**chievable |
| **CNR** | **C**ontrast to **N**oise **R**atio |
| **CT** | **C**omputed **T**omography |
| **ESF** | **E**dge **S**pread **F**unction |
| **FOV** | **F**ield **O**f **V**iew |
| **LSF** | **L**ine **S**pread **F**unction |
| **LSI** | **L**inear and **S**hift **I**nvariant |
| **MRE** | **M**ean **R**elative **E**rror |
| **MTF** | **M**odulation **T**ransfer **F**unction |
| **NPS** | **N**oise **P**ower **S**pectrum |
| **OID** | **O**bject to **I**maging **D**istance |
| **PDF** | **P**robability **D**ensity **F**unction |
| **PET** | **P**ositron **E**mission **T**omography |
| **PSF** | **P**oint **S**pread **F**unction |
| **ROI** | **R**egion **O**f **I**nterest |
| **SID** | **S**ource to **I**mage **D**istance |
| **SNR** | **S**ignal to **N**oise **R**atio |
| **VGA** | **V**isual **G**rading **A**nalysis |

# Chapter 1

# Introduction

Medical images provide a visual representation of the interior of a body or the function of an organ for diagnostic purposes. Diagnostic testing can involve ionizing or non-ionizing radiation. Despite the usefulness of ionizing radiation, it can be a health hazard. According to the Canadian Institute for Health Information, about 4.4 million Computed Tomography (CT) exams were performed in Canada in 2012. Based on CT use as of 2007, it has been estimated that about 2% of cancer cases in the United States may be due to ionizing radiation delivered in CT examinations [1].

The energy per unit mass deposited in tissue as a result of an exposure to ionizing radiation is known as the radiation dose. In diagnostic imaging using ionizing radiation, doses must be kept as low as reasonably achievable (ALARA) without compromising the quality of the image needed to make a diagnosis. It is important to strike a balance between radiation dose and the diagnostic benefit. Various imaging tasks require different levels of image quality. Therefore, the correct characterization of image quality is essential for an optimal diagnostic test.

New imaging systems that reduce cost, improve access, eliminate the use of ionizing radiation, use scattered radiation or use advanced reconstruction algorithms to reduce the radiation dose and provide diagnostic capabilities currently not available with existing modalities, are being developed. Measurement of image quality allows for the evaluation of imaging systems during design, commissioning, and during routine quality assurance. To date, there is no gold standard for medical image quality assessment.

Image quality characterization methods can be objective, measuring the physical

parameters of an image, or clinically task-based including human observer opinion. In the later approach, measures of diagnostic performance of an image include a visual grading analysis (VGA). In VGA studies, a score is assigned to an imaging system based on the visibility of anatomical structures in the image. Some authors are in favour of the subjective assessment of medical image quality, claiming that clinical quality is not adequately reflected by the objective, purely physical, characterization of medical image quality [2]. However, other authors believe that certain defects can only be detected using the objective physical characterization of imaging systems [2]. It is important to identify a deficiency before it affects a clinical image, and the only way to accomplish this is by using physical characterization.

The more practical objective approach uses physical-technical phantoms to analyze quality parameters. The three most important parameters used to judge the quality of radiographic images are contrast, resolution and noise. Such parameters showed a good correlation with clinical quality assessment in CT VGA studies [3]. However, the current approaches used in finding these parameters are prone to error and are influenced by the user making the measurement. The current conventional methods require the acquisition of a high exposure image to evaluate the imaging system in terms of metrics such as the Signal to Noise Ratio (SNR) and Modulation Transfer Function (MTF). However, imaging systems such as Positron Emission Tomography (PET) are characterized by poor SNR, which makes image quality assessment tasks challenging and might require smoothing of the data used to execute the assessment. Smoothing can cause the loss or distortion of information.

This thesis presents a novel user-independent systematic image quality assessment method and evaluates its accuracy and precision compared to conventional methods. This method is aimed towards the quality assessment of imaging systems during design, commissioning, and during routine quality assurance. The SNR is a limiting factor of the ability to measure a system's performance. The method will be evaluated at varying SNR levels to conclude the SNR level of the imaging system that is required to give accurate quality assessment. Although it is desirable to design a quality assessment

method that is applicable to all imaging modalities, the current design is applicable to a planar x-ray imaging system. As this is a feasibility study, planar x-ray imaging was chosen as a simple medical imaging technique that does not require image reconstruction and can be assumed to be quantum noise limited. The theory behind the image analysis approach used to develop the proposed method is described in detail in Chapter 4 and uses the fundamental image theory that the output of an imaging system can be predicted if the input and the characteristics of the system are known. Chapter 2 introduces the fundamentals of image theory, and the three parameters used to assess the quality of an image: contrast, resolution and noise. In chapter 3, different methods and challenges of image quality assessment will be discussed, as will the motivation and research questions of this thesis. Chapter 4 will cover the Methods and Materials used in this thesis. The results of testing the proposed method at varying settings are shown in chapter 5, and discussed in chapter 6. Chapter 7 summarizes and concludes this work and suggests areas for future research.

# Chapter 2

# Theoretical background

## 2.1 Fundamentals of Image Theory

### 2.1.1 Linear systems

The output of an imaging system is a function of the input, where the function is called the system response or transfer function. This applies to imaging systems of any number of dimensions, but to ensure consistency throughout this document, functions are expressed with two dependent variables ($x$ and $y$) representing 2D images. For a continuous 2D imaging system, the output ($g$) to input ($f$) relationship can be described by

$$g(x,y) = H\{f(x,y)\} \tag{2.1}$$

where $H$ is the system transfer function. Equation 2.1 implies that the output of an imaging system can be predicted if the input and the characteristics of the system are known. Image analysis using this approach is greatly simplified by making two fundamental assumptions: linearity and shift invariance (LSI). These assumptions imply that there is a common transfer function that applies to all pixels within the image [4].

**Linearity**

The output of a linear system can be expressed as a weighted sum of input components. To illustrate, the output of a system presented with two inputs $f_1$ and $f_2$ is

$$H\{af_1(x,y) + bf_2(x,y)\} = H\{af_1(x,y)\} + H\{bf_2(x,y)\} = ag_1(x,y) + bg_2(x,y). \quad (2.2)$$

The response of many imaging systems is either approximately linear or can be linearized. With linearity assumption, the transfer function can be formulated as the following integral

$$g(x,y) = \iint f(x',y')H(x,y,x',y')dx'\,dy'. \quad (2.3)$$

This applies to an analog imaging system. For a digital imaging system, the output is given as an array of discrete values, with the transfer function represented by the multiplication of a matrix $H$ as follows:

$$g = Hf, \quad (2.4)$$

Each element in $g$ of a digital system is known as a 'pixel' or 'pixel element' in 2D and a 'voxel' or 'volume element' in 3D, while each element in $f$ is known as a 'del' or 'detector element' of the digital system. The value of each pixel is the result of a unique weighted sum of the dels. Therefore, the size of $H$ in Equation 2.4 is the size of $g$ (or $f$) squared; for an $m \times n$ elements $f$, $H$ has $(mn)^2$ elements [4].

**Shift invariance**

Shift invariance implies that the system response is the same throughout the image. Thus, the system transfer function $H$ is not directly dependent on position and can be formulated without specifying the point of origin. With this assumption, the integral in Equation 2.3 can be written as a convolution:

$$g(x,y) = \iint f(x',y')h(x-x',y-y')dx'\,dy'. \quad (2.5)$$

where the system transfer function, $h$, became a function of two variables instead of four variables for $H$ in Equation 2.3. For a digital shift invariant system, $H$ in Equation 2.3 is a Toeplitz matrix. The Toeplitz matrix is a diagonal-constant matrix, that has constant entries along each descending diagonal from left to right. The Toeplitz matrix is often approximated by a circulant matrix where each row vector is rotated one element to the right relative to the preceding row vector. This is valid for the case where the size of the detector is large compared to the size of the point spread function (PSF). $H$ in Equation 2.4 now has only $mn$ distinct elements instead of $(mn)^2$ when assuming an LSI system. This allows the construction of a new matrix $h$ from $H$, and Equation 2.4 becomes

$$g = h \circledast f, \tag{2.6}$$

where $\circledast$ is the circulant convolution operator. For the case of a 2D detector, the system response function $h$, the input $f$ and output $g$ in Equation 2.6 are all $m \times n$ distinct elements matrices cyclically extended in each direction.

Most imaging systems are not truly shift invariant. For example, considering diffusion between detector elements, and systems where a pixel value is equal to the average of the signals received by multiple dels, pixels within an image do not have the same number of neighbouring pixels in each direction, making the system shift variant. Also, as the size of dels is not infinitesimal, a shift in space with a magnitude smaller than the dimension of one del gives a different image of the object. However, if blurring between pixels is small compared to the size of the image, then most systems can be treated as being shift invariant [4].

### 2.1.2 Stochastic properties

In addition to degradation from blurring, images from all real imaging systems are degraded by the presence of noise. Several sources contribute to noise within an image, including the generation, propagation and transformation of the signal carriers (photons in case of x-ray imaging), and additive noise sources such as the imaging electronics. Each image will have a unique realization of noise. Equation 2.4, which represents

image transfer in a digital system, can be modified to reflect the addition of noise as follows:

$$\dot{g} = Hf + \dot{n}, \tag{2.7}$$

where the diacritic emphasizes a uniqueness. This is a simplification since some noise is acted upon by the transfer function, as it is generated intrinsically within an input, while noise such as the electronics noise is not acted upon by the transfer function.

Due to the presence of noise, the performance of an imaging system needs to be evaluated statistically. The nature of the noise present while recording the image and characteristics of the imaging system will both have an effect on the resulting image. The linearity assumption of a system or its linearizability helps makes the treatment of images with added noise, tractable. However, an assumption that the noise is stationary is necessary. A shift in time or space does not change a stationary stochastic noise process. A process in which only the mean and covariance are stationary is known as weak or wide sense stationary. A Poisson process is modelled by one parameter, the mean, while a Gaussian process is modelled by two parameters, the mean and variance. Therefore, an imaging system is typically required to be wide sense stationary. In general, noise in almost all imaging systems is commonly treated as being Gaussian with a zero mean.

To estimate the actual signal in a pixel devoid of noise, the value in that pixel can be averaged over multiple images of the same scene to minimize the effect of noise on the measured signal. Similarly, the noise in a pixel can be estimated by the standard deviation of the measured value of that pixel over multiple images of the same scene. It is time consuming to carry out calculations of such methods as they require the acquisition and processing of many images in order to achieve the necessary accuracy. However, the assumption of ergodicity, that is, a single realization being representative of statistical properties, simplifies this problem. Therefore, the average of a signal can be estimated by either averaging over a region of a uniform scene in a single image or by averaging a single pixel over multiple images [4].

### 2.1.3 Sampling Theory

In contrary to screen film images that are continuously defined throughout the field of the image, digital images are only defined at discrete sampling points. Continuous signal values are integrated over a finite region of space within a del to give the measurement for a sampling point. Each del has a sampling aperture that defines the region over which the signal is integrated, while the distance between the centers of adjacent dels defines the sampling pitch. An idealized 2D detector would have a del sampling aperture square in shape. The fill factor of such a detector is the squared ratio of the square aperture dimension $a'$ and the pitch $a$: $(a'/a)^2$. The fill factor can be less than one, due to the presence of regions that are not sensitive to the signal carriers. It can also be greater than one, in cases where the signal stimulates a region with dimensions larger than the sampling pitch. The resolution of a system is limited by the sampling aperture when it is larger than the sampling pitch.

A continuous function $f(x, y)$ sampled on a regular grid with spacing $a$ can be represented by the function multiplied by a Dirac comb, $comb_a$. The equivalent of multiplying by the comb function in the spatial domain is given by the convolution of its Fourier transform in the Fourier space. The Fourier transform of $comb_a$ is a comb with $\frac{1}{a}$ spacing, $comb_{\frac{1}{a}}$. The convolution of the Fourier transform of $f(x, y)$ with $comb_{\frac{1}{a}}$ is an infinite sum of replicates of the Fourier transform of $f(x, y)$ at grid points with a spacing of $\frac{1}{a}$. The frequency $\frac{1}{a}$ is known as the sampling rate. Sampling captures all frequency components below one-half of the sampling rate $\frac{1}{2a}$. This limiting frequency is known as the Nyquist-Shannon frequency. Higher frequency components present before sampling will be lost due to aliasing. Aliasing misidentifies higher frequency components in the scene as lower frequency components resulting in errors in the sampled image. Therefore, sampling must be at a frequency at least twice the maximum frequency in the function being sampled in order to avoid aliasing. However, it is not always possible to avoid aliasing in system designs [4].

## 2.2 Contrast

Contrast can be defined as the ratio of the difference in signal between two tissues or materials, to the mean signal. A small difference in signal is negligible when the signal mean is large, giving low contrast. Contrary, a small difference is significant when the signal mean is small, giving high contrast. A high contrast is a desired aspect in medical imaging, to allow easy visualization of disease features. A common definition of contrast in medical imaging is the Weber contrast, or local contrast, defined as:

$$C = \frac{f_f - f_b}{f_b}, \tag{2.8}$$

where $f_f$ and $f_b$ are the signals of the feature and background, respectively. The definition of contrast in Equation 2.9 is applicable to signal in terms of the scene $f$, image $g$, or any quantity used to display a feature. A common use of the local contrast is when analyzing small features within a large uniform background. Another common definition of contrast in medical imaging is the Michelson or modulation contrast:

$$C_M = \frac{f_{max} - f_{min}}{f_{max} + f_{min}}, \tag{2.9}$$

where $f_{max}$ and $f_{min}$ are the highest and lowest signals within an image, respectively. The modulation contrast is used when the amounts of bright and dark features within an image are similar [4].

## 2.3 Unsharpness

A relevant image degradation effect when measuring the contrast of an object in an image is blurring. Blurring transforms a focused point into a diffused point by spreading the signal laterally. The contrast of a small object is reduced by blurring when measured at the spatial domain. The peak signal of an object is only affected when the width of the blurring function is larger than the size of the object. Therefore, the contrast of larger objects is not decreased by blurring [4].

### 2.3.1 Quantifying unsharpness

The response of an LSI imaging system can be measured from the image of an impulse function. Mathematically, setting the input function to equal a delta function, the right side of Equation 2.5 becomes:

$$g(x,y) = \iint \delta(x',y')h(x-x',y-y')dx'\,dy' = h(x,y). \tag{2.10}$$

The system transfer or response function in the spatial domain is referred to as the point spread function (PSF). Depending upon the imaging system, the PSF is commonly assumed to be either separable:

$$h(x,y) = h(x)h(y), \tag{2.11}$$

or radially symmetric:

$$h(r) = h(x,y). \tag{2.12}$$

The blurring of an object can also be quantified in the Fourier domain. To illustrate, a given input signal such as

$$f(x,y) = A + B\,\sin(2\pi(ux+vy)), \tag{2.13}$$

is degraded by the system transfer function $\tilde{h}(u,v)$ to give an output

$$g(x,y) = A\tilde{h}(0,0) + B\,|\tilde{h}(u,v)|\,\sin(2\pi(ux+vy)). \tag{2.14}$$

Ignoring any phase shift of the output relative to the input for simplicity, the modulation contrast of the input is:

$$C_f = \frac{A+B-(A-B)}{A+B+A-B} = \frac{B}{A}, \tag{2.15}$$

while the modulation contrast of the output is:

$$C_g = \frac{B\,|\tilde{h}(u,v)|}{A\tilde{h}(0,0)}. \tag{2.16}$$

The absolute value ratio of $\frac{C_g}{C_f}$ at a given spatial frequency $(u, v)$ is known as the modulation transfer function (MTF):

$$MTF = \frac{|\tilde{h}(u,v)|}{\tilde{h}(0,0)}, \tag{2.17}$$

which is used as a function to quantify contrast amplitude or blurring as a function of spatial frequency. The MTF has been used in the evaluation of focal spots [5, 6, 7], films [8], screens [9], motion, and total systems in diagnostic radiography [10].

The 2D or 3D PSF and MTF of 2D or 3D imaging systems are measured as a response to an impulse function. An impulse function can be generated by a point source phantom such as a pinhole in radiography, or a wire in a slice in axial Computed Tomography (CT). However, MTF is more commonly measured in a single dimension. This can be accomplished by imaging a thin slit formed by two metal bars in radiography. The slit is used to measure the line spread function (LSF). To improve the definition of the LSF tails, multiple slit images are superimposed. The LSF is the integral of the 2D PSF, and the LSF and the 1D MTF are Fourier transform pairs. The LSF is defined to have an integral over all space equal to unity, which implies that the MTF must have an amplitude of one at zero-frequency. Therefore, it is recommended by the International Electrotechnical Commission (IEC) to scale the MTF at all frequencies to force the zero-frequency value to unity [11].

Another method used to measure the 1D MTF is to image an edge [12, 10]. The profile is known as the edge spread function (ESF), or edge response function, and is the integral of the LSF. The ESF is the currently preferred method of measuring radiographic systems response. The reason is that it is easy to produce an edge for most imaging systems, and the ESF allows the measurement of the presampled MTF of digital systems, which is discussed later in this section [4].

### 2.3.2 Measuring unsharpness

#### Limiting spatial resolution

Spatial resolution refers to the ability of an imaging system to differentiate two objects. The maximum spatial frequency that can be modulated by the imaging system without aliasing is the system's limiting spatial resolution. High contrast objects with sharp edges are used to measure the limiting spatial resolution. Traditionally, objects used in radiology resolution measurement contain line patterns or star patterns. Thus, the units used to describe the limiting spatial resolution is typically line pairs (lp) per unit length. Contrary, the MTF is defined in terms of sine waves, thus specified as a function of spatial frequencies in cycles per unit length.

The limiting spatial resolution is not strictly related to a particular MTF value. The square wave response measured using a line or star pattern can be related to the MTF sinusoidal response by the Coltman transform. However, the signal to noise ratio (SNR) affects the ability to detect an object [4]. An imaging system resolution is commonly expressed by quoting the frequency where the MTF is 3%, 5% or 10% [13].

#### MTF

To measure the MTF of an analog system, a film for example, the image used in the measurement is first digitized. Digitization must be at a sampling rate greater or equal to the Nyquist-Shannon frequency to avoid aliasing. This can be accomplished by designing digitizer optics that eliminate aliasing, for the case of digitizing a film. The measured MTF of the digitized film image will be:

$$MTF_m = MTF_a \cdot MTF_d, \tag{2.18}$$

where $MTF_m$ is the measured MTF, $MTF_a$ is the MTF of the analog film, and $MTF_d$ is the MTF of the digitizer. The MTF of the film (or the analog system) in Equation 2.18 can be recovered if the condition that $MTF_d > 0$ is valid for the frequencies of interest.

Aliasing is unavoidable for many systems, such as for the case of amorphous-selenium based x-ray detectors. The limiting spatial resolution of selenium is much higher than what the detector pixel pitch can handle. There are two requirements to predict the correct image recorded by such a system. One is that the location of imaged objects relative to the matrix of the detector needs to be known with subpixel precision. The second is the knowledge of the system blurring before sampling, which can be determined from the presampling MTF. The presampling MTF is measured in a way that eliminates the blurring effect of the sampling aperture. A digital image of a well-defined edge at a small angle ($1.5°-3°$) relative to the matrix of pixels is used. The exact angle of the slanted edge is determined from the image. A supersampled ESF is constructed after computation of the distance of each pixel to the edge. The LSF can be calculated from the supersampled ESF, and its Fourier transform gives the MTF. This is known as the slanted edge method, and is the currently preferred method for measuring the MTF [4].

### 2.3.3 Cascaded imaging systems resolution

Cascaded systems analysis is often used with imaging systems composed of a series of individual components. The MTF of an image from such a system is determined by the blurring effect of different components, such as the blurring of the focal spot and the detector. This is a generalization of the situation where the measured MTF is the product of the MTF of the analog system and the MTF of the digitizer in Equation 2.18. The process can be described by the input image being increasingly blurred as it passes sequentially through the series of components. The use of this principle helps in improving system designs by allowing the determination of the blurring effect contribution of different components of the system [4]. Scattering of x-rays by the measurement object is an external blurring effect contributor that is also included in the analysis.

## 2.4 Noise

Image noise is a random variation of the recorded signal. Noise can be a limiting factor in the detection of objects in an image. Specifically, it has been shown that the

signal to noise ratio (SNR) is related to the ability to detect an object as will be discussed in this section [14].

### 2.4.1 Poisson nature of photons

X-ray quanta are produced according to a random process. X-ray quantum noise is seen as intrinsic fluctuation of emitted photons that follows a Poisson distribution. Given the mean number of photons arriving at a detector '$\lambda$', the probability of receiving '$n$' photons is

$$P(n, \lambda) = \frac{\lambda^n e^{-\lambda}}{n!}, \tag{2.19}$$

where $n$ is an integer and $\lambda$ is strictly positive. The variance, $\sigma^2$, of the Poisson distribution is equal to the mean. The Poisson distribution is positively skewed for a small mean. As the mean increases, the distribution becomes more symmetrical and can be approximated by a Gaussian distribution.

The mean-variance relationship of the Poisson distribution plays an essential rule in noise treatment for x-ray quantum noise limited systems. The primary determinant of image noise in an X-ray quantum noise limited system is the number of recorded photons. This can be confirmed by a log-log plot of the mean and standard deviation as a function of dose. The slope of this curve is equal to $\frac{1}{2}$ if the system is quantum noise limited. A system can be quantum noise limited over a defined range of air kerma or detector dose, which can be determined by the mentioned log-log slope method [4].

### 2.4.2 Variance and correlation

The spectrum of uncorrelated noise, also known as white noise, has equal power at all frequencies. As the production of photons is uncorrelated in both time and space, noise in x-ray imaging systems starts as white noise. Correlation can be introduced by the diffusion of secondary carriers created by the photon signal. The spread of the recorded signal from a single photon among multiple pixels results in the reduction of pixel variance, and the introduction of neighbouring pixel correlation. Noise correlation

can also be a result of spatial non-uniformity in the imaging system, such as differences in sensitivity among detector elements.

Noise correlation and covariance are not discussed further as they are beyond the scope of this thesis. However, it is worthwhile to mention that the noise properties of a system can also be analyzed in the spatial frequency domain using the noise power spectrum (NPS). The NPS is calculated from the Fourier transform of the spatial density fluctuations. Quantum noise frequencies higher than supported by the sampling grid are aliased in the same fashion as high frequency signals. It is not possible to eliminate the effect of aliasing and measure a 'presampling NPS'. Finally, whether noise aliasing is beneficial or detrimental is dependent on the imaging task [4].

### 2.4.3 Noise of a cascaded imaging system

Noise arises from a variety of sources within an imaging system, including the primary x-ray quantum noise, noise from primary to secondary quanta transduction, and additive noise sources such as the imaging electronic circuits. The correlation of the various noise sources is required for the propagation of noise, which makes this a more complicated task compared to the propagation of blurring effects [4]. Again, this topic is beyond the scope of this thesis, as the proposed image quality assessment method assumes a quantum noise limited system, as will be justified in the next section.

#### Image subtraction

Medical imaging techniques commonly involve the operation of adding or subtracting digital images. An example is contrast material enhanced imaging where a projection image with the contrast agent and a mask image, taken before administration of the contrast agent, are subtracted to eliminate the background signal. Since a given pixel value in one image is not correlated to its value in the second image, image noise is increased in the resulting subtraction image. As noise contribution adds in quadrature, the subtraction image has $\sqrt{2}$ greater noise than the source images. The mask image is usually taken at a higher dose to decrease its noise contribution [4].

**Primary and secondary quantum noise**

The concept of quantum accounting can be explained by following the process of image recording in a simple x-ray detector. First, primary photons are incident on a phosphor screen. The screen absorbs a fraction of the primary photons. Then, a large number of secondary photons are produced per absorbed primary photon, at a rate of $\sim$300-3000 secondary per primary. A lens collects a small fraction of the secondary photons, and a fraction of the collected secondary photons produces carriers in the forms of electrons and holes in the optical image receptor.

Each stage in the described process alters the noise seen in the final image. The noise arises from two main sources this model: the primary quantum noise and secondary quantum noise. The secondary quantum noise includes noise resulting from the production of secondary photons in the phosphor, their transmission through the optical system and their transduction into signal carriers in the optical image receptor. The secondary photons and the signal carriers are both identified as secondary quanta.

The generation and selection of x-ray quanta are governed by random processes. A Poisson process controls the production of primary photons. The production of secondary photons from primary photons can be treated as a Gaussian process. Binomial processes control the selection of a fraction of the secondary quanta at the lens and the optical image receptor. While the propagation of these processes can be described mathematically, the number of quanta at different stages of the imaging cascade can be used to estimate the dominant noise source in a medical image. The dominant noise source is assumed to be the stage with the minimum number of quanta. The dose in diagnostic x-ray imaging is very low, resulting in image noise domination by photon statistics [4].

## 2.5 Analysis of signal and noise

### 2.5.1 Quantum signal to noise ratio

The resolution of an imaging system is limited by different factors depending on the contrast of the image. The imaging system intrinsic blurring is the limiting factor of

the resolution of high contrast images. Two high contrast objects separated by a short distance cannot be resolved if the blurring is sufficient to merge them into one object in the image. The limiting factor of measuring the resolution of low contrast images is noise. A low contrast object, even with negligible blurring, is not detectable if the noise in the region containing the object is large, compared to the signal of the object. Since the standard deviation of the signal is used as a measure of noise, this is described as an increase in the relative standard deviation, also known as the coefficient of variation. The sensitivity of an imaging system is measured by the inverse of the coefficient of variation, a quantity known as the Signal to Noise Ratio (SNR):

$$SNR = \frac{\langle g \rangle}{\sigma_g}, \tag{2.20}$$

where $\langle g \rangle$ is the mean signal and $\sigma_g$ is the standard deviation of the signal.

As discussed previously, $\langle g \rangle$ and $\sigma_g$ can be calculated from multiple images provided no correlation with time, or with ergodicity assumption, from a region within a single image. Although x-ray quanta are not spatially correlated, most imaging systems introduce correlation in quantum noise by blurring. Thus, the standard deviation measured over a region of pixels of a uniform scene may not be representative of the actual pixel noise. Another cause of correlation affecting actual noise measurement is residual signal due to lag or ghosting in an imaging system.

The SNR is also defined as the ratio of the signal power to the noise power, often expressed in decibels (dB):

$$SNR = 10 \log \frac{P_{signal}}{P_{noise}} = 10 \log \left( \frac{A_{signal}}{A_{noise}} \right)^2 = 20 \log \frac{A_{signal}}{A_{noise}}, \tag{2.21}$$

where $P$ is the average power and $A$ is the root mean square (RMS) amplitude. This definition is used to describe the sensitivity of systems where the image data are not always positive, while the definition in Equation 2.20 is only useful for positive data [4].

### 2.5.2 Signal to noise ratio

An object might have a high quantum SNR but its visibility is reduced by low contrast relative to the image noise. Therefore, the contrast to noise ratio is often used as an alternative definition to the previously defined SNR. It is used to compare the amplitude of the signal of interest to the background noise. This SNR is defined as the ratio of the difference between the mean signals of two regions or structures, to the noise in those regions:

$$SNR = \frac{| < S_a > - < S_b > |}{\sigma}, \tag{2.22}$$

where $< S_a >$ and $< S_b >$ are the mean signals produced by an object and the background, and $\sigma$ is the standard deviation of the background signal. This SNR is also known by the names signal difference to noise ratio and contrast to noise ratio [4].

### 2.5.3 Object detection limitations

The Rose criterion states that an SNR of at least 5 is needed for an object to be distinguishable from the background [14]. In this criterion, the radiation dose used to generate an image is assumed to be the limiting factor in the detection of an object. This assumption agrees with the general goal in all imaging systems design, which is having a sensitivity limited by x-ray (primary) quantum noise. It should, however, be noted that there are other factors that limit the detection of an object, which will not be discussed in this document, including image artifacts, the impact of the local anatomy, and the abilities of the observer [4].

# Chapter 3

# A summary of methods and challenges in image quality assessment

## 3.1 Modulation Transfer Function (MTF)

The MTF and Point Spread Function (PSF) are frequently employed to evaluate the sharpness of imaging systems. The MTF of a system is traditionally measured from the response of a system to an impulse function. Phantoms which simulate point sources, line-pair structures, or an edge are used to measure the contrast amplitude as a function of spatial frequency. In methods using a scanned point source such as a microbead or a thin wire, a region of interest (ROI) is typically placed on the point source response from which the Line Spread Function (LSF) is obtained by differentiation. The Fourier transform of the LSF gives the MTF. Studies have shown that the MTF estimate can be impacted by the measurement technique and by image acquisition parameters such as beam quality, beam limitation, and processing technique. The impact of different image acquisition parameters will not be discussed as it is beyond the scope of this thesis.

The currently preferred method of measuring the 1D MTF is the slanted edge method. Earlier methods measured the MTF directly from the response of a system in the form of an image of the PSF in 2D or the LSF in 1D. These methods are prone to undersampling and aliasing since imaging an impulse funtion, such as a thin wire or a slit, produces

few data points. In addition, these methods involve somewhat cumbersome alignment requirements and can be impractical in cases such as evaluating a very high resolution imaging system where the dimensions required for the slit become impractically small. Judy [12] proposed an alternative method to measure the MTF from the image of an interface. This method is known as the slanted edge method. The interface produces an Edge Spread Function (ESF) that is differentiated to produce the LSF, and then the MTF is derived from the Fourier transform of the LSF.

When deriving the MTF as a function of frequency, the recommendation by the International Electrotechnical Commission (IEC) is to normalize the MTF by the zero-frequency value [11]. When deriving the MTF from the LSF, the LSF is measured using a finite ROI within the image. The LSF of an imaging system can have tails that are truncated by the finite ROI resulting in a measured LSF with an area less than unity. Therefore, normalizing the MTF derived from the measured LSF by the zero-frequency can lead to incorrect inflation of calculated MTF values at all spatial frequencies. A study in 1964 by Rossmann [15] reported inflation in MTF values due to the truncation of the LSF tails for a radiographic screen-film system. Rossmann has recommended measuring the LSF to at least 1% of its peak value when used to derive the MTF. A study by Carton *et al.* [16] reported a small overall effect of the size of the ROI and slanted edge on the calculated MTF curve, but a significant effect on the low-frequency drop due to glare. Carton *et al.* recommended the use of an edge test piece at least 5 cm in size for measurements.

Friedman and Cunningham [17] suggested the use of open-field normalization to avoid the inflation caused by zero-frequency normalization. The open-field normalization method gave valid estimates of the MTF provided no beam nonuniformities are within the chosen ROI, which was achieved for ROI sizes in the range of 1-15 cm. Equivalent results were obtained for zero-frequency and open-field normalizations in the limit of a large ROI. MTF values were inflated by up to 5%, 11% and 14% when using 10 cm, 2 cm and 1 cm ROIs, respectively, when normalizing by the zero-frequency value. Oscillatory behaviour is observed at high frequencies due to the LSF truncation, which

the open-field normalization method does not correct. Friedman and Cunningham suggested the use of a window function to reduce the oscillation, which is accompanied by the disadvantage of a slight blur of the MTF.

Samei *et al.* [18] compared the relative performance of the slit and edge technique in measuring the MTF. The test piece used in the slit technique was made of 2 mm thick Pb slabs with a 12.5 $\mu$m opening. Two different test pieces were used for the edge method. A translucent edge designed to transmit 10%-50% of incident x-rays was made of Pt-Ir alloy foil of 0.1 mm thickness. An opaque edge designed to absorb all incident x-rays was made of a 2 mm thick W slab. Images were acquired using a flat-panel digital radiographic system. An iterative technique was used to precisely align the slabs used to form the slit by rotating the test pieces sequentially to obtain the maximum slit transmission. To determine the presampled MTF, the slit was angled by about 2°with respect to the detector pixel array and imaged 20 times. The 20 images were summed to better define the tails of the LSF. The edge test pieces were each imaged at an angle of 2°-3°with respect to the detector pixel array. The edges were sequentially shifted away from the center of the field of view by up to 10 cm to investigate the effect of edge misalignment on the MTF measurements. In addition to experimental images, simulated slit and edge with an analytically predetermined MTF were used to evaluate the accuracy of each MTF measurement. The contrast degradation by the scatter of photons within the detector's phosphor layer, known as glare or veiling glare, was also investigated.

The most accurate MTF results in the presence of glare were for the opaque edge method. Misalignment by up to 6 cm did not affect measurements using the edge method. MTF measurements using the translucent edge could be impacted by scattering at higher beam energies. Therefore, it was advised to use an opaque edge for measurements at energies higher than 70 kV. As the MTF result was affected by the presence of glare in the image, the size of the ROI used in the analysis directly impacted the measurement. Samei *et al.* reported an ideal ROI size of $8 \times 8$ cm$^2$. The glare would not be adequately included in the results for smaller ROI sizes resulting in an inflated

MTF curve. On the other hand, using a larger ROI size would average the system's response over a larger area which increases the chance of error due to the heel effect and possible detector nonuniformities or defects in the straightness of the test piece edge.

The highest precision in the results achieved by Samei *et al.* was for the slit technique with very small margins of error for measurements even at high frequencies. The slit method exponentially extrapolates the LSF below 1% of its peak amplitude to prevent ringing due to truncation. Extrapolation results in masking of the attributes of long range glare. Therefore, the edge method was superior in defining the low-frequency drop caused by glare. In addition, the edge test piece was easier to align compared to the slit test piece. The poorer precision of the edge technique is actually not an inherent limitation of the technique but due to smoothing applied to the ESF to reduce the noise that would be enhanced by differentiation to get the LSF. The precision of the edge technique can be improved by averaging multiple images, which was not done in the study by Samei *et al.*.

Earlier, Schneider and Bushong [10] proposed a single step calculation method of the MTF from the ESF without finding the LSF as an intermediate step. They have proved that the direct method produces an MTF that follows a noiseless MTF somewhat more closely than the MTF calculated with the LSF intermediate. All MTFs were calculated for a Gaussian integral as a reasonable approximation of an edge function, with random variation in the data reflecting Gaussian noise. The direct method MTF still diverged from the noiseless MTF. However, an advantage of the direct method is that it is computationally less expensive.

Staude and Goebbels calculated the MTF of a Computed Tomography (CT) system by measuring an edge of a cylinder as in the standard ISO 15708-2:2002. Measurements were performed using cylindrical test pieces with a diameter of 65 mm that were made of brass and aluminum. From a slice perpendicular to the axis of the cylinder, a circle was fitted to the outline of the cylinder to determine the cylinder center. An averaged ESP was calculated from profiles along lines through the determined center. Both direct and non-direct methods of calculating the MTF gave nearly identical results. They have

found the biggest challenge to be the determination of the center of a cylinder with high accuracy. Averaging profiles through the wrong center gives a blurred ESF and a non-meaningfull MTF [19]. However, the size of the region used for ESF harvesting was not reported.

Staude and Goebbels also tested the method of determining the spatial resolution from line-pair structures for comparison with the edge method. They followed the standard FprEN 16016-3:2010 to calculate a contrast factor '$R$' as a function of resolution. The line-pair structures in the test pieces alternate between air and material, have quadratic shape and equal width. The spatial resolutions measured using these structures ranged from 1.25 lp/mm to 0.2 lp/mm. The contrast factor was measured from line profiles as the difference between peak values in the cut-outs and peak values in the material bridges, normalized to the difference between the undisturbed background and undisturbed material values, multiplied by a hundred:

$$R(f) = \frac{S_{cutout}(f) - S_{bridge}(f)}{S_{background} - S_{material}} \times 100. \tag{3.1}$$

Averaged profiles through line-pair structures were used for $R$ calculations even though the standard FprEN 16016-3:2010 advises not to average line-profiles. No resolution-decreasing interpolation is required if the line-pair structures were aligned to the voxel grid. Thus the advice not to average line-profiles is illogical. Averaging increases the SNR and reduced the user influence in selecting a specific profile [19].

Measurement for both compared methods were performed using a brass test piece with a macro-CT device and an aluminum test piece with a micro-CT device. The line-pair structures and the cylinder edge results were nearly identical for the macro-CT device. However, the contrast factor values for micro-CT clustered close to zero frequency, with no possible interpretation of the spatial resolution. It was concluded that the line-pair structures method is not suitable for measuring the spatial resolution of micro-CT devices, as it is difficult to machine structures with sub-millimetre cut-outs. Contrarily, a cylinder can be easily produced with sufficient accuracy for MTF measurement [19].

## 3.2 Noise and contrast

Conventional methods that are commonly used to evaluate image quality are labor intensive. The manual selection of ROIs in uniform areas is commonly implemented in assesssing signal, noise and low-contrast properties, typically reported in terms of contrast to noise ratio (CNR)[1] and signal to noise ratio (SNR)[2] [20, 21, 22, 23, 24, 25]. The ROI-based methods are impractical for regular quality assurance routines and allow inter-user variability. Automated ROI selection allows algorithm-influence and may require priori information for low contrast objects such as the object location in reference to a detectable point in the image [26, 27].

Pierce II *et al.* developed an automated algorithm for localizing the spheres in Positron Emission Tomography/Computed Tomography (PET/CT) scans of the National Electrical Manufacturers Association (NEMA) NU-2 image quality phantom. The NEMA phantom has six spheres ranging from 10 to 37 mm in diameter, with centers at the corners of a hexagonal shape. The detection of the smallest spheres in the PET images is challenging. Therefore, the algorithm used information from both the PET and CT images to localize the spheres. An alignment between the PET and CT image volumes was crucial. The centers of the three largest spheres within the image were estimated using sphere-shaped matched filters. The centers of the three smallest sphere were estimated based on their known location in reference to the three largest spheres. Pierce II *et al.* reported an expectation of less than 0.2 mm sphere localization deviations over multiple PET acquisitions. The expected variations of signal mean and maximum values in PET ROIs, over multiple PET acquisitions, were 0.5% and 2%, respectively [27]. The accuracy of the algorithm was not reported for the lack of knowledge of the actual sphere center locations.

Christianson *et al.* developed and validated an automated method to measure noise in clinical CT images. Since the noise magnitude varies with location in CT images, they characterized noise by the most frequent noise value in homogeneous tissue regions.

[1] CNR described in previous chapters as SNR.
[2] SNR described in previous chapters as quantum SNR.

This value was called a "global noise level" and was calculated in three steps. The first step was segmenting the image into different tissue types. The analysis was limited to the soft-tissue regions of the image. The second step was generating a noise map of the standard deviation in a kernel surrounding each pixel. Choosing the kernel size was a challenge. A small kernel might exclude the noise low-frequency components. On the other hand, a larger kernel might include an excessive amount of anatomic transitions. Among the 2 to 30 mm kernel sizes investigated, the measured noise was relatively constant for kernel sizes of 6 to 20 mm. The standard deviation of each kernel was calculated using a convolution method. The third step was generating a histogram for the soft tissue standard deviations. The histogram had a high narrow peak representing homogeneous regions and a short broad tail of higher standard deviations representing transitional regions. The mode of the homogeneous regions narrow peak was taken as the global noise level. Christianson *et al.* reported an agreement between the global noise level and image noise measurements using an image subtraction technique, in an anthropomorphic phantom, with an average difference of 3.4%. They also reported an agreement between the global noise level and image noise values in an observer study, for clinical patient CT images, with an average difference of 4.7%.

The reported challenges of image quality assessment were for CT imaging systems where high exposure images were acquired to execute the quality measurement. Such challenges are expected to be more prominent with poor SNR imaging systems.

## 3.3 Motivation and Research Question

### 3.3.1 Motivation

The goal of this research is to develop a novel user-independent image quality assessment method. The two factors that motivated this study are: 1. the user-influence in manually selecting a ROI, or the algorithm-influence in automatically selecting a ROI, in measurements of a signal mean, a signal standard deviation, and a signal representing the system response such as in the form of an ESF, LSF or PSF. 2. the influence of

the ROI size, noise, and artifacts on the interpretation of the system response. The task of selecting a uniform ROI becomes more challenging as the SNR of an imaging system decreases. The need for smoothing of the data used in the execution of the image quality measurement increases as the SNR of an imaging system decreases. The probability of loss of information caused by smoothing is expected to increase.

### 3.3.2 Research Question

Can the accuracy of medical image quality assessment, especially of poor SNR imaging systems, be improved by a user-independent and systematic method that simultaneously estimates image degradation factors, applies them to the known object in the image, and compares the output with the test image to measure quality metrics? As noise is unique in every image and can only be evaluated statistically, the proposed technique uses the histogram of the non-smoothed test image of the phantom and compares it with a predicted histogram of an output image of the phantom with certain degradation factors applied. The use of a histogram of the whole image removes the spatial dependence present in ROI-based methods. The image quality assessment method is described in detail in the next chapter.

# Chapter 4

# Methods

## 4.1 Study design

The image quality assessment method described in this chapter is valid under the following assumptions:

1. The imaging system is linear.
2. The imaging system is shift-invariant.
3. The imaging system is isotropic, with a point spread function (PSF) represented by a Gaussian radially symmetric kernel.
4. The imaging system is quantum noise limited.

### 4.1.1 The cumulative histogram of a 2D disk image

Equation 2.1 implies that the output of an imaging system can be predicted if the input and the characteristics of the system are known. Image analysis using this approach is simplified by making two assumptions: linearity and shift invariance (LSI). These assumptions imply that there is a common transfer function that applies to all pixels within the image. For a 2D digital imaging systems, the blurred image output ($g$) to input ($f$) relationship can be described by

$$g = h \circledast f \,, \tag{4.1}$$

where $g$ represents the acquired image, $f$ represents the intrinsic object, $\circledast$ represents the convolution operation, and $h$ represents the point spread function (PSF) of the imaging system. A circular region '$c(r, R_{disk})$' of radius '$R_{disk}$' centered at the origin can be defined as

$$c(r, R_{disk}) = \begin{cases} 1, & \text{if } r < R_{disk} \\ \frac{1}{2}, & \text{if } r = R_{disk} \\ 0, & \text{if } r > R_{disk} \end{cases} . \tag{4.2}$$

Assuming a radially symmetric PSF, a radiograph of a disk object made of an attenuating material such as lead foil can be modeled as

$$\dot{g}(r) = h(r) \circledast [(I_{disk} - I_{BG})c(r, R_{disk}) + I_{BG}] + \dot{n} , \tag{4.3}$$

where $I_{disk}$ is the non-degraded signal value inside the circular region, $I_{BG}$ is the non-degraded background signal value outside the circular region, $R_{disk}$ is the radius of the circular region, and $\dot{n}$ is a unique realization of noise.

The advantage of choosing a disk shape phantom for this study is its rotational symmetry;

1. A disk set-up when acquiring the degraded image in a quality assurance (QA) process does not require any angular alignment with respect to the detector matrix.

2. A sharp-edged circular disk gives the ESF along many angular directions across the detector in one image.

3. A 1D profile extending from the center of a disk in a 2D image, to the farthest point within the image from the disk center, can be used to estimate the cumulative histogram of the image pixel values, given that the disk is located approximately at the center of the image or there is a rapid falloff in the ESF such that the mean pixel values near the four image edges are the same. The cumulative number of pixels within an image having a pixel value of $I_i$ at a distance $r_i$ from the center

of the disk is linear with the area of a circle with radius $r_i$. The assumption of a radially symmetric PSF is essential for this to be valid.

The axes of the ascending cumulative histogram of the pixel intensity values of the degraded 2D rectangular image of a disk was derived as a function of the distance between each pixel location and the disk center '$r$': $x(r)$ and $y(r)$, where $x(r)$ is pixel intensity values and $y(r)$ is the cumulative pixel count. The 1D profile through the center of a disk in an image with degraded spatial resolution, but no noise, can be estimated from the 1D convolution of a top-hat function with the LSF of the imaging system. The equation of a Gaussian LSF '$l(r)$' is

$$l(r) = \frac{1}{\sqrt{2\pi{\sigma_{PSF}}^2}} e^{-\frac{r^2}{2{\sigma_{PSF}}^2}} , \tag{4.4}$$

where ${\sigma_{PSF}}^2$ is the variance of the PSF (or LSF). The blurred profile through the center of the disk can be estimated as a function of the pixel location within the image with reference to the disk center by the convolution term in Equation 4.3 in 1D:

$$\begin{aligned} x(r) &= l(r) \otimes [(I_{disk} - I_{BG})c(r, R_{disk}) + I_{BG}] \\ &= \frac{I_{disk} - I_{BG}}{2} \left[ \operatorname{erf}\left( \frac{1}{\sqrt{2\pi{\sigma_{PSF}}^2}} (r + R_{disk}) \right) + \operatorname{erf}\left( \frac{1}{\sqrt{2\pi{\sigma_{PSF}}^2}} (R_{disk} - r) \right) \right] + I_{BG} . \end{aligned} \tag{4.5}$$

The ascending cumulative histogram of the pixel intensity values of the blurred 2D rectangular image of a disk was calculated as a function of $r$ using the equations

$$y_{blurred\,image}(r) = \begin{cases} \pi r^2 - \delta(r, m, n), & \text{if } I_{disk} < I_{BG} \\ mn - \pi r^2 + \delta(r, m, n), & \text{if } I_{disk} > I_{BG} \end{cases} , \tag{4.6}$$

and

$$\begin{aligned} \delta(r, m, n) = 2r^2 \Bigg[ & \pi - \arcsin\left(\frac{m}{2r}\right) - \frac{1}{2}\sin\left(2\arcsin\left(\frac{m}{2r}\right)\right) \\ & - \arcsin\left(\frac{n}{2r}\right) - \frac{1}{2}\sin\left(2\arcsin\left(\frac{n}{2r}\right)\right) \Bigg] , \end{aligned} \tag{4.7}$$

where $m$ and $n$ are the dimensions of the image, and $\delta(r, m, n)$ is the area of a circle of radius $r$ outside a rectangle of dimensions $m \times n$ sharing the same center.[1] As noise is unique in every image and can only be predicted statistically, a single observation is more accurately approximated in the histogram domain rather than the spatial domain. The effect of the additive noise degradation on the image cumulative histogram can be estimated by the superposition of the expected noise probability density function (PDF) and the estimated blurred image cumulative histogram;

$$y\left(r\right) = \sum_{r'} y_{blurred\,image}\left(r'\right) PDF_{noise}\left(x\left(r\right) - x\left(r'\right) + 1, x\left(r\right)\right) \ , \tag{4.8}$$

where $y_{blurred\,image}$ is as in Equation 4.6, for pixel values as determined by $x(r)$ in Equation 4.5. The Poisson $PDF_{noise}$ in Equation 4.8 has a unique variance for each pixel value corresponding to a $y_{blurred\,image}$ value in the convolution. The variance of a quantum noise limited system (${\sigma_{signal}}^2$) can be described as

$${\sigma_{signal}}^2 = \alpha I_{signal} \ , \tag{4.9}$$

or,

$${\sigma_{signal}}^2 = \alpha x(r) \ , \tag{4.10}$$

where $\alpha$ is a transformation factor and $I_{signal}$ is the quantity in which the signal is presented (e.g. intensity or fluence).

In summary, the cumulative histogram of a disk image acquired using an LSI isotropic quantum noise limited system can be estimated from five parameters: the signal within the region of the disk '$I_{disk}$', the signal outside the region of the disk '$I_{BG}$', the radius of the disk '$R_{disk}$', the standard deviation of the PSF or LSF '$\sigma_{PSF}$' to estimate the spatial resolution degradation, and a transformation factor '$\alpha$' to estimated the noise. The measured quality parameters were used to calculate the SNR and the modulation contrast

[1] Full derivation of $\delta(r, m, n)$ is in Appendix A.

'$C_M$' as in the following equations:

$$SNR = \frac{|I_{BG} - I_{disk}|}{\sqrt{\alpha |I_{disk}|}} \tag{4.11}$$

$$C_M = \frac{|I_{BG} - I_{disk}|}{|I_{BG}| + |I_{disk}|} \, . \tag{4.12}$$

### 4.1.2 Curve fitting via optimization

To estimate the parameters of a test image, including non-degraded signals and contrast, noise, spatial resolution, and radius of disk, the minimum Chi-squared ($\chi^2$) method of model fitting was used. The five-variable model described by $y(r)$ in Equation 4.8 *vs.* $x(r)$ in Equation 4.5 was fit to the cumulative histogram of the input test image by minimizing the $\chi^2$ statistic defined as the summed squares of the residuals weighted by the variance.

The following equation of $\chi^2$ was minimized by varying the parameters of the model:

$$\chi^2(\Omega_i) = \sum_j \frac{(O(\Omega_i)_j - E_j)^2}{E_j} \, , \tag{4.13}$$

where $\Omega_i$ is the $i^{th}$ set of predicted variables:

$$\Omega_i = \{R_i, I_{diski}, I_{BGi}, \sigma_{PSFi}, \alpha_i\} \, ,$$

$O$ is the observed cumulative probability of the $j^{th}$ pixel value determined by the model function, and $E$ is the expected value of the cumulative probability for the input test image of the $j^{th}$ pixel value, with $j$ values equal to the input test image pixel values. The expected values were used as estimates of the variances of the $\chi^2$-distribution, which is acceptable for a procedure governed by Poisson statistics.

Assuming the model specified by $y(r)$ in Equation 4.8 *vs.* $x(r)$ in Equation 4.5 is qualitatively correct and the differences between $O$ and $E$ are solely due to statistical fluctuations, $\chi^2$ would have a probability distribution given by the $\chi^2$-distribution with uncertainty in its expectation value. Given the expectation value of the $\chi^2$-distribution

as

$$\langle \chi^2 \rangle = K \,, \tag{4.14}$$

the variance of the $\chi^2$-distribution is

$$\sigma^2_{\chi^2} = 2K \,. \tag{4.15}$$

If the number of degrees of freedom is large, the $\chi^2$-distribution can be approximated by a Gaussian and its standard deviation can be estimated by taking the square root of the variance;

$$\sigma_{\chi^2} = \sqrt{2K} \text{ [28]}. \tag{4.16}$$

Assuming the optimization algorithm can find the correct parameter values and gives $\chi^2_{min} = K$, the confidence limits for the parameters minimizing $\chi^2$ can be estimated from a region of confidence defined by

$$\chi^2 = \left[\chi^2_{min}, \chi^2_{min} + \Delta\right] \,, \tag{4.17}$$

where $\Delta$ was chosen to be $\sqrt{2\,\chi^2_{min}}$, equivalent to a $\sim 68\%$ confidence.

**Optimization variables limits**

TABLE 4.1: Assigned lower and upper bounds to optimization problem variables.

| **Variable** | **Lower bound** | **Upper bound** |
|---|---|---|
| $R$ | 0 | half diagonal of FOV |
| $I_1$ | $I_{min}$ | $\frac{I_{min}+I_{max}}{2}$ |
| $I_2$ | $I_{min}$ | $I_{max}$ |
| $\sigma_{PSF}$ | 0 | $2 \times \sigma_{PSF}$ of a Positron Emission Tomography system[2] |
| $\alpha$ | 0 | $\frac{(I_{max}-I_{min})^2}{9I_{min}}$ |

The lower and upper bounds for the five variables search in the optimization problem are presented in Table (4.1), where $I_1 = min(I_{disk}, I_{BG})$, $I_2 = max(I_{disk}, I_{BG})$, and

[2]Assuming a frequency at 10% Modulation Transfer Function of 0.05 cycle/mm for a Positron Emission Tomography system.

$I_{min}$ and $I_{max}$ are the minimum and maximum pixel values within the input test image, respectively. The upper bound of $\alpha$ was derived based on the convention that nearly all values are taken to lie within three standard deviations of the mean in a normal distribution. For the extreme case where $I_{BG} = I_{disk} = I_{min}$,

$$I_{max} - I_{min} \geqslant 3\sigma_{I_{min}}. \tag{4.18}$$

Substituting for $\sigma$ using the relation $\sigma_{I_{min}} = \sqrt{\alpha I_{min}}$ gives

$$I_{max} - I_{min} \geqslant 3\sqrt{\alpha I_{min}}. \tag{4.19}$$

Solving for $\alpha$ in Equation 4.19 gives the upper bound of $\alpha$ as in Table 4.1.

**'Ferret' evolutionary optimizer**

The problem of minimizing the $\chi^2$ function (Equation 4.13) to determine the deviation from a perfect fit was solved using 'Ferret' evolutionary optimizer from Qubist Global Optimization Toolbox for MATLAB (Jason D. Fiege, Ph.D., nQube Data Science Incorporated, 2010). In global optimization, a 'best' feasible solution or set of solutions are extracted from a problem's parameter space, based on the objectives and constraints of the problem. Ferret is a parallel multi-objective evolutionary optimizer with sophisticated machine-learning features. In evolutionary algorithms, such as Ferret, the principles of biological evolution are used as the basis for a global optimization scheme. Evolution is regarded as a directed stochastic search involving random and non-random processes. The optimization of the genome of a species is achieved by the collaboration of random processes such as mutation and non-random processes such as genetic crossover and natural selection.

Ferret has features that distinguish it from a typical genetic algorithm. These features include, but are not limited to, the following:

- Multi-objective search and parameter space mapping: although the problem in

this study had a single objective, Ferret's ability to spread solutions over an optimal region of parameter space is useful for single objective problems with data containing significant uncertainty. Ferret returns the true optimum and a scattering of solutions within a desired tolerance.

- Built-in parallelization that works independently of MATLAB's parallel computing toolbox.
- Critical parameter detection where parameters that are determined to be unimportant to the optimization are explicitly ignored, reducing the size of the parameter space.
- Linkage learning reduces a multi-parameter problem to a set of smaller sub-problems whenever possible. The linkage between parameters is dynamic and changes throughout the optimization run.
- Advanced lethal solution suppression allows the code to learn and avoid regions of the parameter space where crossovers result in poor quality solutions.
- Strategy auto-adaptation allows Ferret to improve the optimization search by dynamically adapting control parameters, such as the mutation scale and size scale of crossover events, based on the optimization progress. This auto-adaptation is valuable if control parameters are set poorly by the user.

Ferret was used in this study with a single objective, which is the minimization of the $\chi^2$ function, and no constraints. When minimizing $\chi^2$ in Equation 4.13, solutions within the region defined by Equation 4.17 were used to define an optimum predicted value and its uncertainty, with a $\sim 68\%$ confidence, for each parameter. For each generation, a single population was run with 200 individuals. To build the solution set, the optimization was terminated after at least 25 generations from where the cost function of the best solution was stable.

## 4.2 Required image processing

As the electron density of the background material is increased, the signal fall-off near the edges of the beam FOV due to scatter becomes more pronounced; the signal fall-off with a water background is greater than the signal fall-off with a vacuum background. This fall-off is not accounted for in the model estimating the cumulative histogram. Therefore in this case, during a QA, the disk image must be acquired using a larger FOV (e.g. $40 \times 40$ cm$^2$) and cropped to a smaller, global, ROI to get rid of the FOV edge signal fall-off regions.

Artifacts were not introduced to the test images used to evaluate the developed method. Applications of the proposed image analysis method would require flat field correction to get rid of fixed-pattern artifacts due to beam inhomogeneity, detector response nonuniformity, or the heel effect. A flat-field image is acquired without the phantom. Then, the phantom image acquired using the same exposure is corrected by normalization by the flat field image. The relationship between the transformation factor '$\alpha$' and noise would be affected. However, this was left as a possible future work.

## 4.3 Geometrical correction

The significance of the correction to two geometrical sources of error when using the developed method of image quality assessment with divergent beams were examined: decreased beam intensity off the beam axis, and increased attenuation at points off the beam axis due to the longer distance travelled by the beam. For the proposed image quality assessment to be practical, the user is not required to input exact measures of the phantom in the test images to apply the appropriate corrections to the image before analysis. Therefore, the significance of the corrections were assessed by comparing the results of the quality assessment with and without correction. The fluence distribution of the divergent beam was corrected to reflect the expected fluence for a parallel beam normal to the phantom. The inverse-square law corrects for a divergent beam non-uniformity across the scoring plane. The corrected fluence '$\Phi$' at a point of interest was

derived as

$$\Phi_{corrected}(x,y) = \Phi_{scored}(x,y) \cdot \frac{SID}{\sqrt{SID^2 + x^2 + y^2}} \cdot e^{-[(l_{disk}(x,y) - h_{disk}(x,y))\mu_{disk} + (l_{slab}(x,y) - h_{slab}(x,y))\mu_{slab}]}, \tag{4.20}$$

where $\mu$ is the attenuation coefficient, $SID$ is the source-image distance, $l_{disk}$ and $l_{slab}$ are the distances travelled through the disk and the slab, respectively, by a parallel beam normal to the point of interest, and $h_{disk}$ and $h_{slab}$ are the distances travelled through the disk and the slab, respectively, by the divergent beam at an angle $\theta = \arctan \frac{\sqrt{x^2+y^2}}{SID}$.[3]

## 4.4 Monte Carlo simulated images

Realistic test images used to validate the developed method were simulated using the BEAMnrc component of EGSnrc 2015 which is a publicly available Monte Carlo system of radiation transport developed by the National Research Council of Canada (NRCC). The EGSnrc code system is extensively documented and benchmarkd [29, 30]. BEAMnrc is generally used to simulate radiation-therapy external beam sources but applications in diagnostic imaging are possible. It is capable of keeping track of each particle's history (position, energy, direction and charge) at any specified plane to produce a phase-space output, from which planar fluence can be scored in circular, square or rectangular field types. Models in BEAMnrc are built up from a series of individual component modules, each of which occupy a horizontal slab. Component modules are available with cylindrical and square symmetry, which provides flexibility in user-specified geometry.

### 4.4.1 Phantom geometry

The simulated phantom is a disk made of lead, in air or a water tank as in Figure (4.1). The disk center is at the beam axis ($x = 0, y = 0$) and the water tank (slab) goes beyond the FOV. The radius of the disk in the simulated images used for validation was

[3] Formulae used to find $l_{disk}, l_{slab}, h_{disk}$ and $h_{slab}$ values are in Appendix B.

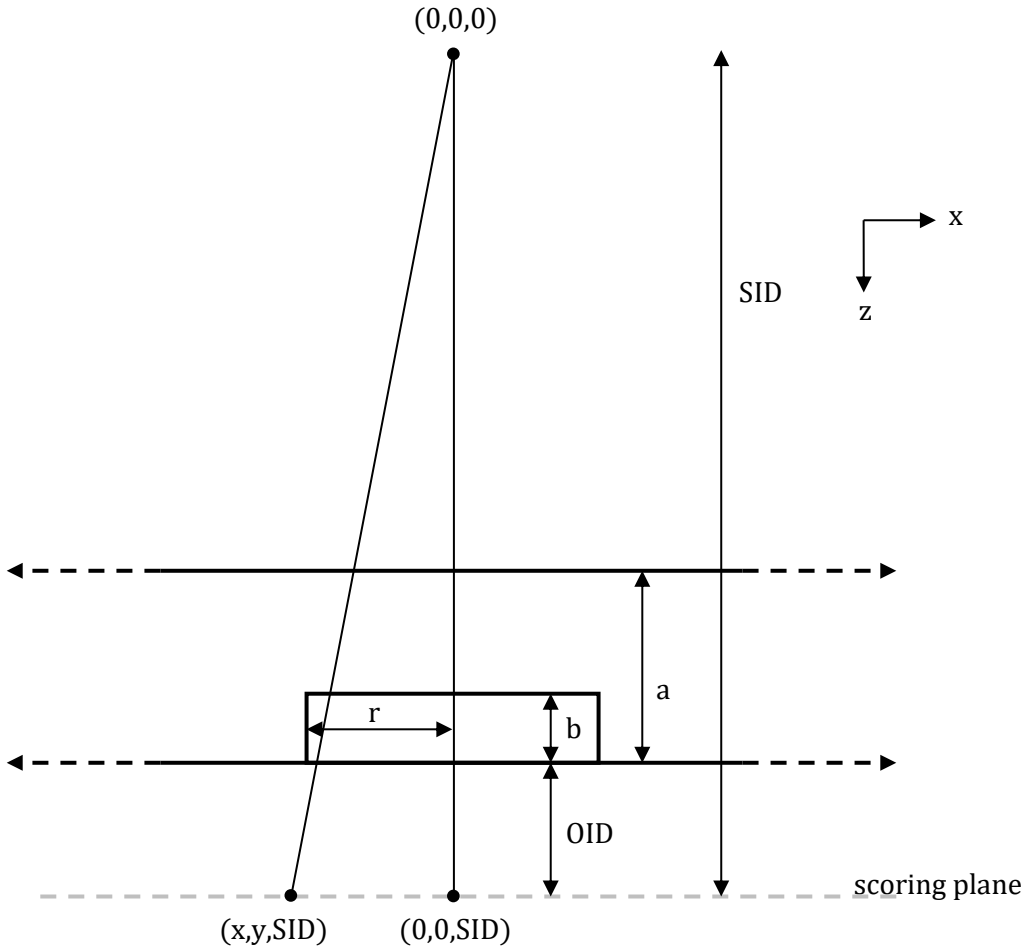


FIGURE 4.1: Simulation setup.

chosen to be 5 cm. The disk thickness was 0.1 mm, and the water slab thickness was varied between 0, 2.5 and 5 cm. Although the results of Samei *et al.* [18] suggested using an opaque edge for MTF measurements, the lead foil thickness used in the simulation allowed the transmission of a fraction of the incident radiation. This is to test the performance of the developed method in assessing the quality of the image and in object detectability as the SNR decreases.

### 4.4.2 Radiation source

Three types of beam geometry were used in the simulations: a parallel rectangular beam normal to the disk, an isotropic point source, and a defined focal spot source (sizes of 0.3, 0.6, 0.9, 1.2, 2, 3 and 4 mm). The incident beam was of 40 keV monoenergetic photons. This effective energy corresponds to a tube potential within the recommended value of $120 \pm 20$ kV for the measurement of MTF in CT [31].

### 4.4.3 Ideal detector scoring plane

The SID and the object to imaging distance (OID) were set to 120 cm and 20 cm, respectively, for all simulations. All photons transmitted through the phantom were included in calculating the fluence at a pixel size of 0.1 mm and a fill factor of 1, unless otherwise specified.

### 4.4.4 Properties of Monte Carlo simulated images

Unless otherwise specified, the following applies to all simulated images used in the assessment of our results:

- The beam energy was 40 keV.
- The simulated disk was made out of lead, had a radius of 5 cm and a thickness of 0.1 mm.
- The source to image distance (SID) was 120 cm and the object to image distance (OID) was 20 cm. The diverging beam magnification was 1.2 .

- The size of the field of view (FOV) was $20 \times 20$ cm$^2$ for parallel beams and point source images with a vacuum background, and $30 \times 30$ cm$^2$ for parallel beams and point source images with a water background. For all other geometries, the size of the FOV was $\pi \times 15^2$ cm$^2$ for images with a vacuum background, and $\pi \times 22.5^2$ cm$^2$ for images with a water background.
- A ROI of $20 \times 20$ cm$^2$ at the center of the FOV was selected for analysis.
- The pixel size used was 0.1 mm with a bit depth of 16.
- The noise was assumed to follow a Poisson distribution in the superposition step of cumulative histogram estimation.
- For the method developed in this thesis, all the parameters were initially assumed to be unknown, while the radius of the disk '$R_{disk}$' was assumed to be known for the conventional methods.
- The proposed geometrical corrections were not applied to the images prior to the quality analysis.

## 4.5 Image quality assessment using conventional methods

The parameters of the Monte Carlo simulated images were also estimated using conventional methods of image quality assessment for comparison. Conventional methods used to determine the MTF from edge devices are very sensitive to the determined edge angle of a straight edge device, or the center of a cylindrical device. Therefore, the radius and center of the disk in Monte Carlo simulated images were used as a priori knowledge. The signal mean and standard deviation at the disk region and background region were estimated from uniform ROIs. The presampled MTF was measured from an oversampled ESF without a priori knowledge of the response function. A MATLAB code was written to complete all measurements.

### 4.5.1 Fluence and noise measurements

Eight ROIs, 20 pixels in radius, were defined within each of the disk and background regions (Figure 4.2). For the background ROIs, each two ROIs were vertically or horizontally aligned at each corner of the image, with a center coordinates halfway between an image edge and the point on the disk edge closest to that edge for each axis. Similarly, each two of the ROIs within the disk region were vertically or horizontally aligned, with a center coordinates halfway between the center of the disk and a point on the disk edge closest to an image edge for each axis.

To find uniform ROIs, the background ROIs were moved towards the nearest image corner until the differences between the mean signals within all background ROIs were no more than 10 %, and the differences between the standard deviations of the signals within all background ROIs were no more than 3 %. Similarily, the disk ROIs were moved towards the center of the disk until the differences between the mean signals within all disk ROIs were no more than 10 %, and the differences between the standard deviations of the signals within all disk ROIs were no more than 3 %. After finding uniform ROIs, the average value of signal means, and the average value of signal standard deviations within the eight ROIs in the background region and the eight ROIs in the disk region were used as estimates of the disk and background signals, and to estimate a noise factor. A signal mean and standard deviation within an ROI was calculated using the MATLAB 'mean' and 'std' functions which use the following formulas, assuming the data is approximately normal,

$$\mu = \frac{1}{N}\sum A_i \tag{4.21}$$

and

$$\sigma = \sqrt{\frac{1}{N-1}\sum |A_i - \mu|^2} \tag{4.22}$$

where $\mu$ is the mean, $N$ is the number of observations, $A_i$'s are the observed data and $\sigma$ is the standard deviation.

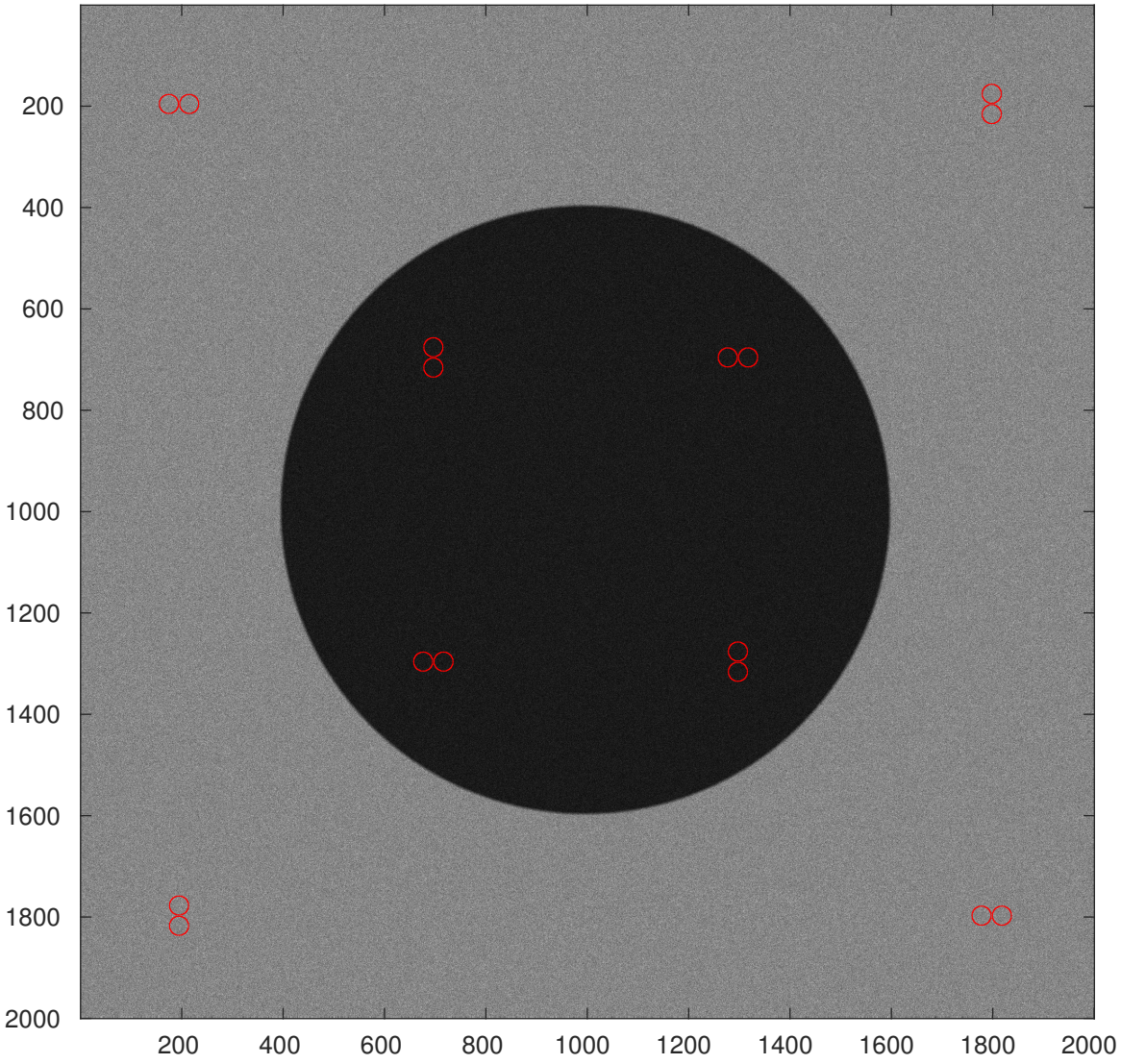


FIGURE 4.2: Initial locations of the ROIs, 20 pixels in radius, defined within each of the disk and background regions in a $2000 \times 2000$ pixels image to estimate the signal mean and standard deviation as in conventional methods.

### 4.5.2 MTF measurement

In the first processing step used to obtain the MTF, the ESF was obtained by reprojecting the image data into a one-dimensional array of sub-pixel elements as a function of distance to the given disk center location. The ESF was smoothed and interpolated at a 0.1 subpixel resolution. In the work done by Samei *et al.*, 0.1 subpixel bin spacing provided a good trade-off between sampling uniformity and noise in the ESF array [32]. The smoothing procedure followed the work by Samei *et al.*, utilizing a fourth order, Gaussian-weighted, moving polynomial fit [32]. After finding the mean ESF for each bin, each mean value was replaced with a value predicted by a second degree polynomial fitted to adjacent elements. The method of non-linear least-squares fitting was used with a Gaussian weighting function in the form of

$$f(i) = exp\left[-\left(\frac{4i}{w-1}\right)^2\right], \tag{4.23}$$

where $w$ is the window width and $i$ is a local variable defined within $[-(w-1)/2, (w-1)/2]$. A 17 element moving widow width was used. Window sizes of $17 \pm 2$ elements were used to estimate measurement uncertainty.

The second processing step to obtain the MTF used the smoothed ESF array to obtain a LSF. The LSF was obtained by numerically differentiating the ESF using the central-difference approximation method. To eliminate noise in the LSF tails, a Hanning filter with a window width of 2 cm was applied to the LSF. A fast Fourier transform (FFT) of the resulting LSF gave the MTF, which was normalized to its value at zero frequency as a final step.

## 4.6 Theoretical estimation of parameters

### 4.6.1 Fluence

The initial exposure '$\Phi_0$' was calculated as the number of incident photons (the number of histories run) divided by the area of the field of view (FOV). Then, the Beer-Lambert law, describing the exponential attenuation of a photon beam, was used to estimate the number of transmitted photons through the phantom '$\Phi$':

$$\Phi = \Phi_0 \, e^{-\left(\frac{\mu}{\rho}\right)\rho x} \, , \tag{4.24}$$

where $\frac{\mu}{\rho}$ is the mass attenuation coefficient, $\mu$ is the attenuation coefficient, $\rho$ is the density and $x$ is the thickness of phantom over which the attenuation takes place. Mass attenuation coefficients were calculated for the photon interaction cross section of lead and water using the PEGS4 program and extracted with the user code EXAMIN distributed with the EGSnrc system. The calculated values of $\frac{\mu}{\rho}$ at 40 keV were 14.36 $cm^2/g$ for lead and 0.2697 $cm^2/g$ for water. The narrow beam $\frac{\mu}{\rho}$ values give the probability of photon interaction with the phantom material, through absorption or scattering processes. Thus, the use of $\frac{\mu}{\rho}$ in Equation 4.24 gives the number of transmitted primary photons, which is a lower bound of the number of transmitted photons. At diagnostic energies, secondary photons, resulting from photon scattering interactions or the emission of fluorescent photons following a photoelectric interaction, can escape the volume over which the attenuation takes place, increasing the fluence measured by the detector. Therefore, the $\frac{\mu}{\rho}$ values were used in estimating a lower bound of the expected results, as the scattering can increase the fluence significantly with an attenuating background material. The error in measurements using the developed image quality analysis was determined based on measurements using the conventional method described in chapter 3. The conventional method measurements are valid estimations because the location and size of the disk are known for the simulated images, and the simulations are artifact free. In our method, the confidence limits for the parameters that minimized $\chi^2$ were estimated from a region of confidence within an estimated one standard deviation

of ${\chi_{min}}^2$. The conventional method's measurements of the fluence signal and standard deviation (and thus the SNR calculated from these values) were estimated with a confidence level of 0.99, as they were used as reference measurements for assessing the accuracy of the developed method.

### 4.6.2 Noise factor '$\alpha$'

The noise factor '$\alpha$' in the proposed model is a function of one parameter, as long as a quantum noise limited system assumption is valid. The theoretical value of $\alpha$ was estimated based on the sampling aperture '$a$', with $\alpha$ as a transformation factor due to conversion from the signal '$S$', the number of detected photons, to photon fluence '$\Phi$'. The Signal to Noise Ratio (SNR) expression before the transformation is

$$SNR = \frac{|S_{BG} - S_{disk}|}{\sqrt{\alpha S_{disk}}} , \tag{4.25}$$

where $\alpha = 1$, and $\sqrt{\alpha S_{disk}}$ is the estimated standard deviation of the signal, the noise, within the disk region based on the assumption of a quantum noise limited system. After the transformation

$$\Phi = \frac{S}{a^2} , \tag{4.26}$$

the SNR becomes

$$SNR = \frac{|\Phi_{BG} - \Phi_{disk}|}{\sqrt{\alpha \Phi_{disk}}} , \tag{4.27}$$

where $\alpha = \frac{1}{a^2}$.

### 4.6.3 Standard deviation of the Point Spread Function '$\sigma_{PSF}$'

The intrinsic blurring of an imaging system, due to the focal spot, imaging geometry and sampling aperture, is the limiting factor for the resolution of high contrast images. The overall Point Spread Function (PSF) of the imaging system is the convolution in the spatial space of the PSFs for individual stages of blurring. The lower limit of the size of the system's PSF can be estimated by the largest of the focal spot and the image receptor PSFs. To test the effectiveness of oversampling, the focal spot size was used in

finding a theoretical PSF lower limit, even when the image's resolution was expected to be limited by sampling.

To estimate the lower bounds of the focal spot and the detector's PSF standard deviation '$\sigma_{PSF}$,' the limiting resolution was assumed to be the spatial frequency where the MTF value is 10%. Assuming a Gaussian LSF, the 1D Fourier transform is the 1D MTF:

$$MTF\,(f) = e^{-2\pi^2 f^2 \sigma^2}\,, \tag{4.28}$$

where $f$ is the spatial frequency in cycles per unit distance. Thus, the limiting spatial frequency is

$$f_{lim} = \frac{1}{\sigma_{PSF}}\sqrt{\frac{\ln 10}{2\pi^2}}. \tag{4.29}$$

The geometric unsharpness, the inverse of the limiting spatial resolution, is a function of the source focal spot size '$X_F$,' source to image distance (SID), and object to image distance (OID):

$$\frac{1}{f_{lim}} = X_F\frac{OID}{SID}, \tag{4.30}$$

which can be divided by the magnification '$m$' to get the unsharpness at the object's plane. Since the $m$ of the object at the image plane is

$$m = \frac{SID}{SID - OID}\,, \tag{4.31}$$

Equation 4.30 can be written as

$$\frac{1}{f_{X_F lim}} = X_F\frac{m-1}{m}. \tag{4.32}$$

Solving for $\sigma_{PSF}$ in Equation 4.29 and substituting $f_{lim}$ with $f_{X_F lim}$ in Equation 4.32, gives the lower bound of $\sigma_{PSF}$, limited by the focal spot size, as

$$\sigma_{PSF\,LB_{X_F}} = \sqrt{\frac{ln10}{2\pi^2}}X_F\frac{m-1}{m} \tag{4.33}$$

at the image plane, and

$$\sigma_{PSFLB_{X_F}} = \sqrt{\frac{ln10}{2\pi^2}} X_F \frac{m-1}{m^2} \tag{4.34}$$

at the object's plane. [4].

To estimate the lower bound of $\sigma_{PSF}$ at the object's plane, limited by the sampling aperture '$a$,' the detector's resolution in the object plane was determined using

$$f_{a_{lim}} = \frac{m}{a}. \tag{4.35}$$

Then, after solving for $\sigma_{PSF}$ in Equation 4.29, $f_{lim}$ was substituted by $f_{a_{lim}}$ in Equation 4.35, to get the lower bound of $\sigma_{PSF}$, limited by the sampling aperture:

$$\sigma_{PSFLB_{detector}} = \sqrt{\frac{ln10}{2\pi^2}} \frac{a}{m}\,. \tag{4.36}$$

The resolution in terms of PSF and MTF will be reported at the object's plane.

## 4.7 Fractional agreement

The fractional agreement between measurements using the histogram method and their expected values was evaluated. For $R_{disk}$, the agreement was based on a measured confidence interval encompassing the actual value of the parameter. For the image background region fluence '$I_{BG}$' and disk region fluence '$I_{disk}$', the agreement was based on a confidence interval of the histogram method overlapping with a confidence interval of the ROI based conventional method. For $\alpha$ and $\sigma_{PSF}$, the agreement was based on a measured confidence interval encompassing the theoretical value of the parameter. The fractional agreement will be reported as a function of SNR level. For each SNR value, one image quality assessment was executed.

# Chapter 5

# Results

## 5.1 Cost function

Figures 5.1 and 5.2 show the progression after 70 and 175 generations, for the image quality analysis optimization problem of a 0.3 mm focal spot source simulated image of the disk in vacuum. The figures illustrate the number of optimal solutions, the average cost function of the solution set, the cost function bounds for the optimal solutions, a visualization of the optimal solutions for two of the optimization variables and a linkage matrix. A dark linkage map indicates that the algorithm found the optimization problem to be easy to solve and was able to divide it into smaller sub-problems instead of having to solve it as a whole. The linkage map was brighter for the assessment of an image simulated using the same source with a lower exposure (Figure 5.3).

For the quality assessments of the $2000 \times 2000$ pixel images, the cost function of the final optimal solution '$\chi^2_{min}$' was plotted for increasing image SNR (Figure 5.4). For images with an SNR of $\geqslant 12.6$ ($\pm 0.4$), $\chi^2_{min}$ had a value of $< 100$ (units of frequency of a pixel value). Unless otherwise indicated, the SNR values reported in this document are based on the conventional method measurements of the fluence and $\alpha$.

### 5.1.1 Theoretical model agreement with simulated Monte Carlo images at varying cost function of the final optimal solution '$\chi^2_{min}$'

Figure 5.5 shows the distribution of the formula $\frac{(O(\Omega_i)_j - E_j)^2}{E_j}$ before summation. This was used to compute $\chi^2_{min}$ values corresponding to the quality analysis of different

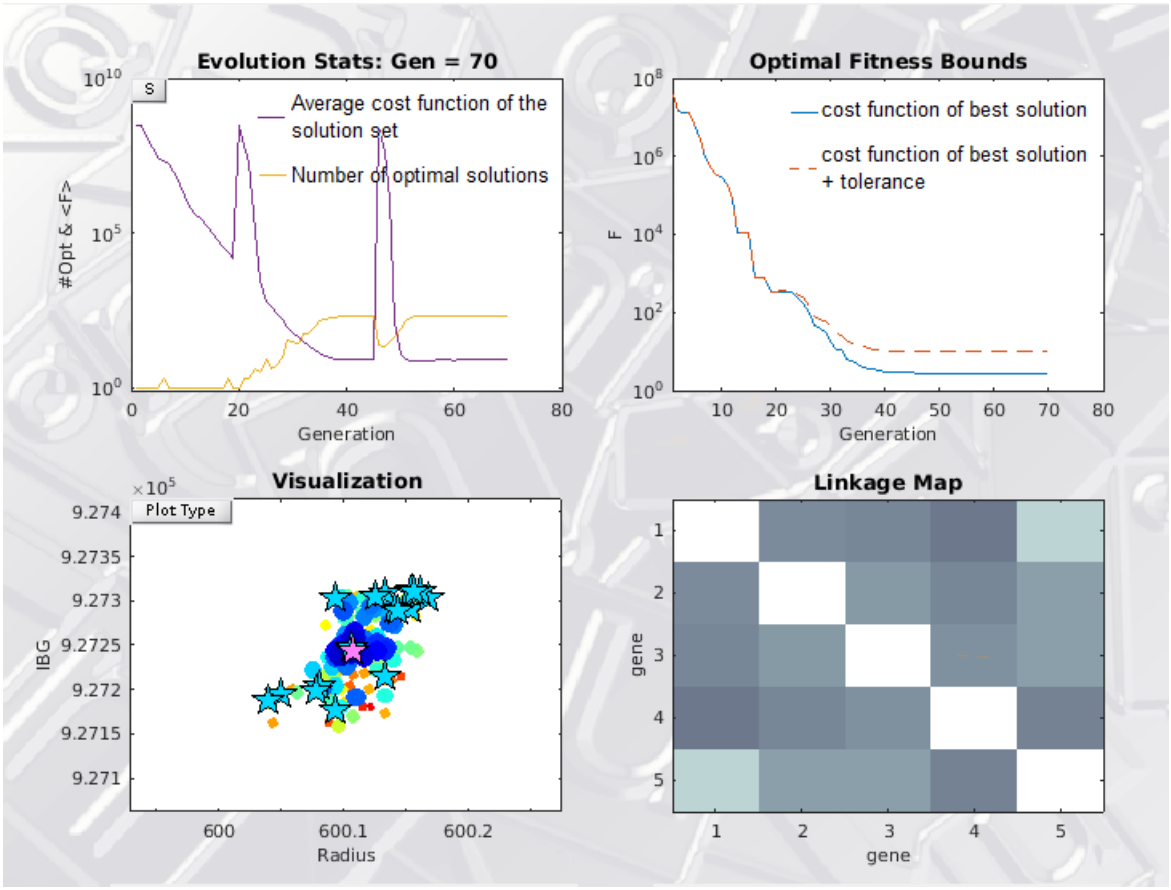


FIGURE 5.1: The Ferret console graphics showing the progression after 70 generations, for the quality analysis of a 17.1 ($\pm$0.5) SNR image of the disk in vacuum simulated using a 0.3 mm focal spot source diverging beams. The bottom-left Figure is a visualization of the optimal solutions for two of the optimization variables (the background fluence and disk radius). The bottom-right Figure is a linkage matrix where the genes are: 1. the disk radius '$R_{disk}$'. 2. the image background region fluence '$I_{BG}$'. 3. the disk region fluence '$I_{disk}$'. 4. the standard deviation of the Point Spread Function $\sigma_{PSF}$. 5. the noise factor '$\alpha$'.

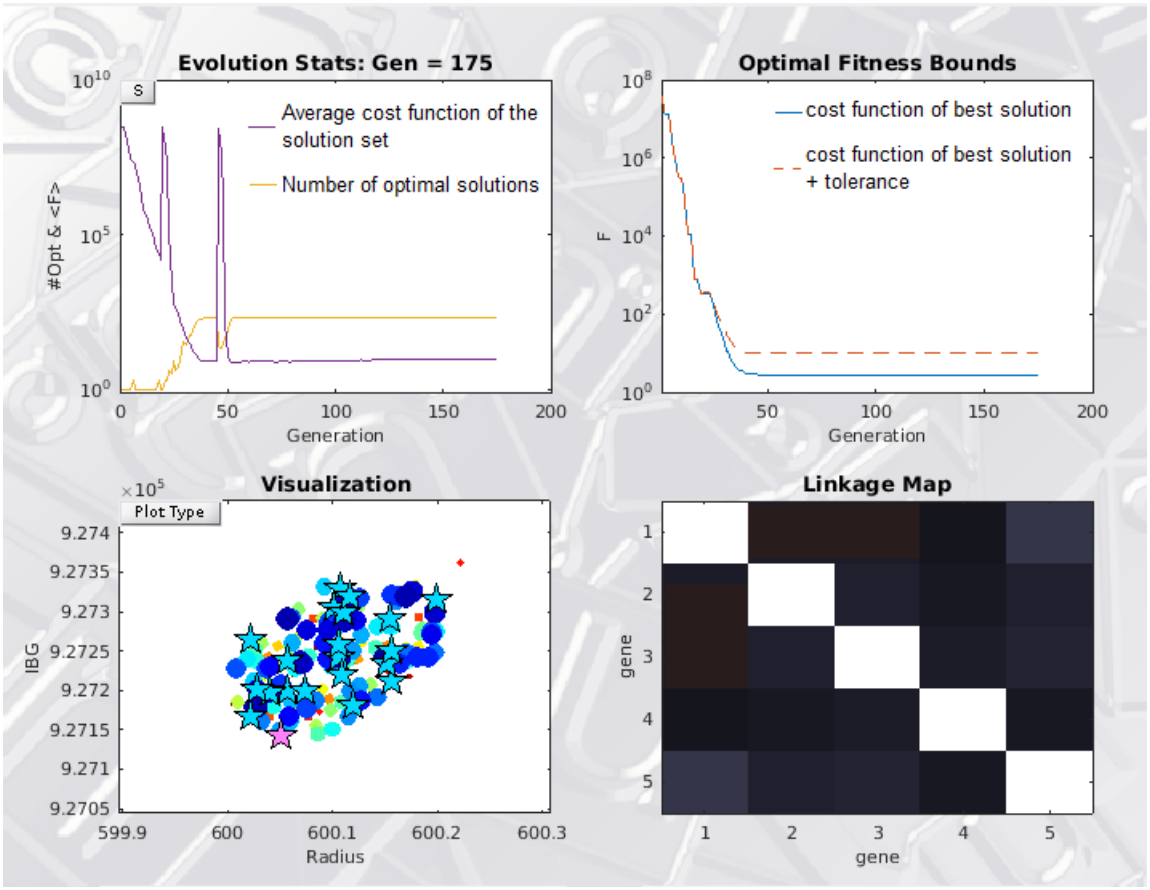


FIGURE 5.2: The Ferret console graphics showing the progression after 175 generations, for the quality analysis of a 17.1 ($\pm$0.5) SNR image of the disk in vacuum simulated using a 0.3 mm focal spot source diverging beams. The bottom-left Figure is a visualization of the optimal solutions for two of the optimization variables (the background fluence and disk radius). The bottom-right Figure is a linkage matrix where the genes are: 1. the disk radius '$R_{disk}$'. 2. the image background region fluence '$I_{BG}$'. 3. the disk region fluence '$I_{disk}$'. 4. the standard deviation of the Point Spread Function $\sigma_{PSF}$. 5. the noise factor '$\alpha$'.

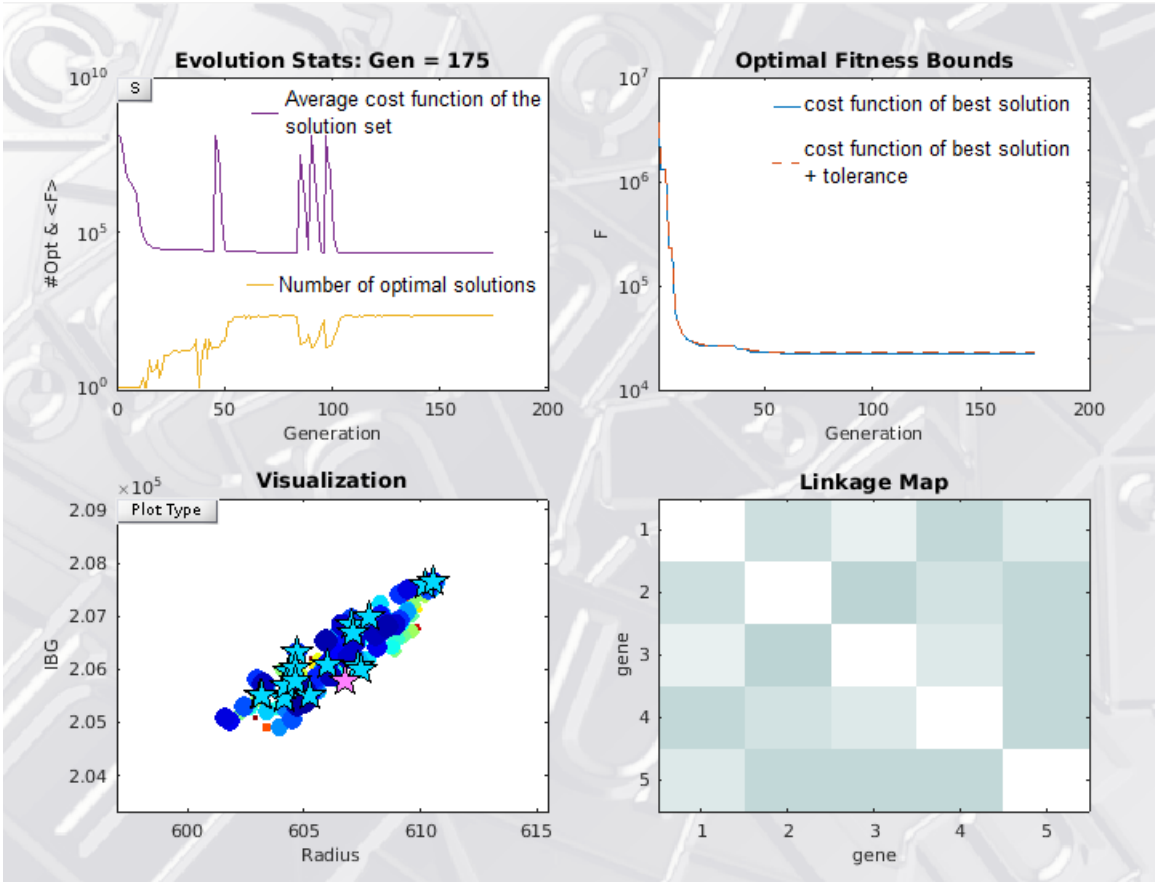


FIGURE 5.3: The Ferret console graphics showing the progression after 175 generations, for the quality analysis of a 8.1 ($\pm$0.3) SNR image of the disk in vacuum simulated using a 0.3 mm focal spot source diverging beams. The bottom-left Figure is a visualization of the optimal solutions for two of the optimization variables (the background fluence and disk radius). The bottom-right Figure is a linkage matrix where the genes are: 1. the disk radius '$R_{disk}$'. 2. the image background region fluence '$I_{BG}$'. 3. the disk region fluence '$I_{disk}$'. 4. the standard deviation of the Point Spread Function $\sigma_{PSF}$. 5. the noise factor '$\alpha$'.

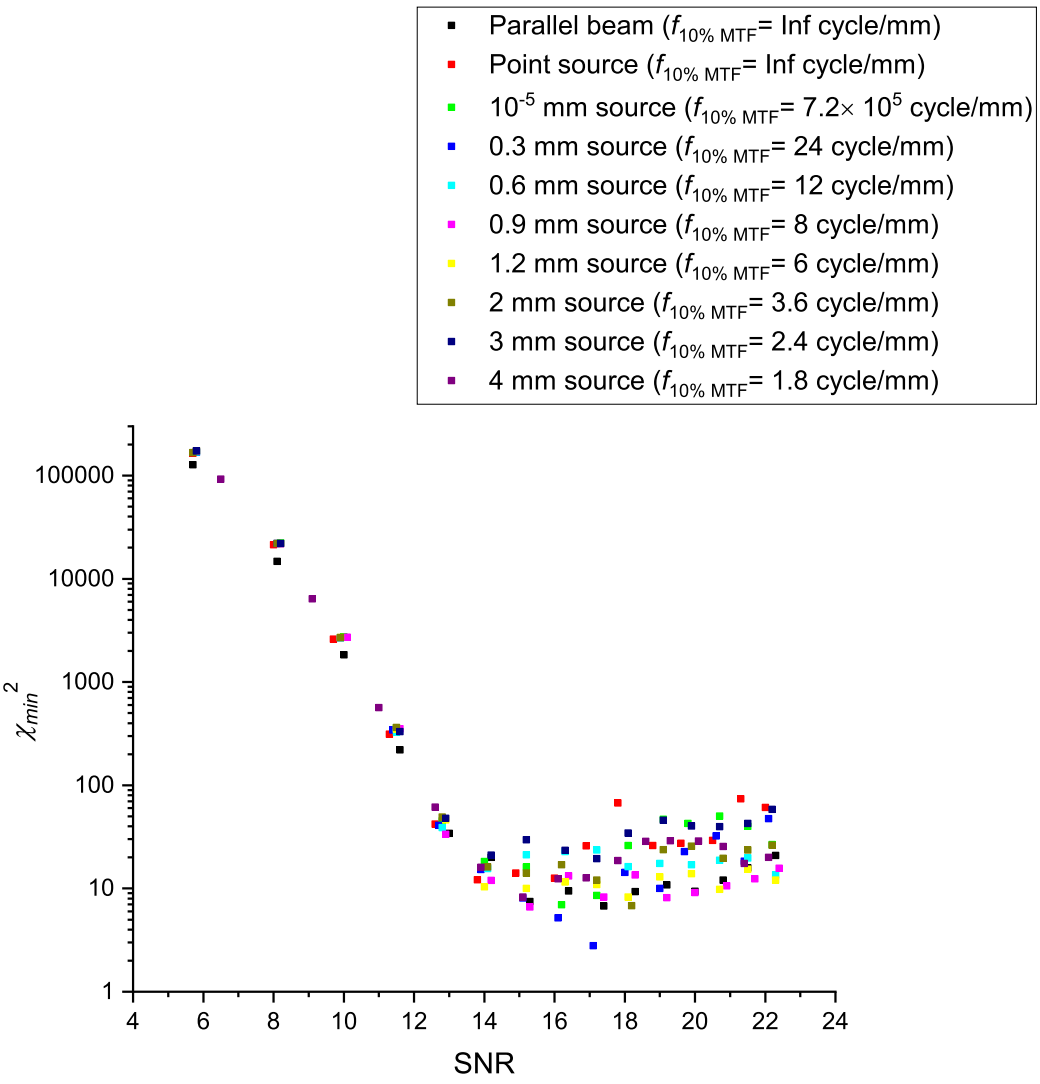


FIGURE 5.4: The final optimal solution cost function '$\chi^2_{min}$' versus SNR for the quality assessments of images simulated using parallel beams and diverging beams of focal spot sizes varying from a point source to 4 mm in diameter.

images of the phantom. As $\chi^2_{min}$ increased, a larger portion of the distribution was non-random. This indicates that the cumulative histogram generated by the theoretical model, based on the predicted parameters, had less agreement with the cumulative histogram of the actual image, as $\chi^2_{min}$ increased. Feeding the parameter values estimated using the conventional methods and the known $R_{disk}$ value into the theoretical model gave larger cost function values compared to the optimization results.

## 5.2 Initial performance assessment

To assess the performance of the developed method in measuring image quality parameters, Monte Carlo simulated images of the disk in vacuum were used. The following results are based on images of variable spatial resolution. The spatial resolution was varied by varying the focal spot size of the radiation source in the simulations. Images were simulated using parallel beams and diverging beams with source focal spot sizes of 0 (point source), $10^{-5}$, 0.3, 0.6, 0.9, 1.2, 2, 3 and 4 mm in diameter. Fifteen different exposure levels, for each beam geometry, were used.

In Figure 5.6, the average fractional agreement is plotted using a dashed line and open symbols for quality assessments of images with an SNR equal or smaller than the SNR value on the x-axis, and using a solid line and filled symbols for quality assessments of images with an SNR equal or greater than the SNR value on the x-axis. The estimated error in measurements of the image quality parameters is shown in Figure 5.7.

### 5.2.1 Disk radius '$R_{disk}$'

For SNR values of 5.7 ($\pm$0.3) to 22.4 ($\pm$0.6), the confidence interval for $R_{disk}$ contained the actual value 83% of the time, with a Mean Relative Error (MRE)[1] of 4.32 ($\pm$0.03) %. For SNR values of 9.7 ($\pm$0.3) to 22.4 ($\pm$0.6), the average fractional agreement with the actual value was 95% with an MRE of 1.402 (+0.006, -0.005) %. For SNR values smaller

[1] $MRE = \frac{1}{N}\sum\frac{|O-E|}{|E|}$, where $N$ is the number of data sets, $O$ is the observed value and $E$ is the expected value.

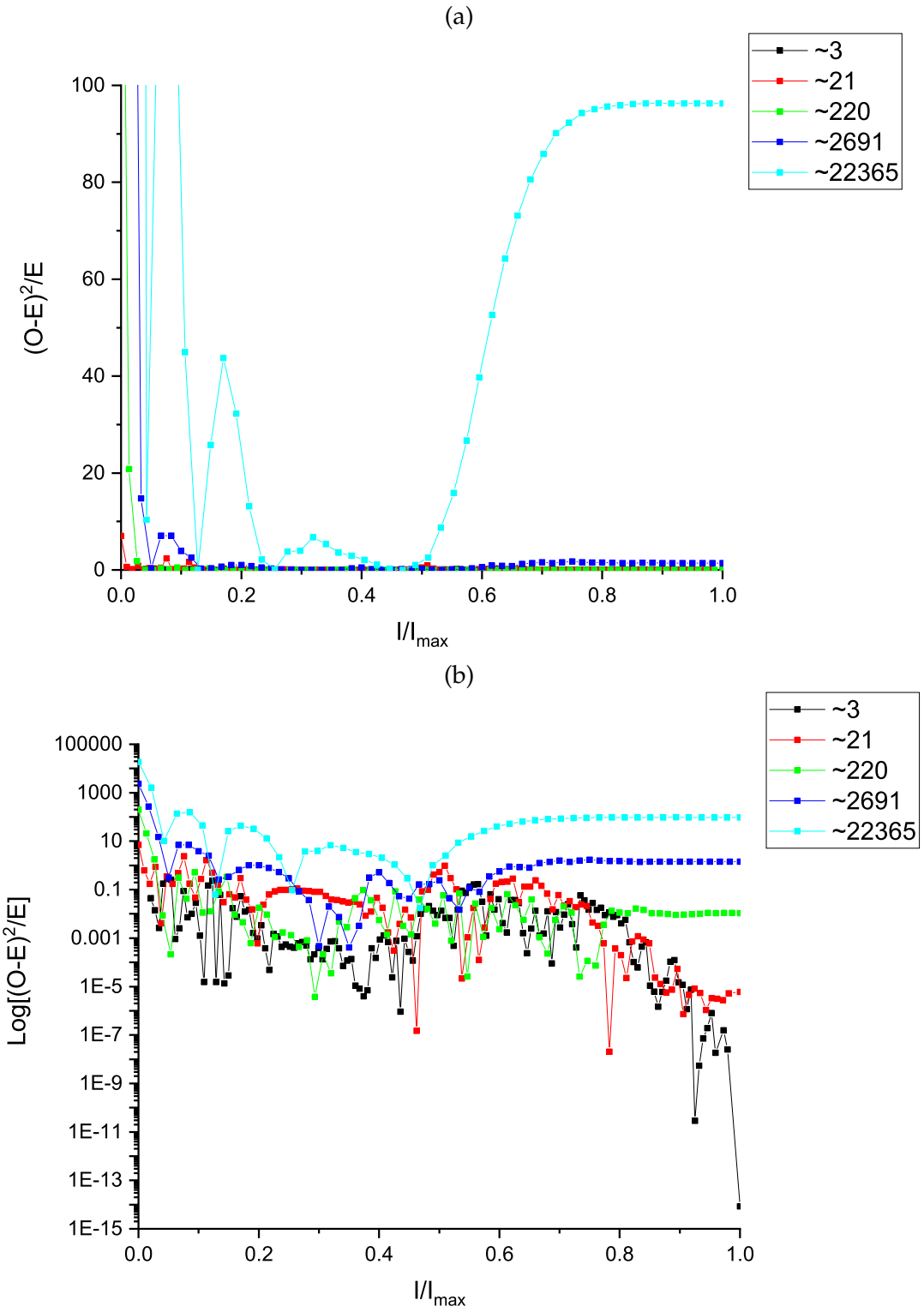


FIGURE 5.5: The distribution of the formula $\frac{(O(\Omega_i)_j - E_j)^2}{E_j}$ as a function of normalized image pixel value (normalized fluence), where $O$ is the estimated image cumulative histogram generated using the developed model and optimized image parameters, and $E$ is the actual image cumulative histogram. The distribution is in (a) linear scale and (b) logarithmic scale. The summation of the distribution gives a cost function as in the legend.

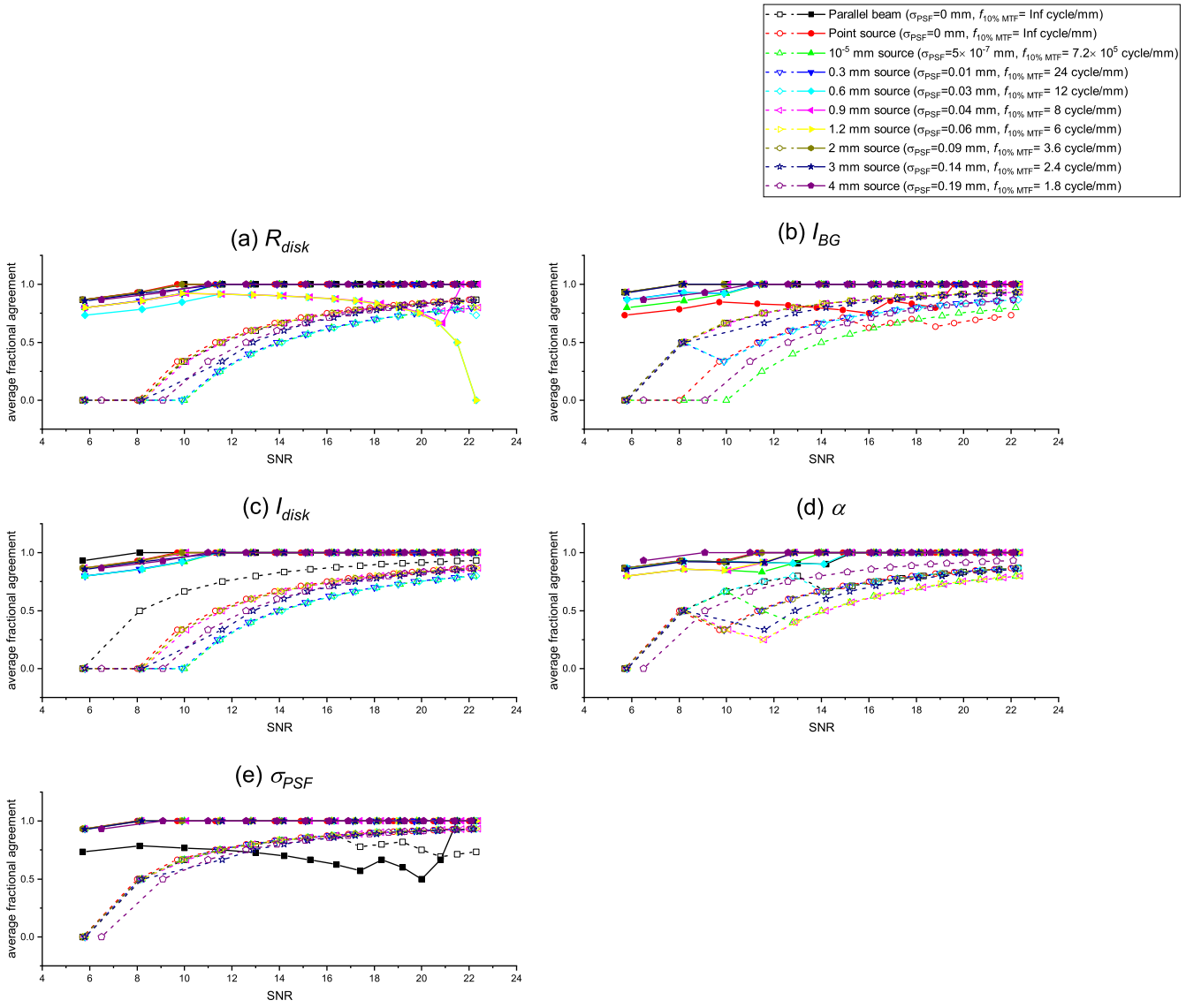


FIGURE 5.6: The average fractional agreement between measurements using the histogram method and their expected values for image quality assessments of the phantom in vacuum. The spatial resolution was adjusted by varying the focal spot size of the radiation source in the simulations. For the disk radius '$R_{disk}$', the agreement was based on a measured confidence interval encompassing the actual value of the parameter. For the image background region fluence '$I_{BG}$' and disk region fluence '$I_{disk}$', the agreement was based on a confidence interval of the histogram method overlapping with a confidence interval of the conventional method. For the transformation factor '$\alpha$' and the standard deviation of the Point Spread Function '$\sigma_{PSF}$', the agreement was based on a measured confidence interval encompassing the theoretical value of the parameter. The average fractional agreement is plotted using a dashed line and open symbols for assessments of images with an SNR equal or smaller than the SNR on the x-axis, and using a solid line and filled symbols for assessments of images with an SNR equal or greater than the SNR on the x-axis.

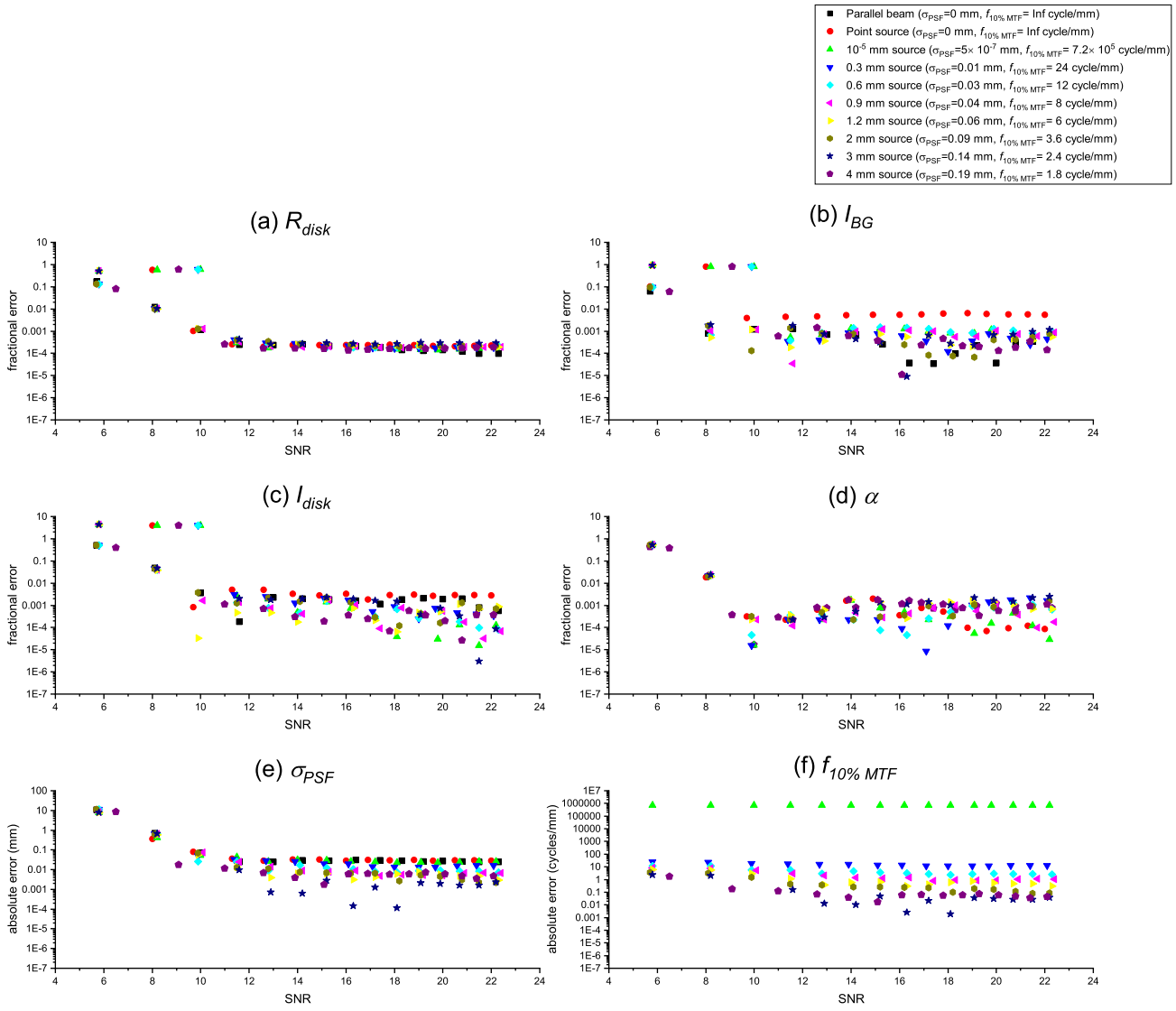


FIGURE 5.7: The magnitude of the error in parameter estimations for image quality assessments of the phantom in vacuum. The spatial resolution was varied by varying the focal spot size of the radiation source in the simulations. The error is presented as a fractional error for the disk radius '$R_{disk}$', the image background region fluence '$I_{BG}$', the disk region fluence '$I_{disk}$' and the noise factor '$\alpha$', and as an absolute error for the standard deviation of the Point Spread Function '$\sigma_{PSF}$' and the frequency at 10% Modulation Transfer Function '$f_{10\%MTF}$'. Expected values of parameters not changing with SNR: E($R_{disk}$)= 5 cm, E($\alpha$)= 10000, E($\sigma_{PSF}$) and E($f_{10\%MTF}$) are as in the legend. The detector's resolution parameters: E($\sigma_{PSF}$)= 0.03 mm, and $f_{a_{lim}}$= 12 cycle/mm. Note: the uncertainty in the error was omitted for data visualization's readability.

than 9.7 (±0.3), there was no agreement and the MRE was 23.1 (±0.2) %. For SNR values of 11.0 (±0.3) to 22.4 (±0.6), the MRE was 0.022 (±0.004) % with an average fractional agreement of 98%. For SNR values smaller than 11.0 (±0.3), the MRE was 23.0 (±0.2) % with an average fractional agreement of 18%. All errors were positive; the value of $R_{disk}$ was overestimated.

### 5.2.2 Image background region fluence '$I_{BG}$'

For SNR values of 5.7 (±0.3) to 22.4 (±0.6), the average fractional agreement between the confidence intervals of the histogram and conventional methods was 88%. The MRE, based on the conventional method measurements as the expected values, was 6.12 (±0.06) %. For SNR values of 11.0 (±0.3) to 22.4 (±0.6), the MRE was 0.11 (±0.03) %, and the average fractional agreement was 98%. For SNR values smaller than 11.0 (±0.3), the MRE was 32.1 (±0.3) %, with 43% agreement with the expected values. The error had a negative mean at SNRs < 10.1 (±0.3), and a positive mean at SNRs $\geqslant$ 10.1 (±0.3).

### 5.2.3 Disk region fluence '$I_{disk}$'

For SNR values of 5.7 (±0.3) to 22.4 (±0.6), the average fractional agreement was 85% and the MRE was 30.1 (±0.3) %. For SNR values of 10.1 (±0.3) to 22.4 (±0.6), the MRE was 0.11 (±0.06) %, with a 100% agreement with the expected values. For SNR values smaller than 10.1 (±0.3), the MRE was 166 (±2) %, with 19% agreement with the expected values. The error had a positive mean.

### 5.2.4 Noise factor '$\alpha$'

For SNR values of 5.7 (±0.3) to 22.4 (±0.6), the average fractional agreement with the theoretical value was 85%, and the MRE was 3.60 (+0.1, -0.2) %. For SNR values of 9.1 (±0.3) to 22.4 (±0.6), there was a 91% agreement with the theoretical value, and the MRE was 0.07 (+0.03, -0.05) %. For SNR values smaller than 9.1 (±0.3), the MRE was

28 (±1) %, with a 47% agreement with the theoretical value. The error had a negative mean; $\alpha$ was underestimated.

For SNR values of 5.7 (±0.3) to 22.4 (±0.6), the confidence interval of the conventional method contained the theoretical value of $\alpha$ 99% of the time, and the MRE was less than 1%.

### 5.2.5 Standard deviation of the Point Spread Function '$\sigma_{PSF}$'

For SNR values of 5.7 (±0.3) to 22.4 (±0.6), the average fractional agreement with the theoretical lower bound of $\sigma_{PSF}$ was 91%, and the mean absolute error, calculated with the theoretical lower bound as an expected value, was 0.70 (±0.03) mm. For SNR values smaller than 8.0 (±0.4), there was no agreement with the theoretical lower bound, and the the mean absolute error was 9.6 (+0.3, -0.5) mm. For SNR values of 8.0 (±0.4) to 22.4 (±0.6), the average fractional agreement was 98%, and the mean absolute error was 0.05 (+0.03, -0.01) mm. For SNR values from 9.1 (±0.3) to 22.4 (±0.6), the results had an average fractional agreement of 98% and a mean absolute error of 0.017 (+0.007, -0.004) mm. For SNR values smaller than 9.1 (±0.3), the average fractional agreement was 47%, and the mean absolute error was 5.3 (±0.3) mm. The error had a positive mean.

## 5.3 Performance assessment with variable settings

### 5.3.1 Performance with parallel and diverging beam geometries

The image quality assessment method developed in this thesis is based on a model that assumes a parallel beam geometry (excluding the proposed geometrical corrections). The applicability of the method in assessing diverging beam images, simulated with the specified beam geometry parameters (SID of 120 cm and OID of 20 cm), was tested. The results for the image quality analysis of simulations of the disk in vacuum, imaged using parallel beams and a point source diverging beams were compared.

In Figure 5.8, the fractional agreement is plotted for parallel and diverging beam geometries. The estimated error in measurements of the image quality parameters is

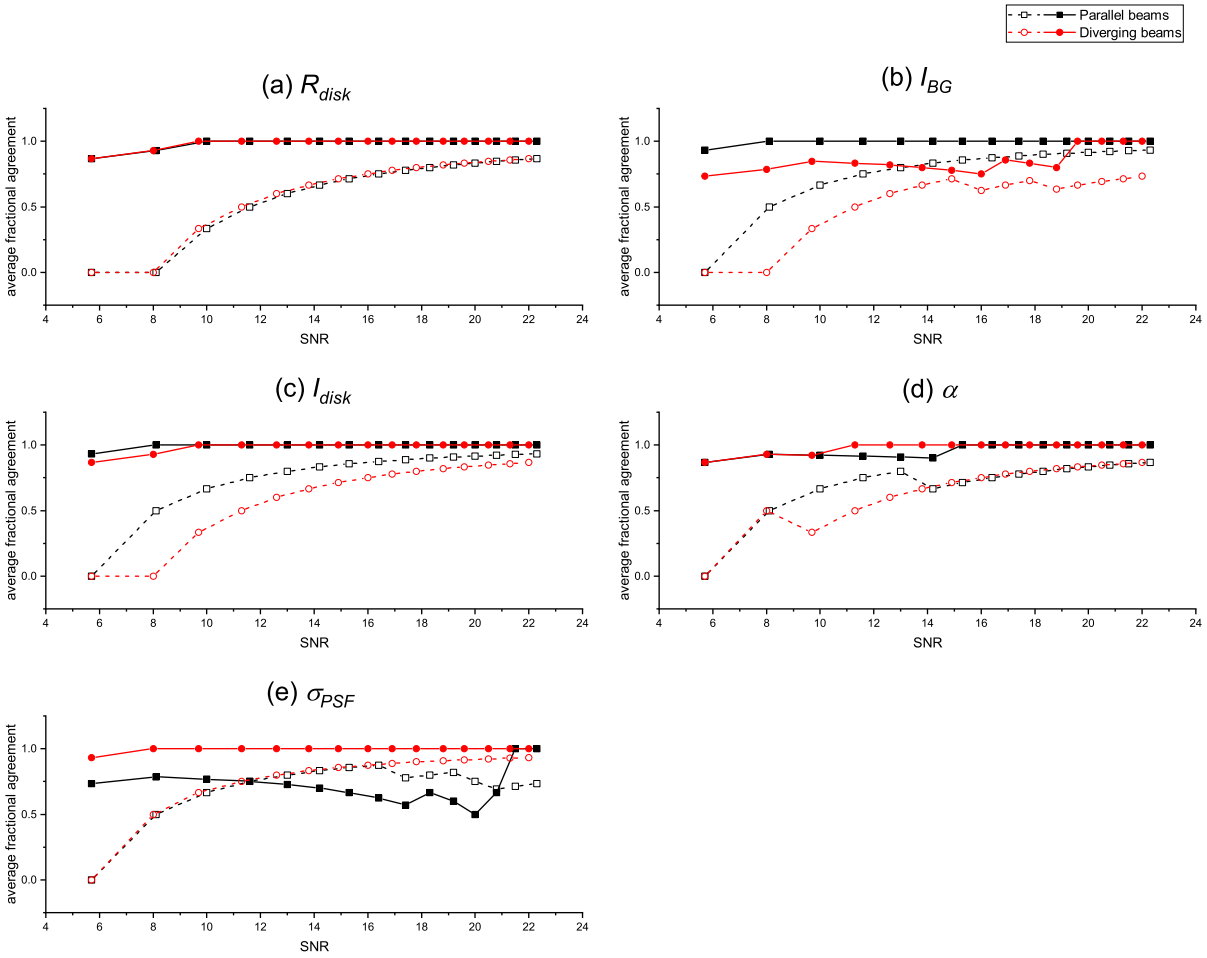


FIGURE 5.8: The average fractional agreement between measurements using the histogram method and their expected values for image quality assessments of the phantom in vacuum, imaged using parallel beams and a point source diverging beams. For the disk radius '$R_{disk}$', the agreement was based on a measured confidence interval encompassing the actual value of the parameter. For the image background region fluence '$I_{BG}$' and disk region fluence '$I_{disk}$', the agreement was based on a confidence interval of the histogram method overlapping with a confidence interval of the conventional method. For the transformation factor '$\alpha$' and the standard deviation of the Point Spread Function '$\sigma_{PSF}$', the agreement was based on a measured confidence interval encompassing the theoretical value of the parameter. The average fractional agreement is plotted using a dashed line and open symbols for assessments of images with an SNR equal or smaller than the SNR on the x-axis, and using a solid line and filled symbols for assessments of images with an SNR equal or greater than the SNR on the x-axis.

shown in Figure 5.9. For $R_{disk}$, the agreement was similar for the point source and parallel beam images, but the average decrease in the relative error with increasing exposure was larger for parallel beam sample images. For $I_{BG}$, the agreement was larger, and the relative error was always smaller, for parallel beam images. For $I_{disk}$, the agreement in assessments of parallel beam simulated images was only larger by 1 in 15 compared to point source simulated images. The relative error was mostly smaller for the parallel beam images, but the MRE was similar for the point source and parallel beam images. For $\alpha$, the agreement was similar for parallel beams and point source simulated images. Where there was not an agreement, $\alpha$ was underestimated. For $\sigma_{PSF}$, there was an agreement for 11 out of 15 parallel beams images and 14 out of 15 point source images. The estimated error in measurements of the resolution of parallel beams and point source simulated images (theoretical $f_{10\%MTF} = Inf$) will not be discussed. However, the larger agreement with the theoretical value for point source image assessments was associated with a larger uncertainty.

### 5.3.2 Performance with vacuum and water image backgrounds, and parallel beam geometry

The effect of increasing signal scattering, by changing the background material from vacuum to water, on the performance of the developed method was assessed. The results for the image quality analysis of the disk in vacuum and 5 cm water depth were compared for a parallel beam geometry.

In Figure 5.10, the fractional agreement is plotted for assessments of images with vacuum and water backgrounds. The estimated error in measurements of the image quality parameters is shown in Figure 5.11. For $R_{disk}$, $I_{disk}$ and $\sigma_{PSF}$, the average fractional agreement was larger for images with a water background. The exposure, for assessed samples with an agreement, corresponded to smaller SNR values for the simulated images with a water background. For $I_{BG}$ and $\alpha$, the agreement was larger for images with a vacuum background. The average relative uncertainty in $I_{BG}$ and $\alpha$ was

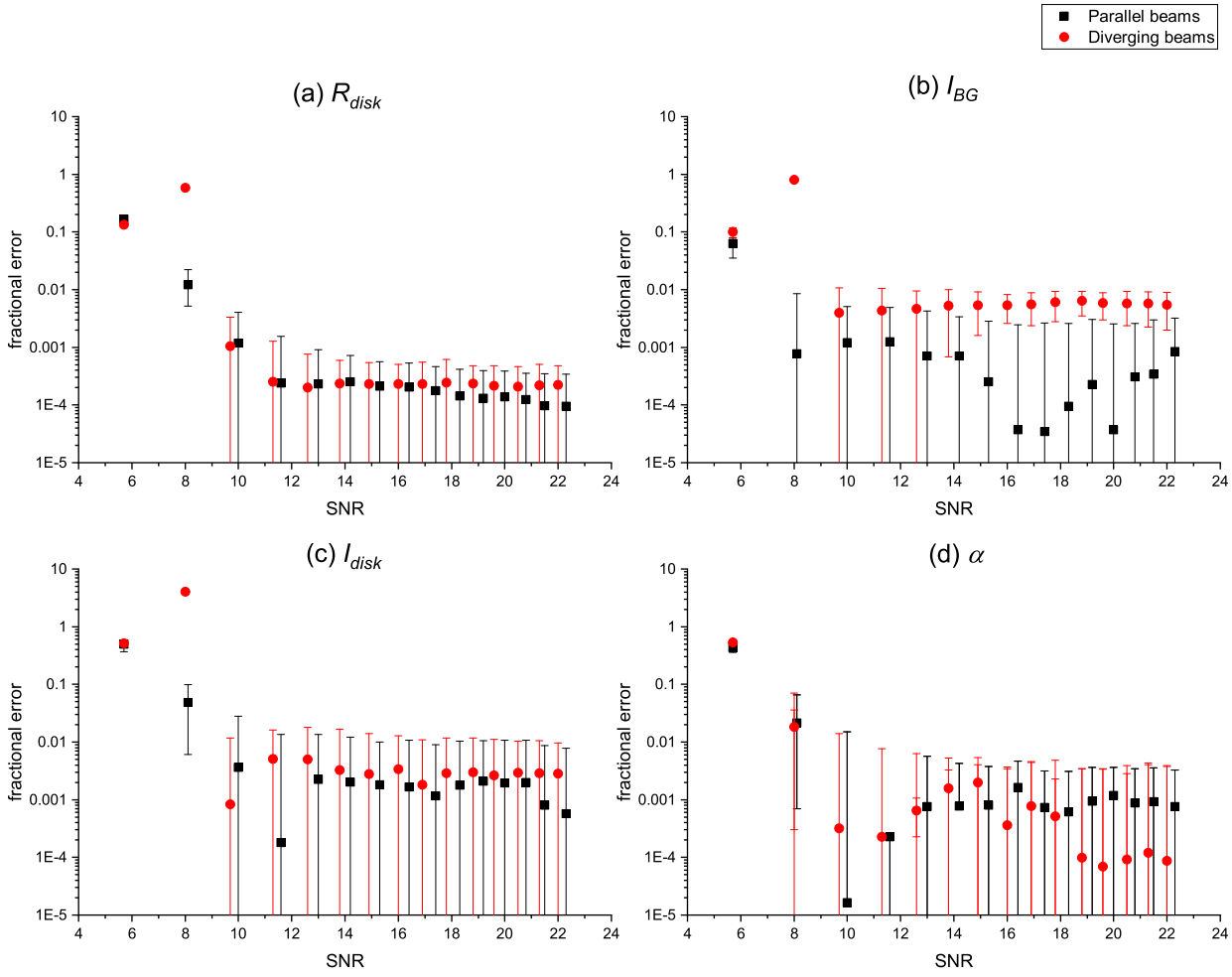


FIGURE 5.9: The magnitude of the error in parameter estimations for image quality assessments of the phantom in vacuum, imaged using parallel beams and a point source diverging beams. The error is presented as a fractional error for the disk radius '$R_{disk}$', the image background region fluence '$I_{BG}$', the disk region fluence '$I_{disk}$' and the noise factor '$\alpha$'. Expected values of parameters not changing with SNR: E($R_{disk}$)= 5 cm, E($\alpha$)= 10000, E($\sigma_{PSF}$)= 0 mm, and E($f_{10\%MTF}$)= Inf cycle/mm. The detector's resolution parameters: E($\sigma_{PSF}$)= 0.03 mm, and $f_{a_{lim}}$= 10 cycle/mm for parallel beam geometry and 12 cycle/mm for diverging beam geometry.

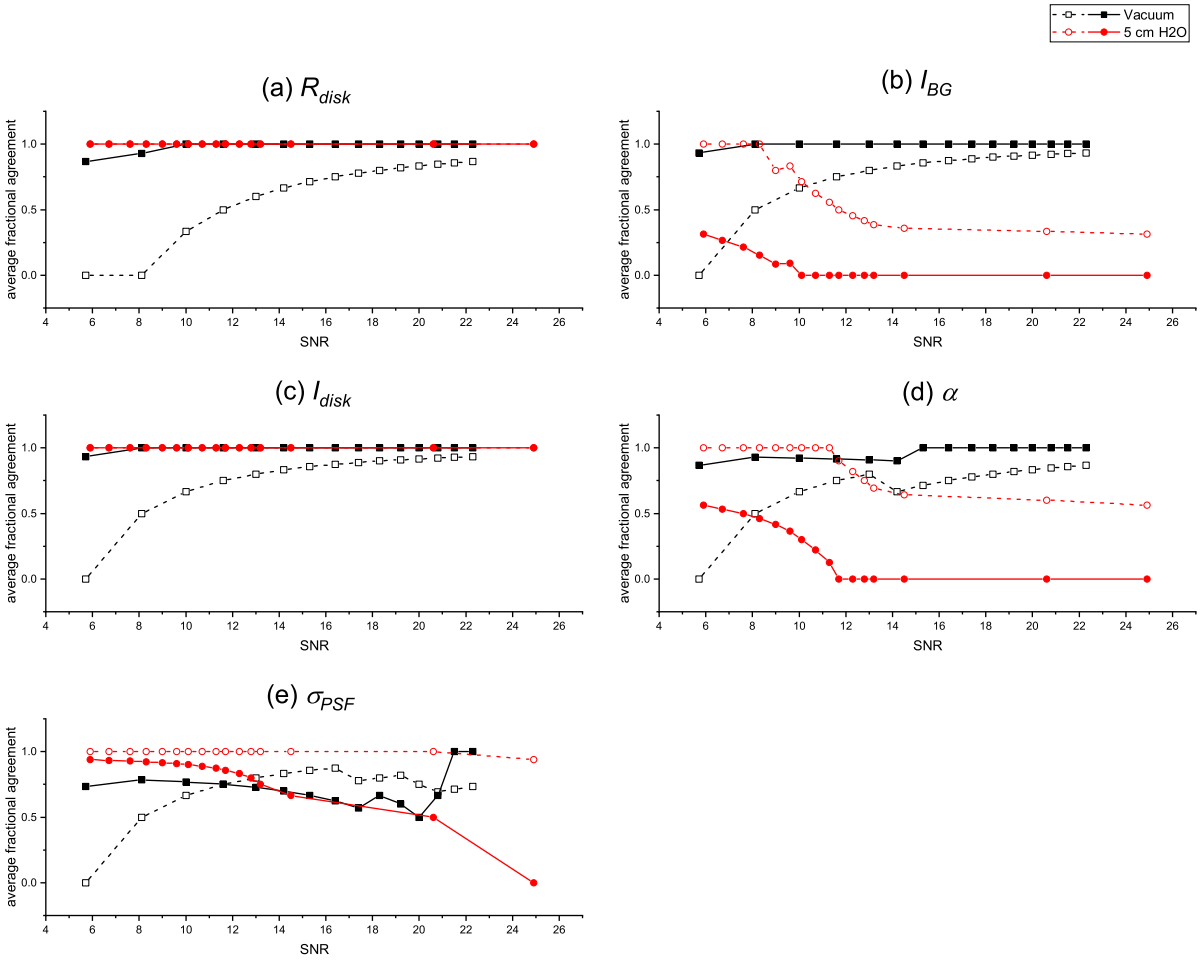


FIGURE 5.10: The average fractional agreement between measurements using the histogram method and their expected values for image quality assessments of the phantom in vacuum and 5 cm water depth, imaged using parallel beams. For the disk radius '$R_{disk}$', the agreement was based on a measured confidence interval encompassing the actual value of the parameter. For the image background region fluence '$I_{BG}$' and disk region fluence '$I_{disk}$', the agreement was based on a confidence interval of the histogram method overlapping with a confidence interval of the conventional method. For the transformation factor '$\alpha$' and the standard deviation of the Point Spread Function '$\sigma_{PSF}$', the agreement was based on a measured confidence interval encompassing the theoretical value of the parameter. The average fractional agreement is plotted using a dashed line and open symbols for assessments of images with an SNR equal or smaller than the SNR on the x-axis, and using a solid line and filled symbols for assessments of images with an SNR equal or greater than the SNR on the x-axis.

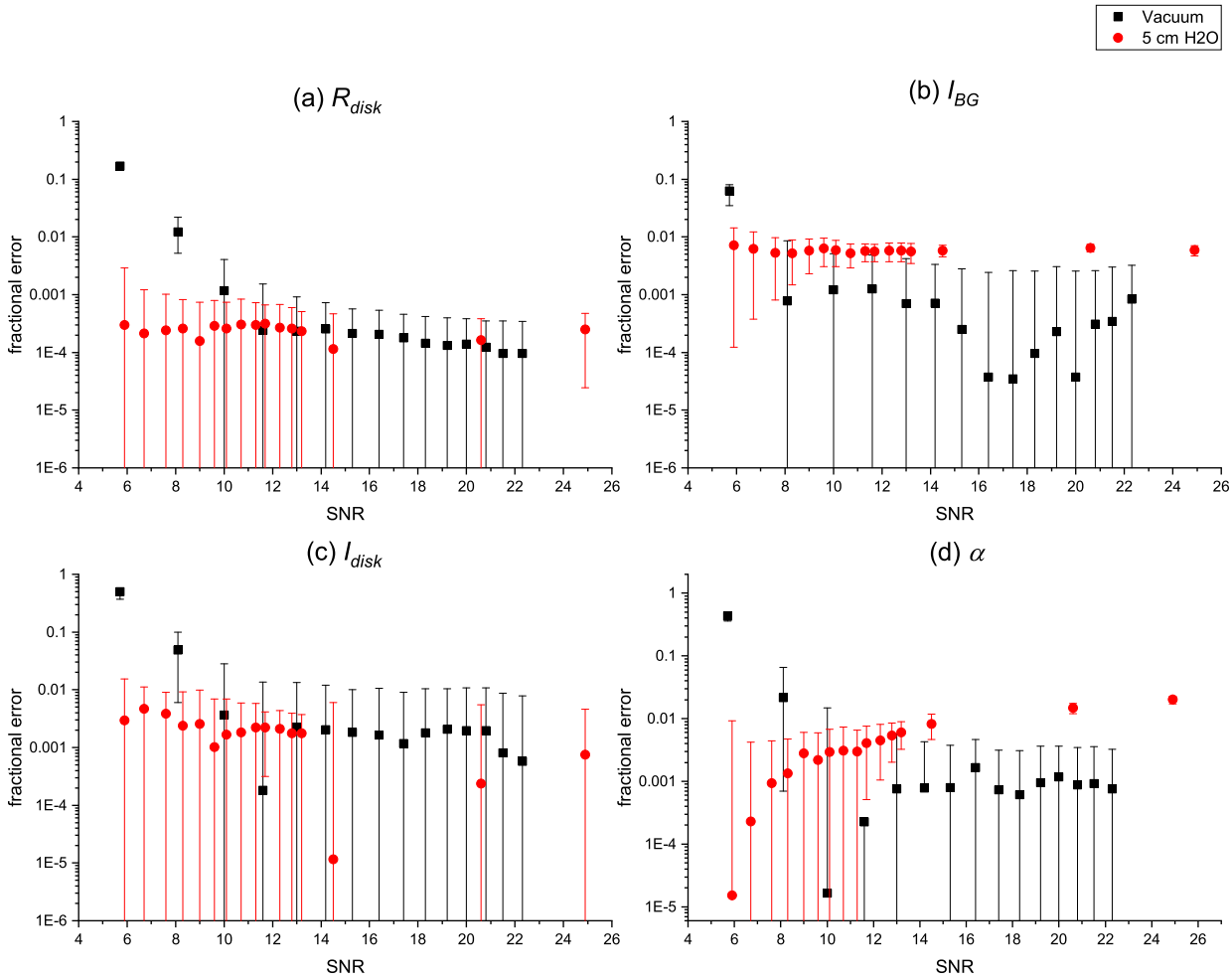


FIGURE 5.11: The magnitude of the error in parameter estimations for image quality assessments of the phantom in vacuum and 5 cm water depth, imaged using parallel beams. The error is presented as a fractional error for the disk radius '$R_{disk}$', the image background region fluence '$I_{BG}$', the disk region fluence '$I_{disk}$' and the noise factor '$\alpha$'. Expected values of parameters not changing with SNR: E($R_{disk}$)= 5 cm, E($\alpha$)= 10000, E($\sigma_{PSF}$)= 0 mm, and E($f_{10\%MTF}$)= Inf cycle/mm. The detector's resolution parameters: E($\sigma_{PSF}$)= 0.03 mm, and $f_{a_{lim}}$= 10 cycle/mm.

smaller for images with a water background, further decreasing the probability of agreement with the expected values. For $I_{BG}$, $\alpha$ and $\sigma_{PSF}$, the agreement decreased as the exposure was increased in images with a water background. For all parameters, at the smallest tested SNR value, the error magnitude was smaller for the simulated images with a water background. For $I_{BG}$ and $\alpha$, the MRE was smaller for images with a vacuum background. For $\alpha$, the relative error increased, and the relative uncertainty decreased, as the exposure was increased in images with a water background.

The confidence intervals of the conventional method for $\alpha$ always encompassed the theoretical value. There was no relationship between the error in measurements by the conventional method and the level of exposure or the background material of the image.

### 5.3.3 Performance with vacuum and water image backgrounds, and diverging beam geometry

The effect of increasing signal scattering, by changing the background material from vacuum to water, on the performance of the developed method was assessed for diverging beam geometries. The results for the image quality analysis of the disk in vacuum, 2.5 cm water depth and 5 cm water depth were compared for a point source and a 4 mm focal spot source simulations.

In Figures 5.12 and 5.13, the fractional agreement is plotted for images with vacuum and water backgrounds. The estimated error in measurements of the image quality parameters is shown in Figures 5.14 and 5.15. For $R_{disk}$ and $I_{disk}$, the exposure for samples with a confidence interval that contained the actual $R_{disk}$ value, corresponded to smaller SNR values for the simulated images with a water background. For the 5 cm water depth point source images, there was no agreement in measurements of $R_{disk}$ for the two highest tested exposures, as the estimated uncertainty decreased when the exposure was increased. For $I_{BG}$, the agreement was larger for images with a vacuum background. However, the measurement uncertainty was also larger. The MRE increased with the increase in water depth. As the exposure of images with a water background increased, $\alpha$ was further overestimated. For $\sigma_{PSF}$, there was an agreement with

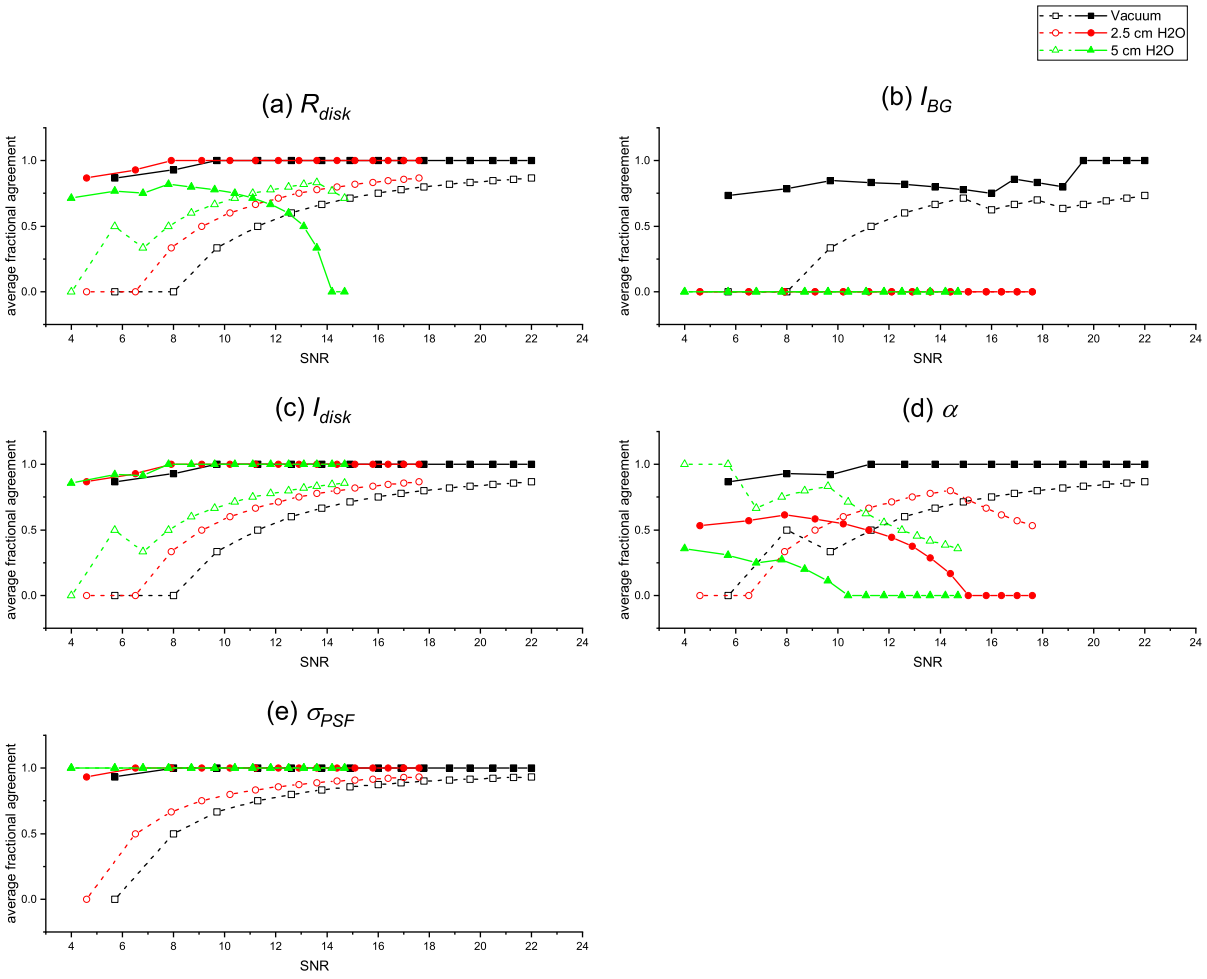


FIGURE 5.12: The average fractional agreement between measurements using the histogram method and their expected values for image quality assessments of the phantom in vacuum and 2.5 and 5 cm water depths, imaged using a point source diverging beams. For the disk radius '$R_{disk}$', the agreement was based on a measured confidence interval encompassing the actual value of the parameter. For the image background region fluence '$I_{BG}$' and disk region fluence '$I_{disk}$', the agreement was based on a confidence interval of the histogram method overlapping with a confidence interval of the conventional method. For the transformation factor '$\alpha$' and the standard deviation of the Point Spread Function '$\sigma_{PSF}$', the agreement was based on a measured confidence interval encompassing the theoretical value of the parameter. The average fractional agreement is plotted using a dashed line and open symbols for assessments of images with an SNR equal or smaller than the SNR on the x-axis, and using a solid line and filled symbols for assessments of images with an SNR equal or greater than the SNR on the x-axis.

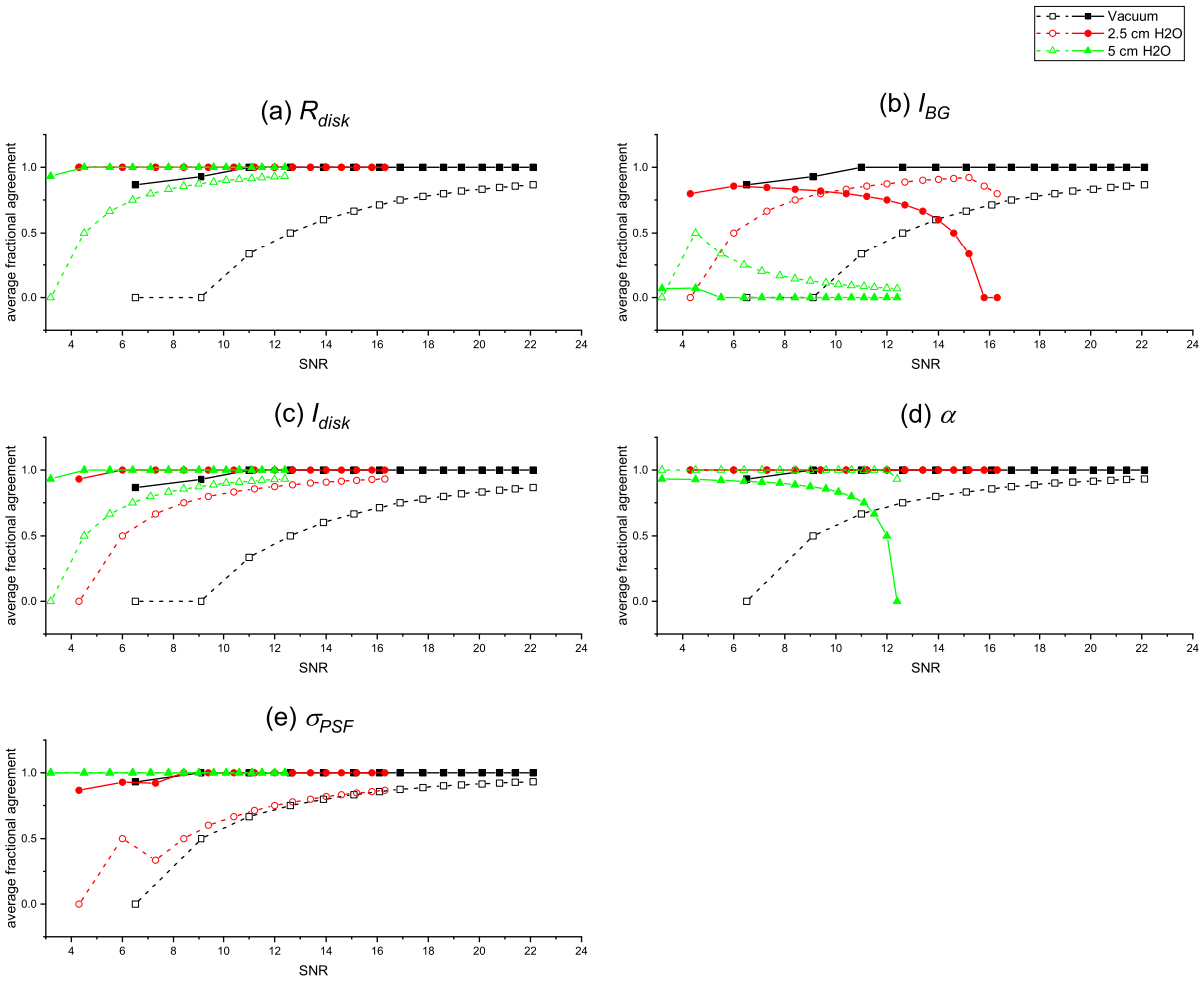


FIGURE 5.13: The average fractional agreement between measurements using the histogram method and their expected values for image quality assessments of the phantom in vacuum and 2.5 and 5 cm water depths, imaged using a 4 mm source diverging beams. For the disk radius '$R_{disk}$', the agreement was based on a measured confidence interval encompassing the actual value of the parameter. For the image background region fluence '$I_{BG}$' and disk region fluence '$I_{disk}$', the agreement was based on a confidence interval of the histogram method overlapping with a confidence interval of the conventional method. For the transformation factor '$\alpha$' and the standard deviation of the Point Spread Function '$\sigma_{PSF}$', the agreement was based on a measured confidence interval encompassing the theoretical value of the parameter. The average fractional agreement is plotted using a dashed line and open symbols for assessments of images with an SNR equal or smaller than the SNR on the x-axis, and using a solid line and filled symbols for assessments of images with an SNR equal or greater than the SNR on the x-axis.

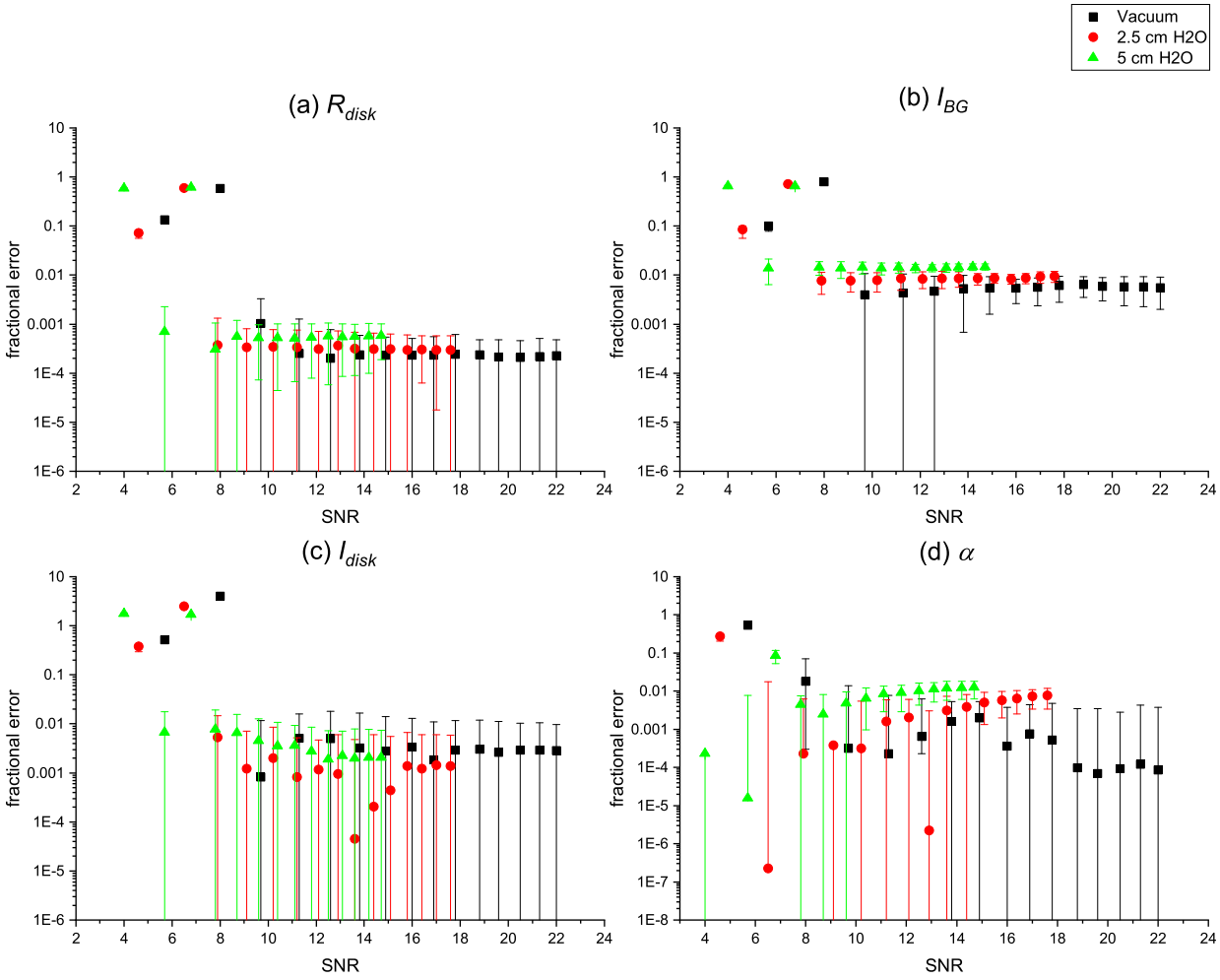


FIGURE 5.14: The magnitude of the error in parameter estimations for image quality assessments of the phantom in vacuum and 2.5 and 5 cm water depths, imaged using a point source diverging beams. The error is presented as a fractional error for the disk radius '$R_{disk}$', the image background region fluence '$I_{BG}$', the disk region fluence '$I_{disk}$' and the noise factor '$\alpha$'. Expected values of parameters not changing with SNR: E($R_{disk}$)= 5 cm, E($\alpha$)= 10000, E($\sigma_{PSF}$)= 0 mm, and E($f_{10\%MTF}$)= Inf cycle/mm. The detector's resolution parameters: E($\sigma_{PSF}$)= 0.03 mm, and $f_{a_{lim}}$= 12 cycle/mm.

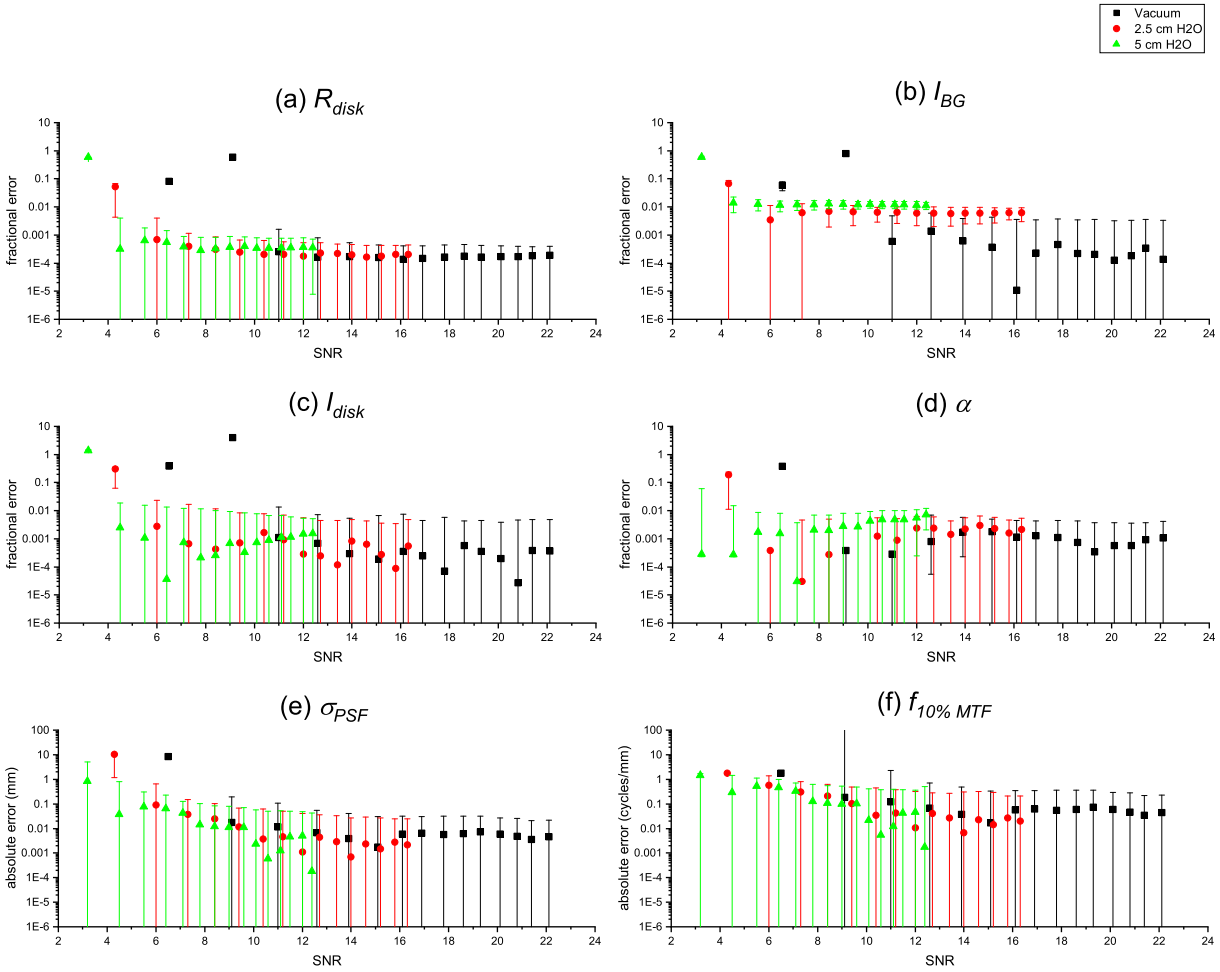


FIGURE 5.15: The magnitude of the error in parameter estimations for image quality assessments of the phantom in vacuum and 2.5 and 5 cm water depths, imaged using a 4 mm source diverging beams. The error is presented as a fractional error for the disk radius '$R_{disk}$', the image background region fluence '$I_{BG}$', the disk region fluence '$I_{disk}$' and the noise factor '$\alpha$', and as an absolute error for the standard deviation of the Point Spread Function '$\sigma_{PSF}$' and the frequency at 10% Modulation Transfer Function '$f_{10\%MTF}$'. Expected values of parameters not changing with SNR: E($R_{disk}$)= 5 cm, E($\alpha$)= 10000, E($\sigma_{PSF}$)= 0.19 mm, and E($f_{10\%MTF}$)= 1.8 cycle/mm. The detector's resolution parameters: E($\sigma_{PSF}$)= 0.03 mm, and $f_{a_{lim}}$= 12 cycle/mm.

the theoretical value at lower SNRs in images with a water background, compared to images with a vacuum background.

### 5.3.4 Performance with variable focal spot sizes

Simulations using sources with varying focal spot sizes were used to test the performance of the developed method in estimating image parameters at varying levels of spatial resolution. The results for the image quality analysis of the disk in vacuum, imaged using a point source and sources with focal spot sizes of $10^{-5}, 0.3, 0.6, 0.9, 1.2, 2, 3$ and 4 mm in diameter were compared.

In Figure 5.16, the fractional agreement is plotted for assessments of images simulated using these sources. The errors in estimating the image quality parameters is shown in Figure 5.17. There was no consistent effect of the focal spot size on the measurements of $R_{disk}$, $I_{BG}$, $I_{disk}$ and $\alpha$. For $\sigma_{PSF}$, there was an agreement with the theoretical value for all sample images with SNR values of 8.0 ($\pm$0.4) and higher. Figure 5.18 shows the error in the frequency at 10% MTF '$f_{10\%MTF}$' corresponding to measured confidence intervals for $\sigma_{PSF}$ for the six largest tested focal spot sizes. On average, the measurement error and uncertainty decreased for an increasing SNR. When there was an agreement, the error was negative for all tested focal spot sizes except the 4 mm source (theoretical focal spot's $f_{10\%MTF}$ of 1.8 cycle/mm). The measurement uncertainty and relative uncertainty decreased for an increasing focal spot size. For the focal spot resolution just satisfying the Nyquist criterion (6 cycle/mm), at SNR values $> 12$, the variability was smaller in the measurements using the histogram method, compared to the conventional method following the work by Samei *et al.* in 1998. At lower resolutions, the variability and average uncertainty were smaller in measurements using the histogram method, compared to the conventional method.

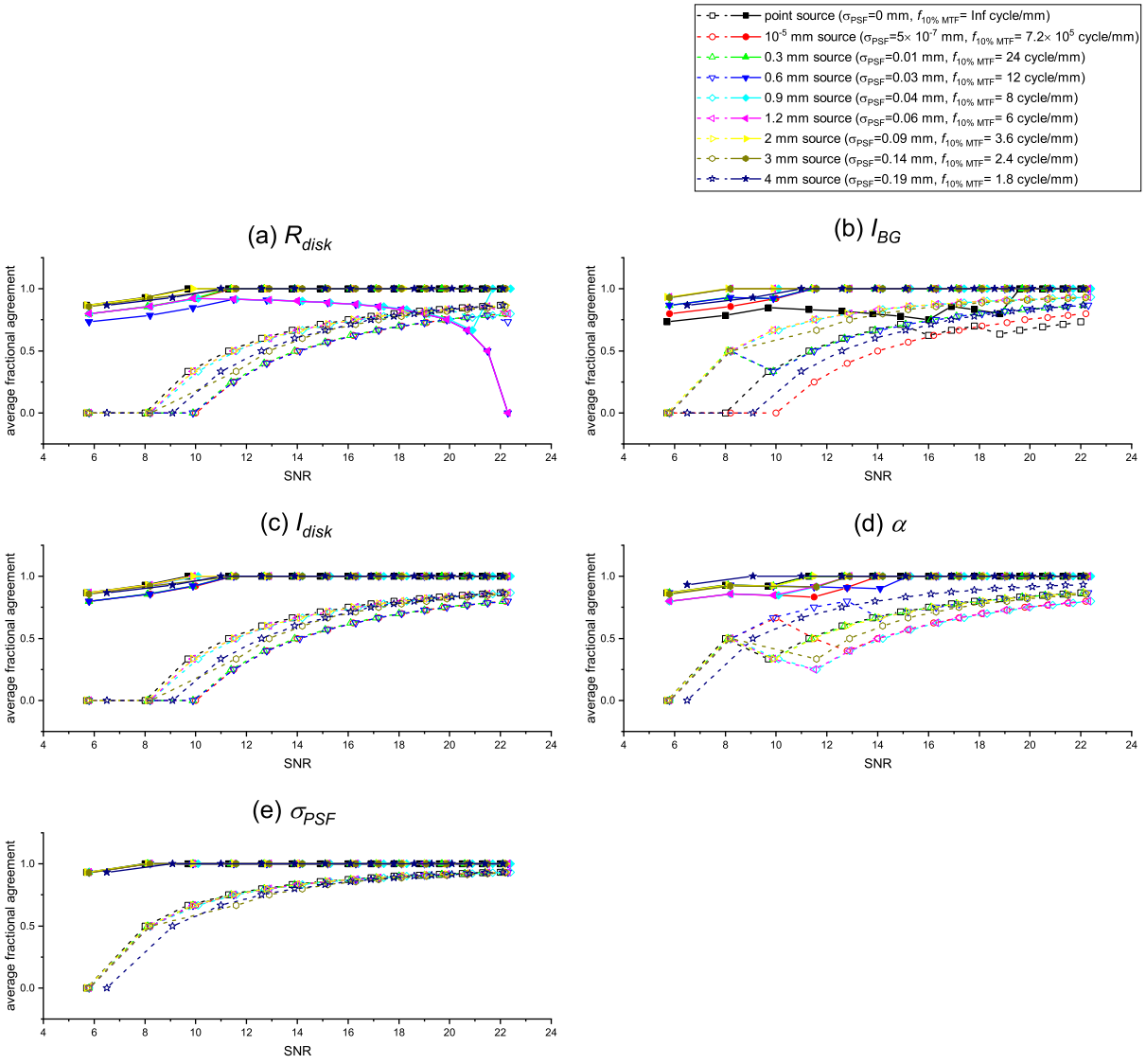


FIGURE 5.16: The average fractional agreement between measurements using the histogram method and their expected values for image quality assessments of the phantom in vacuum, imaged using a point source and sources with focal spot sizes of $10^{-5}, 0.3, 0.6, 0.9, 1.2, 2, 3$ and 4 mm. For the disk radius '$R_{disk}$', the agreement was based on a measured confidence interval encompassing the actual value of the parameter. For the image background region fluence '$I_{BG}$' and disk region fluence '$I_{disk}$', the agreement was based on a confidence interval of the histogram method overlapping with a confidence interval of the conventional method. For the transformation factor '$\alpha$' and the standard deviation of the Point Spread Function '$\sigma_{PSF}$', the agreement was based on a measured confidence interval encompassing the theoretical value of the parameter. The average fractional agreement is plotted using a dashed line and open symbols for assessments of images with an SNR equal or smaller than the SNR on the x-axis, and using a solid line and filled symbols for assessments of images with an SNR equal or greater than the SNR on the x-axis.

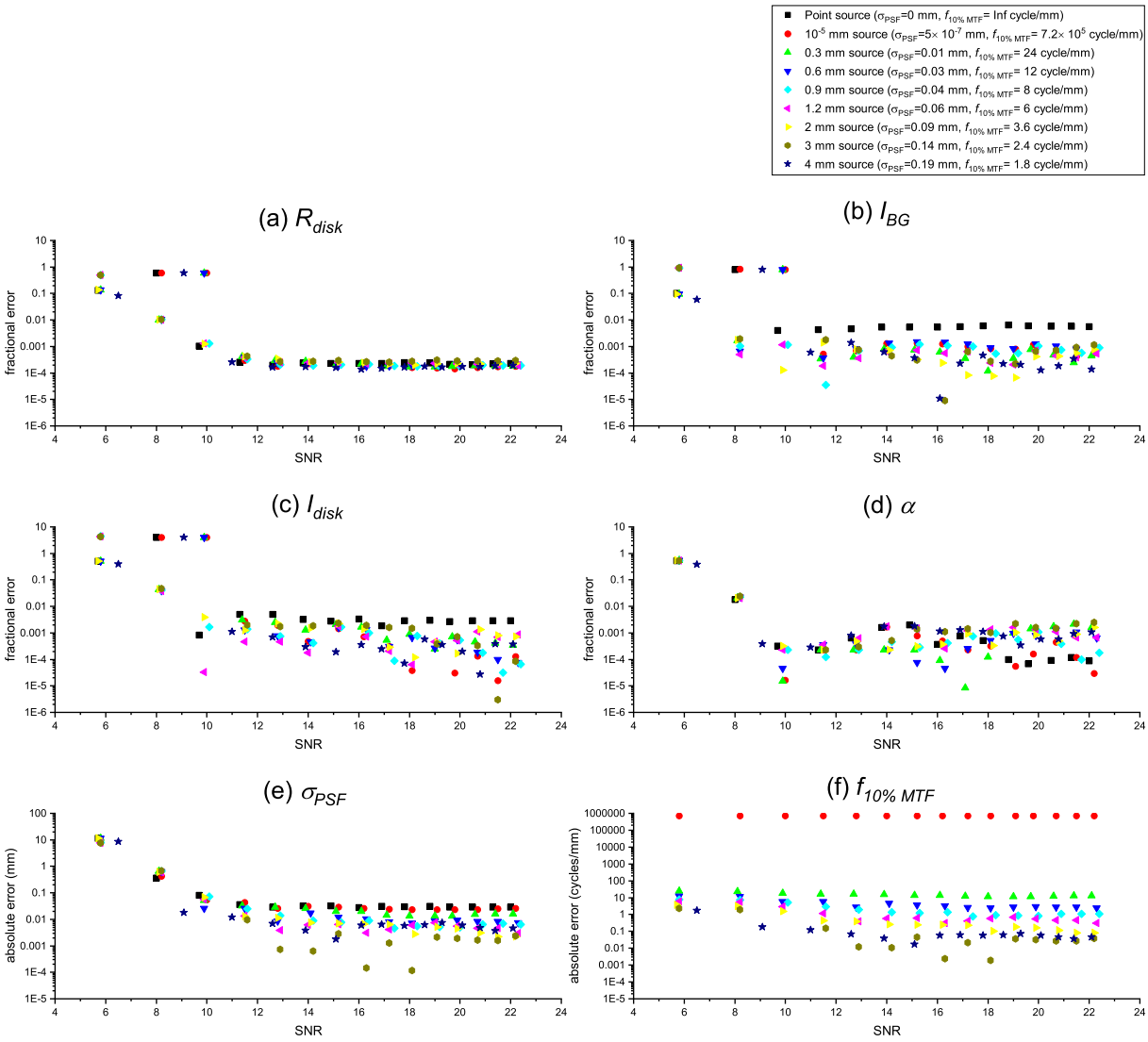


FIGURE 5.17: The magnitude of the error in parameter estimations for image quality assessments of the phantom in vacuum, imaged using a point source and sources with focal spot sizes of $10^{-5}, 0.3, 0.6, 0.9, 1.2, 2, 3$ and 4 mm. The error is presented as a fractional error for the disk radius '$R_{disk}$', the image background region fluence '$I_{BG}$', the disk region fluence '$I_{disk}$' and the noise factor '$\alpha$', and as an absolute error for the standard deviation of the Point Spread Function '$\sigma_{PSF}$' and the frequency at 10% Modulation Transfer Function '$f_{10\%MTF}$'. Expected values of parameters not changing with SNR: E($R_{disk}$)= 5 cm, E($\alpha$)= 10000, E($\sigma_{PSF}$) and E($f_{10\%MTF}$) are as in the legend. The detector's resolution parameters: E($\sigma_{PSF}$)= 0.03 mm, and $f_{a_{lim}}$= 12 cycle/mm. Note: the uncertainty in the error was omitted for data visualization's readability.

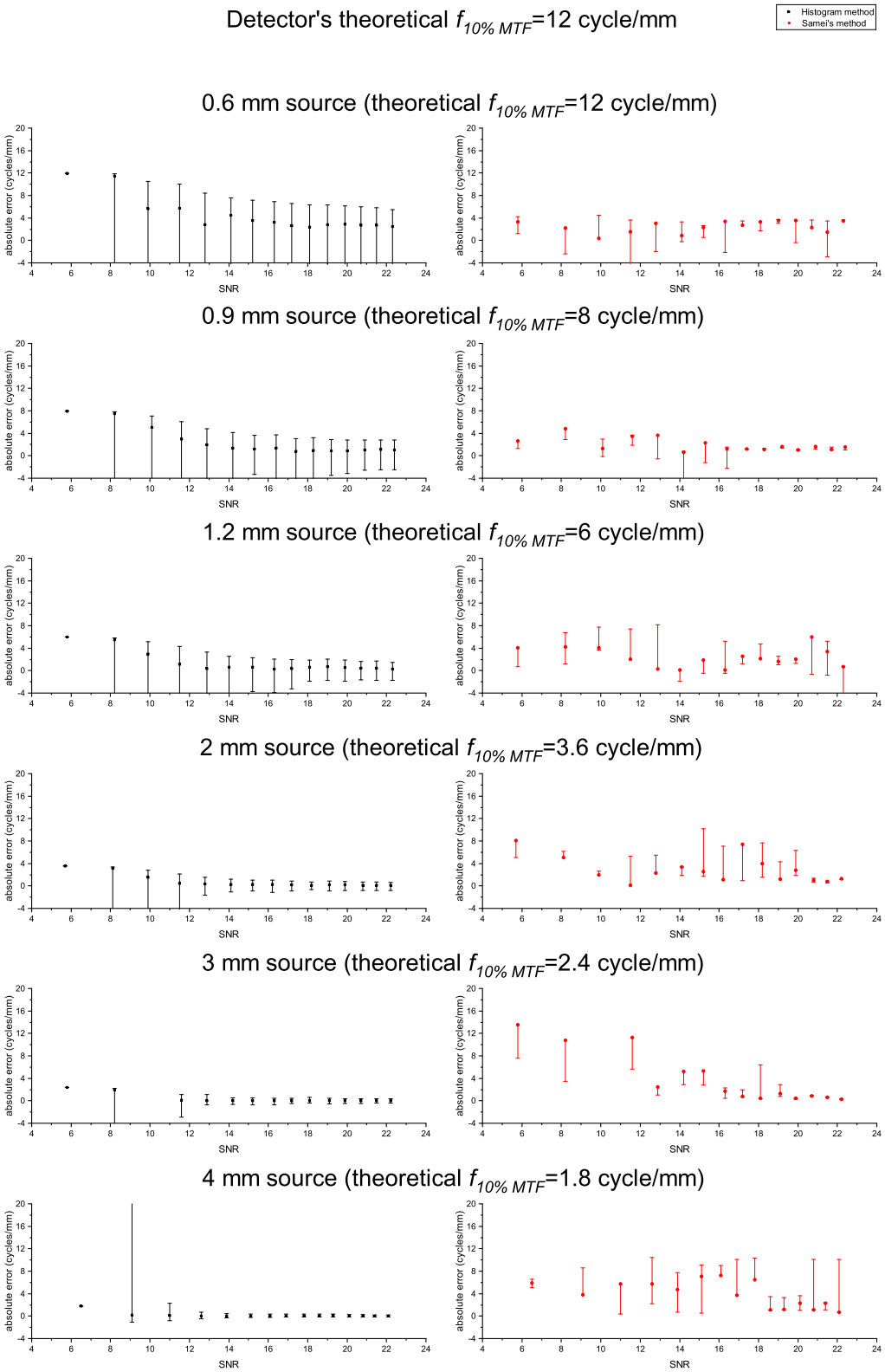


FIGURE 5.18: The absolute errors in $f_{10\%MTF}$ for image quality assessments of the phantom in vacuum, imaged using a point source and sources with focal spot sizes of $10^{-5}$, 0.3, 0.6, 0.9, 1.2, 2, 3 and 4 mm.

### 5.3.5 Performance with varying water depths, with and without divergent beam corrections

The performance of the developed method in estimating image parameters with and without geometrical corrections was evaluated. Images of the disk in vacuum, 2.5 cm and 5 cm water depth, simulated using a 4 mm focal spot source were used.

In Figures 5.19, 5.20 and 5.21, the fractional agreement is plotted for the different image background settings, with and without divergent beam corrections. The estimated error in measurements of the image quality parameters is shown in Figures 5.22, 5.23 and 5.24. For $R_{disk}$, applying the corrections resulted in a decrease in the agreement with the actual value. The measurement uncertainty was smallest without the corrections for images with a vacuum background, but largest without the corrections for images with a 5 cm water depth. For $I_{BG}$, the agreement was largest without the corrections in assessments of images with a water background. The MRE was smallest without the corrections in assessments of images with a vacuum background. For $I_{disk}$, the agreement decreased after applying the corrections. The MRE converged to a smaller value without the corrections. The least negative effect of applying the corrections was for images with a 5 cm water depth. For $\alpha$, applying the corrections decreased the agreement with the theoretical value. For $\sigma_{PSF}$, applying the corrections decreased the agreement with the theoretical value for assessments of images with a 5 cm water depth. There was no consistent effect of the corrections on the MRE of measurements of $\alpha$ and $\sigma_{PSF}$.

### 5.3.6 Performance with varying noise nature assumptions, and parallel beam geometry

The performance of the developed method in estimating image parameters with Gaussian and Poisson noise assumptions was tested. Images of the disk in vacuum, simulated using parallel beams were used.

In Figure 5.25, the fractional agreement is plotted for quality assessments with Gaussian and Poisson noise assumptions. The errors in estimating the image quality param-

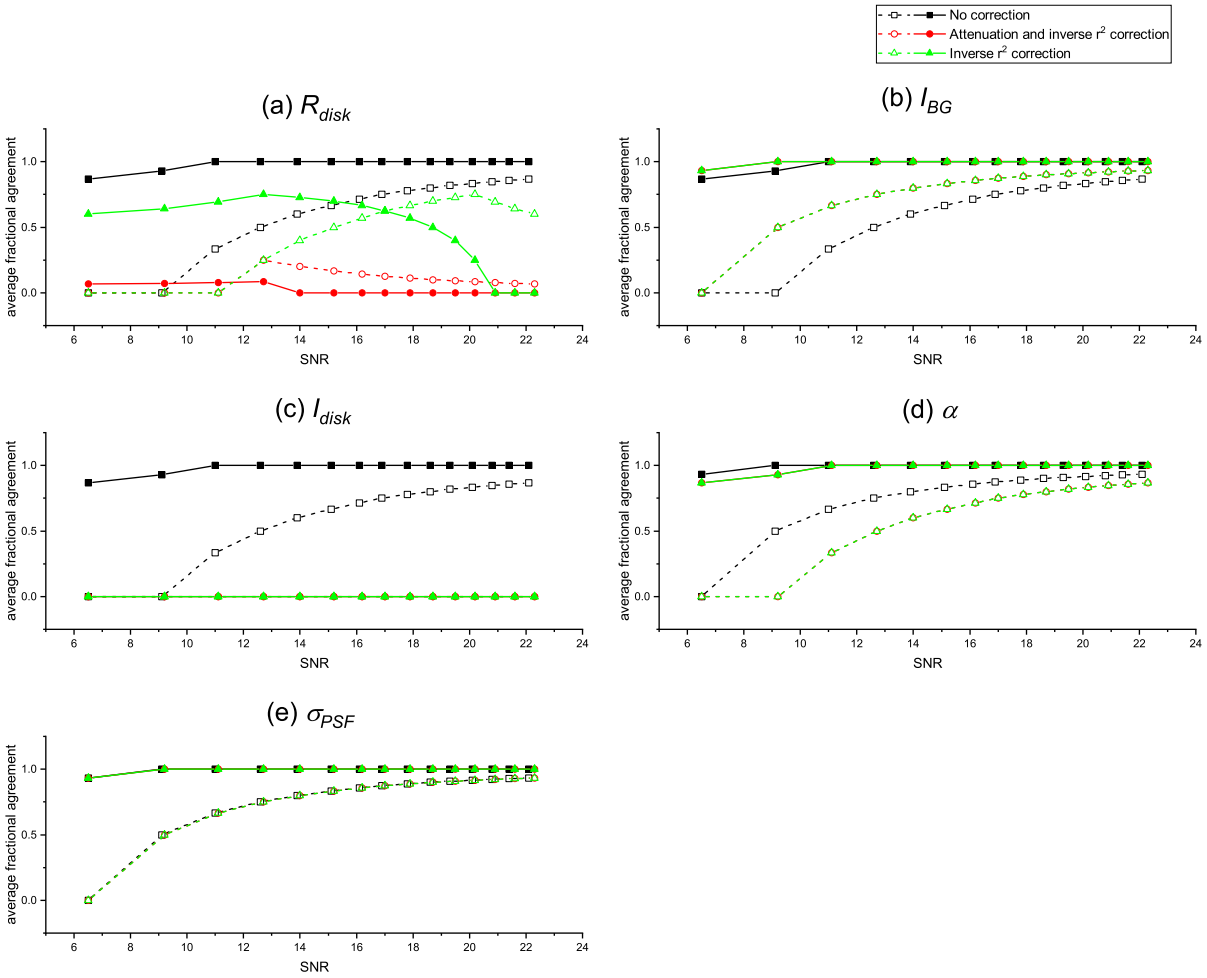


FIGURE 5.19: The average fractional agreement between measurements using the histogram method and their expected values for image quality assessments of the phantom in vacuum, imaged using a 4 mm source diverging beams, with and without diverging beam corrections. For the disk radius '$R_{disk}$', the agreement was based on a measured confidence interval encompassing the actual value of the parameter. For the image background region fluence '$I_{BG}$' and disk region fluence '$I_{disk}$', the agreement was based on a confidence interval of the histogram method overlapping with a confidence interval of the conventional method. For the transformation factor '$\alpha$' and the standard deviation of the Point Spread Function '$\sigma_{PSF}$', the agreement was based on a measured confidence interval encompassing the theoretical value of the parameter. The average fractional agreement is plotted using a dashed line and open symbols for assessments of images with an SNR equal or smaller than the SNR on the x-axis, and using a solid line and filled symbols for assessments of images with an SNR equal or greater than the SNR on the x-axis. Note: For $I_{BG}$, $I_{disk}$, $\alpha$ and $\sigma_{PSF}$, similar agreement with the expected values was achieved when the attenuation and inverse square corrections were applied as when only the inverse square correction was applied.

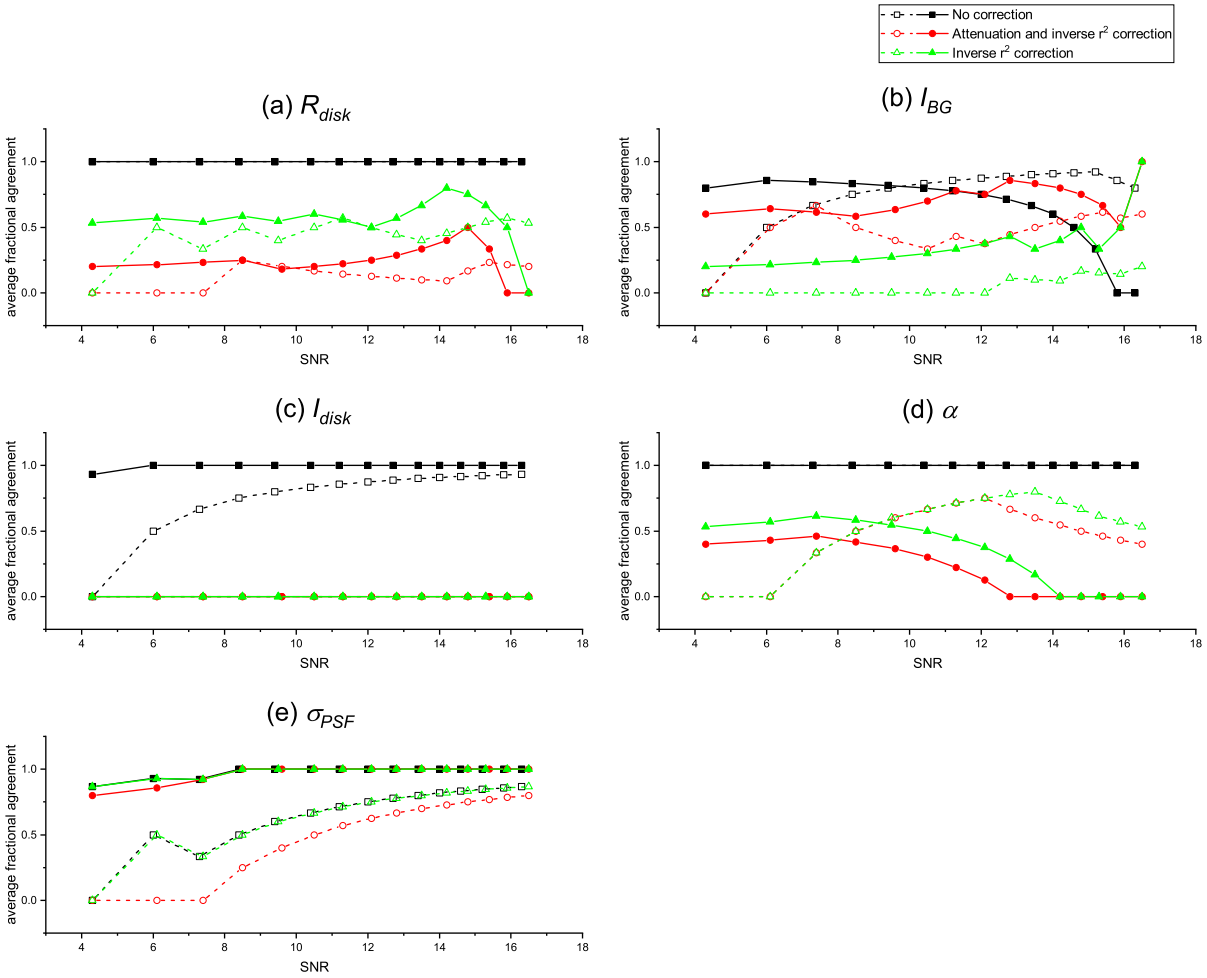


FIGURE 5.20: The average fractional agreement between measurements using the histogram method and their expected values for image quality assessments of the phantom in 2.5 cm water depth, imaged using a 4 mm source diverging beams, with and without diverging beam corrections. For the disk radius '$R_{disk}$', the agreement was based on a measured confidence interval encompassing the actual value of the parameter. For the image background region fluence '$I_{BG}$' and disk region fluence '$I_{disk}$', the agreement was based on a confidence interval of the histogram method overlapping with a confidence interval of the conventional method. For the transformation factor '$\alpha$' and the standard deviation of the Point Spread Function '$\sigma_{PSF}$', the agreement was based on a measured confidence interval encompassing the theoretical value of the parameter. The average fractional agreement is plotted using a dashed line and open symbols for assessments of images with an SNR equal or smaller than the SNR on the x-axis, and using a solid line and filled symbols for assessments of images with an SNR equal or greater than the SNR on the x-axis. Note: For $I_{disk}$, similar agreement with the expected values was achieved when the attenuation and inverse square corrections were applied as when only the inverse square correction was applied.

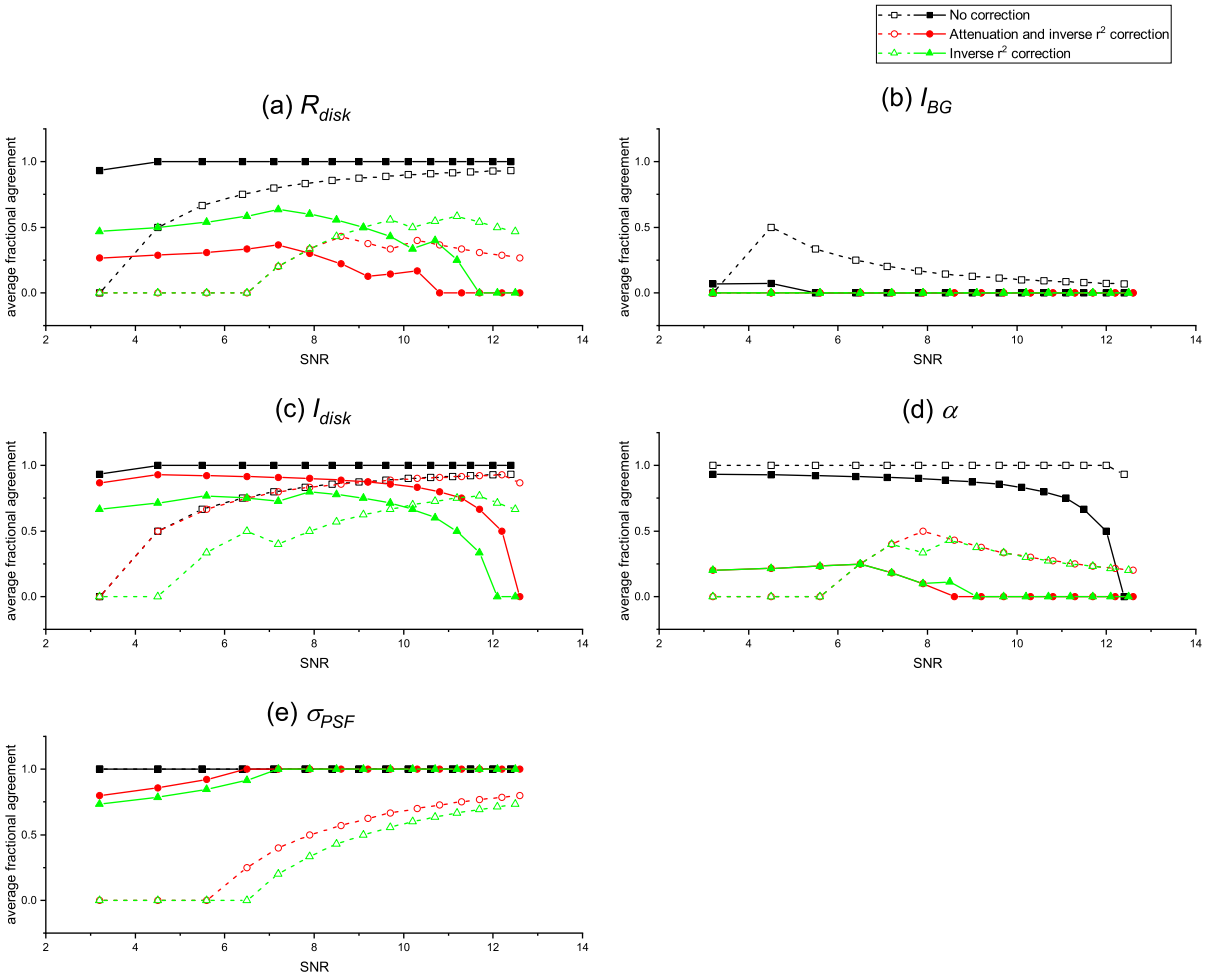


FIGURE 5.21: The average fractional agreement between measurements using the histogram method and their expected values for image quality assessments of the phantom in 5 cm water depth, imaged using a 4 mm source diverging beams, with and without diverging beam corrections. For the disk radius '$R_{disk}$', the agreement was based on a measured confidence interval encompassing the actual value of the parameter. For the image background region fluence '$I_{BG}$' and disk region fluence '$I_{disk}$', the agreement was based on a confidence interval of the histogram method overlapping with a confidence interval of the conventional method. For the transformation factor '$\alpha$' and the standard deviation of the Point Spread Function '$\sigma_{PSF}$', the agreement was based on a measured confidence interval encompassing the theoretical value of the parameter. The average fractional agreement is plotted using a dashed line and open symbols for assessments of images with an SNR equal or smaller than the SNR on the x-axis, and using a solid line and filled symbols for assessments of images with an SNR equal or greater than the SNR on the x-axis. Note: For $I_{BG}$, similar agreement with the expected values was achieved when the attenuation and inverse square corrections were applied as when only the inverse square correction was applied.

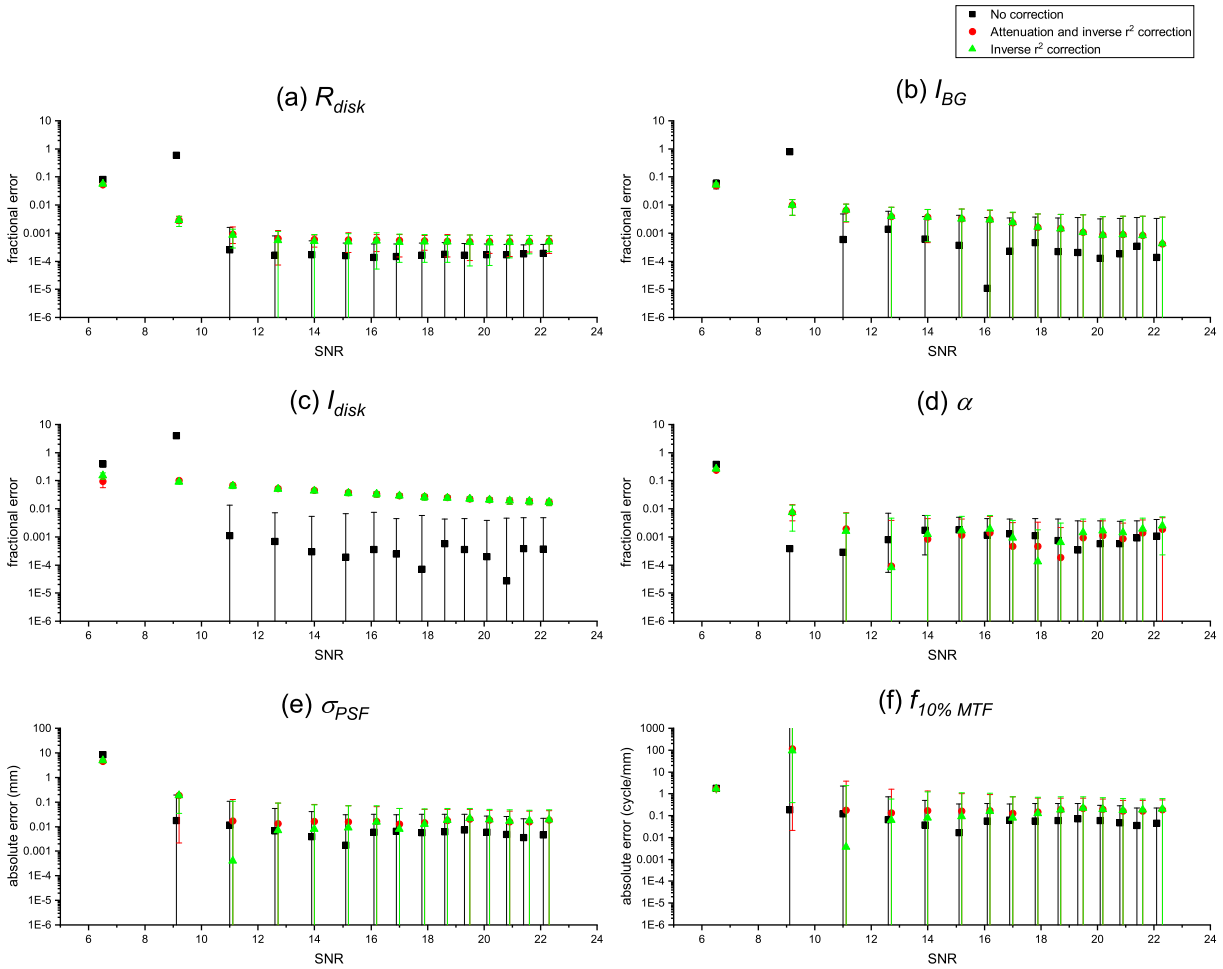


FIGURE 5.22: The magnitude of the error in parameter estimations for image quality assessments of the phantom in vacuum, imaged using a 4 mm source diverging beams, with and without diverging beam corrections. The error is presented as a fractional error for the disk radius '$R_{disk}$', the image background region fluence '$I_{BG}$', the disk region fluence '$I_{disk}$' and the noise factor '$\alpha$', and as an absolute error for the standard deviation of the Point Spread Function '$\sigma_{PSF}$' and the frequency at 10% Modulation Transfer Function '$f_{10\%MTF}$'. Expected values of parameters not changing with SNR: E($R_{disk}$)= 5 cm, E($\alpha$)= 10000, E($\sigma_{PSF}$)= 0.19 mm, and E($f_{10\%MTF}$)= 1.8 cycle/mm. The detector's resolution parameters: E($\sigma_{PSF}$)= 0.03 mm, and $f_{a_{lim}}$= 12 cycle/mm.

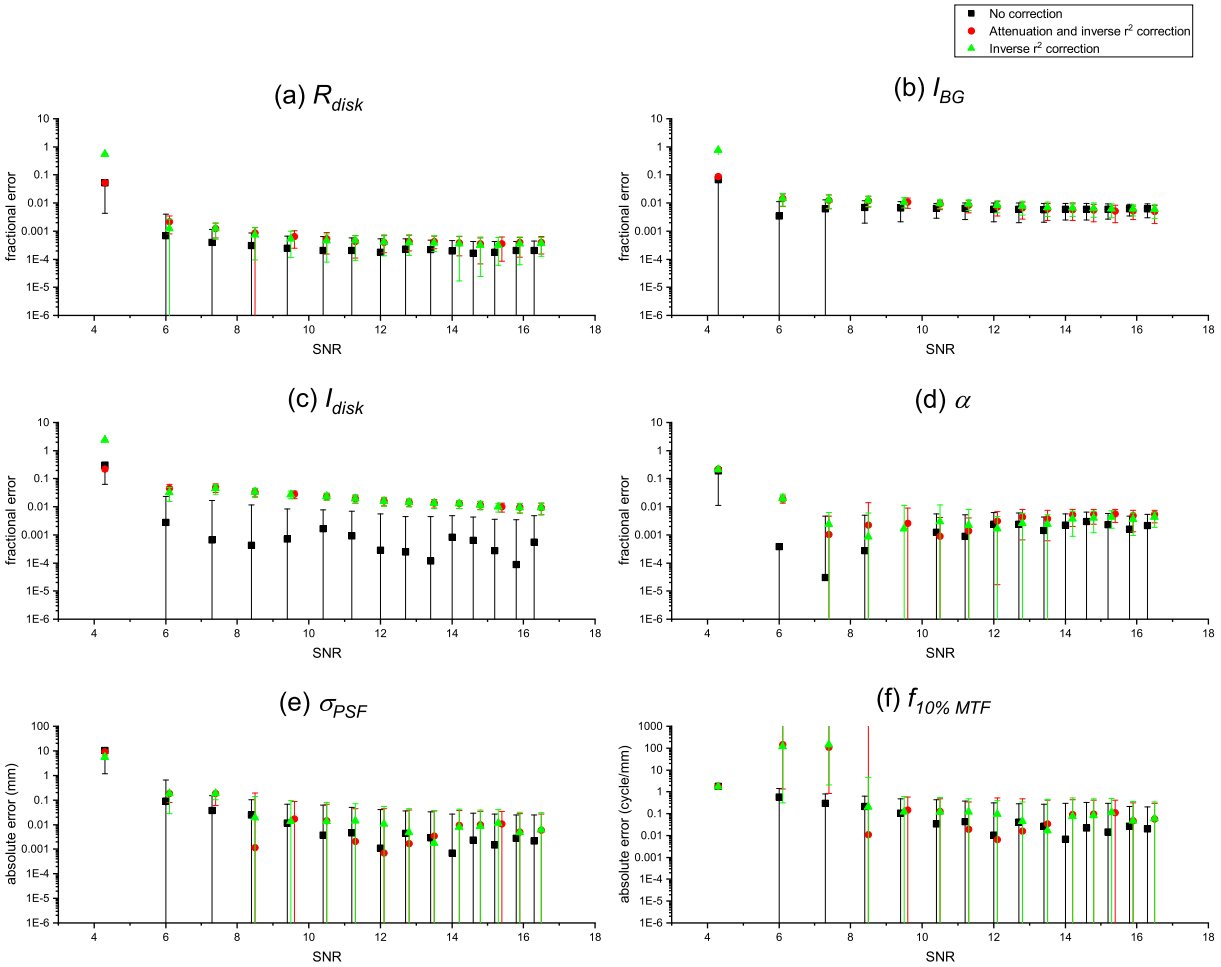


FIGURE 5.23: The magnitude of the error in parameter estimations for image quality assessments of the phantom in 2.5 cm water depth, imaged using a 4 mm source diverging beams, with and without diverging beam corrections. The error is presented as a fractional error for the disk radius '$R_{disk}$', the image background region fluence '$I_{BG}$', the disk region fluence '$I_{disk}$' and the noise factor '$\alpha$', and as an absolute error for the standard deviation of the Point Spread Function '$\sigma_{PSF}$' and the frequency at 10% Modulation Transfer Function '$f_{10\%MTF}$'. Expected values of parameters not changing with SNR: E($R_{disk}$)= 5 cm, E($\alpha$)= 10000, E($\sigma_{PSF}$)= 0.19 mm, and E($f_{10\%MTF}$)= 1.8 cycle/mm. The detector's resolution parameters: E($\sigma_{PSF}$)= 0.03 mm, and $f_{a_{lim}}$= 12 cycle/mm.

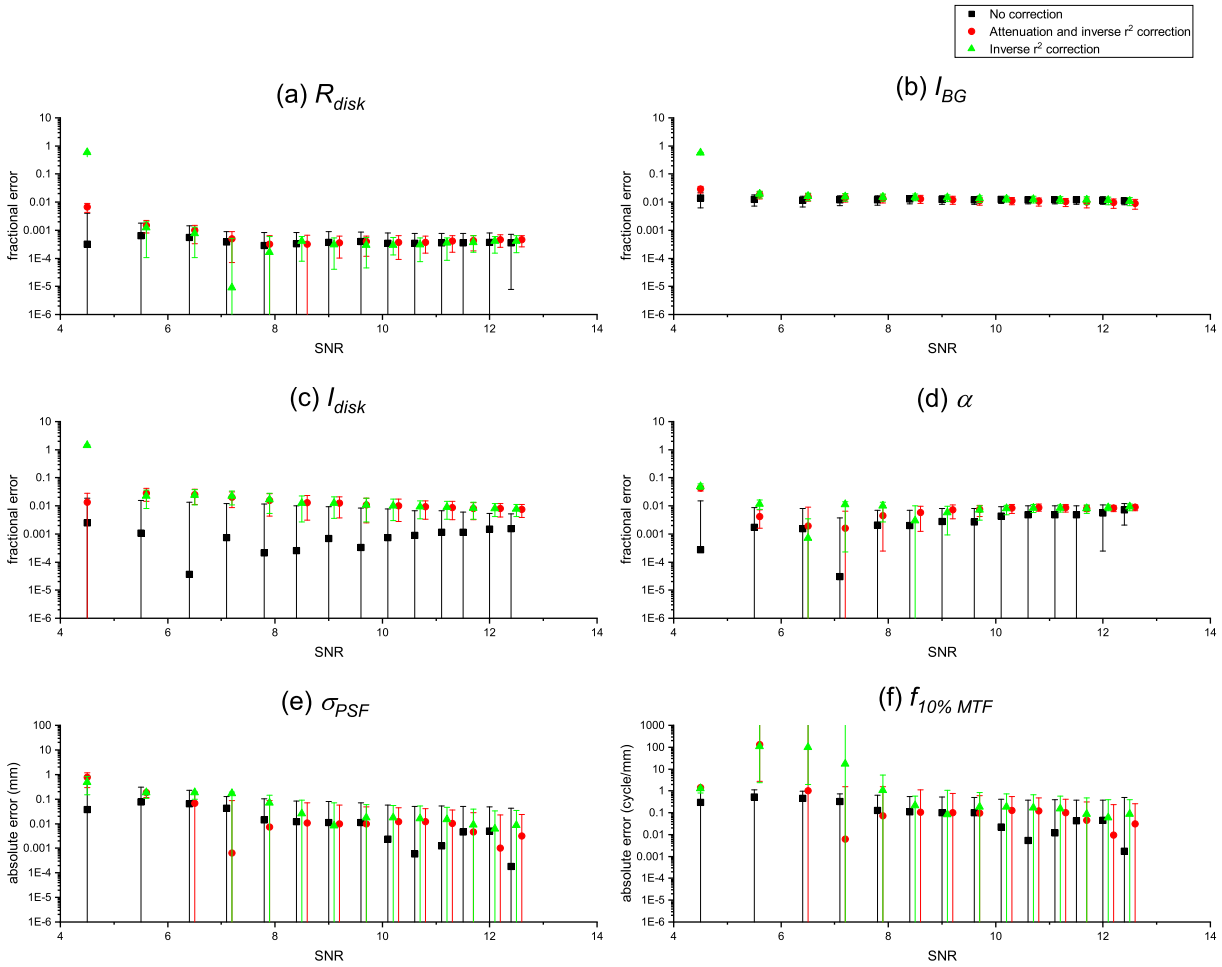


FIGURE 5.24: The magnitude of the error in parameter estimations for image quality assessments of the phantom in 5 cm water depth, imaged using a 4 mm source diverging beams, with and without diverging beam corrections. The error is presented as a fractional error for the disk radius '$R_{disk}$', the image background region fluence '$I_{BG}$', the disk region fluence '$I_{disk}$' and the noise factor '$\alpha$', and as an absolute error for the standard deviation of the Point Spread Function '$\sigma_{PSF}$' and the frequency at 10% Modulation Transfer Function '$f_{10\%MTF}$'. Expected values of parameters not changing with SNR: E($R_{disk}$)= 5 cm, E($\alpha$)= 10000, E($\sigma_{PSF}$)= 0.19 mm, and E($f_{10\%MTF}$)= 1.8 cycle/mm. The detector's resolution parameters: E($\sigma_{PSF}$)= 0.03 mm, and $f_{a_{lim}}$= 12 cycle/mm.

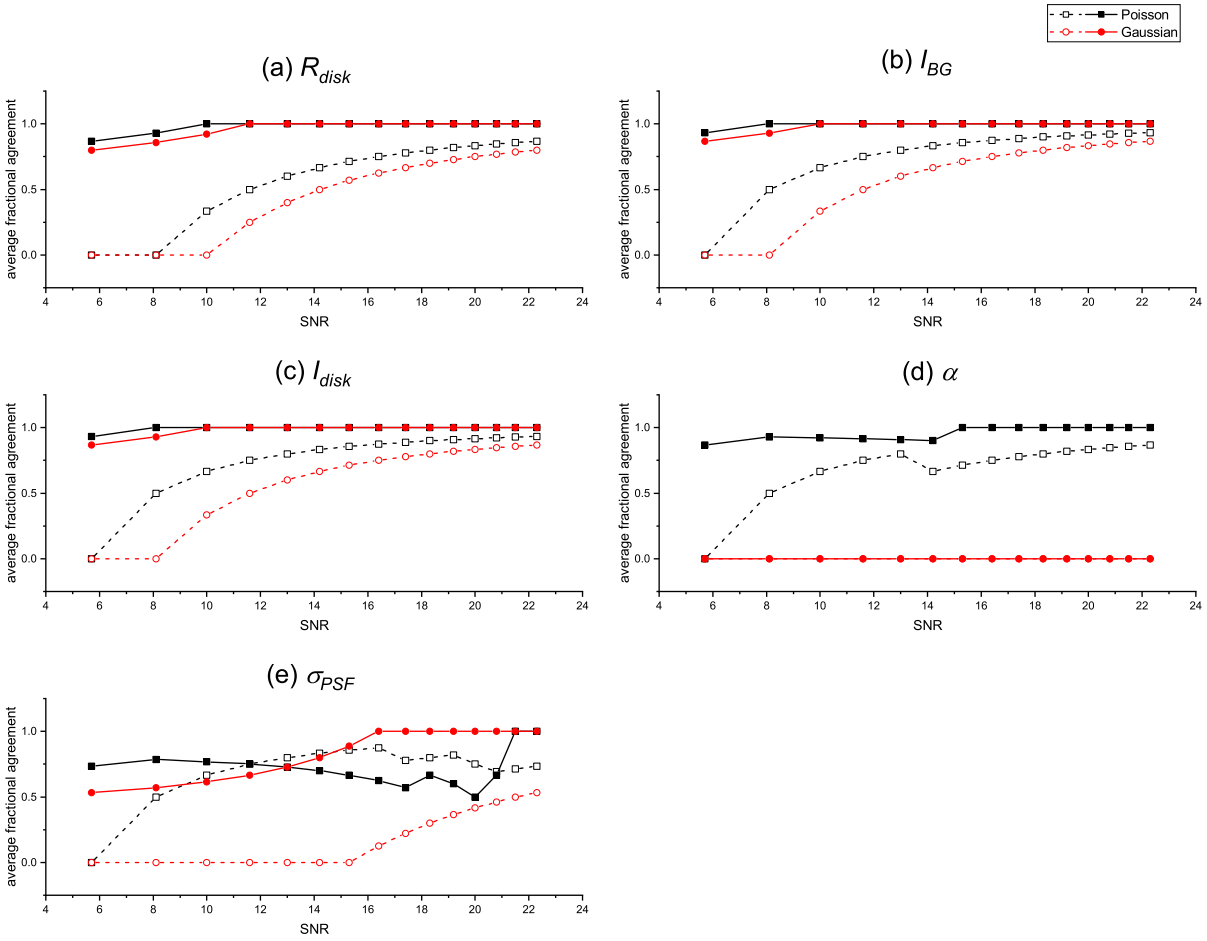


FIGURE 5.25: The average fractional agreement between measurements using the histogram method and their expected values for image quality assessments of the phantom in vacuum, with Gaussian and Poisson noise assumptions, imaged using parallel beams. For the disk radius '$R_{disk}$', the agreement was based on a measured confidence interval encompassing the actual value of the parameter. For the image background region fluence '$I_{BG}$' and disk region fluence '$I_{disk}$', the agreement was based on a confidence interval of the histogram method overlapping with a confidence interval of the conventional method. For the transformation factor '$\alpha$' and the standard deviation of the Point Spread Function '$\sigma_{PSF}$', the agreement was based on a measured confidence interval encompassing the theoretical value of the parameter. The average fractional agreement is plotted using a dashed line and open symbols for assessments of images with an SNR equal or smaller than the SNR on the x-axis, and using a solid line and filled symbols for assessments of images with an SNR equal or greater than the SNR on the x-axis.

eters is shown in Figure 5.26. For all quality parameters, the fractional agreement was increased, and the MRE was smaller, for assessments with a Poisson noise assumption. The uncertainty was larger in the estimations of all quality parameters when a Gaussian noise was assumed.

### 5.3.7 Performance with varying sizes of the ROI within the FOV, and parallel beam geometry

The performance of the developed method in estimating image parameters with varying sizes of the global ROI within the beam FOV was evaluated. Images of the disk with 5 cm water depth in the background, simulated using parallel beams, were used. The size of the ROI was set to $20 \times 20$, $22 \times 22$, $24 \times 24$, $26 \times 26$, $28 \times 28$ and $30 \times 30$ $cm^2$, and located at the center of the $30 \times 30$ cm$^2$ FOV.

In Figure 5.27, the fractional agreement is plotted for quality assessments with these ROI sizes. The errors in estimating the image quality parameters is shown in Figure 5.28. For measurements of $R_{disk}$, $I_{disk}$ and $\alpha$, the MRE increased with an increasing ROI size. For $I_{BG}$, the MRE did not monotonically increase with an increasing ROI size since the same ROI size was used when obtaining a pair of observed and expected values. The interpretation of the larger agreement with the theoretical value of $\sigma_{PSF}$ for larger ROI sizes was that an overestimation of $\alpha$ allowed the model to predict smaller values of $\sigma_{PSF}$. A higher noise can override the effect of image degradation by blurring in a cumulative histogram.

### 5.3.8 Performance with varying sizes of the ROI within the FOV, and diverging beam geometry

The performance of the histogram method in estimating the quality parameters of images with a spatial resolution of 1.8 cycle/mm and varying sizes of the global ROI within the FOV and was evaluated. Images of the disk with 5 cm water depth in the background, simulated using a 4 mm focal spot source, were used. The global ROI was set to $20 \times 20$, $22 \times 22$, $24 \times 24$ cm$^2$ in size at the center of a circular $\pi \times 22.5^2$ cm$^2$ FOV.

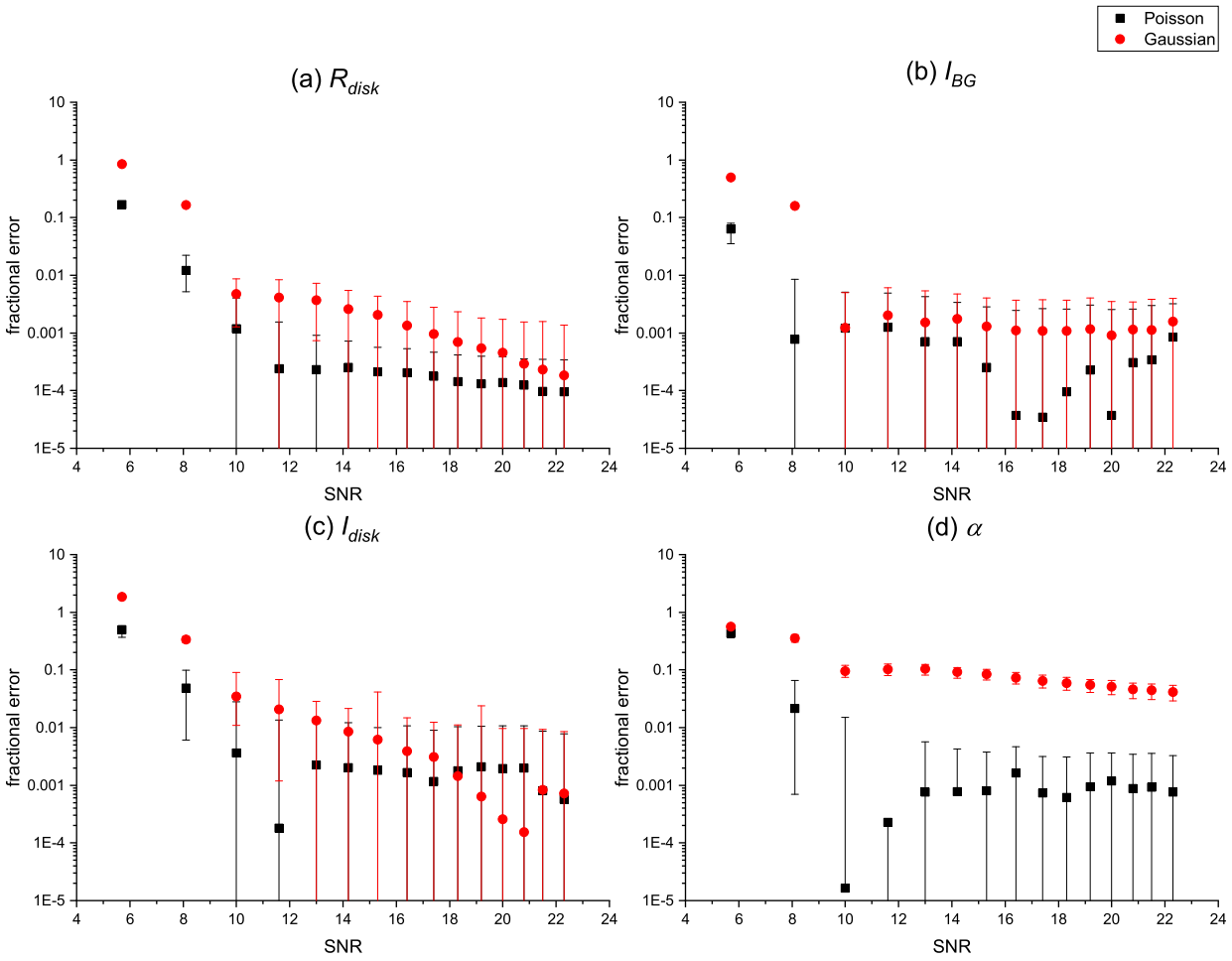


FIGURE 5.26: The magnitude of the error in parameter estimations for image quality assessments of the phantom in vacuum, with Gaussian and Poisson noise assumptions, imaged using parallel beams. The error is presented as a fractional error for the disk radius '$R_{disk}$', the image background region fluence '$I_{BG}$', the disk region fluence '$I_{disk}$' and the noise factor '$\alpha$'. Expected values of parameters not changing with SNR: E($R_{disk}$)= 5 cm, E($\alpha$)= 10000, E($\sigma_{PSF}$)= 0 mm, and E($f_{10\%MTF}$)= Inf cycle/mm. The detector's resolution parameters: E($\sigma_{PSF}$)= 0.03 mm, and $f_{a_{lim}}$= 10 cycle/mm.

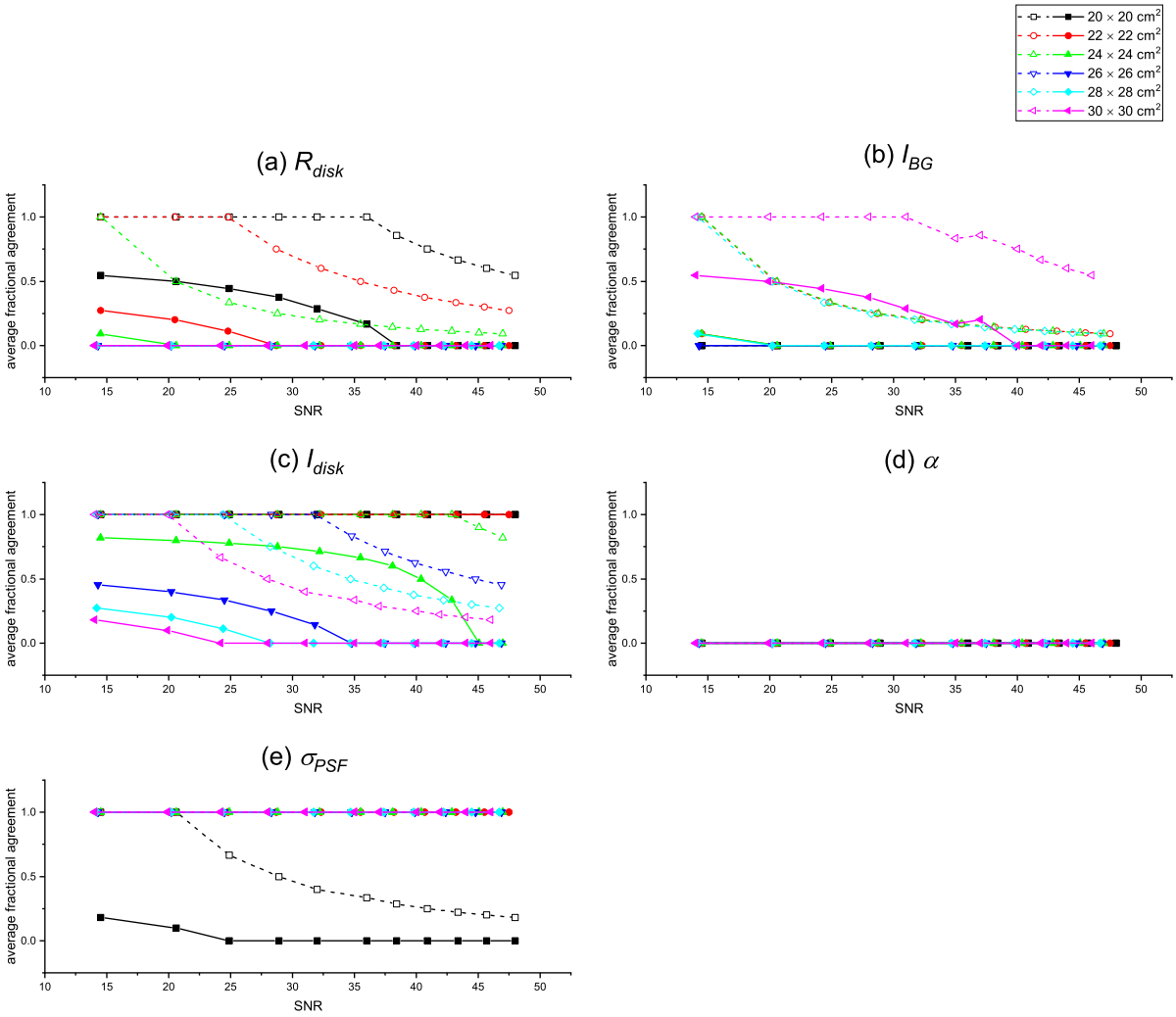


FIGURE 5.27: The average fractional agreement between measurements using the histogram method and their expected values for image quality assessments of the phantom in 5 cm water depth, imaged using parallel beams. The ROI was set to $20 \times 20$, $22 \times 22$, $24 \times 24$, $26 \times 26$, $28 \times 28$ and $30 \times 30$ $cm^2$ in size, and located at the center of the $30 \times 30$ cm$^2$ FOV. For the disk radius '$R_{disk}$', the agreement was based on a measured confidence interval encompassing the actual value of the parameter. For the image background region fluence '$I_{BG}$' and disk region fluence '$I_{disk}$', the agreement was based on a confidence interval of the histogram method overlapping with a confidence interval of the conventional method. For the transformation factor '$\alpha$' and the standard deviation of the Point Spread Function '$\sigma_{PSF}$', the agreement was based on a measured confidence interval encompassing the theoretical value of the parameter. The average fractional agreement is plotted using a dashed line and open symbols for assessments of images with an SNR equal or smaller than the SNR on the x-axis, and using a solid line and filled symbols for assessments of images with an SNR equal or greater than the SNR on the x-axis.

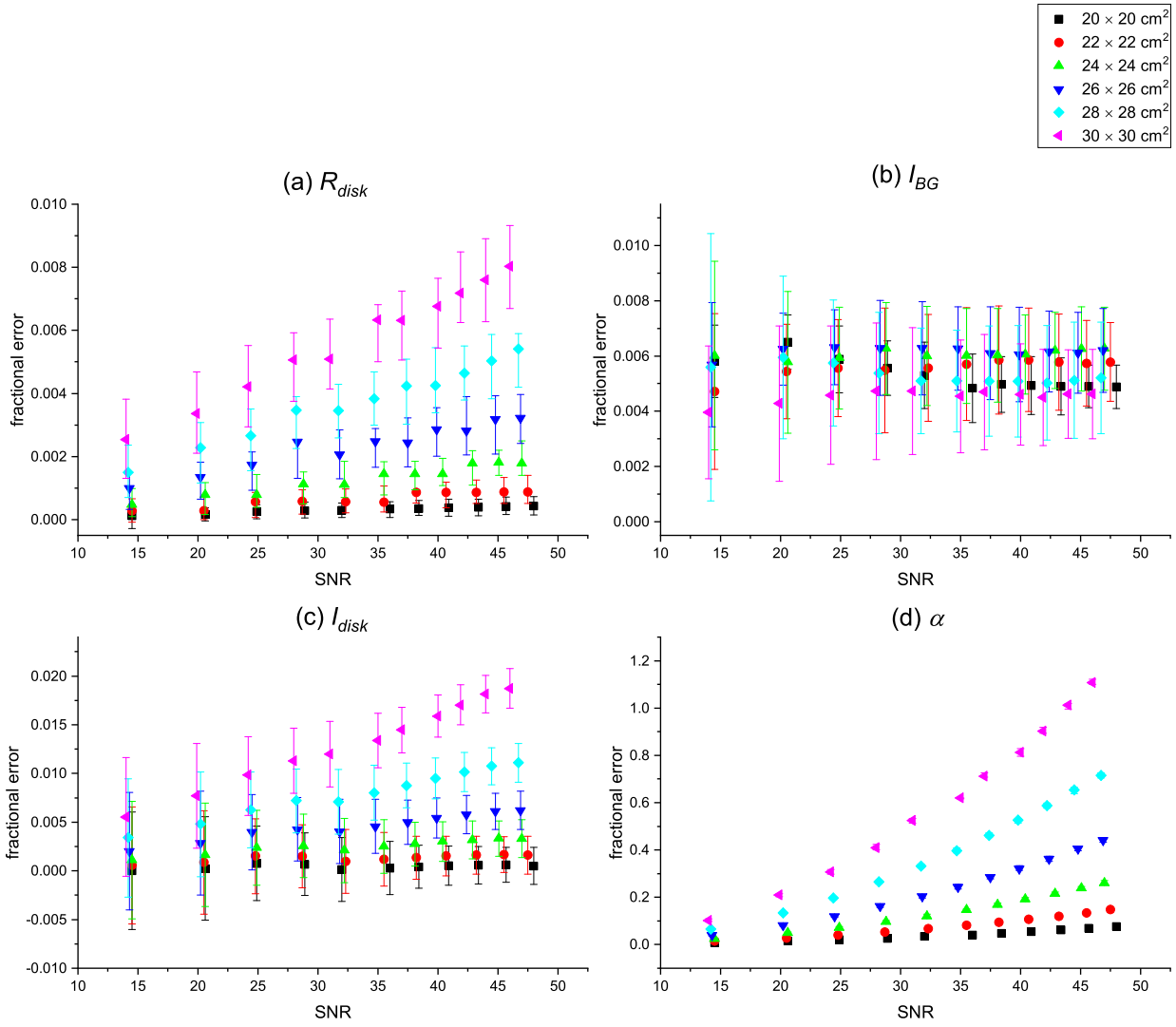


FIGURE 5.28: The magnitude of the error in parameter estimations for image quality assessments of the phantom in 5 cm water depth, imaged using parallel beams. The ROI was set to $20 \times 20$, $22 \times 22$, $24 \times 24$, $26 \times 26$, $28 \times 28$ and $30 \times 30$ $cm^2$ in size, and located at the center of the $30 \times 30$ cm$^2$ FOV. The error is presented as a fractional error for the disk radius '$R_{disk}$', the image background region fluence '$I_{BG}$', the disk region fluence '$I_{disk}$' and the noise factor '$\alpha$'.. Expected values of parameters not changing with SNR: E($R_{disk}$)= 5 cm, E($\alpha$)= 10000, E($\sigma_{PSF}$)= 0 mm, and E($f_{10\%MTF}$)= Inf cycle/mm. The detector's resolution parameters: E($\sigma_{PSF}$)= 0.03 mm, and $f_{a_{lim}}$= 10 cycle/mm.

In Figure 5.29, the fractional agreement is plotted for quality assessments with these ROI sizes. The errors in estimating the image quality parameters is shown in Figure 5.30. In measurements of $\alpha$, the fractional agreement decreased, and the MRE increased, when the size of the ROI was increased. The lack of agreement in measurements of $I_{BG}$ was interpreted as a result of image background non-homogeneity. The mean uncertainty in estimations of $R_{disk}$, $I_{disk}$, $\alpha$ and $\sigma_{PSF}$ increased when the size of the ROI was increased.

### 5.3.9 Performance when the disk radius '$R_{disk}$' is known or unknown, with parallel beam geometry

The performance of the histogram method in estimating image quality parameters when $R_{disk}$ is known versus unknown was evaluated for parallel beam geometry. Images of the disk in vacuum, simulated using parallel beams were used.

In Figure 5.31, the fractional agreement is plotted for known and unknown $R_{disk}$ assessments. The errors in estimating the image quality parameters is shown in Figure 5.32. In measurements of $\sigma_{PSF}$, the average fractional agreement increased when $R_{disk}$ was known. The fractional agreement for the other quality parameters was not affected by setting $R_{disk}$ as *a priori*. In measurements of $\alpha$, the MRE was smaller when $R_{disk}$ was known.

### 5.3.10 Performance when $R_{disk}$ is known or unknown, with diverging beam geometry

The performance of the histogram method in estimating image quality parameters when $R_{disk}$ was known versus unknown was evaluated for diverging beam geometry. Images of the disk in vacuum, simulated using a 1.2 mm focal spot source were used.

In Figure 5.33, the fractional agreement is plotted for known and unknown $R_{disk}$ assessments. The errors in estimating the image quality parameters is shown in Figure 5.34. In measurements of $\alpha$ and $\sigma_{PSF}$, the average fractional agreement increased and the MRE decreased when $R_{disk}$ was known. The agreement with the theoretical value of

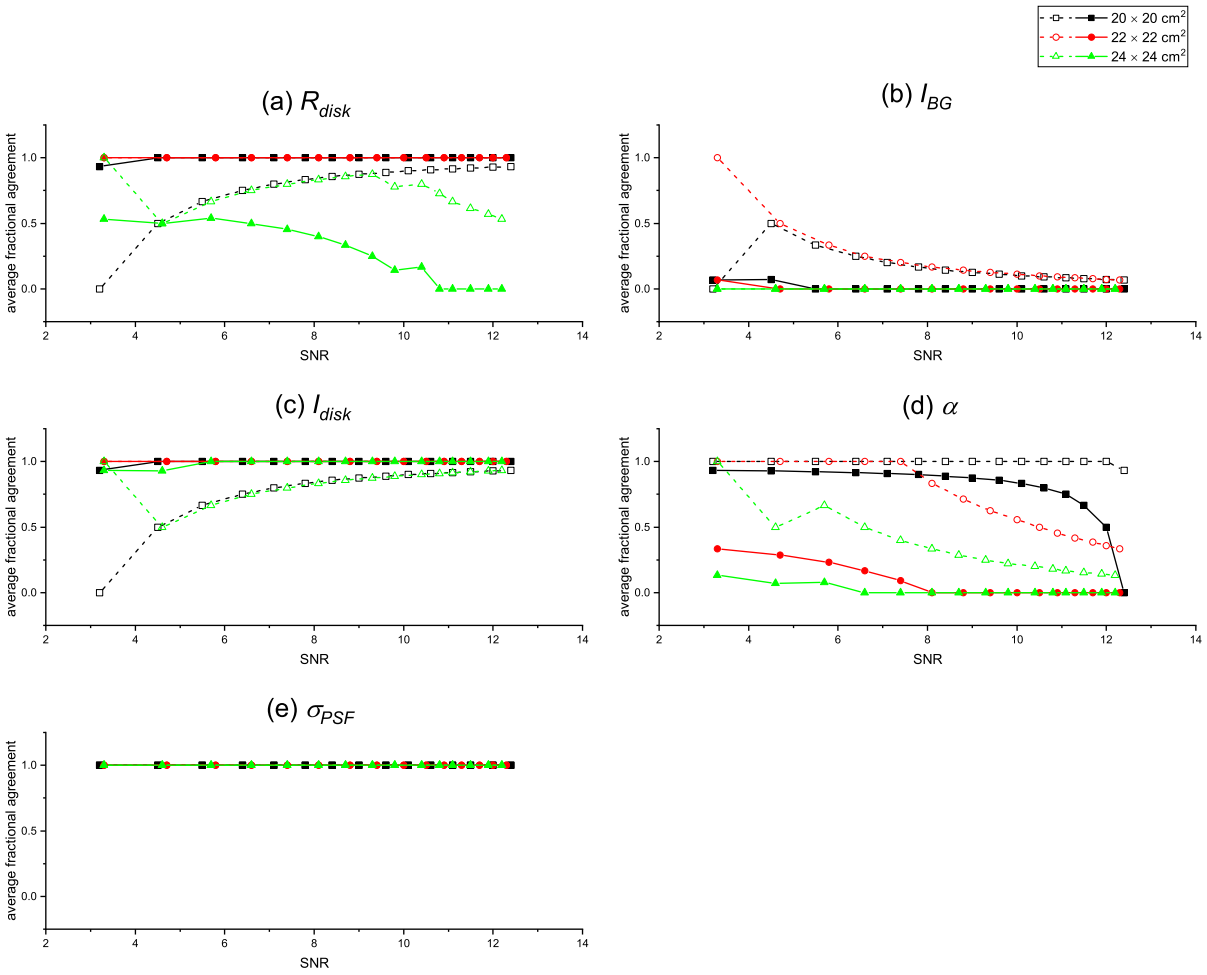


FIGURE 5.29: The average fractional agreement between measurements using the histogram method and their expected values for image quality assessments of the phantom in 5 cm water depth, imaged using a 4 mm source diverging beams. The ROI was set to $20 \times 20$, $22 \times 22$, $24 \times 24$ cm$^2$ in size at the center of the circular $22.5^2\pi$ cm$^2$ FOV. For the disk radius '$R_{disk}$', the agreement was based on a measured confidence interval encompassing the actual value of the parameter. For the image background region fluence '$I_{BG}$' and disk region fluence '$I_{disk}$', the agreement was based on a confidence interval of the histogram method overlapping with a confidence interval of the conventional method. For the transformation factor '$\alpha$' and the standard deviation of the Point Spread Function '$\sigma_{PSF}$', the agreement was based on a measured confidence interval encompassing the theoretical value of the parameter. The average fractional agreement is plotted using a dashed line and open symbols for assessments of images with an SNR equal or smaller than the SNR on the x-axis, and using a solid line and filled symbols for assessments of images with an SNR equal or greater than the SNR on the x-axis.

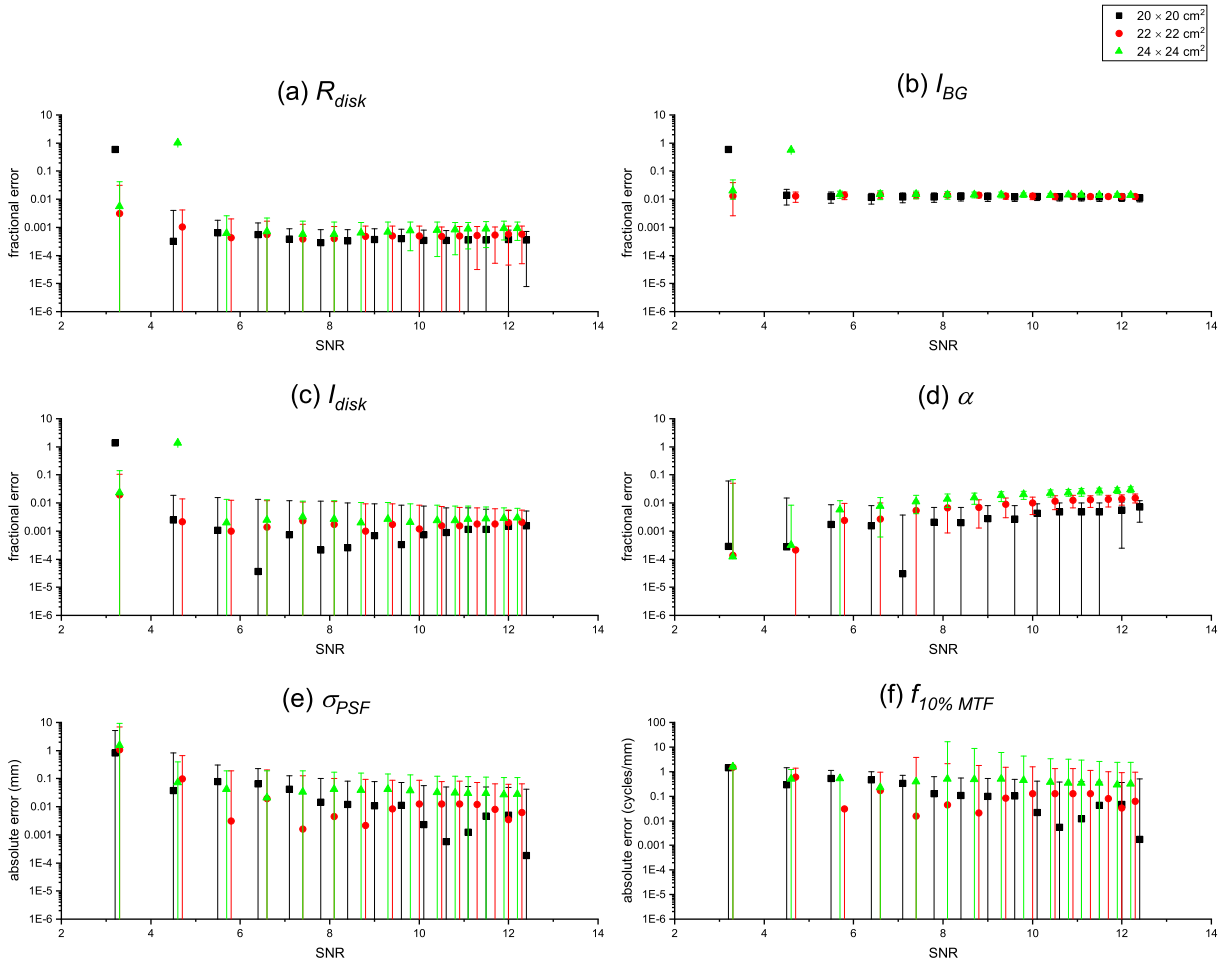


FIGURE 5.30: The magnitude of the error in parameter estimations for image quality assessments of the phantom in 5 cm water depth, imaged using a 4 mm source diverging beams. The ROI was set to 20 × 20, 22 × 22, 24 × 24 cm$^2$ in size at the center of the circular $\pi \times 22.5^2$ cm$^2$ FOV. The error is presented as a fractional error for the disk radius '$R_{disk}$', the image background region fluence '$I_{BG}$', the disk region fluence '$I_{disk}$' and the noise factor '$\alpha$', and as an absolute error for the standard deviation of the Point Spread Function '$\sigma_{PSF}$' and the frequency at 10% Modulation Transfer Function '$f_{10\%MTF}$'. Expected values of parameters not changing with SNR: E($R_{disk}$)= 5 cm, E($\alpha$)= 10000, E($\sigma_{PSF}$)= 0.19 mm, and E($f_{10\%MTF}$)= 1.8 cycle/mm. The detector's resolution parameters: E($\sigma_{PSF}$)= 0.03 mm, and $f_{a_{lim}}$= 12 cycle/mm.

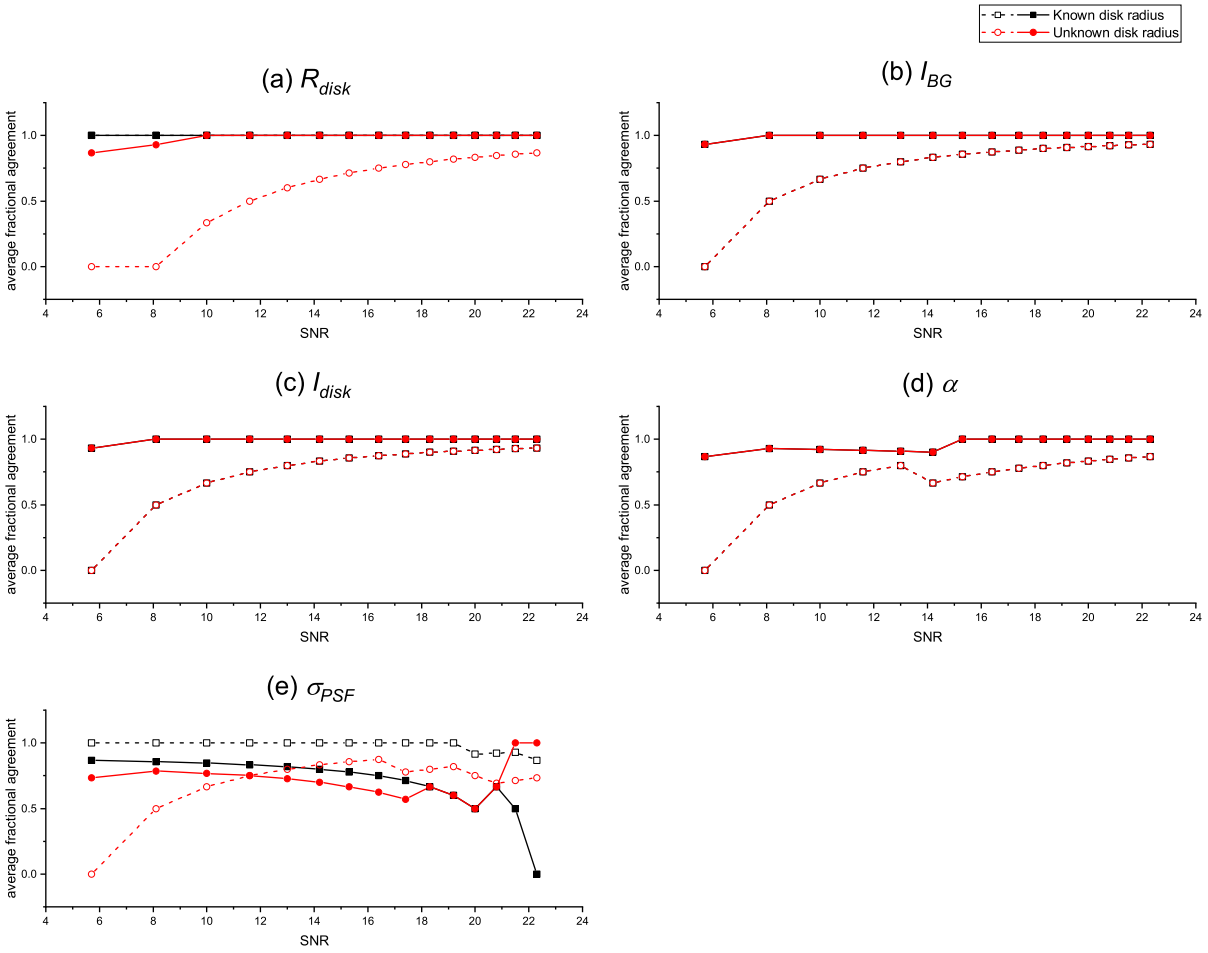


FIGURE 5.31: The average fractional agreement between measurements using the histogram method and their expected values for image quality assessments of the phantom in vacuum, imaged using parallel beams, when $R_{disk}$ was known or unknown. For the disk radius '$R_{disk}$', the agreement was based on a measured confidence interval encompassing the actual value of the parameter. For the image background region fluence '$I_{BG}$' and disk region fluence '$I_{disk}$', the agreement was based on a confidence interval of the histogram method overlapping with a confidence interval of the conventional method. For the transformation factor '$\alpha$' and the standard deviation of the Point Spread Function '$\sigma_{PSF}$', the agreement was based on a measured confidence interval encompassing the theoretical value of the parameter. The average fractional agreement is plotted using a dashed line and open symbols for assessments of images with an SNR equal or smaller than the SNR on the x-axis, and using a solid line and filled symbols for assessments of images with an SNR equal or greater than the SNR on the x-axis.

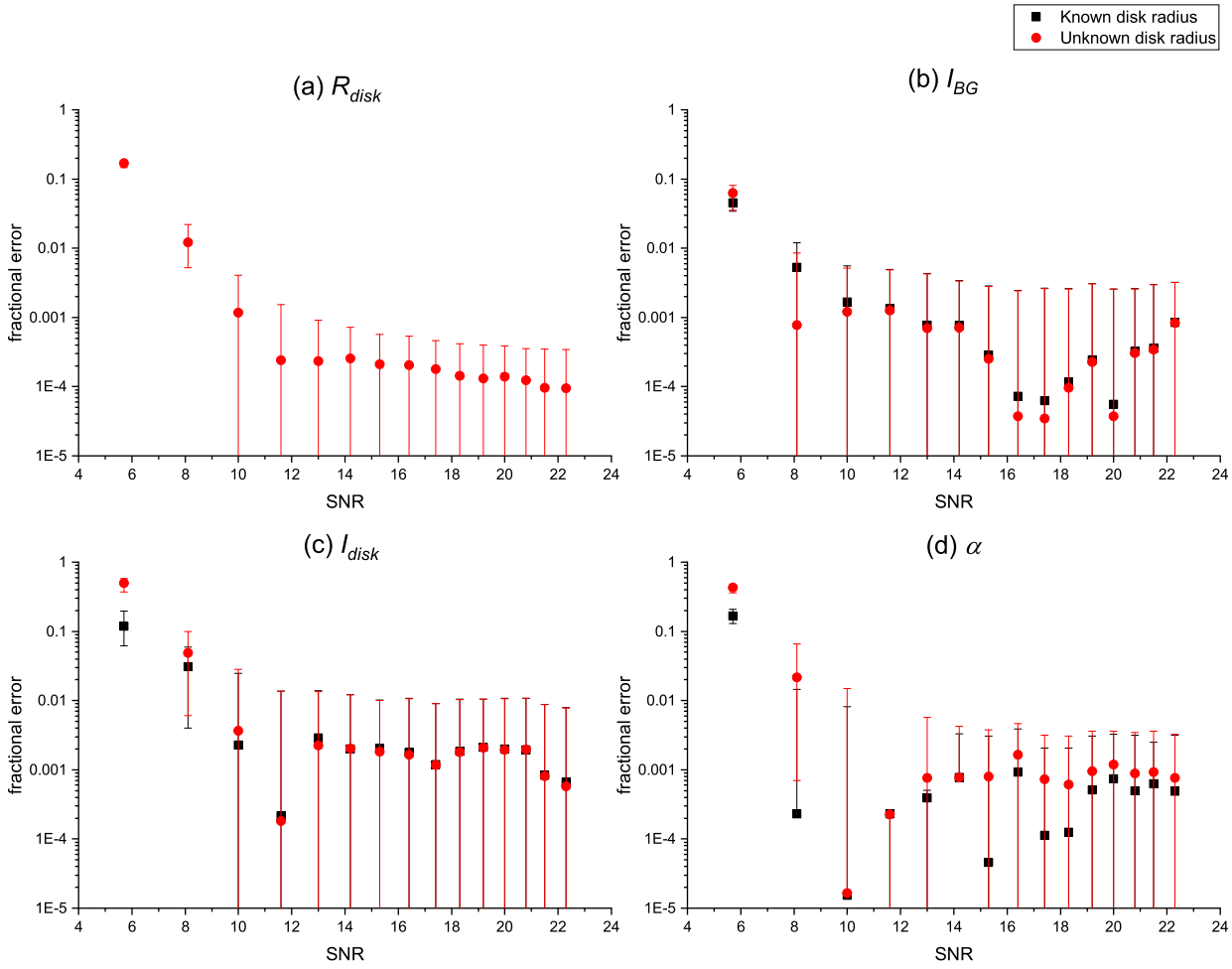


FIGURE 5.32: The magnitude of the error in parameter estimations for image quality assessments of the phantom in vacuum, imaged using parallel beams, when $R_{disk}$ was known or unknown. The error is presented as a fractional error for the disk radius '$R_{disk}$', the image background region fluence '$I_{BG}$', the disk region fluence '$I_{disk}$' and the noise factor '$\alpha$'. Expected values of parameters not changing with SNR: E($R_{disk}$)= 5 cm, E($\alpha$)= 10000, E($\sigma_{PSF}$)= 0 mm, and E($f_{10\%MTF}$)= Inf cycle/mm. The detector's resolution parameters: E($\sigma_{PSF}$)= 0.03 mm, and $f_{a_{lim}}$= 10 cycle/mm.

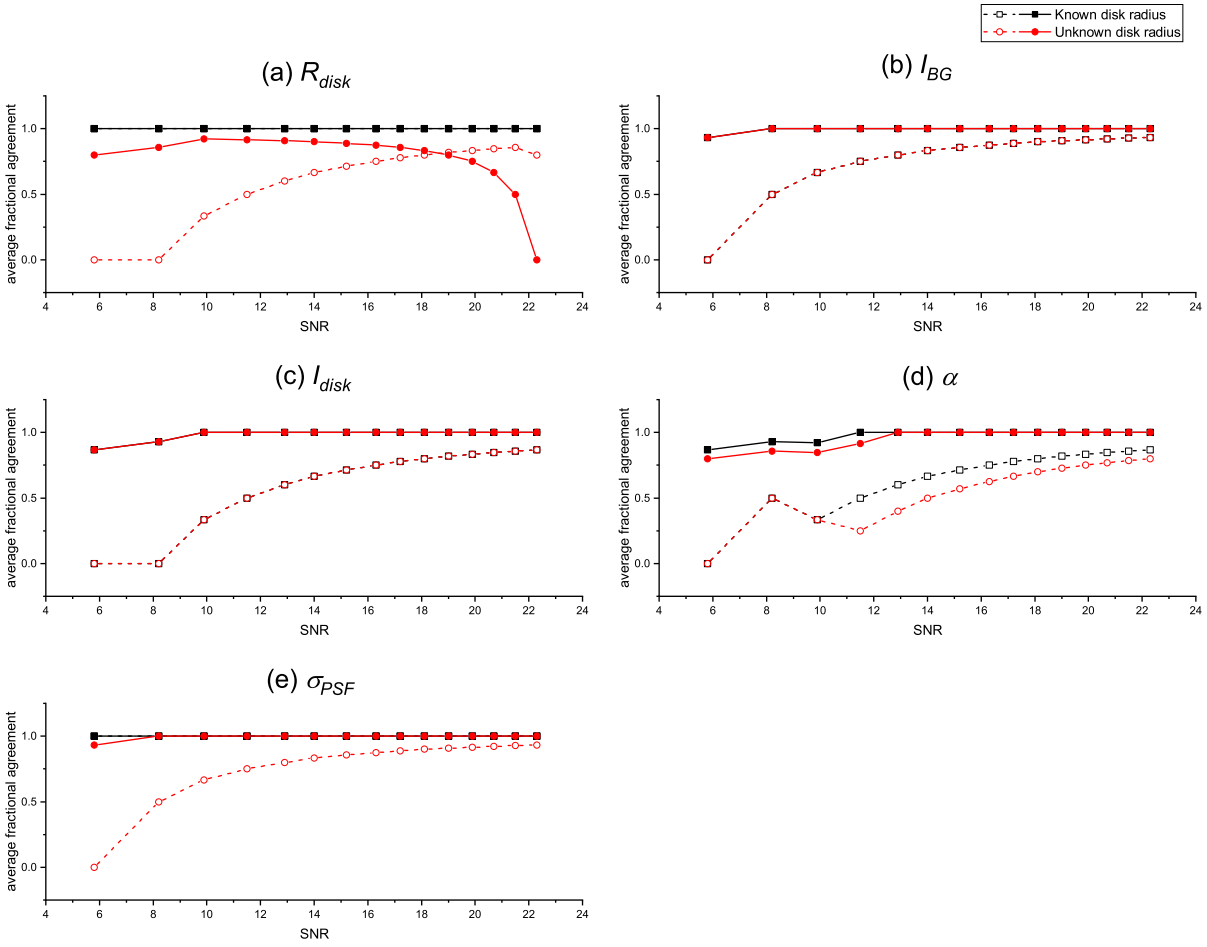


FIGURE 5.33: The average fractional agreement between measurements using the histogram method and their expected values for image quality assessments of the phantom in vacuum, imaged using a 1.2 mm diverging beams, when $R_{disk}$ was known or unknown. For the disk radius '$R_{disk}$', the agreement was based on a measured confidence interval encompassing the actual value of the parameter. For the image background region fluence '$I_{BG}$' and disk region fluence '$I_{disk}$', the agreement was based on a confidence interval of the histogram method overlapping with a confidence interval of the conventional method. For the transformation factor '$\alpha$' and the standard deviation of the Point Spread Function '$\sigma_{PSF}$', the agreement was based on a measured confidence interval encompassing the theoretical value of the parameter. The average fractional agreement is plotted using a dashed line and open symbols for assessments of images with an SNR equal or smaller than the SNR on the x-axis, and using a solid line and filled symbols for assessments of images with an SNR equal or greater than the SNR on the x-axis.

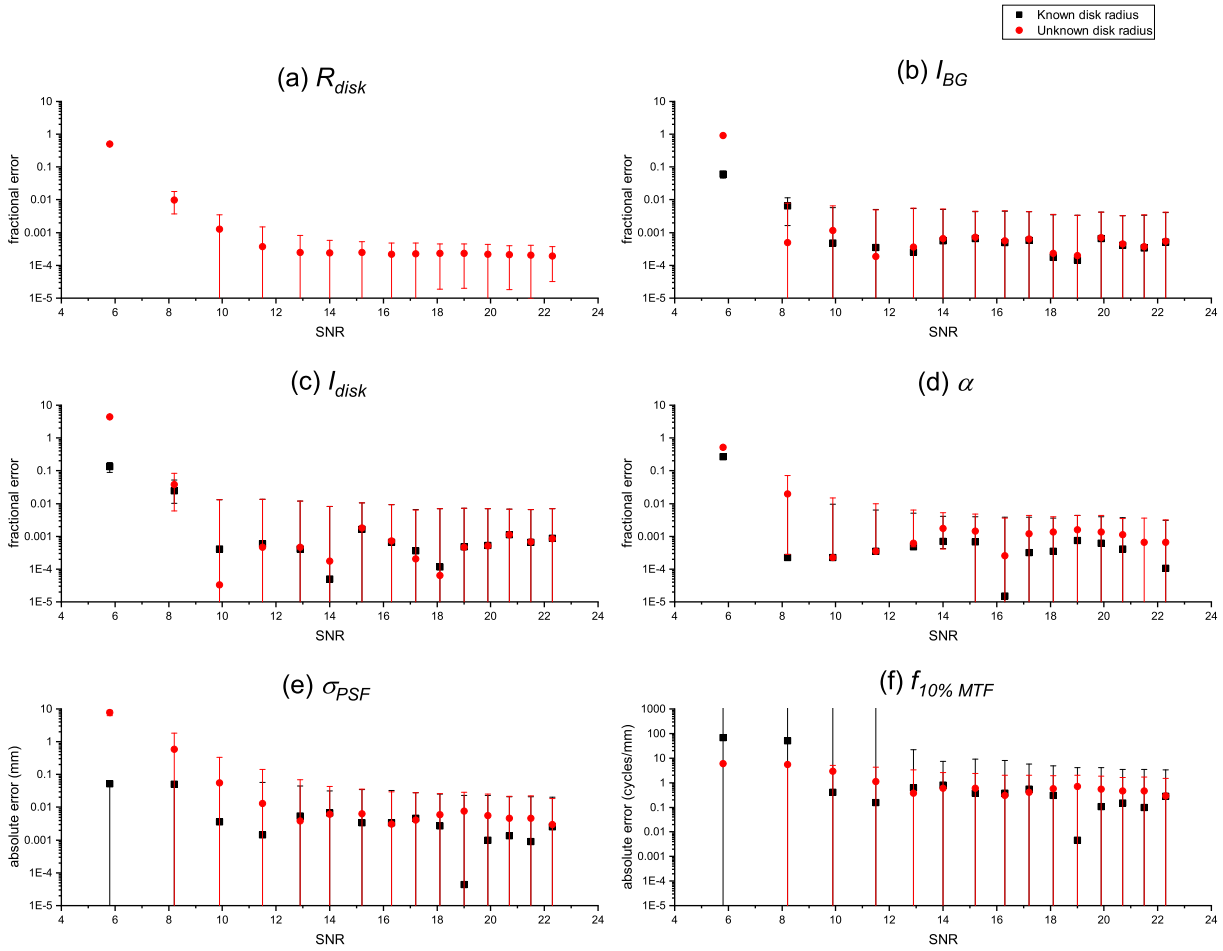


FIGURE 5.34: The magnitude of the error in parameter estimations for image quality assessments of the phantom in vacuum, imaged using a 1.2 mm diverging beams, when $R_{disk}$ was known or unknown. The error is presented as a fractional error for the disk radius '$R_{disk}$', the image background region fluence '$I_{BG}$', the disk region fluence '$I_{disk}$' and the noise factor '$\alpha$', and as an absolute error for the standard deviation of the Point Spread Function '$\sigma_{PSF}$' and the frequency at 10% Modulation Transfer Function '$f_{10\%MTF}$'. Expected values of parameters not changing with SNR: E($R_{disk}$)= 5 cm, E($\alpha$)= 10000, E($\sigma_{PSF}$)= 0.06 mm, and E($f_{10\%MTF}$)= 6 cycle/mm. The detector's resolution parameters: E($\sigma_{PSF}$)= 0.03 mm, and $f_{a_{lim}}$= 12 cycle/mm.

$\alpha$ was affected by setting $R_{disk}$ as *a priori* in diverging beams images, but not in parallel beams images.

### 5.3.11 Performance with varying pixel sizes, and diverging beam geometry (3.6 cycle/mm resolution)

The performance of the developed method in estimating image quality parameters with varying pixel sizes was evaluated. Images of the disk in vacuum simulated using a 2 mm focal spot source were used. The pixel sizes compared were 0.05 mm and 0.1 mm.

In Figure 5.35, the fractional agreement is plotted for assessments of images with these pixel sizes. The estimated error in measurements of the image quality parameters is shown in Figure 5.36. For $R_{disk}$ and $I_{BG}$, the average fractional agreement was larger with the 0.1 mm than with the 0.05 mm pixel size. For $I_{BG}$, the relative error was smaller for the larger pixel size. In measurements of $I_{disk}$ and $\alpha$, there was no consistent effect of the pixel size on the relative error. In most measurements of $\sigma_{PSF}$, the error was smaller for images of the 0.05 mm pixel size. The smaller pixel size did not significantly improve the results for SNR values less than 10. For most measurements of all parameters, the relative uncertainty was smaller for the smaller pixel size.

### 5.3.12 Performance with varying pixel sizes, and diverging beam geometry (1.8 cycle/mm resolution)

The performance of the histogram method in estimating image quality parameters with varying pixel sizes was tested for a spatial resolution different from described in the previous section 5.3.11. Images of the disk in vacuum simulated using a 4 mm focal spot source were used. The pixel sizes compared were 0.05 and 0.1 mm.

In Figure 5.37, the fractional agreement is plotted for assessments of images with these pixel sizes. The estimated error in measurements of the image quality parameters is shown in Figure 5.38. For $R_{disk}$ and $\alpha$, the average fractional agreement was larger for images with the 0.1 mm than with the 0.05 mm pixel size. In measurements of

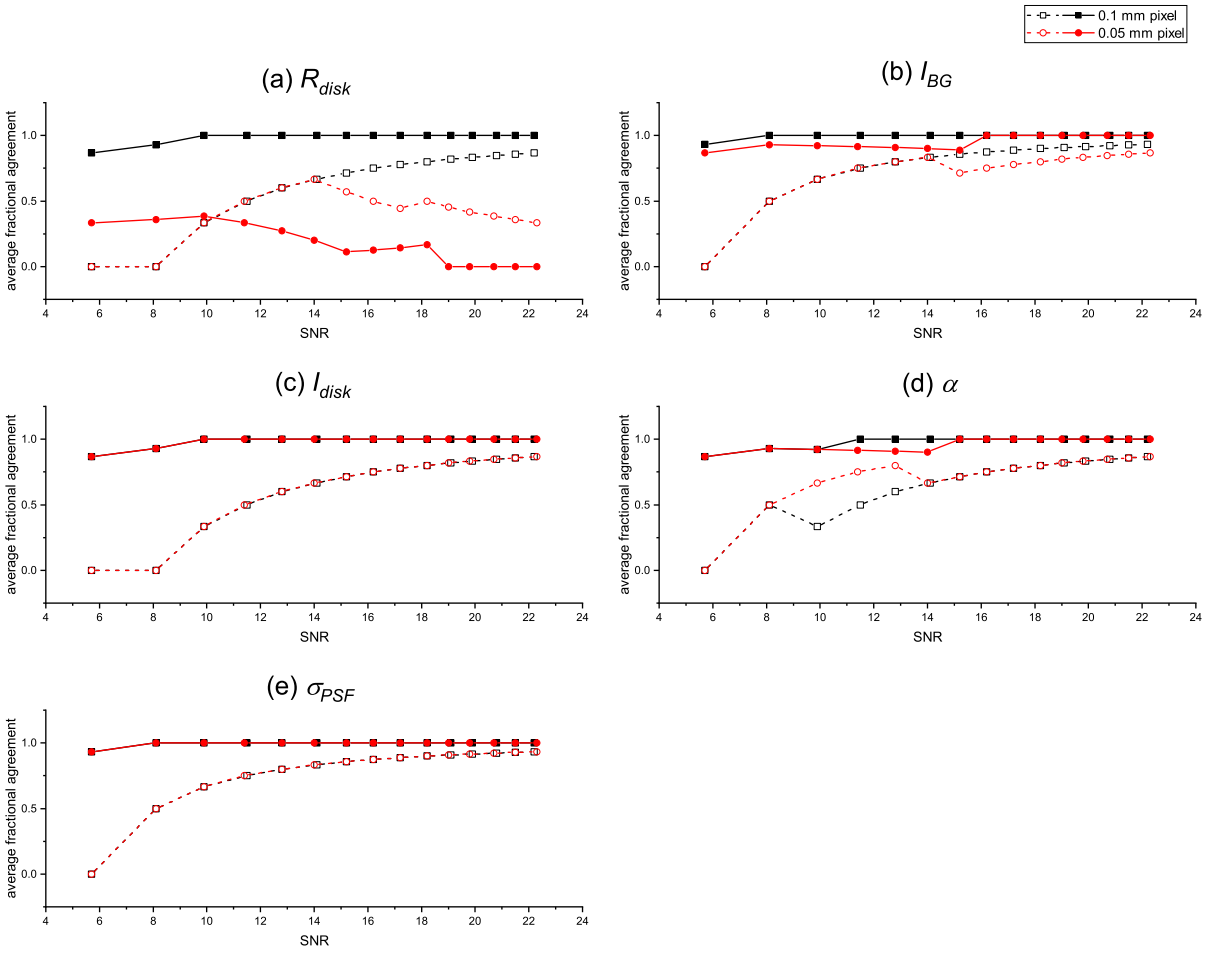


FIGURE 5.35: The average fractional agreement between measurements using the histogram method and their expected values for image quality assessments of the phantom in vacuum, imaged using a 2 mm source diverging beams, with pixel sizes of 0.05 and 0.1 mm. For the disk radius '$R_{disk}$', the agreement was based on a measured confidence interval encompassing the actual value of the parameter. For the image background region fluence '$I_{BG}$' and disk region fluence '$I_{disk}$', the agreement was based on a confidence interval of the histogram method overlapping with a confidence interval of the conventional method. For the transformation factor '$\alpha$' and the standard deviation of the Point Spread Function '$\sigma_{PSF}$', the agreement was based on a measured confidence interval encompassing the theoretical value of the parameter. The average fractional agreement is plotted using a dashed line and open symbols for assessments of images with an SNR equal or smaller than the SNR on the x-axis, and using a solid line and filled symbols for assessments of images with an SNR equal or greater than the SNR on the x-axis.

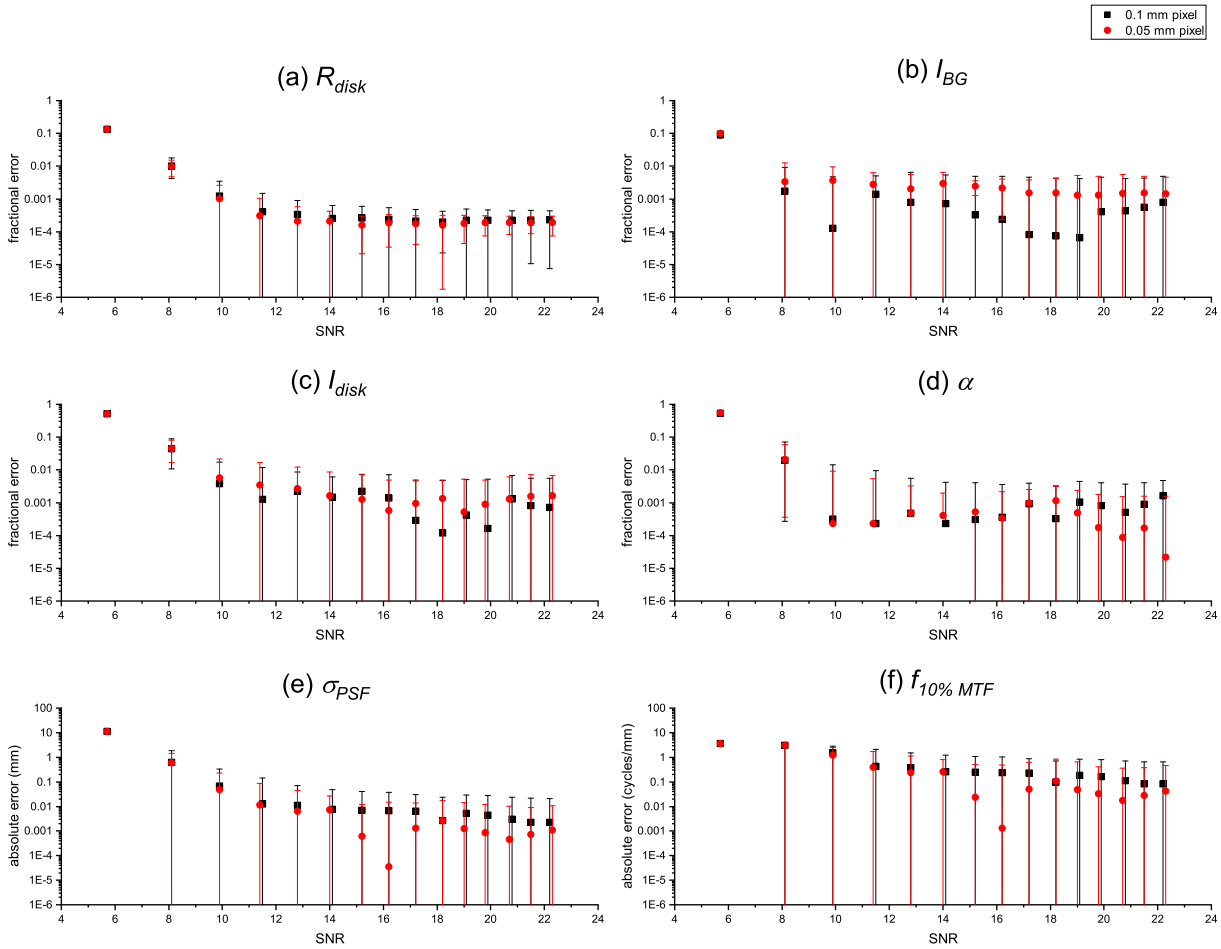


FIGURE 5.36: The magnitude of the error in parameter estimations for image quality assessments of the phantom in vacuum, imaged using a 2 mm source diverging beams, with pixel sizes of 0.05 and 0.1 mm. The error is presented as a fractional error for the disk radius '$R_{disk}$', the image background region fluence '$I_{BG}$', the disk region fluence '$I_{disk}$' and the noise factor '$\alpha$', and as an absolute error for the standard deviation of the Point Spread Function '$\sigma_{PSF}$' and the frequency at 10% Modulation Transfer Function '$f_{10\%MTF}$'. Expected values of parameters not changing with SNR: E($R_{disk}$)= 5 cm, E($\alpha$)= 10000 for the 0.1 mm pixel size and 40000 for the 0.05 mm pixel size, E($\sigma_{PSF}$)= 0.09 mm, and E($f_{10\%MTF}$)= 3.6 cycle/mm. The detector's resolution parameters: E($\sigma_{PSF}$)= 0.03 mm for the 0.1 mm pixel size and 0.01 mm for the 0.05 mm pixel size, and $f_{a_{lim}}$= 12 cycle/mm for the 0.1 mm pixel size and 24 cycle/mm for the 0.05 mm pixel size.

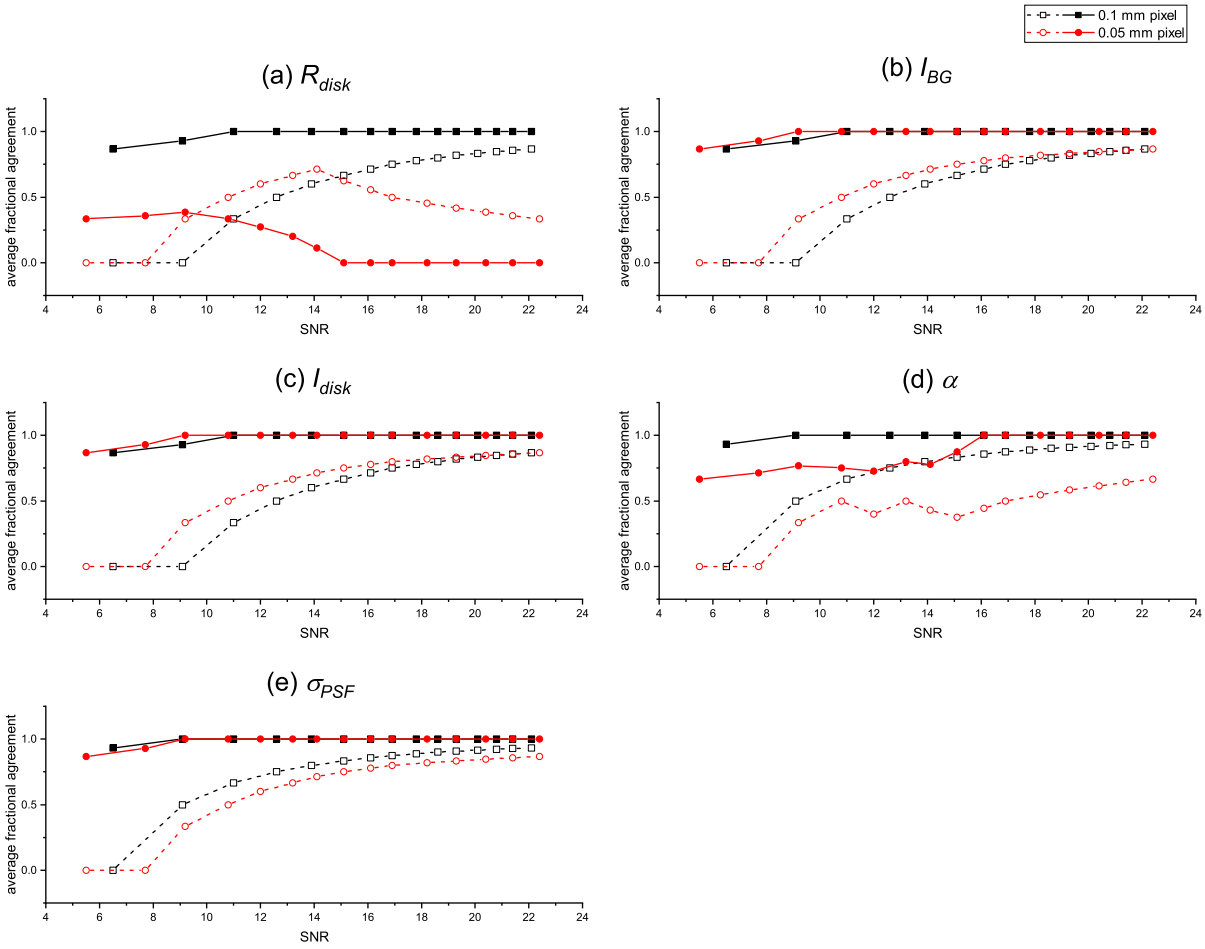


FIGURE 5.37: The average fractional agreement between measurements using the histogram method and their expected values for image quality assessments of the phantom in vacuum, imaged using a 4 mm source diverging beams, with pixel sizes of 0.05 and 0.1 mm. For the disk radius '$R_{disk}$', the agreement was based on a measured confidence interval encompassing the actual value of the parameter. For the image background region fluence '$I_{BG}$' and disk region fluence '$I_{disk}$', the agreement was based on a confidence interval of the histogram method overlapping with a confidence interval of the conventional method. For the transformation factor '$\alpha$' and the standard deviation of the Point Spread Function '$\sigma_{PSF}$', the agreement was based on a measured confidence interval encompassing the theoretical value of the parameter. The average fractional agreement is plotted using a dashed line and open symbols for assessments of images with an SNR equal or smaller than the SNR on the x-axis, and using a solid line and filled symbols for assessments of images with an SNR equal or greater than the SNR on the x-axis.

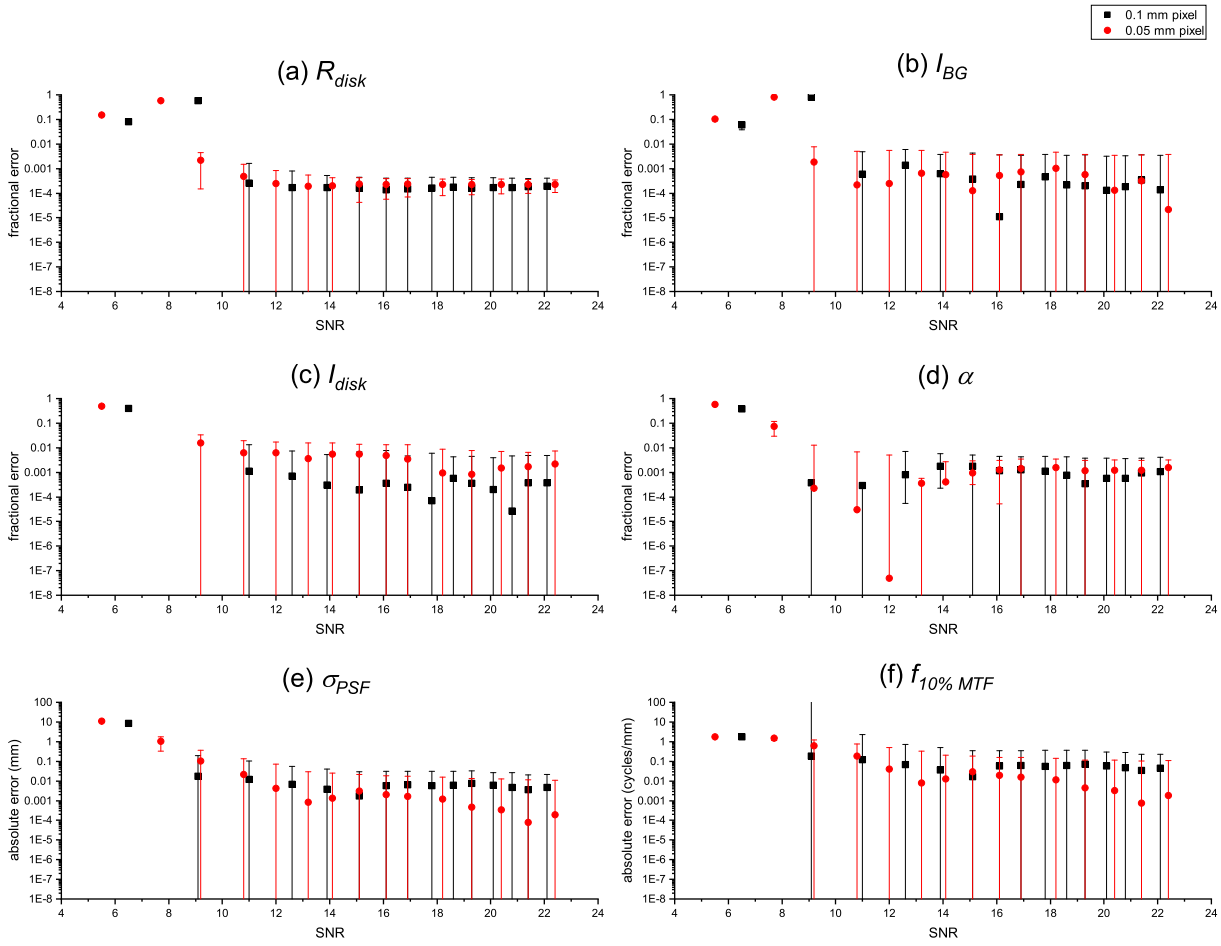


FIGURE 5.38: The magnitude of the error in parameter estimations for image quality assessments of the phantom in vacuum, imaged using a 4 mm source diverging beams, with pixel sizes of 0.05 and 0.1 mm. The error is presented as a fractional error for the disk radius '$R_{disk}$', the image background region fluence '$I_{BG}$', the disk region fluence '$I_{disk}$' and the noise factor '$\alpha$', and as an absolute error for the standard deviation of the Point Spread Function '$\sigma_{PSF}$' and the frequency at 10% Modulation Transfer Function '$f_{10\%MTF}$'. Expected values of parameters not changing with SNR: E($R_{disk}$)= 5 cm, E($\alpha$)= 10000 for the 0.1 mm pixel size and 40000 for the 0.05 mm pixel size, E($\sigma_{PSF}$)= 0.19 mm, and E($f_{10\%MTF}$)= 1.8 cycle/mm. The detector's resolution parameters: E($\sigma_{PSF}$)= 0.03 mm for the 0.1 mm pixel size and 0.01 mm for the 0.05 mm pixel size, and $f_{a_{lim}}$= 12 cycle/mm for the 0.1 mm pixel size and 24 cycle/mm for the 0.05 mm pixel size.

$I_{BG}$ and $\alpha$, there was no consistent effect of the pixel size on the relative error. For most measurements of $I_{disk}$, the relative error was smaller for the 0.1 mm pixel size. In measurements of $\sigma_{PSF}$, the error became smaller for the 0.05 mm pixel size, than the 0.1 mm pixel size, as the SNR was increased. Decreasing the pixel size did not improve the results for images with SNR values less than 10. For most measurements of all parameters, the relative uncertainty was smaller for the smaller pixel size.

The consistency between the two tested spatial resolutions was in measurements of $R_{disk}$ and $\sigma_{PSF}$, where the agreement with the actual value of $R_{disk}$ was larger with the larger pixel size, and the error in measurements of $\sigma_{PSF}$ became smaller for the 0.05 mm pixel size, than the 0.1 mm pixel size, as the SNR was increased.

### 5.3.13 Performance with the absence and presence of the disk

The performance of the histogram method in recognizing the absence of the disk was evaluated. Images of a flat-field 5 cm water background simulated using parallel beams were used.

The confidence interval contained the actual $R_{disk}$ value of zero for 17 out of 31 images simulated at varying exposure levels. For 2 out of the 31 assessed sample images, the confidence interval spanned the assigned optimization variable range, from the lower to the upper bound, as the disk could have an area of zero or span the whole image.

## 5.4 Summary of the results

### 5.4.1 Quality parameters

As the results of the initial assessment were based on various focal spot sizes (including non-realistic point sources and parallel beams, and focal spot sizes not satisfying the Nyquist criterion), they were not used to reach conclusions as to the performance of the image quality assessment method.

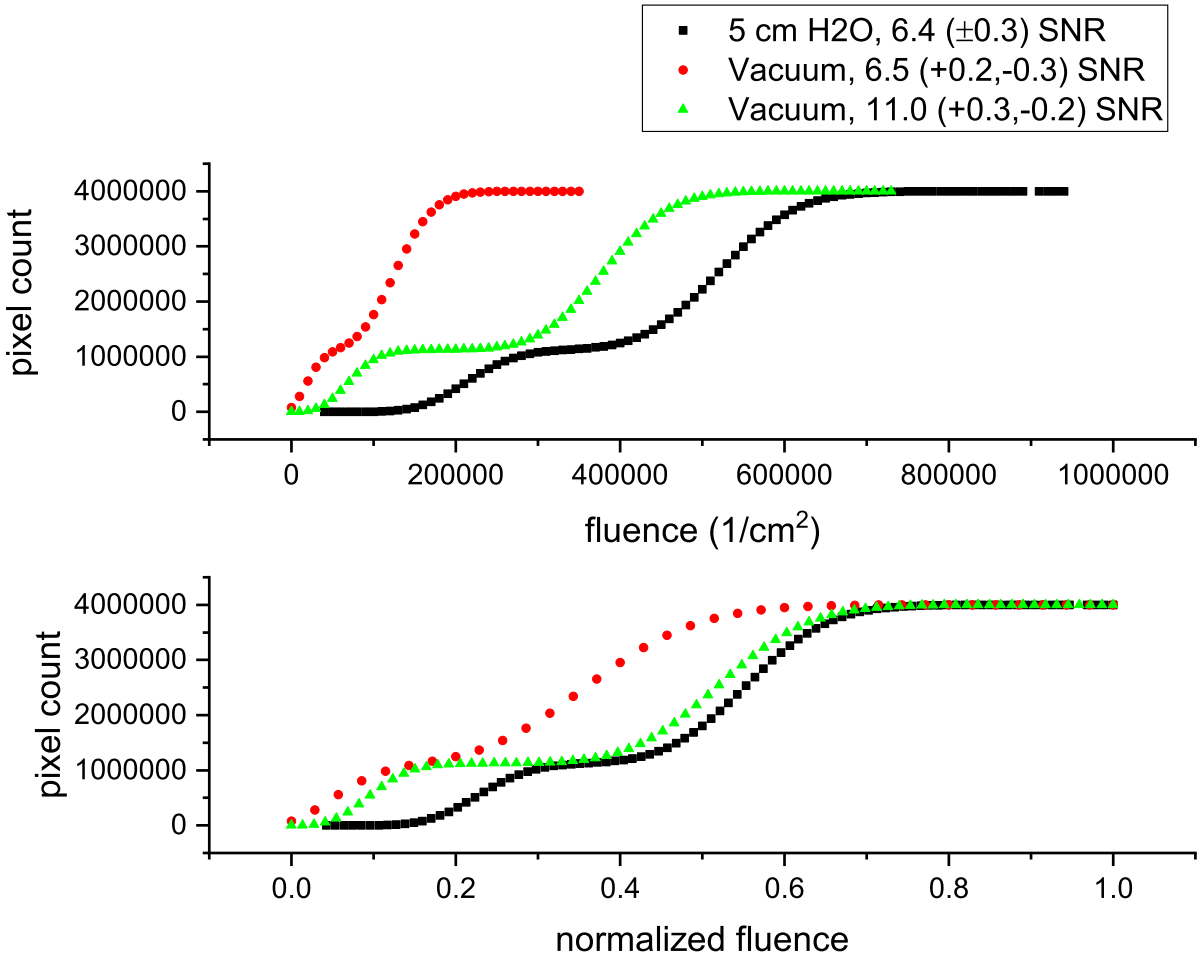


FIGURE 5.39: Cumulative histograms for images with vacuum and water backgrounds at varying SNR levels, simulated using a 4 mm focal spot source.

As expected, the SNR level was a limiting factor of the ability to measure the quality parameters by a cumulative histogram fit. Figure 5.39 shows the cumulative histograms for images with vacuum and water backgrounds at varying SNR levels, simulated using a 4 mm focal spot source. As the SNR level decreases, the number of data points in the fitting process decreases. Also, as the SNR level decreases, the noise degradation effect on the shape of the cumulative histogram overrides the blurring degradation effect. This is observed as fewer points forming a segment of the curve with a slope of zero at $\pi \times (R_{disk} \times m/a)^2$ ($\sim$ 1130973 pixel count), where $m$ is the magnification and $a$ is the sampling aperture.

The measurement of the spatial resolution in terms of $\sigma_{PSF}$ was affected by the size of the focal spot size, the background material in the image, and whether $R_{disk}$ was *a priori* or not. The estimated uncertainty and relative uncertainty of measurements of $\sigma_{PSF}$ decreased for an increasing focal spot size. For images with similar SNRs, the measurements of $\sigma_{PSF}$ improved when the background material was changed from vacuum to water. However, for images with a 5 cm water depth, $I_{BG}$ was always overestimated, by an average value of 1.2 ($\pm$0.1) %, and the error in measurements of $\alpha$ increased as the exposure was increased. When the focal spot size and the background material of the image were not varied, the error of measurements of $\sigma_{PSF}$ decreased when $R_{disk}$ was *a priori*. However, there was an increase in the uncertainty of the measurements.

For the 4 mm focal spot images of the disk in vacuum, the results improved at an SNR value of 11.0 (+0.3, -0.2) (section C.4 of Appendix C). For this beam geometry, no images with an SNR value > 9.1 (+0.3, -0.2) and < 11.0 (+0.3, -0.2) were tested. Based on simulated images of the phantom in vacuum, using diverging beams with a focal spot size of 4 mm in diameter ($f_{10\%MTF} = 1.8$ cycle/mm), with SNR values of 11.0 (+0.3, -0.2) to 22.4 ($\pm$0.6), the agreement with the expected values, and the accuracy of measurements of the quality parameters are listed in Table 5.1. The corresponding error distribution is presented in Figure 5.40, and the uncertainty in measurements of the quality parameters is in Table 5.2. The error in the measured optimal values of $R_{disk}$

TABLE 5.1: Agreement with the expected values and error in measurements of the quality parameters at SNR values of 11.0 (+0.3, -0.2) to 22.1 (+0.6, -0.5), based on 4 mm focal spot ($\sigma_{PSF} = 0.19$ mm,$f_{10\%MTF} = 1.8$ cycle/mm) diverging beams simulations of the disk in vacuum.

| Parameter | Average fractional agreement | | Mean error | $\delta_{-_{mean\ error}}$ | $\delta_{+_{mean\ error}}$ |
|---|---|---|---|---|---|
| Radius | 100 | % | 0.02% | 0.01% | 0.01% |
| Background fluence | 100 | % | 0 % | 0.1% | 0.1% |
| Disk fluence | 100 | % | 0 % | 0.2% | 0.2% |
| Noise factor | 100 | % | 0.1% | 0.1% | 0.1% |
| PSF standard deviation | 100 | % | 0.01 mm | 0.01 mm | 0.01 mm |
| Frequency at 10% MTF | 100 | % | 0.1 $\frac{\text{cycle}}{\text{mm}}$ | 0.1 $\frac{\text{cycle}}{\text{mm}}$ | 0.2 $\frac{\text{cycle}}{\text{mm}}$ |

and $f_{10\%MTF}$ was always positive. The MRE in measurements of $R_{disk}$ was 0.02 ($\pm$0.01) %. Therefore, a subpixel accuracy was obtained (the MRE was less than the pixel size

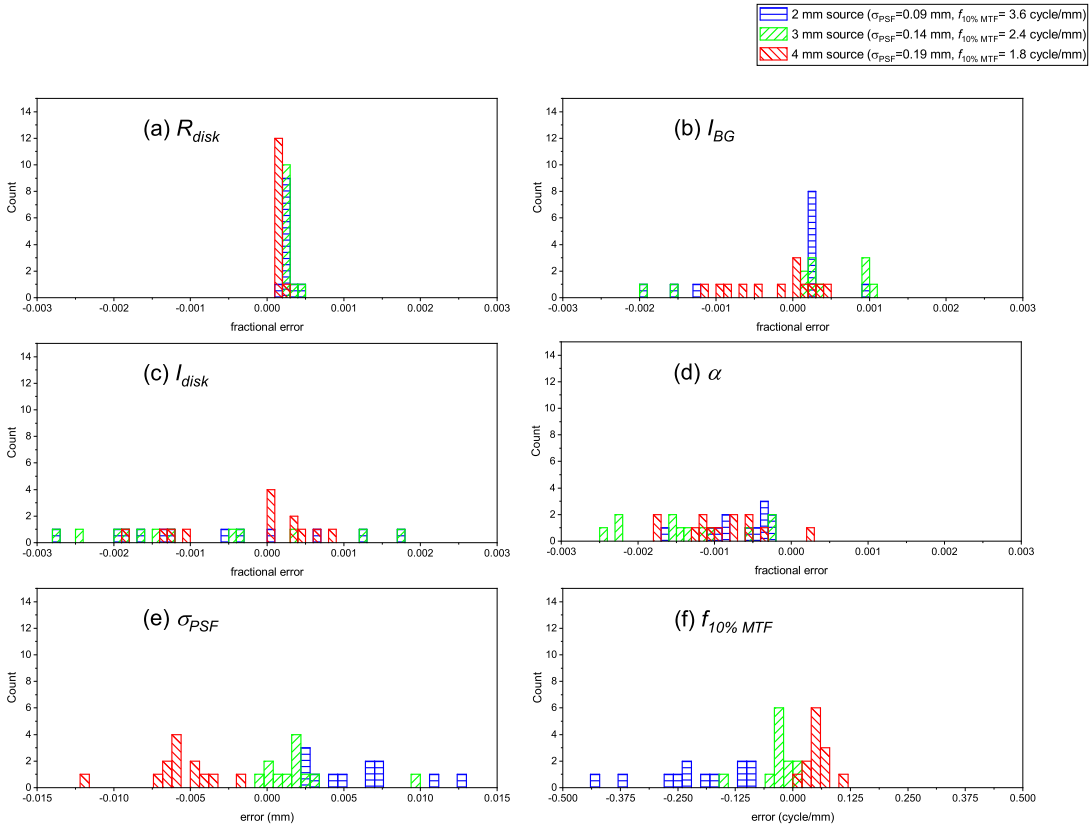


FIGURE 5.40: The error distribution for image quality assessments of the phantom in vacuum, imaged using 2, 3 and 4 mm focal spot sources. The SNR of the images was 11.0 (+0.3, -0.2) to 22.2 (+0.7, -0.6). The error is presented as a fractional error for the disk radius '$R_{disk}$', the image background region fluence '$I_{BG}$', the disk region fluence '$I_{disk}$' and the noise factor '$\alpha$', and as an absolute error for the standard deviation of the Point Spread Function '$\sigma_{PSF}$' and the frequency at 10% Modulation Transfer Function '$f_{10\%MTF}$'. Expected values of parameters not changing with SNR: E($R_{disk}$)= 5 cm, E($\alpha$)= 10000, E($\sigma_{PSF}$) and E($f_{10\%MTF}$) are as in the legend. The detector's resolution parameters: E($\sigma_{PSF}$)= 0.03 mm, and $f_{a_{lim}}$= 12 cycle/mm.

TABLE 5.2: Uncertainty in measurements of the quality parameters at SNR values of 11.0 (+0.3, -0.2) to 22.1 (+0.6, -0.5), based on 4 mm focal spot ($\sigma_{PSF} = 0.19$ mm,$f_{10\%MTF} = 1.8$ cycle/mm) diverging beams simulations of the disk in vacuum.

| Parameter | Average positive uncertainty | Minimum positive uncertainty | Maximum positive uncertainty |
|---|---|---|---|
| Radius | 0.04% | 0.02% | 0.1% |
| Background fluence | 0.03% | 0.01% | 0.1% |
| Disk fluence | 0.1% | 0.05% | 0.3% |
| Noise factor | 0.3% | 0.0002% | 0.4% |
| PSF standard deviation | 0.04 mm | 0.02 mm | 0.2 mm |
| Frequency at 10% MTF | $0.5\frac{\text{cycle}}{\text{mm}}$ | $0.2\frac{\text{cycle}}{\text{mm}}$ | $2\ \frac{\text{cycle}}{\text{mm}}$ |
| **Parameter** | **Average negative uncertainty** | **Minimum negative uncertainty** | **Maximum negative uncertainty** |
| Radius | 0.03% | 0.02% | 0.1% |
| Background fluence | 0.02% | 0.01% | 0.09% |
| Disk fluence | 0.1% | 0.06% | 0.6% |
| Noise factor | 0.4% | 0.3% | 1 % |
| PSF standard deviation | 0.03 mm | 0.02 mm | 0.09 mm |
| Frequency at 10% MTF | $0.3\frac{\text{cycle}}{\text{mm}}$ | $0.2\frac{\text{cycle}}{\text{mm}}$ | $0.9\frac{\text{cycle}}{\text{mm}}$ |

divided by the actual $R_{disk}$ value and the magnification: 0.1 mm/ 6 cm). The error in measurements of $f_{10\%MTF}$ was expected to be negative since it was calculated based on an upper bound expectation. However, in measurements of focal spot sizes with theoretical $f_{10\%MTF}$ values of 2.4 cycle/mm and 3.6 cycle/mm, the error was negative most of the time (Figure 5.40, sections C.3 and C.2 of Appendix C). The estimated uncertainty of measurements of $f_{10\%MTF}$ decreased as the SNR of an image increased (Figure 5.41).

For images of the disk in 5 cm water depth with SNR values of 7.8 ($\pm$0.3) to 12.4 ($\pm$0.3), the mean error in measurements of $f_{10\%MTF}$ was similar to the mean error reported for images of the disk in vacuum with SNR values between 11.0 (+0.3, -0.2) and 22.1 (+0.6, -0.5). However, the error in measurements of the other quality parameters was larger for images with a 5 cm water depth compared to a vacuum background, for reasons discussed in the next chapter.

### 5.4.2 Quality metrics

#### SNR

The SNR estimation was affected by the size of the ROI; increasing the size of the ROI resulted in a lower estimation of the SNR by both of the histogram and conventional methods. This was due to the estimation of a smaller value of $I_{BG}$ as the ROI size was

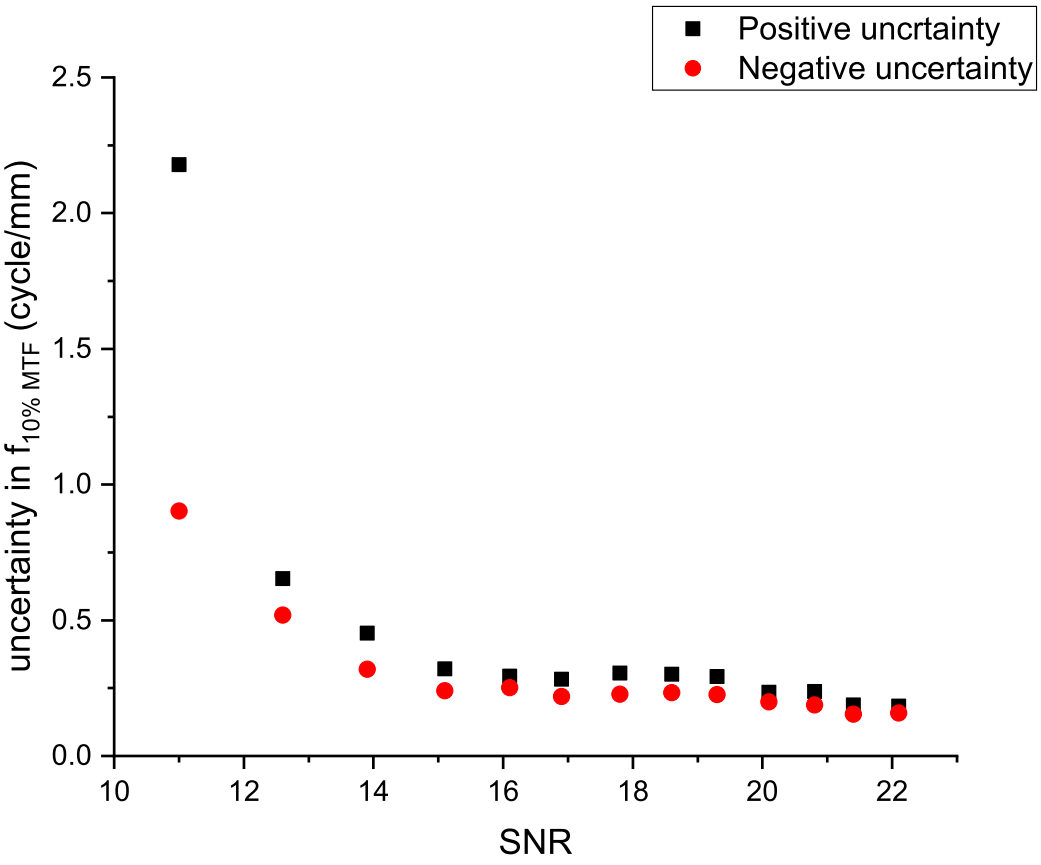


FIGURE 5.41: The uncertainty in measurements of $f_{10\%MTF}$ for image quality assessments of the phantom in vacuum, imaged using a 4 mm focal spot source ($f_{10\%MTF}$ = 1.8 cycle/mm). The uncertainty decreased for an increasing SNR.

increased. The following discussion is based on quality assessments where a ROI size of $20 \times 20$ cm$^2$ was used.

For the quality assessments of 4 mm focal spot diverging beams images of the disk in vacuum, the SNR measurements of the histogram and conventional methods were in agreement at an SNR of 11.0 (+0.3, -0.2) and higher. No images with an SNR lower than 6.5 (+0.2, -0.3) were tested. Theoretical SNR values were estimated based on the narrow beam $\frac{\mu}{\rho}$ values. The confidence interval of the conventional method encompassed the theoretical SNR value for all images with a measured SNR of 6.5 (+0.2, -0.3) to 22.1 (+0.6, -0.5), with an average difference between the measured and theoretical values of $-0.3$. All differences had a negative value. The theoretical SNR was larger due to an estimation of a smaller value of noise magnitude. The noise magnitude was calculated as the theoretical value of $\alpha$ multiplied by the theoretical value of the mean signal in the disk region. The theoretical estimation of the signal in the disk region was based on the narrow beam $\frac{\mu}{\rho}$. For the same images, the histogram method calculated confidence intervals of the SNR never encompassed the theoretical value. The histogram method had smaller estimation uncertainties compared to the conventional method.

For the quality assessments of 4 mm focal spot diverging beams images of the disk in 5 cm water depth, the SNR measurements of the histogram and conventional methods were in agreement at an SNR of 4.5 ($\pm$0.3) and higher. The lowest SNR of the tested images was 3.2 (+0.1, -0.2). The developed and conventional methods measurements never encompassed the theoretical SNR value. For both of the histogram and conventional methods, the differences between the measured and theoretical values of the SNR were negative and increased in magnitude when the exposure was increased.

**Modulation contrast '$M_C$'**

For the quality assessments of 4 mm focal spot diverging beams images of the disk in vacuum, measurements of the modulation contrast '$M_C$' by the histogram and conventional methods were in agreement at an SNR of 9.1 (+0.3, -0.2) and higher. Theoretical $M_C$ values were estimated based on the narrow beam $\frac{\mu}{\rho}$ values. At SNR values

of 6.5 (+0.2, -0.3) to 22.1 (+0.6, -0.5), the confidence interval of the conventional method encompassed the theoretical $M_C$ value for nine out of fifteen images, with an average relative difference between the measured and theoretical values of -0.81%. All differences had a negative value. For the same fifteen images, the histogram method calculated confidence intervals of the $M_C$ encompassed the theoretical value for only one image. The histogram method had smaller estimation uncertainties compared to the conventional method, which is an expected result of a confidence level of one standard deviation for the histogram method and three standard deviations for the conventional method. For images with SNR values of 9.1 (+0.3, -0.2) to 22.1 (+0.6, -0.5), the average relative difference between measurements of the $M_C$ using the histogram method and the conventional method was 0.0076%, and the average absolute relative difference was 0.038%. For images with SNR values of 12.6 ($\pm$0.3) to 22.1 (+0.6, -0.5), all differences were negative.

For the quality assessments of 4 mm focal spot diverging beams images of the disk in 5 cm water depth, the $M_C$ measurements for the histogram and conventional methods were in agreement at an SNR of 3.2 (+0.1, -0.2) and higher. The confidence intervals of the histogram and conventional methods did not encompass the theoretical value for any of the tested images. For images with SNR values of 9.1 (+0.3, -0.2) to 22.1 (+0.6, -0.5), the average relative difference between the values measured using the conventional method and the theoretical value was -27%. All differences had a negative value. As expected, the histogram method had smaller estimation uncertainties compared to the conventional method. For images with SNR values of 3.2 (+0.1, -0.2) to 22.1 (+0.6, -0.5), the average relative difference between measurements of the $M_C$ using the histogram method and the conventional method was 1.5%. All differences were positive.

# Chapter 6

# Discussion

Since our approach assumes parallel beam geometry, the first evaluation of the results compared the performance with point sources and parallel beam geometries. The agreement was either similar or lower for the point source images except for the standard deviation of the point spread function $\sigma_{PSF}$' where the agreement was higher for the point source images. However the higher agreement was associated with a larger uncertainty. The notable difference in these comparisons was the measurement of the image background region fluence '$I_{BG}$'. With diverging beams, the dose reduction in a vacuum is dictated by the inverse square law. Thus, the background fluence was not uniform. The developed image quality assessment method treats the image as a whole, without the need to select local ROIs for measurements. Therefore, the optimization overestimated the background fluence to accommodate the increased variance of the background. This was triggered by the correlation of the noise with the signal by the noise factor '$\alpha$'. A higher signal (or fluence) value was required to generate a background region distribution with a higher variance.

Another factor affecting the homogeneity of the background region was the signal fall-off near the edges of the beam due to scatter. The performance obtained with images where the background was a vacuum was compared to images with a water background. Although the parameter errors and uncertainties of measurements converged to smaller values for images with a vacuum background, the convergence occurred at a smaller SNR for images with a water background. The final optimal solution cost function '$\chi^2_{min}$' also converged to smaller values for images with a vacuum background

when comparing simulations using the same focal spot size, indicating a better agreement with the theoretical model. For $\chi^2_{min}$ to converge, with increasing SNR, the mean image signal in the region with the higher attenuation (the disk region) must have at least ten photons recorded by the detector. The fit to a Poisson noise distribution at lower signal levels depended on the accurate estimation of the mean signals within the disk and background regions and $\alpha$ as a transformation factor, as for lower signals the Poisson distribution is more skewed. As the background water depth was increased, the signal under the disk had a lower SNR. This explains the improvement in parameter measurement at a smaller SNR for images with a water background, compared to images with a vacuum background.

In Figure 5.10, the fractional agreement for images with a water background decreased with increasing SNR. As the exposure increased, the field edge signal fall-off and the increased attenuation in proportion to the inverse square of the distance from the diverging beams source induced a higher variation in the background region. As the developed image quality assessment method treats the image as a whole, the optimization overestimated the background fluence and $\alpha$ to accommodate the increased variance of the background.

The fit, especially for images with a water background where there is a higher signal variation that is not associated with noise, could be improved by splitting $\alpha$ into a transformation factor and a noise factor. This approach would enable the model to accommodate non-quantum-noise-limited imaging systems. Setting the transformation factor as *a priori* would enable the noise factor to be measured with improved accuracy. Alternatively, a less attenuating disk, either of a thickness smaller than 0.1 mm or made out of a material that is less attenuating than lead, would yield an image with a lower SNR from a mean signal at the detector that is greater than ten photons in a vacuum background. A vacuum background is preferred because the field edge signal fall-off and the increased attenuation in proportion to the inverse square of the distance from the diverging beam source are of smaller effects compared to an attenuating background. At lower SNR, the improved agreement between the measured and theoretical

focal spot's $\sigma_{PSF}$ for images with a water background, compared to images with a vacuum background, was associated with a greater agreement in the measurements of $\alpha$ and its theoretical value. The reason for the correlation between measurements of $\sigma_{PSF}$ and $\alpha$ was the noise degradation effect on the expected and observed cumulative histograms fit, where the noise degradation effect overrides the blur degradation effect as the SNR decreased.

The error and uncertainty in the measurements of the disk radius '$R_{disk}$', fluences and $\alpha$ did not correlate with the focal spot size. For all tested focal spot sizes, the confidence intervals for the measured $\sigma_{PSF}$ encompassed its theoretical value for SNRs as low as 8.0 (+0.4, -0.3). The frequency at 10% Modulation Transfer Function '$f_{10\%MTF}$' corresponding to the measured and theoretical values of $\sigma_{PSF}$ were calculated. The Nyquist criterion is satisfied if the focal spot's $f_{10\%MTF}$ is equal or less than half of the detector's limiting frequency. When the Nyquist criterion was not satisfied, the error in the measured $f_{10\%MTF}$ always increased as the theoretical $f_{10\%MTF}$ increased. At SNR values ranging from 16.4 (+0.4, -0.5) to 22.4 (+0.5, -0.6), the theoretical focal spot's $f_{10\%MTF}$ equal to 1, 3/4 and 1/2 of the detector's limiting frequency, were underestimated by averages of $\sim$20 %, $\sim$10 % and $\sim$8 %, respectively, based on the optimal measured value. For the same SNR range, at $f_{10\%MTF}$'s smaller than the frequency satisfying the Nyquist criterion, the average magnitude of error was 0.0 (+0.2, -0.1) cycle/mm to 0.1 (+0.4, -0.2) cycle/mm (1 (+8, -6) % to 4 (+10, -6) %). Therefore, at SNR values of $\sim$16 to $\sim$22, the method could measure the image resolutions for a typical CT scanner's resolution of 2 cycle/mm, with an uncertainty of $\sim$0.3 cycle/mm for a 0.1 mm detector's aperture. Similar results could be achieved at lower SNRs by changing the phantom attenuation, as suggested above.

Applying geometrical corrections did not improve the results of the image quality assessments. The mass attenuation coefficient '$\frac{\mu}{\rho}$' values used in the correction expressions predicted fluence values that disagreed with the conventional method measurements for images with a water background. The lack of improvement, when applying the corrections, might be due to the use of a narrow beam attenuation coefficient for $\frac{\mu}{\rho}$.

More accurate values of $\frac{\mu}{\rho}$ for the simulations could be estimated from parallel beam simulations, using the known exposure and fluence measurements using the conventional method. However, this would only be applicable for such artifact free, ideal detector simulations. Moreover, the method of assessing an improvement was not ideal. The used expected and observed value pairs were obtained by analyzing the same diverging beams image, either with or without the correction. More accurate expected values can be obtained by analyzing parallel beams simulated images (ideal images, as expected by the model) of the same exposure levels as the tested diverging beams images.

The significance of the noise distribution in the cumulative histogram fit was further demonstrated by comparing the performance with Poisson and Gaussian noise assumptions. The average error and uncertainty were larger with the Gaussian noise assumption at all tested SNR values, including images where the disk signal was triggered by more than ten photons.

The size of the ROI selected for analysis controls the extent of the effects of (a) the field edge signal fall-off and (b) the increased attenuation in proportion to the inverse square of the distance from the diverging beams source. The performance of the image quality assessment was tested with ROIs of various sizes for parallel and diverging beams simulations of the disk in water. To accommodate the increased variance of the background due to non-uniformity, the optimization results overestimated $\alpha$ as the ROI size was increased. The image was treated globally, and the model assumed that any signal variation was due to noise or blurring at the disk edge. The model assumed that an increase in the signal variation within the background region must be associated with an increase in the signal variation within the disk region. This need for increased signal variation, therefore, triggered an overestimation of $R_{disk}$ as the ROI increased. This, in turn, was associated with the overestimation of the mean signal in the disk region '$I_{disk}$', as the portion of background fluence included within the assumed disk spatial region had a higher signal value.

For parallel beams images of the disk in water, $I_{BG}$ values measured using the developed method was always higher than the conventional method measurement due to the higher variance. The difference between $I_{BG}$ measured using the developed method and the conventional method was not affected by the size of the ROI. For the diverging beam simulations, $I_{BG}$ was further overestimated by the developed method as the ROI size increased. This was due to the inclusion of a larger portion of the inverse square increased attenuation. As suggested above, a vacuum background would be preferred, as decreasing the ROI to smaller than $20 \times 20$ cm$^2$ is expected to truncate valuable information of the edge spread function. Changing the parameters of the diverging beam geometry, including the OID and SID, was not tested. These parameters affect the degree of non-homogeneity of the signal due to beam divergence.

The accuracy of the calculated $R_{disk}$ affected the estimation of other parameters when the ROI size was increased, in assessments of images with a water background. The impact of setting $R_{disk}$ as *a priori* was tested for a ROI of $20 \times 20$ cm$^2$ in both parallel and diverging beams simulated images of the disk in vacuum. At lower SNR values, the error and uncertainty were significantly smaller when the radius was *a priori*. In assessments of diverging beam simulations where $R_{disk}$ was not *a priori*, the increased signal variation in the background, due to the inverse square effect, resulted in an overestimation of $R_{disk}$. When $R_{disk}$ was *a priori*, the increased signal variation resulted in an increase in the uncertainty in measurements of $f_{10\%MTF}$. The uncertainties decreased as the SNR increased, for both known and unknown radius assessments. At higher SNR values, the error was not always smaller for the known $R_{disk}$ assessments . Therefore, for images of the disk in vacuum and the tested ROI size, *a priori* $R_{disk}$ would be of less significance if the limitations of $\alpha$ measurements at low SNR was overcome.

When evaluating the performance with a variable pixel size (0.05 and 0.1 mm pixel sizes) the results varied among the quality parameters. For the smaller pixel size assessments, the estimated uncertainty was smaller for all parameters. For $R_{disk}$, the agreement with the actual value within uncertainty was higher for the 0.1 mm pixel size. The smaller uncertainty associated with the measurements with the smaller pixel size

reduced the probability of the measured confidence interval encompassing the actual value of $R_{disk}$. For assessments of images simulated using two different focal spot sizes, the errors in the measured optimal value of $R_{disk}$ were similar for the 0.05 mm and 0.1 mm pixel sizes. The measurements of $\alpha$ did not correlate with the pixel size. The smaller error, in measurements of $I_{BG}$ or $I_{disk}$, with the larger pixel size appeared to be caused by an averaging effect. When comparing images simulated with the same focal spot size source, the error in measuring the $f_{10\%MTF}$ of the focal spot was lower for the smaller pixel size. This was because it is easier to measure the variance of the edge spread function with a higher sampling rate.

When the developed method was tested with flat field images, the reliability of accurate prediction of a zero radius decreased as the exposure was increased. The ratio of the magnitude of the noise to the dose fall-off at the field edge decreased as the exposure was increased. The non-uniformity of the image triggered the algorithm to predict the presence of the disk, with which the background can be convolved, resulting in non-homogeneity. The disk size and the off-centring of the disk within the FOV are factors that might affect the performance of the image quality analysis, but these are left for future work.

For low SNR images of the disk in vacuum, the confidence intervals for the parameters did not encompass the theoretical, actual, or the value measured using the conventional methods. The limit of the region of confidence of $\chi^2$ in the optimization problem was equal to one 'estimated' standard deviation. The inability to have an agreement between the results of the model within one standard deviation was not felt to be sufficient reason to increase the confidence limits. As discussed earlier, the lack of agreement was associated with the noise degradation effect overriding the blurring degradation effect on the cumulative histogram curve, and the decrease in the number of data points in the fitting process.

# Chapter 7

# Conclusions

In this thesis, the feasibility of a user-independent method for systematic medical image quality assessment was studied. The proposed approach uses a simple technical disk phantom to quantitatively measure the quality of the imaging system's performance. The analysis was based on theoretical principles, notably that the output of an imaging system can be predicted if the input and the characteristics of the system are known. The developed image quality assessment method predicts image degradation factors, applies them to the known object in the image and compares the output with the test image. The comparison is carried out in the histogram space of the whole image. One advantage of this method is that it eliminates user influence in selecting a local Region of Interest (ROI). In conventional methods, an ROI is typically used to measure the signal mean, standard deviation, or a signal representing the system frequency response, such as the edge spread function (ESF). A second advantage of the proposed method is that no smoothing is required to interpret the system's response (blurring effect); instead, the noise and blur are measured simultaneously.

The method reported by Samei *et al.* to measure a system's reponse was tested [32]. Samei *et al.*'s method was found to be sensitive to the window size of the smoothing function. In line with the work of Samei *et al.*, a window size of 17 elements of 0.1 subpixel size was used in testing, and window sizes of the same width $\pm 2$ elements were used to estimate the measurement uncertainty. At a sampling rate that satisfies the Nyquist criterion, the average uncertainties using Samei *et al.*'s method were greater than the uncertainties of our approach. The difference between the measured values of

the frequency at 10% Modulation Transfer Function (MTF) '$f_{10\%MTF}$' and the estimated theoretical value was calculated for both our method and that proposed by Samei *et al.*. These differences were greater for Samei *et al.*'s method than were our results. Unlike Samei *et al.*'s method, when increasing the signal to noise ratio (SNR) of images of the same resolution, our approach had less variability in $f_{10\%MTF}$ as a function of SNR and converged to a $f_{10\%MTF}$ value of 0 (+0.2, -0.1) cycle/mm to 0.1 (+0.4, -0.2) cycle/mm (1 (+8, -6) % to 4 (+10, -6) %) from the theoretical.

The histogram method's performance in estimating the quality parameters varied as a function of SNR. As the SNR decreases, the noise degradation effect overrides the blurring degradation effect on the cumulative histogram curve, and the number of data points in the fitting process decreases. Aside from SNR level, multiple factors affected the fit of the proposed cumulative histogram model to the cumulative histogram of the Monte Carlo simulated images. One factor was the increased attenuation that was observed in proportion to the inverse square of the distance from the diverging beam source. Another factor that affected the fit was the dose fall-off at the edge of the field of view (FOV). The extent of the effect of these factors on the accuracy and precision of the results varied. The variability was triggered by the variation of phantom background materials and the size of the global ROI within the FOV. The reported results of the developed method's image quality analysis showed that best results were achieved at an SNR value of at least 11.0 (+0.3, -0.2). For optimal results, potentially at even lower SNR values, further testing is required to determine the appropriate phantom geometry, disk and background materials, beam geometry including the Object to Image Distance (OID), Source to Image Distance (SID), and the size of the global ROI in relation to the size of the FOV.

The proposed method was challenged by factors that are intrinsic to a divergent beam geometry that is typically used when obtaining clinical or quality assurance images. The quality assessment of images obtained using clinical imaging system is further challenged by the presence of artifacts such as fixed-pattern artifacts due to beam inhomogeneity or detector response nonuniformity. Although such artifacts were not

introduced, the proposed method did not produce promising results for low SNR images (SNR less than 10, or less than 20 db). In measurements of noise and spatial resolution, the error and uncertainty at such low SNR values were larger for the proposed method than the tested conventional methods. Therefore, the proposed method is not expected to be superior to conventional methods in quality assessments of low dose imaging systems such as Positron Emission Tomography.

The 'No free lunch theorem' in search and optimization states the following: averaged over all types of mathematical problems, the computational cost of finding a solution is the same for any solution method. There are no guidelines for the best solution method for a particular type of mathematical problems. The genetic algorithm is routinely used to generate useful solutions to global optimization and search problems. However, the challenges discussed earlier are related to the modelling of the cumulative histogram estimation, and the optimization results were of lower accuracy and precision at certain settings, where scattering induced a higher signal variation within uniform regions with a water background material compared to vacuum background material, due to the inadequate agreement between the simulated image and the proposed model. Therefore, using other optimization techniques is not expected to improve the results. Such challenges could be overcome by utilizing non-linear statistical data modelling tools, such as Neural Networks. Instead of finding an exact solution, neural networks are used to find patterns in data and model complex relationships between a problem's input and output. Neural Networks 'learn' to recognize patterns via training. After training using input and output data sets with various classifications, a neural network can classify an input it has not seen before. Learning the patterns, caused by the diverging beam geometry and the FOV edge dose fall-off, could potentially allow the applicability of the proposed systematic method, with a reduced necessity of a diverging beam correction or a FOV and ROI size restriction, and would form the basis of possible future work.

# Appendix A

# Derivation of the area of a circle of radius $r$ outside a rectangle of dimensions $m \times n$ having the same center

The equation of a circle can be written as

$$x^2 + y^2 = r^2,$$

which can be rearranged to an $x$ function of $r$ and $y$ on the interval $|y| < r$

$$x(r, y) = \pm\sqrt{r^2 - y^2},$$

or a $y$ function of $r$ and $x$ on the interval $|x| < r$

$$y(r, x) = \pm\sqrt{r^2 - x^2}.$$

To find the area of a circle, either $x(r, y)$ or $y(r, x)$ can be used as bounds to evaluate the double integral $\int\int dxdy$. Similarly, to find the area of a circle of radius $r$ outside a rectangle of dimensions $m \times n$ sharing the same center, the double integral $\int\int dxdy$ is

evaluated bounded by $x(r, y)$ on the intervals $y = [\frac{n}{2}, r]$ and $y = [-r, -\frac{n}{2}]$, and bounded by $y(r, x)$ on the intervals $x = [\frac{m}{2}, r]$ and $y = [-r, -\frac{m}{2}]$ as follows:

$$\begin{aligned}\delta(r, m, n) &= 2\int_{\frac{n}{2}}^{r}\int_{-\sqrt{r^2-y^2}}^{\sqrt{r^2-y^2}} dx\, dy + 2\int_{\frac{m}{2}}^{r}\int_{-\sqrt{r^2-x^2}}^{\sqrt{r^2-x^2}} dy\, dx \\ &= 4\int_{\frac{n}{2}}^{r}\sqrt{r^2-y^2}\, dy + 4\int_{\frac{m}{2}}^{r}\sqrt{r^2-x^2}\, dx.\end{aligned} \tag{A.1}$$

Using the substitution $x = y = r\sin t$, $dx = dy = r\cos t dt$ and the identity $\cos^2 t + \sin^2 t = 1$, the integrals become

$$\delta(r, m, n) = 4r^2\int_{\arcsin\frac{n}{2r}}^{\frac{\pi}{2}}\cos^2 t\, dt + 4r^2\int_{\arcsin\frac{m}{2r}}^{\frac{\pi}{2}}\cos^2 t\, dt. \tag{A.2}$$

Then, using the identity $2\cos^2 t = 1 + \cos 2t$,

$$\begin{aligned}\delta(r, m, n) &= 2r^2\int_{\arcsin\frac{n}{2r}}^{\frac{\pi}{2}}(1+\cos 2t)\, dt + 2r^2\int_{\arcsin\frac{m}{2r}}^{\frac{\pi}{2}}(1+\cos 2t)\, dt \\ &= 2r^2\left(\left(t+\frac{1}{2}\sin 2t\right)\Big|_{t=\arcsin\frac{n}{2r}}^{t=\frac{\pi}{2}} + \left(t+\frac{1}{2}\sin 2t\right)\Big|_{t=\arcsin\frac{m}{2r}}^{t=\frac{\pi}{2}}\right) \\ &= 2r^2\left(\pi - \arcsin\frac{m}{2r} - \frac{1}{2}\sin\left(2\arcsin\frac{m}{2r}\right) - \arcsin\frac{n}{2r} - \frac{1}{2}\sin\left(2\arcsin\frac{n}{2r}\right)\right).\end{aligned} \tag{A.3}$$

# Appendix B

# Divergent beam attenuation correction parameters

The following describes correction to fluence distribution of a divergent beam to reflect the expected fluence for a parallel beam, a beam that travelled the same distance as a pencil beam normal to the point at the center of the divergent beam, where the distance travelled is through material composition identical to the material composition that a line normal to the point of interested go through. The attenuation correction is

$$\Phi_{corrected}(x,y) = \Phi_{scored}(x,y) \cdot e^{-[(l_{disk}(x,y)-h_{disk}(x,y))\mu_{disk}+(l_{slab}(x,y)-h_{slab}(x,y))\mu_{slab}]}, \tag{B.1}$$

where $l_{disk}$ and $l_{slab}$ are the distances travelled through the disk and the slab, respectively, by a pencil beam normal to the point of interest, and $h_{disk}$ and $h_{slab}$ are the distances travelled through the disk and the slab, respectively, by a pencil beam at an angle $\theta = \arctan \frac{\sqrt{x^2+y^2}}{SID}$. Refer to figure (B.1) for definition of $m, n, k, q$ and $s$.

$$q = OID$$

$$k = OID \cdot \frac{\sqrt{SID^2 + x^2 + y^2}}{SID}$$

$$m = \sqrt{x^2 + y^2} - \sqrt{k^2 + q^2}$$

$$= \sqrt{x^2 + y^2} - \sqrt{\left[\left(\frac{OID}{SID}\right)^2 \left(SID^2 + x^2 + y^2\right)\right] - OID^2}$$

$$s = b \cdot \frac{\sqrt{x^2 + y^2}}{SID}$$

$$n = m - s$$

$$= m - b \cdot \frac{\sqrt{x^2 + y^2}}{SID}$$

CASE 1: $n > r$

$$l_{disk} = 0$$

$$h_{disk} = 0$$

$$l_{slab} = a$$

$$h_{slab} = \sqrt{SID^2 + x^2 + y^2} \cdot \frac{(a)}{SID}$$

CASE 2: $m < r$

$$l_{disk} = b$$

$$h_{disk} = \sqrt{SID^2 + x^2 + y^2} \cdot \frac{(b)}{SID}$$

$$l_{slab} = a - b$$

$$h_{slab} = \sqrt{SID^2 + x^2 + y^2} \cdot \frac{(a-b)}{SID}$$

CASE 3: $m > r$, $n < r$

$$l_{disk} = SID \cdot \frac{(r-n)}{\sqrt{x^2 + y^2}}$$

$$h_{disk} = \sqrt{SID^2 + x^2 + y^2} \cdot \left(\frac{(b)}{SID} - \frac{m-r}{\sqrt{x^2 + y^2}}\right)$$

$$l_{slab} = a - b + SID \cdot \frac{m-r}{\sqrt{x^2 + y^2}}$$

$$h_{slab} = \sqrt{SID^2 + x^2 + y^2} \cdot \left(\frac{(a-b)}{SID} + \frac{m-r}{\sqrt{x^2 + y^2}}\right)$$

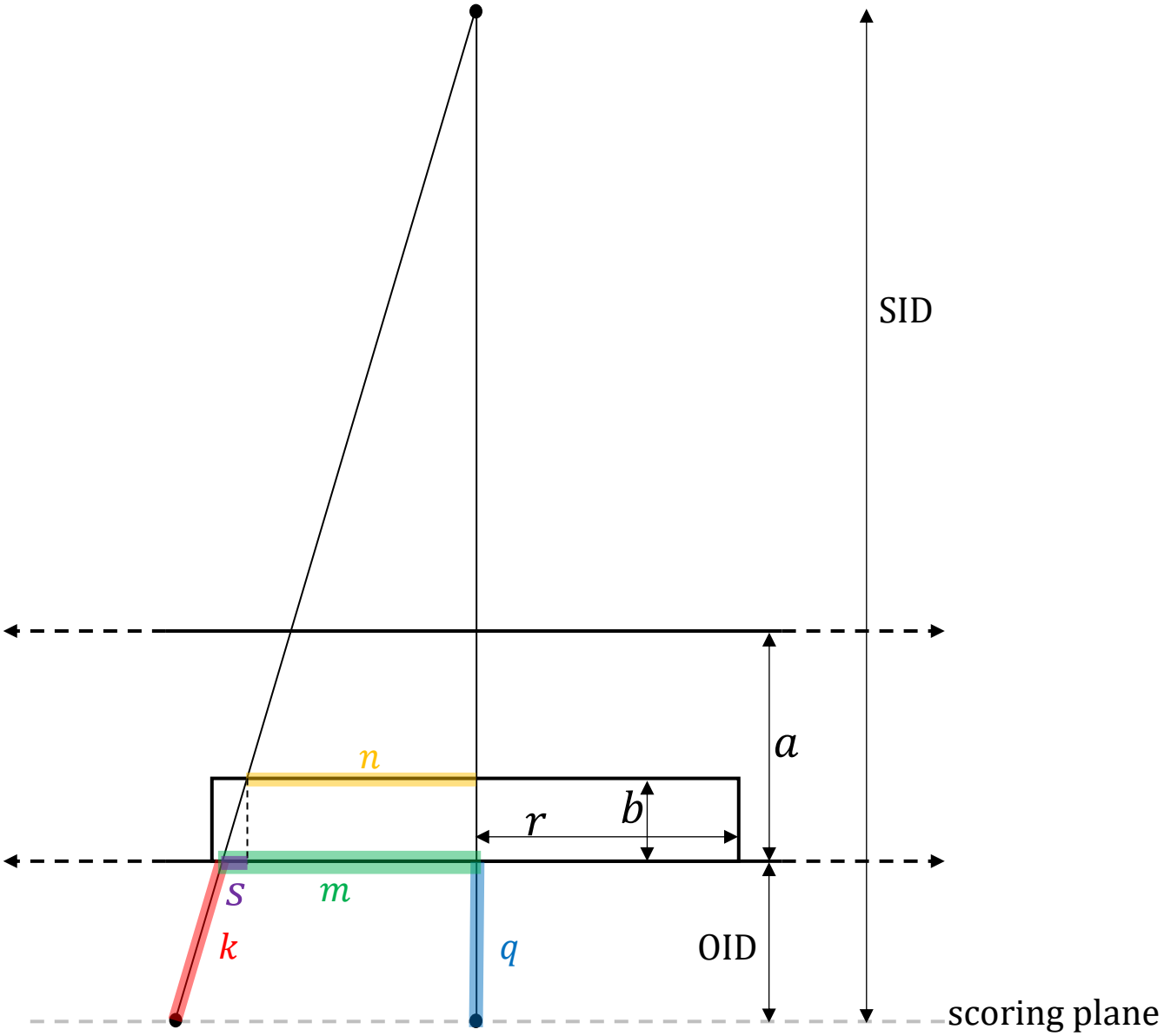


FIGURE B.1: Divergent beam geometry.

## Appendix C

# Image quality analysis results

## C.1 1.2 mm focal spot size

Beam Energy: 40 keV.

Beam geometry: diverging.

$X_F$: 1.2 mm ($f_{10\%MTF}$ = 6 cycle/mm).

FOV: 15 cm radius circle.

Disk thickness: 0.1 mm.

Water depth: 0 cm.

ROI: $20 \times 20$ cm$^2$.

Pixel size: 0.1 mm ($f_{a_{lim}}$ = 12 cycle/mm).

Bit depth: 16.

Noise assumption for developed method: Poisson.

TABLE C.1: 1.2 mm focal spot size images: cost function for image quality analysis using developed method

| Histories | Cost function |
|---|---|
| 72 666 600 | 173 152.0625 |
| 145 333 200 | 22 026.637 920 814 9 |
| 217 999 800 | 2690.563 481 575 02 |
| 290 666 400 | 349.443 523 708 204 |
| 363 333 000 | 46.300 296 433 473 2 |
| 435 999 600 | 10.423 095 306 478 8 |
| 508 666 200 | 10.038 388 244 802 1 |
| 581 332 800 | 11.557 330 885 771 6 |
| 653 999 400 | 10.923 765 325 519 9 |
| 726 666 000 | 8.244 078 286 543 68 |
| 799 332 600 | 12.964 879 394 857 6 |
| 871 999 300 | 13.900 057 676 37 |
| 944 665 900 | 9.848 201 134 420 75 |
| 1 017 332 500 | 15.396 538 830 721 7 |
| 1 089 999 100 | 12.046 082 033 843 8 |

TABLE C.2: 1.2 mm focal spot size images: SNR measured using conventional method

| Histories | $SNR_{measured}$ | $\delta_{-_{SNR}}$ | $\delta_{+_{SNR}}$ |
|---|---|---|---|
| 72 666 600 | 5.8 | 0.3 | 0.3 |
| 145 333 200 | 8.2 | 0.3 | 0.2 |
| 217 999 800 | 9.9 | 0.2 | 0.3 |
| 290 666 400 | 11.5 | 0.3 | 0.3 |
| 363 333 000 | 12.9 | 0.4 | 0.3 |
| 435 999 600 | 14 | 0.4 | 0.5 |
| 508 666 200 | 15.2 | 0.5 | 0.5 |
| 581 332 800 | 16.3 | 0.5 | 0.4 |
| 653 999 400 | 17.2 | 0.5 | 0.6 |
| 726 666 000 | 18.1 | 0.5 | 0.5 |
| 799 332 600 | 19 | 0.5 | 0.5 |
| 871 999 300 | 19.9 | 0.5 | 0.5 |
| 944 665 900 | 20.7 | 0.5 | 0.6 |
| 1 017 332 500 | 21.5 | 0.5 | 0.5 |
| 1 089 999 100 | 22.3 | 0.6 | 0.5 |

TABLE C.3: 1.2 mm focal spot size images: Measured radius for image quality analysis using developed method

| Histories | $R_{actual}$ mm | $R_{measured}$ mm | $\delta_{-_R}$ mm | $\delta_{+_R}$ mm |
|---|---|---|---|---|
| 72 666 600 | 5 | 7.5 | 0.05 | 0.06 |
| 145 333 200 | 5 | 5.05 | 0.03 | 0.04 |
| 217 999 800 | 5 | 5.01 | 0.01 | 0.01 |
| 290 666 400 | 5 | 5.002 | 0.005 | 0.005 |
| 363 333 000 | 5 | 5.001 | 0.002 | 0.003 |
| 435 999 600 | 5 | 5.001 | 0.001 | 0.002 |
| 508 666 200 | 5 | 5.001 | 0.001 | 0.002 |
| 581 332 800 | 5 | 5.001 | 0.001 | 0.001 |
| 653 999 400 | 5 | 5.001 | 0.001 | 0.001 |
| 726 666 000 | 5 | 5.001 | 0.001 | 0.001 |
| 799 332 600 | 5 | 5.001 | 0.001 | 0.001 |
| 871 999 300 | 5 | 5.001 | 0.001 | 0.001 |
| 944 665 900 | 5 | 5.001 | 0.001 | 0.001 |
| 1 017 332 500 | 5 | 5.001 | 0.001 | 0.001 |
| 1 089 999 100 | 5 | 5.001 | 0.0008 | 0.0009 |

TABLE C.4: 1.2 mm focal spot size images: Measured background fluence for image quality analysis using developed method

| Histories | $I_{BG\,theoretical_{LB}}$ $\frac{1}{cm^2}$ | $I_{BG\,measured}$ $\frac{1}{cm^2}$ | $\delta_{-_{I_{BG}}}$ $\frac{1}{cm^2}$ | $\delta_{+_{I_{BG}}}$ $\frac{1}{cm^2}$ |
|---|---|---|---|---|
| 72 666 600 | 102 802.209 668 28 | 10 000 | 3000 | 2000 |
| 145 333 200 | 205 604.419 336 56 | 206 000 | 1000 | 2000 |
| 217 999 800 | 308 406.629 004 841 | 309 100 | 500 | 600 |
| 290 666 400 | 411 208.838 673 121 | 412 200 | 300 | 300 |
| 363 333 000 | 514 011.048 341 401 | 515 200 | 200 | 200 |
| 435 999 600 | 616 813.258 009 681 | 618 200 | 100 | 200 |
| 508 666 200 | 719 615.467 677 961 | 721 200 | 100 | 200 |
| 581 332 800 | 822 417.677 346 242 | 824 200 | 100 | 200 |
| 653 999 400 | 925 219.887 014 522 | 927 200 | 100 | 200 |
| 726 666 000 | 1 028 022.096 682 8 | 1 030 300 | 200 | 100 |
| 799 332 600 | 1 130 824.306 351 08 | 1 133 300 | 200 | 100 |
| 871 999 300 | 1 233 626.657 490 42 | 1 236 300 | 100 | 200 |
| 944 665 900 | 1 336 428.867 158 7 | 1 339 300 | 100 | 100 |
| 1 017 332 500 | 1 439 231.076 826 98 | 1 442 300 | 100 | 200 |
| 1 089 999 100 | 1 542 033.286 495 26 | 1 545 300 | 100 | 200 |

TABLE C.5: 1.2 mm focal spot size images: Measured background fluence for image quality analysis using conventional method

| Histories | $I_{BG\,theoretical_{LB}}$ $\frac{1}{cm^2}$ | $I_{BGUB}$ $\frac{1}{cm^2}$ | $\delta_{-_{I_{BG}}}$ $\frac{1}{cm^2}$ | $\delta_{+_{I_{BG}}}$ $\frac{1}{cm^2}$ |
|---|---|---|---|---|
| 72 666 600 | 102 802.209 668 28 | 103 000 | 1000 | 2000 |
| 145 333 200 | 205 604.419 336 56 | 206 200 | 900 | 800 |
| 217 999 800 | 308 406.629 004 841 | 309 000 | 2000 | 1000 |
| 290 666 400 | 411 208.838 673 121 | 412 000 | 2000 | 2000 |
| 363 333 000 | 514 011.048 341 401 | 515 000 | 3000 | 3000 |
| 435 999 600 | 616 813.258 009 681 | 618 000 | 3000 | 3000 |
| 508 666 200 | 719 615.467 677 961 | 721 000 | 3000 | 2000 |
| 581 332 800 | 822 417.677 346 242 | 824 000 | 4000 | 3000 |
| 653 999 400 | 925 219.887 014 522 | 927 000 | 4000 | 3000 |
| 726 666 000 | 1 028 022.096 682 8 | 1 030 000 | 3000 | 3000 |
| 799 332 600 | 1 130 824.306 351 08 | 1 133 000 | 4000 | 4000 |
| 871 999 300 | 1 233 626.657 490 42 | 1 235 000 | 4000 | 5000 |
| 944 665 900 | 1 336 428.867 158 7 | 1 339 000 | 4000 | 4000 |
| 1 017 332 500 | 1 439 231.076 826 98 | 1 442 000 | 5000 | 4000 |
| 1 089 999 100 | 1 542 033.286 495 26 | 1 545 000 | 6000 | 5000 |

TABLE C.6: 1.2 mm focal spot size images: Measured disk fluence for image quality analysis using developed method

| Histories | $I_{disk\,theoretical_{LB}}$ $\frac{1}{cm^2}$ | $I_{disk\,measured}$ $\frac{1}{cm^2}$ | $\delta_{-_{I_{disk}}}$ $\frac{1}{cm^2}$ | $\delta_{+_{I_{disk}}}$ $\frac{1}{cm^2}$ |
|---|---|---|---|---|
| 72 666 600 | 20 150.095 596 360 3 | 110 000 | 2000 | 2000 |
| 145 333 200 | 40 300.191 192 720 7 | 39 000 | 1000 | 2000 |
| 217 999 800 | 60 450.286 789 081 | 61 600 | 700 | 300 |
| 290 666 400 | 80 600.382 385 441 3 | 82 400 | 400 | 200 |
| 363 333 000 | 100 750.477 981 802 | 103 100 | 300 | 100 |
| 435 999 600 | 120 900.573 578 162 | 123 600 | 100 | 200 |
| 508 666 200 | 141 050.669 174 522 | 144 200 | 100 | 200 |
| 581 332 800 | 161 200.764 770 883 | 164 900 | 200 | 100 |
| 653 999 400 | 181 350.860 367 243 | 185 500 | 200 | 200 |
| 726 666 000 | 201 500.955 963 603 | 206 100 | 100 | 100 |
| 799 332 600 | 221 651.051 559 964 | 226 700 | 100 | 200 |
| 871 999 300 | 241 801.174 885 839 | 247 300 | 100 | 200 |
| 944 665 900 | 261 951.270 482 199 | 267 900 | 100 | 200 |
| 1 017 332 500 | 282 101.366 078 559 | 288 600 | 200 | 100 |
| 1 089 999 100 | 302 251.461 674 92 | 309 200 | 200 | 100 |

TABLE C.7: 1.2 mm focal spot size images: Measured disk fluence for image quality analysis using conventional method

| Histories | $I_{disk\,theoretical_{LB}}$ $\frac{1}{cm^2}$ | $I_{disk\,measured}$ $\frac{1}{cm^2}$ | $\delta_{-_{I_{disk}}}$ $\frac{1}{cm^2}$ | $\delta_{+_{I_{disk}}}$ $\frac{1}{cm^2}$ |
|---|---|---|---|---|
| 72 666 600 | 20 150.095 596 360 3 | 20 400 | 500 | 600 |
| 145 333 200 | 40 300.191 192 720 7 | 41 000 | 400 | 400 |
| 217 999 800 | 60 450.286 789 081 | 61 600 | 800 | 700 |
| 290 666 400 | 80 600.382 385 441 3 | 82 000 | 1000 | 1000 |
| 363 333 000 | 100 750.477 981 802 | 103 000 | 1000 | 1000 |
| 435 999 600 | 120 900.573 578 162 | 124 000 | 1000 | 1000 |
| 508 666 200 | 141 050.669 174 522 | 144 000 | 1000 | 2000 |
| 581 332 800 | 161 200.764 770 883 | 165 000 | 1000 | 1000 |
| 653 999 400 | 181 350.860 367 243 | 185 000 | 1000 | 2000 |
| 726 666 000 | 201 500.955 963 603 | 206 000 | 1000 | 1000 |
| 799 332 600 | 221 651.051 559 964 | 227 000 | 2000 | 1000 |
| 871 999 300 | 241 801.174 885 839 | 247 000 | 1000 | 2000 |
| 944 665 900 | 261 951.270 482 199 | 268 000 | 2000 | 1000 |
| 1 017 332 500 | 282 101.366 078 559 | 288 000 | 1000 | 2000 |
| 1 089 999 100 | 302 251.461 674 92 | 309 000 | 2000 | 2000 |

TABLE C.8: 1.2 mm focal spot size images: Measured noise factor for image quality analysis using developed method

| Histories | $\alpha_{theoretical}$ | $\alpha_{measured}$ | $\delta_{-_\alpha}$ | $\delta_{+_\alpha}$ |
|---|---|---|---|---|
| 72 666 600 | 10 000 | 4800 | 600 | 600 |
| 145 333 200 | 10 000 | 9800 | 500 | 200 |
| 217 999 800 | 10 000 | 10 000 | 100 | 0 |
| 290 666 400 | 10 000 | 10 000 | 100 | 0 |
| 363 333 000 | 10 000 | 9990 | 50 | 10 |
| 435 999 600 | 10 000 | 9980 | 30 | 20 |
| 508 666 200 | 10 000 | 9990 | 40 | 30 |
| 581 332 800 | 10 000 | 10 000 | 40 | 30 |
| 653 999 400 | 10 000 | 9990 | 30 | 30 |
| 726 666 000 | 10 000 | 9990 | 30 | 20 |
| 799 332 600 | 10 000 | 9980 | 20 | 30 |
| 871 999 300 | 10 000 | 9990 | 30 | 30 |
| 944 665 900 | 10 000 | 9990 | 30 | 20 |
| 1 017 332 500 | 10 000 | 9990 | 30 | 30 |
| 1 089 999 100 | 10 000 | 9990 | 20 | 30 |

TABLE C.9: 1.2 mm focal spot size images: Measured noise factor for image quality analysis using conventional method

| Histories | $\alpha_{theoretical}$ | $\alpha_{measured}$ | $\delta_{-_\alpha}$ | $\delta_{+_\alpha}$ |
|---|---|---|---|---|
| 72 666 600 | 10 000 | 9900 | 300 | 400 |
| 145 333 200 | 10 000 | 10 000 | 300 | 300 |
| 217 999 800 | 10 000 | 10 100 | 300 | 200 |
| 290 666 400 | 10 000 | 10 000 | 200 | 300 |
| 363 333 000 | 10 000 | 10 000 | 300 | 200 |
| 435 999 600 | 10 000 | 10 000 | 400 | 400 |
| 508 666 200 | 10 000 | 10 000 | 400 | 400 |
| 581 332 800 | 10 000 | 10 000 | 400 | 300 |
| 653 999 400 | 10 000 | 10 000 | 400 | 400 |
| 726 666 000 | 10 000 | 10 100 | 400 | 400 |
| 799 332 600 | 10 000 | 10 000 | 300 | 400 |
| 871 999 300 | 10 000 | 10 000 | 400 | 300 |
| 944 665 900 | 10 000 | 10 000 | 400 | 300 |
| 1 017 332 500 | 10 000 | 10 000 | 300 | 300 |
| 1 089 999 100 | 10 000 | 10 000 | 400 | 300 |

TABLE C.10: 1.2 mm focal spot size images: Measured PSF standard deviation for image quality analysis using developed method

| Histories | $\sigma_{PSF\,LB_{X_F}}$ mm | $\sigma_{PSF\,LB_{detector}}$ mm | $\sigma_{PSF\,measured}$ mm | $\delta_{-\sigma_{PSF}}$ mm | $\delta_{+\sigma_{PSF}}$ mm |
|---|---|---|---|---|---|
| 72 666 600 | 0.056 923 516 798 537 | 0.028 461 758 399 268 5 | 8 | 2 | 1 |
| 145 333 200 | 0.056 923 516 798 537 | 0.028 461 758 399 268 5 | 0.6 | 0.6 | 1.3 |
| 217 999 800 | 0.056 923 516 798 537 | 0.028 461 758 399 268 5 | 0.1 | 0.1 | 0.3 |
| 290 666 400 | 0.056 923 516 798 537 | 0.028 461 758 399 268 5 | 0.07 | 0.07 | 0.13 |
| 363 333 000 | 0.056 923 516 798 537 | 0.028 461 758 399 268 5 | 0.06 | 0.04 | 0.07 |
| 435 999 600 | 0.056 923 516 798 537 | 0.028 461 758 399 268 5 | 0.06 | 0.03 | 0.04 |
| 508 666 200 | 0.056 923 516 798 537 | 0.028 461 758 399 268 5 | 0.06 | 0.02 | 0.03 |
| 581 332 800 | 0.056 923 516 798 537 | 0.028 461 758 399 268 5 | 0.06 | 0.03 | 0.03 |
| 653 999 400 | 0.056 923 516 798 537 | 0.028 461 758 399 268 5 | 0.06 | 0.02 | 0.03 |
| 726 666 000 | 0.056 923 516 798 537 | 0.028 461 758 399 268 5 | 0.06 | 0.02 | 0.02 |
| 799 332 600 | 0.056 923 516 798 537 | 0.028 461 758 399 268 5 | 0.06 | 0.02 | 0.03 |
| 871 999 300 | 0.056 923 516 798 537 | 0.028 461 758 399 268 5 | 0.06 | 0.02 | 0.02 |
| 944 665 900 | 0.056 923 516 798 537 | 0.028 461 758 399 268 5 | 0.06 | 0.02 | 0.02 |
| 1 017 332 500 | 0.056 923 516 798 537 | 0.028 461 758 399 268 5 | 0.06 | 0.02 | 0.02 |
| 1 089 999 100 | 0.056 923 516 798 537 | 0.028 461 758 399 268 5 | 0.06 | 0.02 | 0.02 |

TABLE C.11: 1.2 mm focal spot size images: Measured PSF standard deviation for image quality analysis using conventional method

| Histories | $\sigma_{PSF\,LB_{X_F}}$ mm | $\sigma_{PSF\,LB_{detector}}$ mm | $\sigma_{PSF\,measured}$ mm | $\delta_{-\sigma_{PSF}}$ mm | $\delta_{+\sigma_{PSF}}$ mm |
|---|---|---|---|---|---|
| 72 666 600 | 0.056 923 516 798 537 | 0.028 461 758 399 268 5 | 0.03 | 0 | 0.02 |
| 145 333 200 | 0.056 923 516 798 537 | 0.028 461 758 399 268 5 | 0.03 | 0 | 0.02 |
| 217 999 800 | 0.056 923 516 798 537 | 0.028 461 758 399 268 5 | 0.034 | 0.009 | 0.001 |
| 290 666 400 | 0.056 923 516 798 537 | 0.028 461 758 399 268 5 | 0.04 | 0.01 | 0 |
| 363 333 000 | 0.056 923 516 798 537 | 0.028 461 758 399 268 5 | 0.05 | 0.03 | 0 |
| 435 999 600 | 0.056 923 516 798 537 | 0.028 461 758 399 268 5 | 0.06 | 0.02 | 0 |
| 508 666 200 | 0.056 923 516 798 537 | 0.028 461 758 399 268 5 | 0.04 | 0 | 0.02 |
| 581 332 800 | 0.056 923 516 798 537 | 0.028 461 758 399 268 5 | 0.06 | 0.03 | 0 |
| 653 999 400 | 0.056 923 516 798 537 | 0.028 461 758 399 268 5 | 0.04 | 0 | 0.007 |
| 726 666 000 | 0.056 923 516 798 537 | 0.028 461 758 399 268 5 | 0.04 | 0.01 | 0 |
| 799 332 600 | 0.056 923 516 798 537 | 0.028 461 758 399 268 5 | 0.045 | 0.005 | 0.003 |
| 871 999 300 | 0.056 923 516 798 537 | 0.028 461 758 399 268 5 | 0.042 | 0 | 0.005 |
| 944 665 900 | 0.056 923 516 798 537 | 0.028 461 758 399 268 5 | 0.03 | 0 | 0.03 |
| 1 017 332 500 | 0.056 923 516 798 537 | 0.028 461 758 399 268 5 | 0.04 | 0.01 | 0.03 |
| 1 089 999 100 | 0.056 923 516 798 537 | 0.028 461 758 399 268 5 | 0.06 | 0.03 | 0 |

TABLE C.12: 1.2 mm focal spot size images: Frequency at 10% MTF corresponding to measured PSF standard deviation for image quality analysis using developed method

| Histories | $f_{10\%MTF_{UB_{X_F}}}$ $\frac{\text{cycle}}{\text{mm}}$ | $f_{10\%MTF_{UB_{detector}}}$ $\frac{\text{cycle}}{\text{mm}}$ | $f_{10\%MTF_{measured}}$ $\frac{\text{cycle}}{\text{mm}}$ | $\delta_{-_{f_{10\%MTF}}}$ $\frac{\text{cycle}}{\text{mm}}$ | $\delta_{+_{f_{10\%MTF}}}$ $\frac{\text{cycle}}{\text{mm}}$ |
|---|---|---|---|---|---|
| 72 666 600 | 6 | 12 | 0.04 | 0 | 0.01 |
| 145 333 200 | 6 | 12 | 0.5 | 0.3 | Inf |
| 217 999 800 | 6 | 12 | 3 | 2 | Inf |
| 290 666 400 | 6 | 12 | 5 | 3 | Inf |
| 363 333 000 | 6 | 12 | 6 | 3 | 14 |
| 435 999 600 | 6 | 12 | 5 | 2 | 6 |
| 508 666 200 | 6 | 12 | 5 | 1 | 5 |
| 581 332 800 | 6 | 12 | 6 | 2 | 4 |
| 653 999 400 | 6 | 12 | 6 | 2 | 3 |
| 726 666 000 | 6 | 12 | 5 | 1 | 3 |
| 799 332 600 | 6 | 12 | 5 | 1 | 3 |
| 871 999 300 | 6 | 12 | 5 | 1 | 3 |
| 944 665 900 | 6 | 12 | 6 | 2 | 2 |
| 1 017 332 500 | 6 | 12 | 6 | 2 | 2 |
| 1 089 999 100 | 6 | 12 | 6 | 1 | 2 |

TABLE C.13: 1.2 mm focal spot size images: Frequency at 10% MTF corresponding to measured PSF standard deviation for image quality analysis using conventional method

| Histories | $f_{10\%MTF_{UB_{X_F}}}$ $\frac{\text{cycle}}{\text{mm}}$ | $f_{10\%MTF_{UB_{detector}}}$ $\frac{\text{cycle}}{\text{mm}}$ | $f_{10\%MTF_{measured}}$ $\frac{\text{cycle}}{\text{mm}}$ | $\delta_{-_{f_{10\%MTF}}}$ $\frac{\text{cycle}}{\text{mm}}$ | $\delta_{+_{f_{10\%MTF}}}$ $\frac{\text{cycle}}{\text{mm}}$ |
|---|---|---|---|---|---|
| 72 666 600 | 6 | 12 | 10 | 3 | 0 |
| 145 333 200 | 6 | 12 | 10 | 3 | 3 |
| 217 999 800 | 6 | 12 | 10 | 0 | 4 |
| 290 666 400 | 6 | 12 | 8 | 0 | 5 |
| 363 333 000 | 6 | 12 | 6 | 0 | 8 |
| 435 999 600 | 6 | 12 | 6 | 0 | 2 |
| 508 666 200 | 6 | 12 | 8 | 2 | 0 |
| 581 332 800 | 6 | 12 | 6 | 0 | 5 |
| 653 999 400 | 6 | 12 | 9 | 2 | 0 |
| 726 666 000 | 6 | 12 | 8 | 0 | 3 |
| 799 332 600 | 6 | 12 | 7.6 | 0.5 | 0.9 |
| 871 999 300 | 6 | 12 | 8.1 | 0.8 | 0 |
| 944 665 900 | 6 | 12 | 12 | 7 | 0 |
| 1 017 332 500 | 6 | 12 | 9 | 4 | 2 |
| 1 089 999 100 | 6 | 12 | 5 | 0 | 6 |

## C.2 2 mm focal spot size

Beam Energy: 40 keV.

Beam geometry: diverging.

$X_F$: 2 mm ($f_{10\%MTF}$ = 3.6 cycle/mm).

FOV: 15 cm radius circle.

Disk thickness: 0.1 mm.

Water depth: 0 cm.

ROI: $20 \times 20$ cm$^2$.

Pixel size: 0.1 mm ($f_{a_{lim}}$ = 12 cycle/mm).

Bit depth: 16.

Noise assumption for developed method: Poisson.

TABLE C.14: 2 mm focal spot size images: cost function for image quality analysis using developed method

| Histories | Cost function |
|---|---|
| 72 666 700 | 167 482.8125 |
| 145 333 300 | 21 965.653 004 456 4 |
| 217 999 900 | 2694.300 809 048 27 |
| 290 666 500 | 363.333 433 879 388 |
| 363 333 100 | 49.264 310 592 873 5 |
| 435 999 700 | 16.186 930 441 728 3 |
| 508 666 300 | 14.084 152 372 201 2 |
| 581 332 900 | 16.950 124 669 222 3 |
| 653 999 500 | 12.055 442 294 421 2 |
| 726 666 100 | 6.801 014 311 856 2 |
| 799 332 700 | 23.800 450 912 461 3 |
| 871 999 300 | 25.662 758 666 647 9 |
| 944 665 900 | 19.599 710 684 924 |
| 1 017 332 500 | 23.671 719 156 696 8 |
| 1 089 999 100 | 26.205 456 713 039 |

TABLE C.15: 2 mm focal spot size images: SNR measured using conventional method

| Histories | $SNR_{measured}$ | $\delta_{-_{SNR}}$ | $\delta_{+_{SNR}}$ |
|---|---|---|---|
| 72 666 700 | 5.7 | 0.2 | 0.3 |
| 145 333 300 | 8.1 | 0.2 | 0.2 |
| 217 999 900 | 9.9 | 0.3 | 0.3 |
| 290 666 500 | 11.5 | 0.3 | 0.4 |
| 363 333 100 | 12.8 | 0.3 | 0.4 |
| 435 999 700 | 14.1 | 0.4 | 0.4 |
| 508 666 300 | 15.2 | 0.4 | 0.4 |
| 581 332 900 | 16.2 | 0.4 | 0.5 |
| 653 999 500 | 17.2 | 0.4 | 0.5 |
| 726 666 100 | 18.2 | 0.5 | 0.5 |
| 799 332 700 | 19.1 | 0.5 | 0.5 |
| 871 999 300 | 19.9 | 0.5 | 0.5 |
| 944 665 900 | 20.8 | 0.6 | 0.5 |
| 1 017 332 500 | 21.5 | 0.6 | 0.6 |
| 1 089 999 100 | 22.2 | 0.6 | 0.7 |

TABLE C.16: 2 mm focal spot size images: Measured radius for image quality analysis using developed method

| Histories | $R_{actual}$ mm | $R_{measured}$ mm | $\delta_{-_R}$ mm | $\delta_{+_R}$ mm |
|---|---|---|---|---|
| 72 666 700 | 5 | 5.67 | 0.05 | 0.05 |
| 145 333 300 | 5 | 5.05 | 0.03 | 0.04 |
| 217 999 900 | 5 | 5.01 | 0.01 | 0.01 |
| 290 666 500 | 5 | 5.002 | 0.005 | 0.005 |
| 363 333 100 | 5 | 5.002 | 0.003 | 0.002 |
| 435 999 700 | 5 | 5.001 | 0.001 | 0.002 |
| 508 666 300 | 5 | 5.001 | 0.001 | 0.002 |
| 581 332 900 | 5 | 5.001 | 0.001 | 0.002 |
| 653 999 500 | 5 | 5.001 | 0.001 | 0.001 |
| 726 666 100 | 5 | 5.001 | 0.001 | 0.001 |
| 799 332 700 | 5 | 5.001 | 0.001 | 0.001 |
| 871 999 300 | 5 | 5.001 | 0.001 | 0.001 |
| 944 665 900 | 5 | 5.001 | 0.001 | 0.001 |
| 1 017 332 500 | 5 | 5.001 | 0.001 | 0.001 |
| 1 089 999 100 | 5 | 5.001 | 0.001 | 0.001 |

TABLE C.17: 2 mm focal spot size images: Measured background fluence for image quality analysis using developed method

| Histories | $I_{BG theoretical_{LB}}$ $\frac{1}{cm^2}$ | $I_{BG measured}$ $\frac{1}{cm^2}$ | $\delta_{-_{I_{BG}}}$ $\frac{1}{cm^2}$ | $\delta_{+_{I_{BG}}}$ $\frac{1}{cm^2}$ |
|---|---|---|---|---|
| 72 666 700 | 102 802.351 139 341 | 113 000 | 2000 | 1000 |
| 145 333 300 | 205 604.560 807 621 | 206 000 | 1000 | 2000 |
| 217 999 900 | 308 406.770 475 901 | 309 100 | 500 | 600 |
| 290 666 500 | 411 208.980 144 181 | 412 200 | 400 | 300 |
| 363 333 100 | 514 011.189 812 461 | 515 200 | 200 | 200 |
| 435 999 700 | 616 813.399 480 742 | 618 200 | 100 | 200 |
| 508 666 300 | 719 615.609 149 022 | 721 200 | 100 | 200 |
| 581 332 900 | 822 417.818 817 302 | 824 200 | 100 | 200 |
| 653 999 500 | 925 220.028 485 582 | 927 200 | 100 | 200 |
| 726 666 100 | 1 028 022.238 153 86 | 1 030 300 | 200 | 100 |
| 799 332 700 | 1 130 824.447 822 14 | 1 133 300 | 200 | 200 |
| 871 999 300 | 1 233 626.657 490 42 | 1 236 300 | 200 | 200 |
| 944 665 900 | 1 336 428.867 158 7 | 1 339 300 | 100 | 200 |
| 1 017 332 500 | 1 439 231.076 826 98 | 1 442 300 | 100 | 200 |
| 1 089 999 100 | 1 542 033.286 495 26 | 1 545 400 | 200 | 100 |

TABLE C.18: 2 mm focal spot size images: Measured background fluence for image quality analysis using conventional method

| Histories | $I_{BG theoretical_{LB}}$ $\frac{1}{cm^2}$ | $I_{BGUB}$ $\frac{1}{cm^2}$ | $\delta_{-_{I_{BG}}}$ $\frac{1}{cm^2}$ | $\delta_{+_{I_{BG}}}$ $\frac{1}{cm^2}$ |
|---|---|---|---|---|
| 72 666 700 | 102 802.351 139 341 | 103 000 | 1000 | 2000 |
| 145 333 300 | 205 604.560 807 621 | 206 000 | 1000 | 1000 |
| 217 999 900 | 308 406.770 475 901 | 309 000 | 1000 | 1000 |
| 290 666 500 | 411 208.980 144 181 | 413 000 | 2000 | 1000 |
| 363 333 100 | 514 011.189 812 461 | 516 000 | 3000 | 3000 |
| 435 999 700 | 616 813.399 480 742 | 619 000 | 3000 | 3000 |
| 508 666 300 | 719 615.609 149 022 | 721 000 | 3000 | 4000 |
| 581 332 900 | 822 417.818 817 302 | 824 000 | 3000 | 4000 |
| 653 999 500 | 925 220.028 485 582 | 927 000 | 4000 | 4000 |
| 726 666 100 | 1 028 022.238 153 86 | 1 030 000 | 4000 | 5000 |
| 799 332 700 | 1 130 824.447 822 14 | 1 133 000 | 4000 | 5000 |
| 871 999 300 | 1 233 626.657 490 42 | 1 236 000 | 5000 | 5000 |
| 944 665 900 | 1 336 428.867 158 7 | 1 339 000 | 5000 | 5000 |
| 1 017 332 500 | 1 439 231.076 826 98 | 1 442 000 | 6000 | 5000 |
| 1 089 999 100 | 1 542 033.286 495 26 | 1 544 000 | 6000 | 6000 |

TABLE C.19: 2 mm focal spot size images: Measured disk fluence for image quality analysis using developed method

| Histories | $I_{disk\,theoretical_{LB}}$ $\frac{1}{cm^2}$ | $I_{disk\,measured}$ $\frac{1}{cm^2}$ | $\delta_{-_{I_{disk}}}$ $\frac{1}{cm^2}$ | $\delta_{+_{I_{disk}}}$ $\frac{1}{cm^2}$ |
|---|---|---|---|---|
| 72 666 700 | 20 150.123 325 875 1 | 10 000 | 1000 | 1000 |
| 145 333 300 | 40 300.218 922 235 5 | 39 000 | 1000 | 2000 |
| 217 999 900 | 60 450.314 518 595 8 | 61 500 | 600 | 400 |
| 290 666 500 | 80 600.410 114 956 1 | 82 400 | 400 | 200 |
| 363 333 100 | 100 750.505 711 316 | 103 000 | 200 | 200 |
| 435 999 700 | 120 900.601 307 677 | 123 600 | 200 | 100 |
| 508 666 300 | 141 050.696 904 037 | 144 200 | 200 | 200 |
| 581 332 900 | 161 200.792 500 397 | 164 800 | 100 | 200 |
| 653 999 500 | 181 350.888 096 758 | 185 400 | 100 | 200 |
| 726 666 100 | 201 500.983 693 118 | 206 100 | 200 | 100 |
| 799 332 700 | 221 651.079 289 478 | 226 700 | 200 | 200 |
| 871 999 300 | 241 801.174 885 839 | 247 300 | 200 | 200 |
| 944 665 900 | 261 951.270 482 199 | 267 900 | 200 | 200 |
| 1 017 332 500 | 282 101.366 078 559 | 288 500 | 200 | 200 |
| 1 089 999 100 | 302 251.461 674 92 | 309 200 | 200 | 200 |

TABLE C.20: 2 mm focal spot size images: Measured disk fluence for image quality analysis using conventional method

| Histories | $I_{disk\,theoretical_{LB}}$ $\frac{1}{cm^2}$ | $I_{disk\,measured}$ $\frac{1}{cm^2}$ | $\delta_{-_{I_{disk}}}$ $\frac{1}{cm^2}$ | $\delta_{+_{I_{disk}}}$ $\frac{1}{cm^2}$ |
|---|---|---|---|---|
| 72 666 700 | 20 150.123 325 875 1 | 20 500 | 600 | 500 |
| 145 333 300 | 40 300.218 922 235 5 | 41 200 | 300 | 300 |
| 217 999 900 | 60 450.314 518 595 8 | 61 700 | 500 | 600 |
| 290 666 500 | 80 600.410 114 956 1 | 82 500 | 800 | 800 |
| 363 333 100 | 100 750.505 711 316 | 103 200 | 600 | 700 |
| 435 999 700 | 120 900.601 307 677 | 123 800 | 500 | 500 |
| 508 666 300 | 141 050.696 904 037 | 144 600 | 700 | 600 |
| 581 332 900 | 161 200.792 500 397 | 165 100 | 1000 | 900 |
| 653 999 500 | 181 350.888 096 758 | 185 500 | 800 | 800 |
| 726 666 100 | 201 500.983 693 118 | 206 100 | 900 | 900 |
| 799 332 700 | 221 651.079 289 478 | 227 000 | 1000 | 1000 |
| 871 999 300 | 241 801.174 885 839 | 247 000 | 1000 | 2000 |
| 944 665 900 | 261 951.270 482 199 | 268 000 | 2000 | 1000 |
| 1 017 332 500 | 282 101.366 078 559 | 288 000 | 1000 | 2000 |
| 1 089 999 100 | 302 251.461 674 92 | 309 000 | 1000 | 1000 |

TABLE C.21: 2 mm focal spot size images: Measured noise factor for image quality analysis using developed method

| Histories | $\alpha_{theoretical}$ | $\alpha_{measured}$ | $\delta_{-_\alpha}$ | $\delta_{+_\alpha}$ |
|---|---|---|---|---|
| 72 666 700 | 10 000 | 4600 | 300 | 400 |
| 145 333 300 | 10 000 | 9800 | 500 | 200 |
| 217 999 900 | 10 000 | 10 000 | 100 | 0 |
| 290 666 500 | 10 000 | 10 000 | 90 | 0 |
| 363 333 100 | 10 000 | 10 000 | 50 | 0 |
| 435 999 700 | 10 000 | 10 000 | 40 | 0 |
| 508 666 300 | 10 000 | 10 000 | 40 | 20 |
| 581 332 900 | 10 000 | 10 000 | 40 | 30 |
| 653 999 500 | 10 000 | 9990 | 30 | 30 |
| 726 666 100 | 10 000 | 10 000 | 30 | 20 |
| 799 332 700 | 10 000 | 9990 | 30 | 30 |
| 871 999 300 | 10 000 | 9990 | 30 | 30 |
| 944 665 900 | 10 000 | 9990 | 30 | 40 |
| 1 017 332 500 | 10 000 | 9990 | 30 | 30 |
| 1 089 999 100 | 10 000 | 9980 | 30 | 30 |

TABLE C.22: 2 mm focal spot size images: Measured noise factor for image quality analysis using conventional method

| Histories | $\alpha_{theoretical}$ | $\alpha_{measured}$ | $\delta_{-_\alpha}$ | $\delta_{+_\alpha}$ |
|---|---|---|---|---|
| 72 666 700 | 10 000 | 10 200 | 300 | 200 |
| 145 333 300 | 10 000 | 10 100 | 300 | 400 |
| 217 999 900 | 10 000 | 10 000 | 300 | 400 |
| 290 666 500 | 10 000 | 10 000 | 400 | 400 |
| 363 333 100 | 10 000 | 10 000 | 400 | 400 |
| 435 999 700 | 10 000 | 10 000 | 400 | 400 |
| 508 666 300 | 10 000 | 10 000 | 400 | 400 |
| 581 332 900 | 10 000 | 10 000 | 400 | 300 |
| 653 999 500 | 10 000 | 10 000 | 300 | 300 |
| 726 666 100 | 10 000 | 9900 | 300 | 400 |
| 799 332 700 | 10 000 | 9900 | 300 | 400 |
| 871 999 300 | 10 000 | 10 000 | 400 | 300 |
| 944 665 900 | 10 000 | 10 000 | 400 | 300 |
| 1 017 332 500 | 10 000 | 10 000 | 400 | 400 |
| 1 089 999 100 | 10 000 | 10 000 | 400 | 400 |

TABLE C.23: 2 mm focal spot size images: Measured PSF standard deviation for image quality analysis using developed method

| Histories | $\sigma_{PSFLB_{X_F}}$ mm | $\sigma_{PSFLB_{detector}}$ mm | $\sigma_{PSFmeasured}$ mm | $\delta_{-\sigma_{PSF}}$ mm | $\delta_{+\sigma_{PSF}}$ mm |
|---|---|---|---|---|---|
| 72 666 700 | 0.094 872 527 997 561 7 | 0.028 461 758 399 268 5 | 11 | 1 | 0 |
| 145 333 300 | 0.094 872 527 997 561 7 | 0.028 461 758 399 268 5 | 0.7 | 0.7 | 1.2 |
| 217 999 900 | 0.094 872 527 997 561 7 | 0.028 461 758 399 268 5 | 0.2 | 0.2 | 0.2 |
| 290 666 500 | 0.094 872 527 997 561 7 | 0.028 461 758 399 268 5 | 0.1 | 0.1 | 0.1 |
| 363 333 100 | 0.094 872 527 997 561 7 | 0.028 461 758 399 268 5 | 0.11 | 0.05 | 0.05 |
| 435 999 700 | 0.094 872 527 997 561 7 | 0.028 461 758 399 268 5 | 0.1 | 0.03 | 0.04 |
| 508 666 300 | 0.094 872 527 997 561 7 | 0.028 461 758 399 268 5 | 0.1 | 0.02 | 0.04 |
| 581 332 900 | 0.094 872 527 997 561 7 | 0.028 461 758 399 268 5 | 0.1 | 0.03 | 0.03 |
| 653 999 500 | 0.094 872 527 997 561 7 | 0.028 461 758 399 268 5 | 0.1 | 0.02 | 0.03 |
| 726 666 100 | 0.094 872 527 997 561 7 | 0.028 461 758 399 268 5 | 0.1 | 0.02 | 0.02 |
| 799 332 700 | 0.094 872 527 997 561 7 | 0.028 461 758 399 268 5 | 0.1 | 0.02 | 0.02 |
| 871 999 300 | 0.094 872 527 997 561 7 | 0.028 461 758 399 268 5 | 0.1 | 0.02 | 0.02 |
| 944 665 900 | 0.094 872 527 997 561 7 | 0.028 461 758 399 268 5 | 0.1 | 0.02 | 0.02 |
| 1 017 332 500 | 0.094 872 527 997 561 7 | 0.028 461 758 399 268 5 | 0.1 | 0.02 | 0.02 |
| 1 089 999 100 | 0.094 872 527 997 561 7 | 0.028 461 758 399 268 5 | 0.1 | 0.02 | 0.02 |

TABLE C.24: 2 mm focal spot size images: Measured PSF standard deviation for image quality analysis using conventional method

| Histories | $\sigma_{PSFLB_{X_F}}$ mm | $\sigma_{PSFLB_{detector}}$ mm | $\sigma_{PSFmeasured}$ mm | $\delta_{-\sigma_{PSF}}$ mm | $\delta_{+\sigma_{PSF}}$ mm |
|---|---|---|---|---|---|
| 72 666 700 | 0.094 872 527 997 561 7 | 0.028 461 758 399 268 5 | 0.03 | 0 | 0.01 |
| 145 333 300 | 0.094 872 527 997 561 7 | 0.028 461 758 399 268 5 | 0.039 | 0.004 | 0 |
| 217 999 900 | 0.094 872 527 997 561 7 | 0.028 461 758 399 268 5 | 0.061 | 0.006 | 0 |
| 290 666 500 | 0.094 872 527 997 561 7 | 0.028 461 758 399 268 5 | 0.09 | 0.05 | 0 |
| 363 333 100 | 0.094 872 527 997 561 7 | 0.028 461 758 399 268 5 | 0.06 | 0.02 | 0 |
| 435 999 700 | 0.094 872 527 997 561 7 | 0.028 461 758 399 268 5 | 0.05 | 0 | 0.01 |
| 508 666 300 | 0.094 872 527 997 561 7 | 0.028 461 758 399 268 5 | 0.06 | 0.04 | 0 |
| 581 332 900 | 0.094 872 527 997 561 7 | 0.028 461 758 399 268 5 | 0.07 | 0.04 | 0 |
| 653 999 500 | 0.094 872 527 997 561 7 | 0.028 461 758 399 268 5 | 0.03 | 0 | 0.04 |
| 726 666 100 | 0.094 872 527 997 561 7 | 0.028 461 758 399 268 5 | 0.05 | 0.02 | 0.02 |
| 799 332 700 | 0.094 872 527 997 561 7 | 0.028 461 758 399 268 5 | 0.07 | 0.03 | 0 |
| 871 999 300 | 0.094 872 527 997 561 7 | 0.028 461 758 399 268 5 | 0.05 | 0.02 | 0.01 |
| 944 665 900 | 0.094 872 527 997 561 7 | 0.028 461 758 399 268 5 | 0.074 | 0.005 | 0.005 |
| 1 017 332 500 | 0.094 872 527 997 561 7 | 0.028 461 758 399 268 5 | 0.077 | 0 | 0.006 |
| 1 089 999 100 | 0.094 872 527 997 561 7 | 0.028 461 758 399 268 5 | 0.07 | 0 | 0.002 |

TABLE C.25: 2 mm focal spot size images: Frequency at 10% MTF corresponding to measured PSF standard deviation for image quality analysis using developed method

| Histories | $f_{10\%MTF_{UB_{X_F}}}$ $\frac{\text{cycle}}{\text{mm}}$ | $f_{10\%MTF_{UB_{detector}}}$ $\frac{\text{cycle}}{\text{mm}}$ | $f_{10\%MTF_{measured}}$ $\frac{\text{cycle}}{\text{mm}}$ | $\delta_{-_{f_{10\%MTF}}}$ $\frac{\text{cycle}}{\text{mm}}$ | $\delta_{+_{f_{10\%MTF}}}$ $\frac{\text{cycle}}{\text{mm}}$ |
|---|---|---|---|---|---|
| 72 666 700 | 3.6 | 12 | 0.03 | 0 | 0.003 |
| 145 333 300 | 3.6 | 12 | 0.5 | 0.3 | Inf |
| 217 999 900 | 3.6 | 12 | 2 | 1 | Inf |
| 290 666 500 | 3.6 | 12 | 3 | 2 | 21 |
| 363 333 100 | 3.6 | 12 | 3 | 1 | 2 |
| 435 999 700 | 3.6 | 12 | 3 | 1 | 2 |
| 508 666 300 | 3.6 | 12 | 3 | 0 | 2 |
| 581 332 900 | 3.6 | 12 | 3 | 0 | 2 |
| 653 999 500 | 3.6 | 12 | 3 | 0 | 1 |
| 726 666 100 | 3.6 | 12 | 3.5 | 0.6 | 0.7 |
| 799 332 700 | 3.6 | 12 | 3 | 0 | 1 |
| 871 999 300 | 3.6 | 12 | 3 | 0 | 1 |
| 944 665 900 | 3.6 | 12 | 3.5 | 0.6 | 0.9 |
| 1 017 332 500 | 3.6 | 12 | 3.5 | 0.6 | 0.9 |
| 1 089 999 100 | 3.6 | 12 | 3.5 | 0.6 | 0.9 |

TABLE C.26: 2 mm focal spot size images: Frequency at 10% MTF corresponding to measured PSF standard deviation for image quality analysis using conventional method

| Histories | $f_{10\%MTF_{UB_{X_F}}}$ $\frac{\text{cycle}}{\text{mm}}$ | $f_{10\%MTF_{UB_{detector}}}$ $\frac{\text{cycle}}{\text{mm}}$ | $f_{10\%MTF_{measured}}$ $\frac{\text{cycle}}{\text{mm}}$ | $\delta_{-_{f_{10\%MTF}}}$ $\frac{\text{cycle}}{\text{mm}}$ | $\delta_{+_{f_{10\%MTF}}}$ $\frac{\text{cycle}}{\text{mm}}$ |
|---|---|---|---|---|---|
| 72 666 700 | 3.6 | 12 | 12 | 3 | 0 |
| 145 333 300 | 3.6 | 12 | 9 | 0 | 1 |
| 217 999 900 | 3.6 | 12 | 5.6 | 0 | 0.6 |
| 290 666 500 | 3.6 | 12 | 4 | 0 | 5 |
| 363 333 100 | 3.6 | 12 | 6 | 0 | 3 |
| 435 999 700 | 3.6 | 12 | 7 | 1 | 0 |
| 508 666 300 | 3.6 | 12 | 6 | 1 | 8 |
| 581 332 900 | 3.6 | 12 | 5 | 0 | 6 |
| 653 999 500 | 3.6 | 12 | 11 | 6 | 0 |
| 726 666 100 | 3.6 | 12 | 8 | 3 | 3 |
| 799 332 700 | 3.6 | 12 | 5 | 0 | 3 |
| 871 999 300 | 3.6 | 12 | 6 | 0 | 4 |
| 944 665 900 | 3.6 | 12 | 4.6 | 0.3 | 0.4 |
| 1 017 332 500 | 3.6 | 12 | 4.4 | 0.3 | 0 |
| 1 089 999 100 | 3.6 | 12 | 4.8 | 0.1 | 0 |

## C.3 3 mm focal spot size

Beam Energy: 40 keV.

Beam geometry: diverging.

$X_F$: 3 mm ($f_{10\%MTF}$ = 2.4 cycle/mm).

FOV: 15 cm radius circle.

Disk thickness: 0.1 mm.

Water depth: 0 cm.

ROI: $20 \times 20$ cm$^2$.

Pixel size: 0.1 mm ($f_{a_{lim}}$ = 12 cycle/mm).

Bit depth: 16.

Noise assumption for developed method: Poisson.

TABLE C.27: 3 mm focal spot size images: cost function for image quality analysis using developed method

| Histories | Cost function |
|---|---|
| 72 666 700 | 173 452.390 625 |
| 145 333 300 | 21 942.898 613 689 8 |
| 290 666 500 | 331.293 052 950 983 |
| 363 333 100 | 47.716 127 324 948 1 |
| 435 999 700 | 21.071 910 633 112 4 |
| 508 666 300 | 29.611 686 990 857 8 |
| 581 332 900 | 23.499 554 262 798 8 |
| 653 999 500 | 19.454 481 649 788 6 |
| 726 666 100 | 34.571 059 798 758 8 |
| 799 332 700 | 45.786 432 836 371 1 |
| 871 999 300 | 40.366 501 305 413 2 |
| 944 665 900 | 39.882 066 469 769 7 |
| 1 017 332 500 | 42.659 323 325 194 7 |
| 1 089 999 100 | 58.643 298 770 716 9 |

TABLE C.28: 3 mm focal spot size images: SNR measured using conventional method

| Histories | $SNR_{measured}$ | $\delta_{-_{SNR}}$ | $\delta_{+_{SNR}}$ |
|---|---|---|---|
| 72 666 700 | 5.8 | 0.3 | 0.4 |
| 145 333 300 | 8.2 | 0.3 | 0.2 |
| 290 666 500 | 11.6 | 0.3 | 0.3 |
| 363 333 100 | 12.9 | 0.4 | 0.4 |
| 435 999 700 | 14.2 | 0.5 | 0.4 |
| 508 666 300 | 15.2 | 0.3 | 0.4 |
| 581 332 900 | 16.3 | 0.4 | 0.4 |
| 653 999 500 | 17.2 | 0.4 | 0.5 |
| 726 666 100 | 18.1 | 0.4 | 0.5 |
| 799 332 700 | 19.1 | 0.5 | 0.5 |
| 871 999 300 | 19.9 | 0.5 | 0.5 |
| 944 665 900 | 20.7 | 0.6 | 0.7 |
| 1 017 332 500 | 21.5 | 0.6 | 0.6 |
| 1 089 999 100 | 22.2 | 0.6 | 0.6 |

TABLE C.29: 3 mm focal spot size images: Measured radius for image quality analysis using developed method

| Histories | $R_{actual}$ mm | $R_{measured}$ mm | $\delta_{-_R}$ mm | $\delta_{+_R}$ mm |
|---|---|---|---|---|
| 72 666 700 | 5 | 7.5 | 0.06 | 0.06 |
| 145 333 300 | 5 | 5.05 | 0.04 | 0.04 |
| 290 666 500 | 5 | 5.002 | 0.004 | 0.005 |
| 363 333 100 | 5 | 5.001 | 0.002 | 0.003 |
| 435 999 700 | 5 | 5.001 | 0.001 | 0.002 |
| 508 666 300 | 5 | 5.001 | 0.001 | 0.002 |
| 581 332 900 | 5 | 5.001 | 0.001 | 0.002 |
| 653 999 500 | 5 | 5.001 | 0.001 | 0.002 |
| 726 666 100 | 5 | 5.001 | 0.001 | 0.002 |
| 799 332 700 | 5 | 5.002 | 0.002 | 0.001 |
| 871 999 300 | 5 | 5.001 | 0.001 | 0.002 |
| 944 665 900 | 5 | 5.001 | 0.001 | 0.002 |
| 1 017 332 500 | 5 | 5.001 | 0.001 | 0.002 |
| 1 089 999 100 | 5 | 5.001 | 0.001 | 0.002 |

TABLE C.30: 3 mm focal spot size images: Measured background fluence for image quality analysis using developed method

| Histories | $I_{BG\,theoretical_{LB}}$ $\frac{1}{cm^2}$ | $I_{BG\,measured}$ $\frac{1}{cm^2}$ | $\delta_{-_{I_{BG}}}$ $\frac{1}{cm^2}$ | $\delta_{+_{I_{BG}}}$ $\frac{1}{cm^2}$ |
|---|---|---|---|---|
| 72 666 700 | 102 802.351 139 341 | 10 000 | 2000 | 2000 |
| 145 333 300 | 205 604.560 807 621 | 206 000 | 1000 | 2000 |
| 290 666 500 | 411 208.980 144 181 | 412 200 | 300 | 300 |
| 363 333 100 | 514 011.189 812 461 | 515 200 | 200 | 200 |
| 435 999 700 | 616 813.399 480 742 | 618 200 | 200 | 200 |
| 508 666 300 | 719 615.609 149 022 | 721 200 | 200 | 200 |
| 581 332 900 | 822 417.818 817 302 | 824 200 | 200 | 200 |
| 653 999 500 | 925 220.028 485 582 | 927 200 | 200 | 200 |
| 726 666 100 | 1 028 022.238 153 86 | 1 030 200 | 200 | 200 |
| 799 332 700 | 1 130 824.447 822 14 | 1 133 200 | 100 | 200 |
| 871 999 300 | 1 233 626.657 490 42 | 1 236 300 | 200 | 200 |
| 944 665 900 | 1 336 428.867 158 7 | 1 339 300 | 200 | 200 |
| 1 017 332 500 | 1 439 231.076 826 98 | 1 442 300 | 200 | 200 |
| 1 089 999 100 | 1 542 033.286 495 26 | 1 545 400 | 300 | 200 |

TABLE C.31: 3 mm focal spot size images: Measured background fluence for image quality analysis using conventional method

| Histories | $I_{BG\,theoretical_{LB}}$ $\frac{1}{cm^2}$ | $I_{BGUB}$ $\frac{1}{cm^2}$ | $\delta_{-_{I_{BG}}}$ $\frac{1}{cm^2}$ | $\delta_{+_{I_{BG}}}$ $\frac{1}{cm^2}$ |
|---|---|---|---|---|
| 72 666 700 | 102 802.351 139 341 | 103 000 | 1000 | 2000 |
| 145 333 300 | 205 604.560 807 621 | 207 000 | 1000 | 1000 |
| 290 666 500 | 411 208.980 144 181 | 413 000 | 2000 | 2000 |
| 363 333 100 | 514 011.189 812 461 | 516 000 | 4000 | 3000 |
| 435 999 700 | 616 813.399 480 742 | 618 000 | 3000 | 4000 |
| 508 666 300 | 719 615.609 149 022 | 721 000 | 3000 | 4000 |
| 581 332 900 | 822 417.818 817 302 | 824 000 | 4000 | 5000 |
| 653 999 500 | 925 220.028 485 582 | 927 000 | 5000 | 5000 |
| 726 666 100 | 1 028 022.238 153 86 | 1 030 000 | 6000 | 6000 |
| 799 332 700 | 1 130 824.447 822 14 | 1 133 000 | 6000 | 6000 |
| 871 999 300 | 1 233 626.657 490 42 | 1 235 000 | 6000 | 7000 |
| 944 665 900 | 1 336 428.867 158 7 | 1 338 000 | 6000 | 7000 |
| 1 017 332 500 | 1 439 231.076 826 98 | 1 441 000 | 7000 | 7000 |
| 1 089 999 100 | 1 542 033.286 495 26 | 1 544 000 | 8000 | 7000 |

TABLE C.32: 3 mm focal spot size images: Measured disk fluence for image quality analysis using developed method

| Histories | $I_{disk\,theoretical_{LB}}$ $\frac{1}{cm^2}$ | $I_{disk\,measured}$ $\frac{1}{cm^2}$ | $\delta_{-_{I_{disk}}}$ $\frac{1}{cm^2}$ | $\delta_{+_{I_{disk}}}$ $\frac{1}{cm^2}$ |
|---|---|---|---|---|
| 72 666 700 | 20 150.123 325 875 1 | 110 000 | 2000 | 2000 |
| 145 333 300 | 40 300.218 922 235 5 | 39 000 | 2000 | 2000 |
| 290 666 500 | 80 600.410 114 956 1 | 82 400 | 400 | 200 |
| 363 333 100 | 100 750.505 711 316 | 103 000 | 200 | 200 |
| 435 999 700 | 120 900.601 307 677 | 123 600 | 200 | 200 |
| 508 666 300 | 141 050.696 904 037 | 144 200 | 200 | 200 |
| 581 332 900 | 161 200.792 500 397 | 164 900 | 200 | 100 |
| 653 999 500 | 181 350.888 096 758 | 185 500 | 200 | 100 |
| 726 666 100 | 201 500.983 693 118 | 206 100 | 200 | 200 |
| 799 332 700 | 221 651.079 289 478 | 226 700 | 200 | 200 |
| 871 999 300 | 241 801.174 885 839 | 247 300 | 200 | 200 |
| 944 665 900 | 261 951.270 482 199 | 267 900 | 200 | 200 |
| 1 017 332 500 | 282 101.366 078 559 | 288 500 | 200 | 200 |
| 1 089 999 100 | 302 251.461 674 92 | 309 100 | 200 | 300 |

TABLE C.33: 3 mm focal spot size images: Measured disk fluence for image quality analysis using conventional method

| Histories | $I_{disk\,theoretical_{LB}}$ $\frac{1}{cm^2}$ | $I_{disk\,measured}$ $\frac{1}{cm^2}$ | $\delta_{-_{I_{disk}}}$ $\frac{1}{cm^2}$ | $\delta_{+_{I_{disk}}}$ $\frac{1}{cm^2}$ |
|---|---|---|---|---|
| 72 666 700 | 20 150.123 325 875 1 | 20 500 | 600 | 600 |
| 145 333 300 | 40 300.218 922 235 5 | 41 200 | 300 | 400 |
| 290 666 500 | 80 600.410 114 956 1 | 82 500 | 600 | 700 |
| 363 333 100 | 100 750.505 711 316 | 103 200 | 500 | 600 |
| 435 999 700 | 120 900.601 307 677 | 123 900 | 700 | 700 |
| 508 666 300 | 141 050.696 904 037 | 144 600 | 700 | 700 |
| 581 332 900 | 161 200.792 500 397 | 165 200 | 800 | 800 |
| 653 999 500 | 181 350.888 096 758 | 185 800 | 700 | 600 |
| 726 666 100 | 201 500.983 693 118 | 206 400 | 700 | 600 |
| 799 332 700 | 221 651.079 289 478 | 226 800 | 600 | 500 |
| 871 999 300 | 241 801.174 885 839 | 247 000 | 1000 | 1000 |
| 944 665 900 | 261 951.270 482 199 | 268 000 | 1000 | 1000 |
| 1 017 332 500 | 282 101.366 078 559 | 288 000 | 1000 | 2000 |
| 1 089 999 100 | 302 251.461 674 92 | 309 000 | 1000 | 1000 |

TABLE C.34: 3 mm focal spot size images: Measured noise factor for image quality analysis using developed method

| Histories | $\alpha_{theoretical}$ | $\alpha_{measured}$ | $\delta_{-_\alpha}$ | $\delta_{+_\alpha}$ |
|---|---|---|---|---|
| 72 666 700 | 10 000 | 4700 | 600 | 600 |
| 145 333 300 | 10 000 | 9800 | 600 | 200 |
| 290 666 500 | 10 000 | 10 000 | 80 | 0 |
| 363 333 100 | 10 000 | 10 000 | 60 | 0 |
| 435 999 700 | 10 000 | 9990 | 40 | 10 |
| 508 666 300 | 10 000 | 9990 | 50 | 30 |
| 581 332 900 | 10 000 | 9990 | 40 | 40 |
| 653 999 500 | 10 000 | 9990 | 40 | 30 |
| 726 666 100 | 10 000 | 9990 | 40 | 40 |
| 799 332 700 | 10 000 | 9980 | 40 | 40 |
| 871 999 300 | 10 000 | 9980 | 30 | 40 |
| 944 665 900 | 10 000 | 9980 | 30 | 40 |
| 1 017 332 500 | 10 000 | 9980 | 40 | 30 |
| 1 089 999 100 | 10 000 | 9980 | 40 | 30 |

TABLE C.35: 3 mm focal spot size images: Measured noise factor for image quality analysis using conventional method

| Histories | $\alpha_{theoretical}$ | $\alpha_{measured}$ | $\delta_{-_\alpha}$ | $\delta_{+_\alpha}$ |
|---|---|---|---|---|
| 72 666 700 | 10 000 | 9900 | 400 | 400 |
| 145 333 300 | 10 000 | 10 000 | 300 | 300 |
| 290 666 500 | 10 000 | 9800 | 300 | 300 |
| 363 333 100 | 10 000 | 9900 | 400 | 300 |
| 435 999 700 | 10 000 | 9900 | 400 | 400 |
| 508 666 300 | 10 000 | 9900 | 300 | 300 |
| 581 332 900 | 10 000 | 9900 | 300 | 300 |
| 653 999 500 | 10 000 | 10 000 | 400 | 300 |
| 726 666 100 | 10 000 | 10 000 | 300 | 300 |
| 799 332 700 | 10 000 | 9900 | 300 | 400 |
| 871 999 300 | 10 000 | 10 000 | 400 | 300 |
| 944 665 900 | 10 000 | 10 000 | 400 | 300 |
| 1 017 332 500 | 10 000 | 10 000 | 400 | 400 |
| 1 089 999 100 | 10 000 | 10 000 | 400 | 400 |

TABLE C.36: 3 mm focal spot size images: Measured PSF standard deviation for image quality analysis using developed method

| Histories | $\sigma_{PSFLB_{X_F}}$ mm | $\sigma_{PSFLB_{detector}}$ mm | $\sigma_{PSFmeasured}$ mm | $\delta_{-\sigma_{PSF}}$ mm | $\delta_{+\sigma_{PSF}}$ mm |
|---|---|---|---|---|---|
| 72 666 700 | 0.142 308 791 996 342 | 0.028 461 758 399 268 5 | 8 | 2 | 1 |
| 145 333 300 | 0.142 308 791 996 342 | 0.028 461 758 399 268 5 | 0.8 | 0.8 | 1.3 |
| 290 666 500 | 0.142 308 791 996 342 | 0.028 461 758 399 268 5 | 0.2 | 0.1 | 0.1 |
| 363 333 100 | 0.142 308 791 996 342 | 0.028 461 758 399 268 5 | 0.14 | 0.04 | 0.07 |
| 435 999 700 | 0.142 308 791 996 342 | 0.028 461 758 399 268 5 | 0.14 | 0.03 | 0.04 |
| 508 666 300 | 0.142 308 791 996 342 | 0.028 461 758 399 268 5 | 0.15 | 0.04 | 0.03 |
| 581 332 900 | 0.142 308 791 996 342 | 0.028 461 758 399 268 5 | 0.14 | 0.03 | 0.04 |
| 653 999 500 | 0.142 308 791 996 342 | 0.028 461 758 399 268 5 | 0.14 | 0.02 | 0.03 |
| 726 666 100 | 0.142 308 791 996 342 | 0.028 461 758 399 268 5 | 0.14 | 0.03 | 0.03 |
| 799 332 700 | 0.142 308 791 996 342 | 0.028 461 758 399 268 5 | 0.14 | 0.02 | 0.03 |
| 871 999 300 | 0.142 308 791 996 342 | 0.028 461 758 399 268 5 | 0.14 | 0.02 | 0.03 |
| 944 665 900 | 0.142 308 791 996 342 | 0.028 461 758 399 268 5 | 0.14 | 0.02 | 0.03 |
| 1 017 332 500 | 0.142 308 791 996 342 | 0.028 461 758 399 268 5 | 0.14 | 0.02 | 0.03 |
| 1 089 999 100 | 0.142 308 791 996 342 | 0.028 461 758 399 268 5 | 0.14 | 0.02 | 0.03 |

TABLE C.37: 3 mm focal spot size images: Measured PSF standard deviation for image quality analysis using conventional method

| Histories | $\sigma_{PSFLB_{X_F}}$ mm | $\sigma_{PSFLB_{detector}}$ mm | $\sigma_{PSFmeasured}$ mm | $\delta_{-\sigma_{PSF}}$ mm | $\delta_{+\sigma_{PSF}}$ mm |
|---|---|---|---|---|---|
| 72 666 700 | 0.142 308 791 996 342 | 0.028 461 758 399 268 5 | 0.02 | 0 | 0.01 |
| 145 333 300 | 0.142 308 791 996 342 | 0.028 461 758 399 268 5 | 0.03 | 0 | 0.03 |
| 290 666 500 | 0.142 308 791 996 342 | 0.028 461 758 399 268 5 | 0.02 | 0 | 0.02 |
| 363 333 100 | 0.142 308 791 996 342 | 0.028 461 758 399 268 5 | 0.07 | 0 | 0.03 |
| 435 999 700 | 0.142 308 791 996 342 | 0.028 461 758 399 268 5 | 0.04 | 0 | 0.02 |
| 508 666 300 | 0.142 308 791 996 342 | 0.028 461 758 399 268 5 | 0.04 | 0 | 0.03 |
| 581 332 900 | 0.142 308 791 996 342 | 0.028 461 758 399 268 5 | 0.08 | 0.01 | 0.04 |
| 653 999 500 | 0.142 308 791 996 342 | 0.028 461 758 399 268 5 | 0.11 | 0.03 | 0 |
| 726 666 100 | 0.142 308 791 996 342 | 0.028 461 758 399 268 5 | 0.12 | 0.08 | 0 |
| 799 332 700 | 0.142 308 791 996 342 | 0.028 461 758 399 268 5 | 0.09 | 0.02 | 0.02 |
| 871 999 300 | 0.142 308 791 996 342 | 0.028 461 758 399 268 5 | 0.122 | 0.004 | 0.004 |
| 944 665 900 | 0.142 308 791 996 342 | 0.028 461 758 399 268 5 | 0.105 | 0.003 | 0.003 |
| 1 017 332 500 | 0.142 308 791 996 342 | 0.028 461 758 399 268 5 | 0.112 | 0.003 | 0.002 |
| 1 089 999 100 | 0.142 308 791 996 342 | 0.028 461 758 399 268 5 | 0.127 | 0.005 | 0.004 |

TABLE C.38: 3 mm focal spot size images: Frequency at 10% MTF corresponding to measured PSF standard deviation for image quality analysis using developed method

| Histories | $f_{10\%MTF_{UB_{X_F}}}$ $\frac{\text{cycle}}{\text{mm}}$ | $f_{10\%MTF_{UB_{detector}}}$ $\frac{\text{cycle}}{\text{mm}}$ | $f_{10\%MTF_{measured}}$ $\frac{\text{cycle}}{\text{mm}}$ | $\delta_{-_{f_{10\%MTF}}}$ $\frac{\text{cycle}}{\text{mm}}$ | $\delta_{+_{f_{10\%MTF}}}$ $\frac{\text{cycle}}{\text{mm}}$ |
|---|---|---|---|---|---|
| 72 666 700 | 2.4 | 12 | 0.044 | 0.007 | 0.009 |
| 145 333 300 | 2.4 | 12 | 0.4 | 0.2 | Inf |
| 290 666 500 | 2.4 | 12 | 2 | 1 | 3 |
| 363 333 100 | 2.4 | 12 | 2 | 0 | 2 |
| 435 999 700 | 2.4 | 12 | 2.4 | 0.6 | 0.6 |
| 508 666 300 | 2.4 | 12 | 2.4 | 0.5 | 0.7 |
| 581 332 900 | 2.4 | 12 | 2.4 | 0.5 | 0.7 |
| 653 999 500 | 2.4 | 12 | 2.4 | 0.4 | 0.5 |
| 726 666 100 | 2.4 | 12 | 2.4 | 0.4 | 0.6 |
| 799 332 700 | 2.4 | 12 | 2.4 | 0.4 | 0.5 |
| 871 999 300 | 2.4 | 12 | 2.4 | 0.4 | 0.5 |
| 944 665 900 | 2.4 | 12 | 2.4 | 0.4 | 0.4 |
| 1 017 332 500 | 2.4 | 12 | 2.4 | 0.4 | 0.4 |
| 1 089 999 100 | 2.4 | 12 | 2.4 | 0.4 | 0.4 |

TABLE C.39: 3 mm focal spot size images: Frequency at 10% MTF corresponding to measured PSF standard deviation for image quality analysis using conventional method

| Histories | $f_{10\%MTF_{UB_{X_F}}}$ $\frac{\text{cycle}}{\text{mm}}$ | $f_{10\%MTF_{UB_{detector}}}$ $\frac{\text{cycle}}{\text{mm}}$ | $f_{10\%MTF_{measured}}$ $\frac{\text{cycle}}{\text{mm}}$ | $\delta_{-_{f_{10\%MTF}}}$ $\frac{\text{cycle}}{\text{mm}}$ | $\delta_{+_{f_{10\%MTF}}}$ $\frac{\text{cycle}}{\text{mm}}$ |
|---|---|---|---|---|---|
| 72 666 700 | 2.4 | 12 | 16 | 6 | 0 |
| 145 333 300 | 2.4 | 12 | 13 | 7 | 0 |
| 290 666 500 | 2.4 | 12 | 14 | 6 | 0 |
| 363 333 100 | 2.4 | 12 | 5 | 2 | 0 |
| 435 999 700 | 2.4 | 12 | 8 | 3 | 0 |
| 508 666 300 | 2.4 | 12 | 8 | 3 | 0 |
| 581 332 900 | 2.4 | 12 | 4 | 1 | 1 |
| 653 999 500 | 2.4 | 12 | 3 | 0 | 1 |
| 726 666 100 | 2.4 | 12 | 3 | 0 | 6 |
| 799 332 700 | 2.4 | 12 | 4 | 1 | 1 |
| 871 999 300 | 2.4 | 12 | 2.8 | 0.1 | 0.1 |
| 944 665 900 | 2.4 | 12 | 3.3 | 0.1 | 0.1 |
| 1 017 332 500 | 2.4 | 12 | 3.05 | 0.06 | 0.09 |
| 1 089 999 100 | 2.4 | 12 | 2.7 | 0.1 | 0.1 |

## C.4 4 mm focal spot size, vacuum background

Beam Energy: 40 keV.

Beam geometry: diverging.

$X_F$: 4 mm ($f_{10\%MTF}$ = 1.8 cycle/mm).

FOV: 15 cm radius circle.

Disk thickness: 0.1 mm.

Water depth: 0 cm.

ROI: $20 \times 20$ cm$^2$.

Pixel size: 0.1 mm ($f_{a_{lim}}$ = 12 cycle/mm).

Bit depth: 16.

Noise assumption for developed method: Poisson.

TABLE C.40: 4 mm focal spot size images: cost function for image quality analysis using developed method

| Histories | Cost function |
|---|---|
| 94 466 580 | 92 455.632 812 5 |
| 186 511 040 | 6416.230 999 969 27 |
| 273 710 960 | 565.820 735 097 309 |
| 353 644 220 | 61.330 514 759 859 7 |
| 426 310 820 | 16.040 196 443 287 9 |
| 498 977 420 | 8.244 701 292 532 08 |
| 566 799 580 | 12.450 646 110 128 5 |
| 632 199 520 | 12.696 330 086 726 7 |
| 697 599 460 | 18.623 954 562 727 9 |
| 762 999 400 | 28.657 350 786 937 1 |
| 828 399 340 | 29.126 220 156 670 5 |
| 893 799 280 | 28.773 118 289 483 |
| 959 199 220 | 25.463 875 920 607 7 |
| 1 024 599 160 | 17.487 905 332 343 9 |
| 1 089 999 100 | 20.036 209 652 478 7 |

TABLE C.41: 4 mm focal spot size images: SNR measured using conventional method

| Histories | $SNR_{measured}$ | $\delta_{-SNR}$ | $\delta_{+SNR}$ |
|---|---|---|---|
| 94 466 580 | 6.5 | 0.3 | 0.2 |
| 186 511 040 | 9.1 | 0.2 | 0.3 |
| 273 710 960 | 11 | 0.2 | 0.3 |
| 353 644 220 | 12.6 | 0.3 | 0.3 |
| 426 310 820 | 13.9 | 0.3 | 0.3 |
| 498 977 420 | 15.1 | 0.3 | 0.3 |
| 566 799 580 | 16.1 | 0.4 | 0.3 |
| 632 199 520 | 16.9 | 0.3 | 0.3 |
| 697 599 460 | 17.8 | 0.4 | 0.4 |
| 762 999 400 | 18.6 | 0.4 | 0.4 |
| 828 399 340 | 19.3 | 0.4 | 0.5 |
| 893 799 280 | 20.1 | 0.5 | 0.5 |
| 959 199 220 | 20.8 | 0.5 | 0.5 |
| 1 024 599 160 | 21.4 | 0.6 | 0.6 |
| 1 089 999 100 | 22.1 | 0.5 | 0.6 |

TABLE C.42: 4 mm focal spot size images: Measured radius for image quality analysis using developed method

| Histories | $R_{actual}$ mm | $R_{measured}$ mm | $\delta_{-R}$ mm | $\delta_{+R}$ mm |
|---|---|---|---|---|
| 94 466 580 | 5 | 5.41 | 0.06 | 0.06 |
| 186 511 040 | 5 | 7.96 | 0.02 | 0.01 |
| 273 710 960 | 5 | 5.001 | 0.005 | 0.007 |
| 353 644 220 | 5 | 5.001 | 0.003 | 0.003 |
| 426 310 820 | 5 | 5.001 | 0.002 | 0.002 |
| 498 977 420 | 5 | 5.001 | 0.002 | 0.001 |
| 566 799 580 | 5 | 5.001 | 0.002 | 0.001 |
| 632 199 520 | 5 | 5.001 | 0.002 | 0.001 |
| 697 599 460 | 5 | 5.001 | 0.002 | 0.001 |
| 762 999 400 | 5 | 5.001 | 0.002 | 0.001 |
| 828 399 340 | 5 | 5.001 | 0.002 | 0.001 |
| 893 799 280 | 5 | 5.001 | 0.001 | 0.001 |
| 959 199 220 | 5 | 5.001 | 0.001 | 0.001 |
| 1 024 599 160 | 5 | 5.001 | 0.001 | 0.001 |
| 1 089 999 100 | 5 | 5.001 | 0.001 | 0.001 |

TABLE C.43: 4 mm focal spot size images: Measured background fluence for image quality analysis using developed method

| Histories | $I_{BG\,theoretical_{LB}}$ $\frac{1}{cm^2}$ | $I_{BG\,measured}$ $\frac{1}{cm^2}$ | $\delta_{-_{I_{BG}}}$ $\frac{1}{cm^2}$ | $\delta_{+_{I_{BG}}}$ $\frac{1}{cm^2}$ |
|---|---|---|---|---|
| 94 466 580 | 133 642.872 568 764 | 141 000 | 2000 | 3000 |
| 186 511 040 | 263 859.146 286 313 | 52 300 | 900 | 600 |
| 273 710 960 | 387 221.797 888 249 | 388 000 | 400 | 400 |
| 353 644 220 | 500 304.228 523 357 | 501 400 | 300 | 200 |
| 426 310 820 | 603 106.438 191 638 | 604 400 | 200 | 100 |
| 498 977 420 | 705 908.647 859 918 | 707 400 | 100 | 100 |
| 566 799 580 | 801 857.376 883 646 | 803 500 | 100 | 200 |
| 632 199 520 | 894 379.365 585 098 | 896 300 | 200 | 100 |
| 697 599 460 | 986 901.354 286 55 | 989 000 | 100 | 200 |
| 762 999 400 | 1 079 423.342 988 | 1 081 800 | 200 | 100 |
| 828 399 340 | 1 171 945.331 689 45 | 1 174 500 | 200 | 200 |
| 893 799 280 | 1 264 467.320 390 91 | 1 267 200 | 200 | 200 |
| 959 199 220 | 1 356 989.309 092 36 | 1 360 000 | 200 | 100 |
| 1 024 599 160 | 1 449 511.297 793 81 | 1 452 700 | 200 | 100 |
| 1 089 999 100 | 1 542 033.286 495 26 | 1 545 400 | 200 | 200 |

TABLE C.44: 4 mm focal spot size images: Measured background fluence for image quality analysis using conventional method

| Histories | $I_{BG\,theoretical_{LB}}$ $\frac{1}{cm^2}$ | $I_{BG\,measured}$ $\frac{1}{cm^2}$ | $\delta_{-_{I_{BG}}}$ $\frac{1}{cm^2}$ | $\delta_{+_{I_{BG}}}$ $\frac{1}{cm^2}$ |
|---|---|---|---|---|
| 94 466 580 | 133 642.872 568 764 | 133 500 | 700 | 800 |
| 186 511 040 | 263 859.146 286 313 | 264 000 | 1000 | 2000 |
| 273 710 960 | 387 221.797 888 249 | 388 000 | 1000 | 2000 |
| 353 644 220 | 500 304.228 523 357 | 502 000 | 2000 | 2000 |
| 426 310 820 | 603 106.438 191 638 | 605 000 | 2000 | 2000 |
| 498 977 420 | 705 908.647 859 918 | 708 000 | 3000 | 2000 |
| 566 799 580 | 801 857.376 883 646 | 804 000 | 3000 | 2000 |
| 632 199 520 | 894 379.365 585 098 | 896 000 | 2000 | 3000 |
| 697 599 460 | 986 901.354 286 55 | 989 000 | 3000 | 4000 |
| 762 999 400 | 1 079 423.342 988 | 1 082 000 | 4000 | 3000 |
| 828 399 340 | 1 171 945.331 689 45 | 1 175 000 | 4000 | 4000 |
| 893 799 280 | 1 264 467.320 390 91 | 1 267 000 | 3000 | 4000 |
| 959 199 220 | 1 356 989.309 092 36 | 1 360 000 | 5000 | 4000 |
| 1 024 599 160 | 1 449 511.297 793 81 | 1 452 000 | 4000 | 5000 |
| 1 089 999 100 | 1 542 033.286 495 26 | 1 545 000 | 5000 | 5000 |

TABLE C.45: 4 mm focal spot size images: Measured disk fluence for image quality analysis using developed method

| Histories | $I_{disk\,theoretical_{LB}}$ $\frac{1}{cm^2}$ | $I_{disk\,measured}$ $\frac{1}{cm^2}$ | $\delta_{-_{I_{disk}}}$ $\frac{1}{cm^2}$ | $\delta_{+_{I_{disk}}}$ $\frac{1}{cm^2}$ |
|---|---|---|---|---|
| 94 466 580 | 26 195.124 275 268 4 | 16 000 | 2000 | 2000 |
| 186 511 040 | 51 718.606 426 839 6 | 264 300 | 600 | 800 |
| 273 710 960 | 75 898.721 142 472 | 77 600 | 500 | 200 |
| 353 644 220 | 98 063.826 298 468 4 | 100 300 | 300 | 100 |
| 426 310 820 | 118 213.921 894 829 | 120 900 | 200 | 100 |
| 498 977 420 | 138 364.017 491 189 | 141 500 | 200 | 100 |
| 566 799 580 | 157 170.773 381 125 | 160 700 | 100 | 200 |
| 632 199 520 | 175 305.859 417 85 | 179 300 | 200 | 100 |
| 697 599 460 | 193 440.945 454 574 | 197 800 | 100 | 200 |
| 762 999 400 | 211 576.031 491 298 | 216 400 | 200 | 200 |
| 828 399 340 | 229 711.117 528 023 | 235 000 | 200 | 200 |
| 893 799 280 | 247 846.203 564 747 | 253 600 | 200 | 100 |
| 959 199 220 | 265 981.289 601 471 | 272 100 | 200 | 200 |
| 1 024 599 160 | 284 116.375 638 195 | 290 600 | 200 | 200 |
| 1 089 999 100 | 302 251.461 674 92 | 309 200 | 200 | 200 |

TABLE C.46: 4 mm focal spot size images: Measured disk fluence for image quality analysis using conventional method

| Histories | $I_{disk\,theoretical_{LB}}$ $\frac{1}{cm^2}$ | $I_{disk\,measured}$ $\frac{1}{cm^2}$ | $\delta_{-_{I_{disk}}}$ $\frac{1}{cm^2}$ | $\delta_{+_{I_{disk}}}$ $\frac{1}{cm^2}$ |
|---|---|---|---|---|
| 94 466 580 | 26 195.124 275 268 4 | 26 700 | 600 | 600 |
| 186 511 040 | 51 718.606 426 839 6 | 52 700 | 600 | 700 |
| 273 710 960 | 75 898.721 142 472 | 77 700 | 900 | 800 |
| 353 644 220 | 98 063.826 298 468 4 | 100 300 | 600 | 600 |
| 426 310 820 | 118 213.921 894 829 | 120 800 | 600 | 600 |
| 498 977 420 | 138 364.017 491 189 | 141 500 | 900 | 900 |
| 566 799 580 | 157 170.773 381 125 | 161 000 | 1000 | 1000 |
| 632 199 520 | 175 305.859 417 85 | 179 300 | 800 | 700 |
| 697 599 460 | 193 440.945 454 574 | 198 000 | 1000 | 1000 |
| 762 999 400 | 211 576.031 491 298 | 216 300 | 800 | 800 |
| 828 399 340 | 229 711.117 528 023 | 235 000 | 1000 | 1000 |
| 893 799 280 | 247 846.203 564 747 | 253 500 | 900 | 900 |
| 959 199 220 | 265 981.289 601 471 | 272 000 | 1000 | 1000 |
| 1 024 599 160 | 284 116.375 638 195 | 291 000 | 2000 | 1000 |
| 1 089 999 100 | 302 251.461 674 92 | 309 000 | 1000 | 1000 |

TABLE C.47: 4 mm focal spot size images: Measured noise factor for image quality analysis using developed method

| Histories | $\alpha_{theoretical}$ | $\alpha_{measured}$ | $\delta_{-_\alpha}$ | $\delta_{+_\alpha}$ |
|---|---|---|---|---|
| 94 466 580 | 10 000 | 6200 | 600 | 700 |
| 186 511 040 | 10 000 | 10 000 | 200 | 0 |
| 273 710 960 | 10 000 | 10 000 | 100 | 0 |
| 353 644 220 | 10 000 | 9990 | 60 | 10 |
| 426 310 820 | 10 000 | 9980 | 40 | 20 |
| 498 977 420 | 10 000 | 9980 | 30 | 30 |
| 566 799 580 | 10 000 | 9990 | 30 | 30 |
| 632 199 520 | 10 000 | 9990 | 30 | 30 |
| 697 599 460 | 10 000 | 9990 | 40 | 30 |
| 762 999 400 | 10 000 | 9990 | 30 | 40 |
| 828 399 340 | 10 000 | 10 000 | 40 | 30 |
| 893 799 280 | 10 000 | 9990 | 30 | 40 |
| 959 199 220 | 10 000 | 9990 | 30 | 40 |
| 1 024 599 160 | 10 000 | 9990 | 30 | 30 |
| 1 089 999 100 | 10 000 | 9990 | 30 | 30 |

TABLE C.48: 4 mm focal spot size images: Measured noise factor for image quality analysis using conventional method

| Histories | $\alpha_{theoretical}$ | $\alpha_{measured}$ | $\delta_{-_\alpha}$ | $\delta_{+_\alpha}$ |
|---|---|---|---|---|
| 94 466 580 | 10 000 | 10 200 | 300 | 400 |
| 186 511 040 | 10 000 | 10 200 | 300 | 300 |
| 273 710 960 | 10 000 | 10 200 | 200 | 300 |
| 353 644 220 | 10 000 | 10 100 | 300 | 300 |
| 426 310 820 | 10 000 | 10 000 | 300 | 300 |
| 498 977 420 | 10 000 | 10 000 | 200 | 200 |
| 566 799 580 | 10 000 | 10 000 | 300 | 200 |
| 632 199 520 | 10 000 | 10 000 | 200 | 300 |
| 697 599 460 | 10 000 | 10 000 | 300 | 300 |
| 762 999 400 | 10 000 | 10 000 | 300 | 400 |
| 828 399 340 | 10 000 | 10 000 | 200 | 300 |
| 893 799 280 | 10 000 | 10 100 | 400 | 300 |
| 959 199 220 | 10 000 | 10 100 | 400 | 300 |
| 1 024 599 160 | 10 000 | 10 100 | 400 | 400 |
| 1 089 999 100 | 10 000 | 10 100 | 400 | 400 |

TABLE C.49: 4 mm focal spot size images: Measured PSF standard deviation for image quality analysis using developed method

| Histories | $\sigma_{PSF\,LB_{X_F}}$ mm | $\sigma_{PSF\,LB_{detector}}$ mm | $\sigma_{PSF\,measured}$ mm | $\delta_{-\sigma_{PSF}}$ mm | $\delta_{+\sigma_{PSF}}$ mm |
|---|---|---|---|---|---|
| 94 466 580 | 0.189 745 055 995 123 | 0.028 461 758 399 268 5 | 9 | 2 | 1 |
| 186 511 040 | 0.189 745 055 995 123 | 0.028 461 758 399 268 5 | 0.2 | 0.2 | 0.3 |
| 273 710 960 | 0.189 745 055 995 123 | 0.028 461 758 399 268 5 | 0.2 | 0.1 | 0.1 |
| 353 644 220 | 0.189 745 055 995 123 | 0.028 461 758 399 268 5 | 0.18 | 0.04 | 0.07 |
| 426 310 820 | 0.189 745 055 995 123 | 0.028 461 758 399 268 5 | 0.19 | 0.04 | 0.04 |
| 498 977 420 | 0.189 745 055 995 123 | 0.028 461 758 399 268 5 | 0.19 | 0.03 | 0.03 |
| 566 799 580 | 0.189 745 055 995 123 | 0.028 461 758 399 268 5 | 0.18 | 0.02 | 0.03 |
| 632 199 520 | 0.189 745 055 995 123 | 0.028 461 758 399 268 5 | 0.18 | 0.02 | 0.03 |
| 697 599 460 | 0.189 745 055 995 123 | 0.028 461 758 399 268 5 | 0.18 | 0.02 | 0.03 |
| 762 999 400 | 0.189 745 055 995 123 | 0.028 461 758 399 268 5 | 0.18 | 0.02 | 0.03 |
| 828 399 340 | 0.189 745 055 995 123 | 0.028 461 758 399 268 5 | 0.18 | 0.02 | 0.03 |
| 893 799 280 | 0.189 745 055 995 123 | 0.028 461 758 399 268 5 | 0.18 | 0.02 | 0.03 |
| 959 199 220 | 0.189 745 055 995 123 | 0.028 461 758 399 268 5 | 0.18 | 0.02 | 0.03 |
| 1 024 599 160 | 0.189 745 055 995 123 | 0.028 461 758 399 268 5 | 0.19 | 0.02 | 0.01 |
| 1 089 999 100 | 0.189 745 055 995 123 | 0.028 461 758 399 268 5 | 0.19 | 0.02 | 0.01 |

TABLE C.50: 4 mm focal spot size images: Measured PSF standard deviation for image quality analysis using conventional method

| Histories | $\sigma_{PSF\,LB_{X_F}}$ mm | $\sigma_{PSF\,LB_{detector}}$ mm | $\sigma_{PSF\,measured}$ mm | $\delta_{-\sigma_{PSF}}$ mm | $\delta_{+\sigma_{PSF}}$ mm |
|---|---|---|---|---|---|
| 94 466 580 | 0.189 745 055 995 123 | 0.028 461 758 399 268 5 | 0.044 | 0.003 | 0.006 |
| 186 511 040 | 0.189 745 055 995 123 | 0.028 461 758 399 268 5 | 0.06 | 0.03 | 0 |
| 273 710 960 | 0.189 745 055 995 123 | 0.028 461 758 399 268 5 | 0.05 | 0 | 0.11 |
| 353 644 220 | 0.189 745 055 995 123 | 0.028 461 758 399 268 5 | 0.05 | 0.02 | 0.04 |
| 426 310 820 | 0.189 745 055 995 123 | 0.028 461 758 399 268 5 | 0.05 | 0.01 | 0.09 |
| 498 977 420 | 0.189 745 055 995 123 | 0.028 461 758 399 268 5 | 0.04 | 0.01 | 0.11 |
| 566 799 580 | 0.189 745 055 995 123 | 0.028 461 758 399 268 5 | 0.038 | 0.006 | 0 |
| 632 199 520 | 0.189 745 055 995 123 | 0.028 461 758 399 268 5 | 0.06 | 0.03 | 0 |
| 697 599 460 | 0.189 745 055 995 123 | 0.028 461 758 399 268 5 | 0.04 | 0.01 | 0 |
| 762 999 400 | 0.189 745 055 995 123 | 0.028 461 758 399 268 5 | 0.12 | 0.06 | 0 |
| 828 399 340 | 0.189 745 055 995 123 | 0.028 461 758 399 268 5 | 0.11 | 0.04 | 0.01 |
| 893 799 280 | 0.189 745 055 995 123 | 0.028 461 758 399 268 5 | 0.08 | 0.02 | 0.04 |
| 959 199 220 | 0.189 745 055 995 123 | 0.028 461 758 399 268 5 | 0.12 | 0.09 | 0 |
| 1 024 599 160 | 0.189 745 055 995 123 | 0.028 461 758 399 268 5 | 0.08 | 0 | 0.04 |
| 1 089 999 100 | 0.189 745 055 995 123 | 0.028 461 758 399 268 5 | 0.1 | 0.1 | 0 |

TABLE C.51: 4 mm focal spot size images: Frequency at 10% MTF corresponding to measured PSF standard deviation for image quality analysis using developed method

| Histories | $f_{10\%MTF_{UB_{X_F}}}$ $\frac{\text{cycle}}{\text{mm}}$ | $f_{10\%MTF_{UB_{detector}}}$ $\frac{\text{cycle}}{\text{mm}}$ | $f_{10\%MTF_{measured}}$ $\frac{\text{cycle}}{\text{mm}}$ | $\delta_{-_{f_{10\%MTF}}}$ $\frac{\text{cycle}}{\text{mm}}$ | $\delta_{+_{f_{10\%MTF}}}$ $\frac{\text{cycle}}{\text{mm}}$ |
|---|---|---|---|---|---|
| 94 466 580 | 1.8 | 12 | 0.04 | 0.01 | 0.01 |
| 186 511 040 | 1.8 | 12 | 2 | 1 | Inf |
| 273 710 960 | 1.8 | 12 | 2 | 1 | 2 |
| 353 644 220 | 1.8 | 12 | 1.9 | 0.6 | 0.6 |
| 426 310 820 | 1.8 | 12 | 1.8 | 0.3 | 0.5 |
| 498 977 420 | 1.8 | 12 | 1.8 | 0.2 | 0.3 |
| 566 799 580 | 1.8 | 12 | 1.9 | 0.3 | 0.3 |
| 632 199 520 | 1.8 | 12 | 1.9 | 0.3 | 0.2 |
| 697 599 460 | 1.8 | 12 | 1.9 | 0.3 | 0.3 |
| 762 999 400 | 1.8 | 12 | 1.9 | 0.3 | 0.3 |
| 828 399 340 | 1.8 | 12 | 1.9 | 0.3 | 0.3 |
| 893 799 280 | 1.8 | 12 | 1.9 | 0.2 | 0.2 |
| 959 199 220 | 1.8 | 12 | 1.8 | 0.1 | 0.3 |
| 1 024 599 160 | 1.8 | 12 | 1.8 | 0.1 | 0.2 |
| 1 089 999 100 | 1.8 | 12 | 1.8 | 0.1 | 0.2 |

TABLE C.52: 4 mm focal spot size images: Frequency at 10% MTF corresponding to measured PSF standard deviation for image quality analysis using conventional method

| Histories | $f_{10\%MTF_{UB_{X_F}}}$ $\frac{\text{cycle}}{\text{mm}}$ | $f_{10\%MTF_{UB_{detector}}}$ $\frac{\text{cycle}}{\text{mm}}$ | $f_{10\%MTF_{measured}}$ $\frac{\text{cycle}}{\text{mm}}$ | $\delta_{-_{f_{10\%MTF}}}$ $\frac{\text{cycle}}{\text{mm}}$ | $\delta_{+_{f_{10\%MTF}}}$ $\frac{\text{cycle}}{\text{mm}}$ |
|---|---|---|---|---|---|
| 94 466 580 | 1.8 | 12 | 7.7 | 0.8 | 0.7 |
| 186 511 040 | 1.8 | 12 | 6 | 0 | 4 |
| 273 710 960 | 1.8 | 12 | 8 | 6 | 0 |
| 353 644 220 | 1.8 | 12 | 8 | 4 | 4 |
| 426 310 820 | 1.8 | 12 | 6 | 4 | 4 |
| 498 977 420 | 1.8 | 12 | 9 | 7 | 2 |
| 566 799 580 | 1.8 | 12 | 9 | 0 | 2 |
| 632 199 520 | 1.8 | 12 | 6 | 0 | 6 |
| 697 599 460 | 1.8 | 12 | 8 | 0 | 4 |
| 762 999 400 | 1.8 | 12 | 3 | 0 | 2 |
| 828 399 340 | 1.8 | 12 | 3 | 0 | 2 |
| 893 799 280 | 1.8 | 12 | 4 | 1 | 1 |
| 959 199 220 | 1.8 | 12 | 3 | 0 | 9 |
| 1 024 599 160 | 1.8 | 12 | 4 | 1 | 0 |
| 1 089 999 100 | 1.8 | 12 | 3 | 0 | 9 |

## C.5 4 mm focal spot size, 5 cm water depth

Beam Energy: 40 keV.

Beam geometry: diverging.

$X_F$: 4 mm ($f_{10\%MTF}$ = 1.8 cycle/mm).

FOV: 22.5 cm radius circle.

Disk thickness: 0.1 mm.

Water depth: 5 cm.

ROI: $20 \times 20$ cm$^2$.

Pixel size: 0.1 mm ($f_{a_{lim}}$ = 12 cycle/mm).

Bit depth: 16.

Noise assumption for developed method: Poisson.

TABLE C.53: 4 mm focal spot size 5 cm water depth images: cost function for image quality analysis using developed method

| Histories | Cost function |
|---|---|
| 589 333 300 | 4805.412 577 058 41 |
| 1 178 666 600 | 32.477 468 556 523 9 |
| 1 767 999 900 | 8.500 495 674 603 76 |
| 2 357 333 200 | 23.443 538 608 696 |
| 2 946 666 500 | 18.163 782 225 824 9 |
| 3 535 999 800 | 28.536 448 738 038 5 |
| 4 125 333 100 | 43.616 610 989 926 5 |
| 4 714 666 400 | 58.924 965 360 505 6 |
| 5 303 999 700 | 89.202 205 276 644 |
| 5 893 333 000 | 86.236 922 443 479 5 |
| 6 482 666 350 | 122.297 864 832 617 |
| 7 071 999 650 | 143.254 748 955 259 |
| 7 661 332 950 | 148.618 155 590 174 |
| 8 250 666 250 | 173.807 348 717 794 |
| 8 839 999 550 | 161.896 207 478 579 |

TABLE C.54: 4 mm focal spot size 5 cm water depth images: SNR measured using conventional method

| Histories | $SNR_{measured}$ | $\delta_{-_{SNR}}$ | $\delta_{+_{SNR}}$ |
|---|---|---|---|
| 589 333 300 | 3.2 | 0.2 | 0.1 |
| 1 178 666 600 | 4.5 | 0.3 | 0.2 |
| 1 767 999 900 | 5.5 | 0.2 | 0.3 |
| 2 357 333 200 | 6.4 | 0.3 | 0.3 |
| 2 946 666 500 | 7.1 | 0.2 | 0.3 |
| 3 535 999 800 | 7.8 | 0.3 | 0.3 |
| 4 125 333 100 | 8.4 | 0.3 | 0.3 |
| 4 714 666 400 | 9 | 0.3 | 0.3 |
| 5 303 999 700 | 9.6 | 0.3 | 0.3 |
| 5 893 333 000 | 10.1 | 0.3 | 0.3 |
| 6 482 666 350 | 10.6 | 0.3 | 0.3 |
| 7 071 999 650 | 11.1 | 0.3 | 0.3 |
| 7 661 332 950 | 11.5 | 0.3 | 0.3 |
| 8 250 666 250 | 12 | 0.3 | 0.3 |
| 8 839 999 550 | 12.4 | 0.3 | 0.3 |

TABLE C.55: 4 mm focal spot size 5 cm water depth images: Measured radius for image quality analysis using developed method

| Histories | $R_{actual}$ mm | $R_{measured}$ mm | $\delta_{-_R}$ mm | $\delta_{+_R}$ mm |
|---|---|---|---|---|
| 589 333 300 | 5 | 8 | 0.1 | 0 |
| 1 178 666 600 | 5 | 5 | 0.01 | 0.02 |
| 1 767 999 900 | 5 | 5.003 | 0.005 | 0.006 |
| 2 357 333 200 | 5 | 5.003 | 0.005 | 0.004 |
| 2 946 666 500 | 5 | 5.002 | 0.003 | 0.002 |
| 3 535 999 800 | 5 | 5.001 | 0.002 | 0.003 |
| 4 125 333 100 | 5 | 5.002 | 0.003 | 0.002 |
| 4 714 666 400 | 5 | 5.002 | 0.003 | 0.002 |
| 5 303 999 700 | 5 | 5.002 | 0.002 | 0.002 |
| 5 893 333 000 | 5 | 5.002 | 0.002 | 0.002 |
| 6 482 666 350 | 5 | 5.002 | 0.002 | 0.002 |
| 7 071 999 650 | 5 | 5.002 | 0.002 | 0.002 |
| 7 661 332 950 | 5 | 5.002 | 0.002 | 0.002 |
| 8 250 666 250 | 5 | 5.002 | 0.002 | 0.002 |
| 8 839 999 550 | 5 | 5.002 | 0.002 | 0.002 |

TABLE C.56: 4 mm focal spot size 5 cm water depth images: Measured background fluence for image quality analysis using developed method

| Histories | $I_{BG\,theoretical_{LB}}$ $\frac{1}{cm^2}$ | $I_{BG\,measured}$ $\frac{1}{cm^2}$ | $\delta_{-_{I_{BG}}}$ $\frac{1}{cm^2}$ | $\delta_{+_{I_{BG}}}$ $\frac{1}{cm^2}$ |
|---|---|---|---|---|
| 589 333 300 | 96 193.777 505 091 9 | 54 000 | 6000 | 1000 |
| 1 178 666 600 | 192 387.555 010 184 | 264 500 | 300 | 800 |
| 1 767 999 900 | 288 581.332 515 276 | 396 800 | 400 | 300 |
| 2 357 333 200 | 384 775.110 020 368 | 529 000 | 400 | 300 |
| 2 946 666 500 | 480 968.887 525 46 | 661 100 | 200 | 300 |
| 3 535 999 800 | 577 162.665 030 552 | 793 300 | 300 | 200 |
| 4 125 333 100 | 673 356.442 535 644 | 925 500 | 300 | 300 |
| 4 714 666 400 | 769 550.220 040 735 | 1 057 700 | 300 | 300 |
| 5 303 999 700 | 865 743.997 545 827 | 1 189 900 | 300 | 300 |
| 5 893 333 000 | 961 937.775 050 919 | 1 322 100 | 300 | 300 |
| 6 482 666 350 | 1 058 131.560 717 25 | 1 454 300 | 300 | 300 |
| 7 071 999 650 | 1 154 325.338 222 34 | 1 586 500 | 300 | 400 |
| 7 661 332 950 | 1 250 519.115 727 43 | 1 718 800 | 400 | 300 |
| 8 250 666 250 | 1 346 712.893 232 52 | 1 851 000 | 300 | 400 |
| 8 839 999 550 | 1 442 906.670 737 62 | 1 983 200 | 300 | 400 |

TABLE C.57: 4 mm focal spot size 5 cm water depth images: Measured background fluence for image quality analysis using conventional method

| Histories | $I_{BG\,theoretical_{LB}}$ $\frac{1}{cm^2}$ | $I_{BG\,measured}$ $\frac{1}{cm^2}$ | $\delta_{-_{I_{BG}}}$ $\frac{1}{cm^2}$ | $\delta_{+_{I_{BG}}}$ $\frac{1}{cm^2}$ |
|---|---|---|---|---|
| 589 333 300 | 96 193.777 505 091 9 | 130 000 | 2000 | 2000 |
| 1 178 666 600 | 192 387.555 010 184 | 261 000 | 2000 | 2000 |
| 1 767 999 900 | 288 581.332 515 276 | 392 000 | 2000 | 2000 |
| 2 357 333 200 | 384 775.110 020 368 | 523 000 | 3000 | 2000 |
| 2 946 666 500 | 480 968.887 525 46 | 653 000 | 3000 | 3000 |
| 3 535 999 800 | 577 162.665 030 552 | 784 000 | 4000 | 3000 |
| 4 125 333 100 | 673 356.442 535 644 | 914 000 | 4000 | 4000 |
| 4 714 666 400 | 769 550.220 040 735 | 1 045 000 | 5000 | 4000 |
| 5 303 999 700 | 865 743.997 545 827 | 1 176 000 | 5000 | 4000 |
| 5 893 333 000 | 961 937.775 050 919 | 1 306 000 | 4000 | 4000 |
| 6 482 666 350 | 1 058 131.560 717 25 | 1 437 000 | 5000 | 5000 |
| 7 071 999 650 | 1 154 325.338 222 34 | 1 568 000 | 6000 | 5000 |
| 7 661 332 950 | 1 250 519.115 727 43 | 1 698 000 | 6000 | 7000 |
| 8 250 666 250 | 1 346 712.893 232 52 | 1 829 000 | 6000 | 7000 |
| 8 839 999 550 | 1 442 906.670 737 62 | 1 961 000 | 7000 | 6000 |

TABLE C.58: 4 mm focal spot size 5 cm water depth images: Measured disk fluence for image quality analysis using developed method

| Histories | $I_{disk\,theoretical_{LB}}$ $\frac{1}{cm^2}$ | $I_{disk\,measured}$ $\frac{1}{cm^2}$ | $\delta_{-_{I_{disk}}}$ $\frac{1}{cm^2}$ | $\delta_{+_{I_{disk}}}$ $\frac{1}{cm^2}$ |
|---|---|---|---|---|
| 589 333 300 | 18 905.712 057 709 6 | 133 000 | 2000 | 4000 |
| 1 178 666 600 | 37 811.424 115 419 3 | 111 000 | 1000 | 0 |
| 1 767 999 900 | 56 717.136 173 128 9 | 166 200 | 600 | 500 |
| 2 357 333 200 | 75 622.848 230 838 5 | 221 600 | 600 | 500 |
| 2 946 666 500 | 94 528.560 288 548 1 | 277 000 | 300 | 400 |
| 3 535 999 800 | 113 434.272 346 258 | 332 600 | 400 | 400 |
| 4 125 333 100 | 132 339.984 403 967 | 388 000 | 400 | 400 |
| 4 714 666 400 | 151 245.696 461 677 | 443 500 | 400 | 400 |
| 5 303 999 700 | 170 151.408 519 387 | 498 900 | 400 | 500 |
| 5 893 333 000 | 189 057.120 577 096 | 554 500 | 400 | 400 |
| 6 482 666 350 | 207 962.834 238 797 | 609 900 | 400 | 500 |
| 7 071 999 650 | 226 868.546 296 507 | 665 400 | 500 | 400 |
| 7 661 332 950 | 245 774.258 354 217 | 720 800 | 500 | 400 |
| 8 250 666 250 | 264 679.970 411 926 | 776 200 | 400 | 500 |
| 8 839 999 550 | 283 585.682 469 636 | 831 800 | 400 | 400 |

TABLE C.59: 4 mm focal spot size 5 cm water depth images: Measured disk fluence for image quality analysis using conventional method

| Histories | $I_{disk\,theoretical_{LB}}$ $\frac{1}{cm^2}$ | $I_{disk\,measured}$ $\frac{1}{cm^2}$ | $\delta_{-_{I_{disk}}}$ $\frac{1}{cm^2}$ | $\delta_{+_{I_{disk}}}$ $\frac{1}{cm^2}$ |
|---|---|---|---|---|
| 589 333 300 | 18 905.712 057 709 6 | 55 500 | 700 | 600 |
| 1 178 666 600 | 37 811.424 115 419 3 | 111 000 | 1000 | 1000 |
| 1 767 999 900 | 56 717.136 173 128 9 | 166 000 | 2000 | 3000 |
| 2 357 333 200 | 75 622.848 230 838 5 | 222 000 | 3000 | 3000 |
| 2 946 666 500 | 94 528.560 288 548 1 | 277 000 | 3000 | 3000 |
| 3 535 999 800 | 113 434.272 346 258 | 333 000 | 4000 | 3000 |
| 4 125 333 100 | 132 339.984 403 967 | 388 000 | 4000 | 4000 |
| 4 714 666 400 | 151 245.696 461 677 | 443 000 | 4000 | 4000 |
| 5 303 999 700 | 170 151.408 519 387 | 499 000 | 4000 | 4000 |
| 5 893 333 000 | 189 057.120 577 096 | 554 000 | 4000 | 4000 |
| 6 482 666 350 | 207 962.834 238 797 | 609 000 | 3000 | 4000 |
| 7 071 999 650 | 226 868.546 296 507 | 665 000 | 4000 | 3000 |
| 7 661 332 950 | 245 774.258 354 217 | 720 000 | 4000 | 3000 |
| 8 250 666 250 | 264 679.970 411 926 | 775 000 | 3000 | 3000 |
| 8 839 999 550 | 283 585.682 469 636 | 830 000 | 2000 | 3000 |

TABLE C.60: 4 mm focal spot size 5 cm water depth images: Measured noise factor for image quality analysis using developed method

| Histories | $\alpha_{theoretical}$ | $\alpha_{measured}$ | $\delta_{-_\alpha}$ | $\delta_{+_\alpha}$ |
|---|---|---|---|---|
| 589 333 300 | 10 000 | 10 000 | 600 | 0 |
| 1 178 666 600 | 10 000 | 10 000 | 200 | 0 |
| 1 767 999 900 | 10 000 | 9980 | 70 | 70 |
| 2 357 333 200 | 10 000 | 9980 | 60 | 70 |
| 2 946 666 500 | 10 000 | 10 000 | 40 | 60 |
| 3 535 999 800 | 10 000 | 10 020 | 50 | 50 |
| 4 125 333 100 | 10 000 | 10 020 | 50 | 50 |
| 4 714 666 400 | 10 000 | 10 030 | 50 | 50 |
| 5 303 999 700 | 10 000 | 10 030 | 50 | 50 |
| 5 893 333 000 | 10 000 | 10 040 | 50 | 50 |
| 6 482 666 350 | 10 000 | 10 050 | 50 | 50 |
| 7 071 999 650 | 10 000 | 10 050 | 50 | 50 |
| 7 661 332 950 | 10 000 | 10 050 | 50 | 50 |
| 8 250 666 250 | 10 000 | 10 060 | 60 | 50 |
| 8 839 999 550 | 10 000 | 10 070 | 50 | 50 |

TABLE C.61: 4 mm focal spot size 5 cm water depth images: Measured noise factor for image quality analysis using conventional method

| Histories | $\alpha_{theoretical}$ | $\alpha_{measured}$ | $\delta_{-_\alpha}$ | $\delta_{+_\alpha}$ |
|---|---|---|---|---|
| 589 333 300 | 10 000 | 10 000 | 300 | 300 |
| 1 178 666 600 | 10 000 | 10 100 | 500 | 500 |
| 1 767 999 900 | 10 000 | 10 100 | 400 | 400 |
| 2 357 333 200 | 10 000 | 10 000 | 300 | 400 |
| 2 946 666 500 | 10 000 | 10 100 | 400 | 300 |
| 3 535 999 800 | 10 000 | 10 000 | 200 | 300 |
| 4 125 333 100 | 10 000 | 10 100 | 300 | 200 |
| 4 714 666 400 | 10 000 | 10 000 | 300 | 300 |
| 5 303 999 700 | 10 000 | 10 000 | 300 | 300 |
| 5 893 333 000 | 10 000 | 10 000 | 300 | 300 |
| 6 482 666 350 | 10 000 | 10 000 | 300 | 300 |
| 7 071 999 650 | 10 000 | 9900 | 200 | 300 |
| 7 661 332 950 | 10 000 | 10 000 | 300 | 300 |
| 8 250 666 250 | 10 000 | 10 000 | 300 | 200 |
| 8 839 999 550 | 10 000 | 10 000 | 300 | 300 |

TABLE C.62: 4 mm focal spot size 5 cm water depth images: Measured PSF standard deviation for image quality analysis using developed method

| Histories | $\sigma_{PSF\,LB_{X_F}}$ mm | $\sigma_{PSF\,LB_{detector}}$ mm | $\sigma_{PSF\,measured}$ mm | $\delta_{-\sigma_{PSF}}$ mm | $\delta_{+\sigma_{PSF}}$ mm |
|---|---|---|---|---|---|
| 589 333 300 | 0.189 745 055 995 123 | 0.028 461 758 399 268 5 | 1 | 1 | 4 |
| 1 178 666 600 | 0.189 745 055 995 123 | 0.028 461 758 399 268 5 | 0.2 | 0.2 | 0.8 |
| 1 767 999 900 | 0.189 745 055 995 123 | 0.028 461 758 399 268 5 | 0.3 | 0.3 | 0.2 |
| 2 357 333 200 | 0.189 745 055 995 123 | 0.028 461 758 399 268 5 | 0.3 | 0.2 | 0.1 |
| 2 946 666 500 | 0.189 745 055 995 123 | 0.028 461 758 399 268 5 | 0.2 | 0.1 | 0.1 |
| 3 535 999 800 | 0.189 745 055 995 123 | 0.028 461 758 399 268 5 | 0.2 | 0.08 | 0.09 |
| 4 125 333 100 | 0.189 745 055 995 123 | 0.028 461 758 399 268 5 | 0.2 | 0.07 | 0.07 |
| 4 714 666 400 | 0.189 745 055 995 123 | 0.028 461 758 399 268 5 | 0.2 | 0.07 | 0.07 |
| 5 303 999 700 | 0.189 745 055 995 123 | 0.028 461 758 399 268 5 | 0.2 | 0.06 | 0.06 |
| 5 893 333 000 | 0.189 745 055 995 123 | 0.028 461 758 399 268 5 | 0.19 | 0.05 | 0.06 |
| 6 482 666 350 | 0.189 745 055 995 123 | 0.028 461 758 399 268 5 | 0.19 | 0.05 | 0.05 |
| 7 071 999 650 | 0.189 745 055 995 123 | 0.028 461 758 399 268 5 | 0.19 | 0.05 | 0.05 |
| 7 661 332 950 | 0.189 745 055 995 123 | 0.028 461 758 399 268 5 | 0.19 | 0.04 | 0.05 |
| 8 250 666 250 | 0.189 745 055 995 123 | 0.028 461 758 399 268 5 | 0.19 | 0.04 | 0.05 |
| 8 839 999 550 | 0.189 745 055 995 123 | 0.028 461 758 399 268 5 | 0.19 | 0.04 | 0.04 |

TABLE C.63: 4 mm focal spot size 5 cm water depth images: Measured PSF standard deviation for image quality analysis using conventional method

| Histories | $\sigma_{PSF\,LB_{X_F}}$ mm | $\sigma_{PSF\,LB_{detector}}$ mm | $\sigma_{PSF\,measured}$ mm | $\delta_{-\sigma_{PSF}}$ mm | $\delta_{+\sigma_{PSF}}$ mm |
|---|---|---|---|---|---|
| 589 333 300 | 0.189 745 055 995 123 | 0.028 461 758 399 268 5 | 0.1 | 0.06 | 0 |
| 1 178 666 600 | 0.189 745 055 995 123 | 0.028 461 758 399 268 5 | 0.02 | 0 | 0.03 |
| 1 767 999 900 | 0.189 745 055 995 123 | 0.028 461 758 399 268 5 | 0.04 | 0 | 0.02 |
| 2 357 333 200 | 0.189 745 055 995 123 | 0.028 461 758 399 268 5 | 0.05 | 0.02 | 0 |
| 2 946 666 500 | 0.189 745 055 995 123 | 0.028 461 758 399 268 5 | 0.04 | 0.02 | 0 |
| 3 535 999 800 | 0.189 745 055 995 123 | 0.028 461 758 399 268 5 | 0.04 | 0 | 0.02 |
| 4 125 333 100 | 0.189 745 055 995 123 | 0.028 461 758 399 268 5 | 0.04 | 0.01 | 0.02 |
| 4 714 666 400 | 0.189 745 055 995 123 | 0.028 461 758 399 268 5 | 0.03 | 0 | 0.01 |
| 5 303 999 700 | 0.189 745 055 995 123 | 0.028 461 758 399 268 5 | 0.04 | 0.02 | 0 |
| 5 893 333 000 | 0.189 745 055 995 123 | 0.028 461 758 399 268 5 | 0.05 | 0 | 0.04 |
| 6 482 666 350 | 0.189 745 055 995 123 | 0.028 461 758 399 268 5 | 0.04 | 0 | 0.09 |
| 7 071 999 650 | 0.189 745 055 995 123 | 0.028 461 758 399 268 5 | 0.03 | 0 | 0.15 |
| 7 661 332 950 | 0.189 745 055 995 123 | 0.028 461 758 399 268 5 | 0.2 | 0.1 | 0 |
| 8 250 666 250 | 0.189 745 055 995 123 | 0.028 461 758 399 268 5 | 0.125 | 0.003 | 0.004 |
| 8 839 999 550 | 0.189 745 055 995 123 | 0.028 461 758 399 268 5 | 0.05 | 0 | 0.05 |

TABLE C.64: 4 mm focal spot size 5 cm water depth images: Frequency at 10% MTF corresponding to measured PSF standard deviation for image quality analysis using developed method

| Histories | $f_{10\%MTF_{UB_{X_F}}}$ $\frac{\text{cycle}}{\text{mm}}$ | $f_{10\%MTF_{UB_{detector}}}$ $\frac{\text{cycle}}{\text{mm}}$ | $f_{10\%MTF_{measured}}$ $\frac{\text{cycle}}{\text{mm}}$ | $\delta_{-_{f_{10\%MTF}}}$ $\frac{\text{cycle}}{\text{mm}}$ | $\delta_{+_{f_{10\%MTF}}}$ $\frac{\text{cycle}}{\text{mm}}$ |
|---|---|---|---|---|---|
| 589 333 300 | 1.8 | 12 | 0.3 | 0.2 | Inf |
| 1 178 666 600 | 1.8 | 12 | 1.501 790 754 422 18 | 1 | 8 |
| 1 767 999 900 | 1.8 | 12 | 1 | 0 | 7 |
| 2 357 333 200 | 1.8 | 12 | 1 | 0 | 3 |
| 2 946 666 500 | 1.8 | 12 | 1 | 0 | 2 |
| 3 535 999 800 | 1.8 | 12 | 2 | 1 | 1 |
| 4 125 333 100 | 1.8 | 12 | 1.7 | 0.4 | 0.9 |
| 4 714 666 400 | 1.8 | 12 | 1.7 | 0.4 | 0.9 |
| 5 303 999 700 | 1.8 | 12 | 1.7 | 0.4 | 0.7 |
| 5 893 333 000 | 1.8 | 12 | 1.8 | 0.4 | 0.7 |
| 6 482 666 350 | 1.8 | 12 | 1.8 | 0.4 | 0.7 |
| 7 071 999 650 | 1.8 | 12 | 1.8 | 0.4 | 0.6 |
| 7 661 332 950 | 1.8 | 12 | 1.8 | 0.4 | 0.5 |
| 8 250 666 250 | 1.8 | 12 | 1.8 | 0.4 | 0.4 |
| 8 839 999 550 | 1.8 | 12 | 1.8 | 0.3 | 0.5 |

TABLE C.65: 4 mm focal spot size 5 cm water depth images: Frequency at 10% MTF corresponding to measured PSF standard deviation for image quality analysis using conventional method

| Histories | $f_{10\%MTF_{UB_{X_F}}}$ $\frac{\text{cycle}}{\text{mm}}$ | $f_{10\%MTF_{UB_{detector}}}$ $\frac{\text{cycle}}{\text{mm}}$ | $f_{10\%MTF_{measured}}$ $\frac{\text{cycle}}{\text{mm}}$ | $\delta_{-_{f_{10\%MTF}}}$ $\frac{\text{cycle}}{\text{mm}}$ | $\delta_{+_{f_{10\%MTF}}}$ $\frac{\text{cycle}}{\text{mm}}$ |
|---|---|---|---|---|---|
| 589 333 300 | 1.8 | 12 | 3 | 0 | 6 |
| 1 178 666 600 | 1.8 | 12 | 15 | 9 | 0 |
| 1 767 999 900 | 1.8 | 12 | 8 | 2 | 1 |
| 2 357 333 200 | 1.8 | 12 | 7 | 0 | 6 |
| 2 946 666 500 | 1.8 | 12 | 10 | 1 | 4 |
| 3 535 999 800 | 1.8 | 12 | 9 | 3 | 0 |
| 4 125 333 100 | 1.8 | 12 | 10 | 4 | 3 |
| 4 714 666 400 | 1.8 | 12 | 12 | 3 | 0 |
| 5 303 999 700 | 1.8 | 12 | 10 | 2 | 4 |
| 5 893 333 000 | 1.8 | 12 | 6 | 2 | 2 |
| 6 482 666 350 | 1.8 | 12 | 8 | 5 | 0 |
| 7 071 999 650 | 1.8 | 12 | 11 | 9 | 2 |
| 7 661 332 950 | 1.8 | 12 | 2 | 0 | 4 |
| 8 250 666 250 | 1.8 | 12 | 2.73 | 0.07 | 0.07 |
| 8 839 999 550 | 1.8 | 12 | 8 | 5 | 0 |

# Bibliography

[1] D. J. Brenner and E. J. Hall, "Computed Tomography — An Increasing Source of Radiation Exposure," *The New England Journal of Medicine*, vol. 357, no. 22, pp. 2277–2284, 2007.

[2] V. A. Gurvich, A. K. Jones, and C. G. Orton, "Physical characterization of the quality of medical images does not adequately re fl ect their clinical quality," *Medical Physics*, vol. 44, no. 10, pp. 4985–4988, 2017.

[3] A. D. Crop, P. Smeets, T. V. Hoof, M. Vergauwen, T. Dewaele, M. V. Borsel, E. Achten, K. Verstraete, K. D'Herde, H. Thierens, and K. Bacher, "Correlation of clinical and physical-technical image quality in chest CT : a human cadaver study applied on iterative reconstruction," *BMC Medical Imaging*, vol. 15, no. 1, 2015. [Online]. Available: http://dx.doi.org/10.1186/s12880-015-0075-y

[4] D. R. Dance, S. Christofides, A. D. A. Maidment, I. D. Mclean, and K. H. Ng, *Diagnostic Radiology Physics: A handbook for teachers and students*. International Atomic Energy Agency, 2014.

[5] J. E. Gray, M. P. Capp, and F. R. Whitehead, "An improved technique for x-ray image evaluation. The two dimensional modulation transfer function." pp. 252–261, 1974.

[6] G. U. Rao and L. M. Bates, "Effective dimensions of roentgen tube focal spots based on measurement of the modulation transfer function," *Acta Radiologica: Therapy, Physics, Biology*, vol. 9, no. 4, pp. 362–368, 1970.

[7] G. U. V. RAO, "A new method to determine the focal spot size of x-ray tubes." *The American journal of roentgenology, radium therapy, and nuclear*

*medicine*, vol. 111, no. 3, pp. 628–633, 1971. [Online]. Available: https://www.ajronline.org/doi/abs/10.2214/ajr.111.3.628

[8] H. K. Genant, K. C. Doi, and J. C. Mall, "Optical versus radiographic magnification for fine-detail skeletal radiography," *Investigative Radiology*, vol. 10, no. 2, pp. 160–172, 1975.

[9] G. U. V. RAO, "Image contrast of sinusoidal signals," *The American journal of roentgenology, radium therapy, and nuclear medicine*, vol. 118, no. 2, pp. 293–299, 1973. [Online]. Available: http://ieeexplore.ieee.org/search/srchabstract.jsp?arnumber=5264301

[10] N. J. Schneiders and S. C. Bushong, "Single-step calculation of the MTF from the ERF," pp. 31–33, 1978.

[11] "Characteristics of digital x-ray imaging devices—Part 1: Determination of the detective quantum efficiency," 2003.

[12] P. F. Judy, "The line spread function and modulation transfer function of a computer tomography scanner," *Medical Physics*, vol. 3, no. 4, pp. 233–236, 1976.

[13] S. W. Smith, "Special Imaging Techniques," in *The Scientist and Engineer's Guide to Digital Signal Processing*. California Technical Publishing, 1997, pp. 423–450.

[14] A. E. Burgess, "The Rose model , revisited," *Journal of the Optical Society of America. A, Optics, image, science, and vision.*, vol. 16, no. 3, pp. 633–646, 1999.

[15] K. Rossmann, "Measurement of the Modulation Transfer Function of Radiographic Systems Containing Fluorescent Screens," *Physics in Medicine and Biology*, vol. 9, no. 4, pp. 551–557, 1964.

[16] A. Carton, D. Vandenbroucke, L. Struye, A. D. A. Maidment, Y. Kao, M. Albert, H. Bosmans, and G. Marchal, "Validation of MTF measurement for digital mammography quality control," *Medical Physics*, vol. 32, no. 6, pp. 1684–1695, 2005.

[17] S. N. Friedman and I. A. Cunningham, "Normalization of the modulation transfer function : The open-field approach," *Medical Physics*, vol. 35, no. 10, pp. 4443–4449, 2008.

[18] E. Samei, N. T. Ranger, J. T. Dobbins III, and Y. Chen, "Intercomparison of methods for image quality characterization . I . Modulation transfer function," *Medical Physics*, vol. 33, no. 5, pp. 1454–1465, 2006.

[19] A. Staude and J. Goebbels, "Determining the Spatial Resolution in Computed Tomography – Comparison of MTF and Line-Pair Structures," 2011.

[20] R. K. Doot, J. S. Scheuermann, P. E. Christian, J. S. Karp, and P. E. Kinahan, "Instrumentation factors affecting variance and bias of quantifying tracer uptake with PET / CT," *Medical Physics*, vol. 37, no. 11, pp. 6035–6046, 2010.

[21] N. E. Makris, M. C. Huisman, P. E. Kinahan, A. A. Lammertsma, and R. Boellaard, "Evaluation of strategies towards harmonization of FDG PET / CT studies in multicentre trials : comparison of scanner validation phantoms and data analysis procedures," *European Journal of Nuclear Medicine and Molecular Imaging*, vol. 40, pp. 1507–1515, 2013.

[22] K. Gulliksrud, C. Stokke, and A. C. Trægde Martinsen, "How to measure CT image quality : Variations in CT-numbers , uniformity and low contrast resolution for a CT quality assurance phantom," *Physica Medica*, vol. 30, no. 4, pp. 521–526, 2014. [Online]. Available: http://dx.doi.org/10.1016/j.ejmp.2014.01.006

[23] B. Donini, S. Rivetti, N. Lanconelli, and M. Bertolini, "Free software for performing physical analysis of systems for digital radiography and mammography," *Medical Physics*, vol. 41, no. 5, pp. 1–10, 2014.

[24] J. Winslow, Y. Zhang, and E. Samei, "A method for characterizing and matching CT image quality across CT scanners from different manufacturers," *Medical Physics*, vol. 44, no. 11, pp. 5705–5717, 2017.

[25] P. Monnin, F. R. Verdun, H. Bosmans, S. R. Perez, and N. W. Marshall, "A comprehensive model for x-ray projection imaging system efficiency and image quality characterization in the presence of scattered radiation," *Physics in Medicine and Biology*, vol. 62, pp. 5691–5722, 2017.

[26] G. Pahn, S. Skornitzke, H.-p. Schlemmer, H.-u. Kauczor, and W. Stiller, "Physica Medica Toward standardized quantitative image quality ( IQ ) assessment in computed tomography ( CT ): A comprehensive framework for automated and comparative IQ analysis based on ICRU Report 87," *Physica Medica*, vol. 32, pp. 104–115, 2016. [Online]. Available: http://dx.doi.org/10.1016/j.ejmp.2015.09.017

[27] L. A. Pierce II, D. W. Byrd, B. F. Elston, J. S. Karp, J. J. Sunderland, and P. E. Kinahan, "An algorithm for automated ROI definition in water or epoxy-filled NEMA NU-2 image quality phantoms," *JOURNAL OF APPLIED CLINICAL MEDICAL PHYSICS*, vol. 17, no. 1, pp. 440–456, 2016.

[28] R. Andrae, T. Schulze-Hartung, and P. Melchior, "Dos and don'ts of reduced chi-squared," *arXiv e-prints*, pp. 1–12, 2010. [Online]. Available: http://arxiv.org/abs/1012.3754

[29] I. Kawrakow, E. Mainegra-Hing, D. W. O. Rogers, F. Tessier, and B. R. B. Walters, "The EGSnrc Code System: Monte Carlo Simulation of Electron and Photon Transport," 2018. [Online]. Available: http://nrc-cnrc.github.io/EGSnrc/doc/pirs701-egsnrc.pdf

[30] D. W. O. Rogers, I. Kawrakow, J. P. Seuntjens, B. R. B. Walters, and E. Mainegra-Hing, "NRC user codes for EGSnrc," 2018. [Online]. Available: http://www.lcr.uerj.br/Manual{_}ABFM/technicalreportPIRS-702revB.pdf

[31] THE INTERNATIONAL COMMISSION ON RADIATION UNITS AND MEASUREMENTS, "RADIATION DOSE AND IMAGE-QUALITY ASSESSMENT IN COMPUTED," *Journal of the ICRU*, vol. 12, no. 1, 2012.

[32] E. Samei, M. J. Flynn, and D. A. Reimann, "A method for measuring the pre-sampled MTF of digital radiographic systems using an edge test device," *Medical Physics*, vol. 25, no. 1, pp. 102–113, 1998.